NUCLEAR WEAK INTERACTION RATES DURING STELLAR EVOLUTION AND COLLAPSE

Thesis by

George Michael Fuller

In Partial Fulfillment of the Requirements

For the Degree of

Doctor of Philosophy

California Institute of Technology

Pasadena, California

1981

(Submitted May 1, 1981)

ACKNOWLEDGMENTS

I would like to thank the people at the Kellogg Radiation Laboratory for providing me with friendship, help, and a stimulating scientific environment. In particular, I thank all the members of the Kellogg technical and secretarial staff. Special thanks go to Evaline Gibbs and Marty Watson for their vigilant assistance in dealing with matters of business and WAF, and to Jan Rasmussen for the expert typing and preparation of much of this thesis. The members of the faculty provided me with excellent teaching and sound advice on my research. The advice of Steve Koonin is particularly appreciated.

My friends over the years have done much to ease the ordeal of studentdom. Barb Cooper, Jack Stemple, Dave Tubbs, and Harold Wilson, among many were the source of much encouragement. My mind and body would have gone long before they did had not Dave and Jean Kodama occasionally dragged me, kicking and screaming, on various mountain/pizza flicks.

Tom Weaver and Stan Woosley have had a profound influence on this work. Stan's enthusiasm for nuclear astrophysics is without bound and his constant reminders of the necessity of this project were helpful. Stan was the one who got me into this nasty stuff while I was still an undergraduate. Stu Bloom has added greatly to my knowledge of the "practical" shell model. Of course, I want to thank crazy Mike Newman, friend and coauthor on several papers. Mike's mathematical and computational expertise are gratefully acknowledged.

Finally, the most enriching aspect of my years at Caltech has come in working with Professor William A. Fowler, my advisor and mentor. This man has an insight into the workings of nature that defies description. Willy has patiently taught me how to do research in physics. Throughout my undergraduate and graduate student years he provided a source of ebullient encouragement, keen physical intuition, and practical nuclear physics know-how. I count myself as very fortunate to have been his student.

The Fannie and John Hertz Foundation Fellowship which has supported me for the tenure of my graduate career is most gratefully acknowledged. I also wish to acknowledge the hospitality of both the Lawrence Livermore and Los Alamos National Laboratories.

I dedicate this thesis to God and to my parents. To God for having created an absurd, albeit fascinating, universe and for not having turned me into a pillar of salt, despite ample provocation! To my parents for having nurtured my early interests in science and providing crucial support in times of need. I owe them everything.

ABSTRACT

Nuclear weak interaction rates, including electron and positron emission rates, and continuum electron and positron capture rates, as well as the associated ν and $\overline{\nu}$ energy loss rates are calculated on a detailed grid of temperature and density for the free nucleons and 226 nuclei with masses between A = 21 and 60. Gamow-Teller and Fermi discrete-state transition matrix element systematics and the Gamow-Teller $T^{<} \rightleftarrows T^{>}$ resonance transitions are discussed in depth and are implemented in the stellar rate calculations. Results of the calculations are presented on an abbreviated grid of temperature and density and comparison is made to terrestrial weak transition rates where possible. Neutron shell blocking of allowed electron capture on heavy nuclei during stellar core collapse is discussed along with several unblocking mechanisms operative at high temperature and density. The results of one-zone collapse calculations are presented which suggest that the effect of neutron shell blocking is to produce a larger core lepton fraction at neutrino trapping which leads to a larger inner-core mass and hence a stronger post-bounce shock.

TABLE OF CONTENTS

TABLE OF CONTENTS (Cont.)

I. INTRODUCTION

Weak interaction processes involving nuclei are important in many phases of stellar evolution, stellar core collapse, and possibly ensuing supernovae explosions. Cooling by URCA neutrino emission is sometimes important for the determination of local temperature and density environments, which in turn influence subsequent evolution and nuclear burning characteristics. Weak transitions between nuclei involving one, or several, of electron or positron emission and electron or positron capture, can be important in determining the nucleosynthesis in any astrophysical process, and are especially important in this regard at the high temperatures and densities encountered in the stellar interior.

Past treatments of the stellar nuclear weak interaction rate problem are reviewed and discussed at the beginning of chapters II (F^2N I) and III (F^2N II). The work embodied in this thesis goes beyond previous attempts at solution of the high temperature, high density nuclear weak rate problem in that it includes, for the first time, a consistent systematic treatment of the $T^< \rightarrow T^>$ and $T^> \rightarrow T^<$ Gamow-Teller resonances, as well as making use of a large amount of recent nuclear level and weak matrix element data. The results of the calculations described here are already finding use in studies of nucleosynthesis during stellar evolution and collapse (Thielemann and Arnett 1981, Weaver and Woosley 1981). It is thus appropriate to give a very cursory overview of present ideas on the late stages of stellar evolution and supernova formation, with a commentary on where the most likely application of these nuclear weak interaction rates may occur.

It is currently held that stars of less than about 8 $M_\odot$ and undergoing normal evolution will experience considerable mass loss through

pulsation and winds and eventually become white dwarfs. Typical stars between 8 and 70 $M_{\odot}$ are thought to form unstable iron cores which collapse to possibly form type II supernovae (hereafter SN II), leaving behind a neutron star or black hole remnant (Wheeler 1981). The origin of type I supernovae (hereafter SN I) is unclear, but is widely believed to result from the thermonuclear explosion, and complete disruption of either massive young stars (see e.g., Woosley et al. 1980), accreting white dwarfs (see e.g., Nomoto 1980 and Arnett 1969), or old, abnormally evolving stars (Wheeler 1978).

The supernovae observed in this and external galaxies are classified as either SN I or II by their spectra. SN II show roughly solar abundances of hydrogen and heavy elements (cf. Kirshner et al. 1973), have characteristic expansion velocities of 5000 km s^{-1}, and absolute magnitudes at peak brightness of between $M_V \sim -17$ to $M_V \sim -19$. The light curves of SN II are consistent with a point explosion in a tenuous red giant envelope, but the lack of homogeneity in these light curves indicates a large range of possible envelope configurations. SN II are seen principally in the spiral arms of galaxies and not seen in ellipticals, indicating that their progenitors are likely massive, recently formed population I stars (Wheeler 1981).

In contrast, SN I have hydrogen deficient spectra (cf. Kirschner et al. 1973, Kirshner and Oke 1975) and show a long exponentially decaying light curve which probably occurs via the radioactive decay of roughly 0.5-1 $M_{\odot}$ of ^{56}Ni (Axelrod 1980) injected during the supernova event. SN I have peak absolute magnitudes of about $M_V \sim -18$ and characteristic expansion velocities of about 11,000 km/s. These supernovae occur in galaxies of all morphological types and are not confined to spiral arms.

The evolution of the supposed massive progenitors of SN II has been studied by Weaver and Woosley (1980), Arnett (1978), and Arnett (1980). The core of the massive star is thought to pass sequentially through hydrogen, helium, carbon/oxygen, neon, and silicon burning. The abundances of the nuclear species and the temperatures in these various burning phases are influenced by nuclear weak transition rates and by the associated neutrino energy loss rates. Neutrino energy losses due to nuclear weak processes are, for example, quite important during carbon and oxygen burning, as pointed out by Woosley, Arnett, and Clayton (1972). Considerable neutronization is thought to occur even before the onset of silicon burning. Weaver and Woosley (1979) have found that some of the electron capture/positron emission transitions discussed in chapter II help make ^{30}Si rather than ^{28}Si, the dominant Si isotope at the onset of silicon burning with interesting modifications in the subsequent core evolution.

Electron capture on heavy nuclei during the collapse of the iron core of a massive star plays an important role in determining the outcome of that collapse. Considerable controversy surrounds the rates of these electron capture reactions (Bethe et al. 1979) at the very high densities and temperatures characteristic of core collapse. Chapter V presents an exposition of the neutron shell blocking of electron capture on heavy nuclei. It is shown in that work that neutron shell blocking may result in a considerable reduction of the overall neutronization rate in the collapsing stellar core, with a concomitant increase in the inner-core mass and hence a possibly larger post-bounce shock strength.

Though the influence of SN II on the overall chemical evolution of the galaxy is not known, it seems clear that SN II are probably responsible for most of the present oxygen abundance, as well as a good deal of

the explosive nucleosynthesis products. Many nuclei from carbon to the iron-peak are, however, produced during the quasi-static presupernova burning phases of stellar evolution and then ejected into the interstellar medium in the supernova explosion (Arnett 1973, Arnett 1978, Woosley and Weaver 1980). The relative abundances of nuclei produced in these quasi-static burning phases frequently depend on stellar nuclear weak transition rates at high temperature and density. What iron-peak elements are ejected in SN II explosions depends sensitively on the mass cut in the collapsing stellar core (Woosley and Weaver 1980) and this, in turn, may depend on the blocking effect mentioned above.

It is widely believed that a good deal of the iron-peak nucleosynthesis may have its origin in the thermonuclear explosion of stellar cores associated with SN I (see Wheeler 1981 and references therein). As pointed out above, SN I may result from a variety of proposed processes which share certain characteristics. In particular, SN I may involve the high temperature, high density combustion of carbon or oxygen. Neutrino losses associated with the convective URCA process are important in determining the characteristic of this burning (Couch and Arnett 1973). In some of these models, collapse of the degenerate core may be initiated by electron capture on intermediate mass nuclei before thermonuclear runaway takes place (Couch and Arnett 1973; Wheeler, Buchler, and Barkat 1973; Bruenn 1973; and Iben 1978). Certainly nuclear weak interaction rates help determine the elemental and isotopic abundances which would result from the disruption of a large fraction of the mass of the star.

Recent observations of the Cas A supernova remnant show knots of what appear to be freshly synthesized heavy elements, mainly the products

of oxygen burning: O, Ne, Si, S, Ar, and Ca (see Wheeler 1981 and references therein). Though it is not clear whether Cas A corresponds to SN I or SN II (there was no recorded optical outburst) the evidence for nucleosynthesis in supernovae is exciting. Other observations show enhanced abundances of oxygen burning products and silicon peak elements in what are thought to be SN I remnants: SN 1006, Kepler, and Tycho.

I feel that the most immediate and fruitful applications of the nuclear weak rates described in this thesis will be in nucleosynthesis calculations in models of SN I, determination of presupernova evolution characteristics and abundances in massive SN II progenitor stars, and in pinning down the dynamics of the supernova mechanism.

Chapter II (F^2N I) outlines the problems associated with the calculation of nuclear weak interaction rates in the stellar interior, including the handling of large numbers of nuclear parent and daughter states, the systematics of discrete-state-transition Gamow-Teller and Fermi matrix elements, and the numerical problems inherent in treating an electron gas of arbitrary degeneracy. The rate calculations described there are particularly important in calculating neutronization and neutrino loss characteristics of a massive presupernova star.

The discussion in chapter III (F^2N II) extends the calculations described in chapter II to include electron and positron emission and electron and positron capture rates, as well as the associated ν and $\bar{\nu}$ energy loss rates, for the free nucleons and 226 nuclei between masses 20 and 60. These calculations include the contribution of the Gamow-Teller resonances which, as described in the text, have very different characteristics for $T^< \rightarrow T^>$ and $T^> \rightarrow T^<$ transitions. These resonance transitions and the techniques used to implement them in the stellar rate calculations are

discussed.

The results of these calculations are discussed in chapter IV (F^2N III). The range of validity of these calculations is discussed and the low temperature, low density rates are compared with tables of known terrestrial weak decay rates. Abbreviated tables of the stellar rates are presented.

The last chapter discusses the neutron shell blocking of electron capture on heavy nuclei during stellar core collapse. This effect is shown to have interesting consequences for the outcome of stellar core collapse, as discussed above.

An appendix provides an outline of shell model calculations of Gamow-Teller strength functions which serve to support the resonance systematics discussed in chapter III.

REFERENCES

Arnett, W. D. 1969, Ap. Space Sci., 5, 180.

Arnett, W. D. 1973, Ann. Rev. Astr. Ap., 11, 73.

Arnett, W. D. 1978, Ap. J., 219, 1008.

Arnett, W. D. 1980, Ann. N.Y. Acad. Sci., 336, 366.

Axelrod, T. S. 1980, Ph.D. thesis, University of California at Santa Cruz, preprint UCRL-52994.

Bethe, H. A., Brown, G. E., Applegate, J., and Lattimer, J. M. 1979, Nucl. Phys., A324, 487.

Bruenn, S. W. 1973, Ap. J. (Letters), 183, L125.

Couch, R. G., and Arnett, W. D. 1973, Ap. J. (Letters), 180, L101.

Iben, I., Jr. 1978, Ap. J., 226, 996.

Kirschner, R. P., Oke, J. B., Penston, M. V., and Searle, S. 1973, Ap. J., 185, 303.

Kirschner, R. P., and Oke, J. B. 1975, Ap. J., 200, 574.

Nomoto, K. 1980, Proceedings of the Texas Workshop on Type-I Supernovae, ed. J. C. Wheeler (Austin: University of Texas Press).

Thielemann, F. K., and Arnett, W. D. 1981, in preparation.

Weaver, T. A., and Woosley, S. E. 1979, private communication.

Weaver, T. A., and Woosley, S. E. 1980, Ann. N.Y. Acad. Sci., 336, 335.

Weaver, T. A., and Woosley, S. E. 1981, in preparation.

Wheeler, J. C. 1978, Ap. J., 225, 212.

Wheeler, J. C. 1981, to be published in Reports on Progress in Physics.

Wheeler, J. C., Buchler, J. R., and Barkat, Z. K. 1973, Ap. J., 184, 997.

Woosley, S. E., Arnett, W. D., and Clayton, D. D. 1972, Ap. J., 175, 731.

Woosley, S. E., and Weaver, T. A. 1980, preprint UCRL-84527.

Woosley, S. E., Weaver, T. A., and Taam R. E. 1980, preprint UCRL-84544.

II. THE STELLAR WEAK INTERACTION RATE PROBLEM

THE ASTROPHYSICAL JOURNAL SUPPLEMENT SERIES, 42:447–473, 1980 March

STELLAR WEAK-INTERACTION RATES FOR *sd*-SHELL NUCLEI. I. NUCLEAR MATRIX ELEMENT SYSTEMATICS WITH APPLICATION TO ^{26}Al AND SELECTED NUCLEI OF IMPORTANCE TO THE SUPERNOVA PROBLEM[1]

GEORGE M. FULLER[2] AND WILLIAM A. FOWLER
W. K. Kellogg Radiation Laboratory, California Institute of Technology
AND
MICHAEL J. NEWMAN
Max-Planck-Institut für Physik und Astrophysik; and Theoretical Division, Los Alamos Scientific Laboratory[3]
Received 1979 July 19; accepted 1979 September 14

ABSTRACT

Astrophysical positron emission, continuum electron capture, and neutrino energy loss rates are calculated for $^{26}\text{Al}\rightarrow{}^{26}\text{Mg}$, $^{30}\text{P}\rightarrow{}^{30}\text{Si}$, $^{31}\text{S}\rightarrow{}^{31}\text{P}$, $^{32}\text{S}\rightarrow{}^{32}\text{P}$, $^{33}\text{S}\rightarrow{}^{33}\text{P}$, and $^{35}\text{Cl}\rightarrow{}^{35}\text{S}$. Measured nuclear level information and matrix elements are used where available. Unmeasured matrix elements for allowed transitions are assigned on the basis of simple shell model arguments and the results of detailed large-scale shell model calculations by Wildenthal and his collaborators. The experimentally determined matrix elements are found to dominate the rates over most of the range of temperatures and densities considered. The uncertainties in the rates are estimated. Appropriate average matrix elements for unmeasured Gamow-Teller transitions are estimated for use in other *sd*-shell nuclei. The rates presented agree roughly with those of Hansen over a wide range of conditions, but potentially important differences in the rates exist at temperatures and densities relevant for the production and destruction of ^{26}Al and for neutronization and neutrino loss in the late stages of presupernova evolution.

Subject headings: neutrinos — nuclear reactions — stars:

I. INTRODUCTION

The problem of nuclear β decay in the stellar environment has been an active area of investigation for many years. Cameron (1959) pointed out the importance of thermally populated excited states in enhancing weak decay rates, while Bahcall (1961, 1962*a*, *b*, *c*, 1964) and Peterson and Bahcall (1963) outlined the role of continuum electron capture and Pauli principle inhibition of phase-space, and the possibility of opening many otherwise unattainable electron capture channels at high density. These and other effects which can make weak-interaction rates in the stellar interior sensitive functions of temperature and density are briefly reviewed in § II. However, a continuing and vexing problem in astrophysical weak decay rate calculations is the assignment of nuclear matrix elements and the estimates of the uncertainties in the resulting stellar rates. Fowler and Hoyle (1964) calculated rates for a number of weak decays of interest in the supernova problem. Hansen (1966) surveyed weak rates for many nuclei using experimental information available at that time and an estimate for unknown matrix elements. Later, Mazurek *et al.* (1974) used a similar technique, but took into account the limitation on the strength of the weak interaction arising from the sum rule and applied it to the case of electron capture at high density. Iben (1978) studied Urca neutrino losses under conditions found in the carbon-oxygen cores of intermediate-mass stars and calculated weak-interaction rates involving a few excited states of parent and daughter nuclei in the mass range $21 \leq A \leq 57$. Takahashi and Yamada (1969), Takahashi (1971), Takahashi, Yamada, and Kondoh (1973), Egawa, Koichi, and Yamada (1975), and Takahashi, El Eid, and Hillebrandt (1978) have used the statistical treatment of the gross theory of β-decay to treat high density electron capture and have estimated ground state rates for many unstable nuclei.

As the temperature rises, additional transitions from nuclear parent states contribute to decay rates, while, as the density rises, electron capture transitions into additional nuclear daughter states also contribute. At the very high temperatures and densities which obtain in the later stages of supernova core collapse ($kT > 1$ MeV and peak

[1]Supported in part by National Science Foundation grant PHY76-83685 at Caltech.
[2]Fannie and John Hertz Foundation Fellow.
[3]Present address.

electron Fermi energies well above 10 MeV) many decay channels contribute to each decay, and a statistical approach becomes possible. In this regime total Fermi and Gamow-Teller strengths, as well as their distribution with daughter excitation energy, become necessary for calculation of detailed rates. However, the technique used by Bethe *et al.* (1979) to treat weak-interaction transitions under these extreme conditions indicates that the dynamics of the collapse phase may be relatively insensitive to the exact electron capture rates.

In contrast, in the regime of less extreme temperatures and densities encountered in the late stages of precollapse evolution (core carbon-oxygen burning through hydrostatic silicon burning and the onset of collapse), and in the explosive burning phases following collapse and bounce, detailed weak-interaction rates of high accuracy may be quite important. The temperatures and densities most relevant to these environments are $0.1 \leq T_9 \leq 5$ and $10^5 \leq \rho/\mu_e \leq 10^9$, corresponding to conditions from mild degeneracy up to Fermi energies near 5 MeV. The nuclei whose rates are usually most important are those of intermediate mass (Weaver and Woosley 1979; Woosley, Arnett, and Clayton 1972). In the series of papers beginning with the present work, we propose to make weak-interaction rates available for general astrophysical application for nuclei of the *sd*-shell ($17 \leq A \leq 40$) over a somewhat larger grid of temperature ($0.01 \leq T_9 \leq 10$) and density ($10 \leq \rho/\mu_e \leq 10^9$).

The weak-interaction rates of the *sd*-shell nuclei at these intermediate temperatures and densities are particularly sensitive to the detailed properties of the low-lying discrete states of parent and daughter nuclei. Fortunately, a large body of experimental information concerning these nuclei has been accumulated in recent years (see the summaries by Endt and van der Leun 1973, 1978). Supplementing this information with shell model calculations for some unknown allowed transitions (shell model calculations are particularly effective for this mass range) and exploiting the isospin purity and symmetry in these nuclei, reliable rates can be obtained and uncertainties caused by unknown nuclear matrix elements can be estimated. We find that the experimentally determined matrix elements and the Fermi transitions dominate the rates over most of the range of temperature and density considered, but it is important to consider estimates of unmeasured Gamow-Teller matrix elements. We use three sources to assign these matrix elements: (1) the results of the detailed large-scale shell model calculations of Wildenthal (1977, 1979) and Chung (1976) where they are available;[4] (2) simple shell model arguments where they can be reliably applied; and (3) an average Gamow-Teller matrix element characteristic of intermediate mass nuclei when a more accurate approach is not available. The average Gamow-Teller matrix element is distilled from experimental results and shell model calculations, and is designed to be applied in a survey of weak-interaction rates for *sd*-shell nuclei to identify those cases for which the considerable effort of a detailed shell model calculation is most urgently needed. The matrix element assignment procedure used here is described in detail in § III.

The recent discovery (Gray and Compston 1974; Lee and Papanastassiou 1974; Lee, Papanastassiou, and Wasserburg 1976) of anomalous amounts of ^{26}Mg in Allende inclusions has led to renewed interest in possible mechanisms for the formation of its unstable progenitor ^{26}Al (e.g., Arnould, Hillebrandt, and Thielemann 1978; Truran and Cameron 1978; Arnett and Wefel 1978). These considerations are complicated by the fact that the $^{26}\text{Al} \rightarrow {}^{26}\text{Mg}$ β-decay rate (mean life 1.04×10^6 years in the laboratory) becomes a sensitive function of temperature and density in the stellar interior. As a first application of our techniques, we present in § IV astrophysical decay rates for $^{26}\text{Al} \rightarrow {}^{26}\text{Mg}$ of relevance to the problem of the ^{26}Mg anomaly. In addition, since the 228 keV isomeric state of ^{26}Al is not thermalized at low temperatures (Ward and Fowler 1979), we have separately tabulated continuum electron capture and positron decay rates for the ground state and isomeric state systems. The simple structure of ^{26}Al and ^{26}Mg (ground states: two holes in the $1d5/2$ shell) makes the shell model particularly appropriate for the description of this decay.

The decay $^{30}\text{P} \rightarrow {}^{30}\text{Si}$ is another example of one in which the shell model is most appropriate. This decay and the decays $^{31}\text{S} \rightarrow {}^{31}\text{P}$, $^{32}\text{S} \rightarrow {}^{32}\text{P}$, $^{33}\text{S} \rightarrow {}^{33}\text{P}$, and $^{35}\text{Cl} \rightarrow {}^{35}\text{S}$ are particularly important (Weaver and Woosley 1979) for determining properties of the evolving stellar core through core oxygen and silicon burning and up to core collapse (Weaver, Woosley, and Zimmerman 1978). In particular, the electron capture and positron decay of these and other nuclei result in considerable neutronization before core collapse even begins. In addition, in the precollapse environment the neutrino energy loss associated with these decays may become competitive with neutrino losses due to thermal processes. This is primarily due to the effect of the degenerate electron gas which inhibits electron-positron pair creation and increases the plasma frequency, thereby restricting plasma decay to only the most energetic photons. Conversely, the high electron density *enhances* nuclear continuum electron capture. The lowering of the core temperature due to neutrino energy losses together with the hydrostatic neutronization influences the core composition in nuclear statistical equilibrium during the collapse phase. Decay rates and neutrino loss rates for these key nuclei are presented in § IV following the discussion of $^{26}\text{Al} \rightarrow {}^{26}\text{Mg}$.

[4] We have used expectation values of doubly reduced (in spin and isospin) β-decay operators from Wildenthal and Chung to calculate weak transition matrix elements.

II. BETA DECAY IN THE STELLAR INTERIOR

The rate of weak decay from the ith state of the parent to the jth state of the daughter nucleus is given by

$$\lambda_{ij}=\ln 2\frac{f_{ij}(T,\rho,U_F)}{(ft)_{ij}}, \tag{1}$$

where $(ft)_{ij}$ is the comparative half-life, which is related to the allowed weak-interaction matrix elements by (Brown, Chung, and Wildenthal 1978)

$$(\log ft)_{GT}=3.596-\log|M_{GT}|^2, \tag{2a}$$

$$(\log ft)_{F}=3.791-\log|M_{F}|^2, \tag{2b}$$

where $|M_{GT}|^2$ and $|M_F|^2$ are the absolute squares of the Gamow-Teller and Fermi matrix elements, respectively. The phase space integral f_{ij} is given by an integral over total energy

$$f_{ij}=\int_1^{q_n} w^2(q_n-w)^2G(\pm Z,w)(1-S_{\mp})(1-S_{\nu})dw \tag{3a}$$

for electron (*upper signs*) or positron (*lower signs*) emission, or by

$$f_{ij}=\int_{w_l}^{\infty} w^2(q_n+w)^2G(\pm Z,w)S_{\mp}(1-S_{\nu})dw \tag{3b}$$

for continuum positron (*lower signs*) or electron (*upper signs*) capture. In equations (3a) and (3b), w is the total rest mass and kinetic energy in units of m_ec^2, and

$$q_n=Q_n/m_ec^2=(M_p-M_d+E_i-E_j)/m_ec^2 \tag{3c}$$

is the β-decay total energy in units of m_ec^2. In equation (3c) M_p is the nuclear mass of the parent and M_d that of the daughter, and E_i, E_j are the excitation energies of the nuclear states involved. We have calculated nuclear masses from the tabulated atomic masses by subtracting the mass of the atomic electrons, neglecting atomic binding energies. The w_l is the capture threshold total energy, rest plus kinetic, in units m_ec^2 for positron (or electron) capture. If the corresponding electron emission (or positron emission) total energy is such that $q_n>-1$, then $w_l=1$, while for $q_n<-1$, $w_l=|q_n|$. S_+, S_-, S_ν are the positron, electron, and neutrino (or antineutrino) distribution functions, respectively. Neglecting possible corrections due to the presence of bound electrons and the ions, these are the Fermi-Dirac distribution functions. For electrons,

$$S_-=\left(\exp\left(\frac{U-U_F}{kT}\right)+1\right)^{-1}, \tag{4a}$$

where $U=(w-1)m_ec^2$ is the kinetic energy, U_F is the electron chemical potential, and U_F/kT is the degeneracy parameter. In the positron distribution function S_+, U_F is replaced by $-U_F-2m_ec^2$. The chemical potential U_F is determined from the density ρ in g cm^{-3} by inverting the relation

$$\rho/\mu_e=\frac{1}{\pi^2N_A}\left(\frac{m_ec}{\hbar}\right)^3\int_0^{\infty}(S_--S_+)p^2dp \text{ moles cm}^{-3}, \tag{4b}$$

where μ_e is the mean molecular weight per electron associated with nuclei in g mole^{-1}, N_A is Avogadro's number in mole^{-1}, $p=(w^2-1)^{1/2}$ is the electron or positron momentum in units of m_ec, and the density of electron-positron pairs has been removed by subtracting S_+ from S_-. In Figure 1 it will be noted that for low density and high temperature $U_F(e^-)=-U_F(e^+)=-m_ec^2=-0.511$ MeV, while for any density and zero temperature

$$U_F(e^-)=\left\{\left[1.02\times10^{-4}(\rho/\mu_e)^{2/3}+1\right]^{1/2}-1\right\}\times0.511 \text{ MeV}$$

$$\approx0.5\times10^{-2}(\rho/\mu_e)^{1/3}\text{MeV} \quad \text{for } \rho/\mu_e\gtrsim10^8. \tag{4c}$$

Note that the inclusion of these electron distribution functions results in the phase-space integrals f_{ij} becoming sensitive functions of temperature and density. For our calculations, inhibition of final neutrino phase space never becomes important, so $S_\nu = 0$.

The remaining factor appearing in the phase space integral is

$$G(\pm Z, w) \equiv (p/w) F(\pm Z, w). \tag{5a}$$

$F(\pm Z, w)$ is the relativistic Coulomb barrier factor, given approximately by

$$F(\pm Z, w) \approx 2(1+s)(2pR)^{2(s-1)} e^{\pi\eta} \left| \frac{\Gamma(s+i\eta)}{\Gamma(2s+1)} \right|^2, \tag{5b}$$

where $s = [1-(\alpha Z)^2]^{1/2}$, Z is the nuclear charge, α the fine structure constant, R the nuclear radius $= 2.908 \times 10^{-3} A^{1/3} - 2.437 A^{-1/3}$ in electron Compton wavelengths (Gove and Martin 1971) with A the nuclear mass number, $\eta = \pm \alpha Z w/p$, and the upper signs are for electron emission and capture, while the lower signs are for positron emission and capture. For emission processes Z is the nuclear charge of the daughter nucleus, while for capture processes it is that of the parent nucleus. Note that in the nonrelativistic limit, $w \approx 1$, $|\eta| \gg 1$ with $s \approx 1 - \frac{1}{2}\alpha^2 Z^2 \approx 1$ in our applications, one has

$$G_- \Rightarrow 2\pi\alpha Z |2\eta pR|^{-\alpha^2 Z^2} = 2\pi\alpha Z (2\alpha ZR)^{-\alpha^2 Z^2}, \tag{5c}$$

$$G_+ \Rightarrow G_- \exp -2\pi|\eta|. \tag{5d}$$

In the extreme relativistic limit $p \approx w \gg 1$, $|\eta| \approx \alpha Z$, one has

$$G_- \Rightarrow (2pR)^{-\alpha^2 Z^2} \exp \pi|\eta|, \tag{5e}$$

$$G_+ \Rightarrow G_- \exp -2\pi|\eta| = (2pR)^{-\alpha^2 Z^2} \exp -\pi|\eta|. \tag{5f}$$

In addition, the neutrino energy loss rate (in $m_e c^2\, s^{-1}$) associated with the transition from level i of the parent to level j of the daughter is formed as in equation (1), except that the phase-space integral is replaced by

$$f_{ij}{}' = \int_1^{q_n} w^2 (q_n - w)^3 G(\pm Z, w)(1 - S_\mp)(1 - S_\nu)\, dw, \tag{6a}$$

for electron (*upper signs*) or positron (*lower signs*) emission, and by

$$f_{ij}{}' = \int_{w_l}^{\infty} w^2 (q_n + w)^3 G(\pm Z, w) S_\mp (1 - S_\nu)\, dw, \tag{6b}$$

for continuum positron (*lower signs*) or electron (*upper signs*) capture.

The phase-space integrals were performed numerically, and checked for electron and positron emission, at low temperature and density against the tables of $\log f$ by Gove and Martin (1971). The definite integrals for the electron and positron emission phase space factors were done by 64-point Gaussian quadrature. The integrands of the electron and positron capture phase-space integrals are modulated strongly by the electron (or positron) distribution function, so that the integrand has a characteristically slowly varying part and an exponentially decaying part, corresponding to the shape of the Fermi-Dirac distribution function. The portion of the improper integrals containing the slowly varying part of the integrand was done with 64-point Gaussian quadrature, and the exponential tail was treated with 32-point Gauss-Laguerre quadrature. For each nucleus a table of phase-space factors for position emission and electron capture as a function of q_n was prepared at each temperature and density grid point, and the f_{ij} and $f_{ij}{}'$ were obtained by cubic spline interpolation in q_n.

In summary, the weak decay rates of nuclei in the stellar environment become sensitive functions of temperature and density through the influence of the lepton distribution functions on the phase-space integrals, and because many decay channels open up due to thermal population of parent excited states and continuum electron capture at high Fermi energy into daughter excited states.

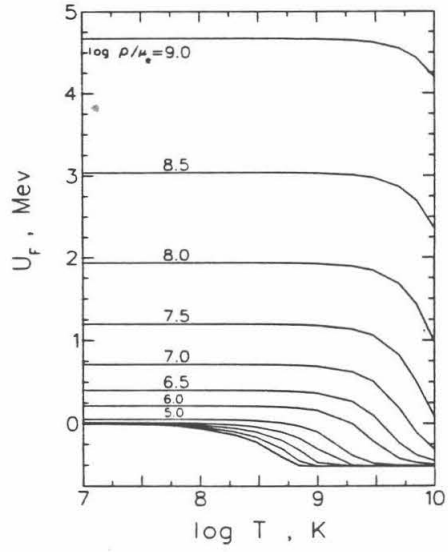

FIG. 1.—Thermodynamic grid employed. The electron chemical potential U_F in MeV is displayed as a function of temperature in kelvins (logarithmic scale) for various values of log ρ/μ_e in moles cm^{-3}. The temperature grid used in all calculations extended from 10^7 to 10^{10} K with 5 points per decade roughly uniformly distributed in log T. Density points were taken at each decade from log $\rho/\mu_e = 1$ to 9 with additional points inserted at log $\rho/\mu_e = 6.5$, 7.5, and 8.5 to improve the coverage in U_F. The curves not labeled correspond to log $\rho/\mu_e = 1.0$, 2.0, 3.0, and 4.0, respectively. Note the approach to the nondegenerate limit $U_F = 0.511$ MeV at sufficiently high temperature at each density.

The temperature and density regime considered in the calculations is shown in Figure 1. We see that the energies, spins, and parities for discrete states will be required for excitation energies up to several MeV in the parent and at least 4 or 5 MeV in the daughter. Typically, we use all discrete states known up to even higher energies in parent and daughter. All nuclear level information was taken from Endt and van der Leun (1978). We then require weak interaction transition matrix elements connecting these states; their assignment is the subject of § III.

We have not considered the effects of bound state electron capture, which is unimportant over most of the range of temperature and density considered, nor have we considered the screening of the nuclear charge by continuum electrons, which has the effect of moving $F(\pm Z, w)$ toward unity and of modifying the energies of charged particles in the plasma. This screening is a small effect over the range of temperature and density considered here (Takahashi, El Eid, and Hillebrandt 1978). While the omission of these corrections is justified along the temperature-density track of typical precollapse conditions ($0.1 \leq T_9 \leq 5$, $10^5 \leq \rho/\mu_e \leq 10^9$), screening corrections affect the rates at low temperature and/or extremely high density.

It finally remains to sum over the parent and daughter states in order to find λ, the destruction rate of the parent or the production rate of the daughter due to the emission or capture process under consideration. The destruction rate for the ith parent state is given by

$$\lambda_i = \sum_j \lambda_{ij}, \tag{7}$$

where the sum is over all states of the daughter to which the parent state is linked by the emission or capture process. The rate for destruction of the parent nucleus is then

$$\lambda = \sum_i P_i \lambda_i, \tag{8}$$

where the sum is over all parent states, and the occupation index P_i of state i is given for thermal equilibrium by

$$P_i = (2J_i + 1)\exp(-E_i/kT)/G, \tag{9a}$$

where J_i is the spin of level i, and G is the nuclear partition function for the parent nucleus

$$G=\sum_i (2J_i+1)\exp(-E_i/kT). \tag{9b}$$

In our temperature range ($T_9 \leq 10$) the number of known discrete states is sufficient to yield an accurate value for G without considering continuum contributions (Tubbs and Koonin 1979).

If one defines the production rate for the jth daughter state as

$$\lambda_j=\sum_i P_i\lambda_{ij}, \tag{10a}$$

then it will be clear that the production of the daughter nucleus and the destruction of the parent nucleus can be stated as

$$\lambda=\sum_j \lambda_j. \tag{10b}$$

We add a note of caution. In this paper we do not present the *reverse* reaction rates to the cases we have treated. For example, we give $^{35}\mathrm{Cl}\rightarrow{}^{35}\mathrm{S}$, but not $^{35}\mathrm{S}\rightarrow{}^{35}\mathrm{Cl}$. We point out that the ground state of ^{35}S decays by electron emission to ^{35}Cl with maximum total energy equal to 0.679 MeV. Thus at low density and low temperature, our tabulated results do not give the complete picture. In a later paper of this series this will be rectified. For the moment we give the logarithm of the laboratory reverse rates due to electron emission. They are: -6.25 for ^{32}P to ^{32}S, -6.50 for ^{33}P to ^{33}S, and -7.04 for ^{35}S to ^{35}Cl. These laboratory reverse rates will hold in stellar environments at low density, $\rho/\mu_e < 10^6$, and temperature, $T_9 < 1$.

III. NUCLEAR MATRIX ELEMENTS

The comparative half-lives $(ft)_{ij}$ required in equation (1) are taken from laboratory measurements where they are available. Since there has been a vast increase in the number of measured β-transitions in recent years, we have used the latest tabulations of Endt and van der Leun (1978). In addition, we have used some unpublished measurements by Wilson and Kavanagh (1978) for the decay $^{30}\mathrm{P}\rightarrow{}^{30}\mathrm{S}$. However, for many important transitions, particularly those involving excited states of parent or daughter nucleus, no measurement is available, and ft-values for these transitions must be assigned in another way. Only allowed transitions are considered in this work. Exploiting the isospin symmetry of these *sd*-shell nuclei allows us to calculate unmeasured Fermi transition matrix elements with great accuracy, and to extend the relevant set of "measured" matrix elements for a decay by considering transitions measured in the appropriate mirror decay. The remaining unmeasured Gamow-Teller matrix elements are handled in several different ways. Simple two-particle shell model approximations to the nuclear wave functions are used to calculate Gamow-Teller matrix elements and appropriate sum rules. This calculation gives a good overview of the Gamow-Teller strength and its distribution for the decays $^{26}\mathrm{Al}\rightarrow{}^{26}\mathrm{Mg}$ and $^{30}\mathrm{P}\rightarrow{}^{30}\mathrm{S}$. In addition, for some transitions in these and the other decays considered, Wildenthal (1979) has provided us with Gamow-Teller matrix elements calculated from the detailed wave functions of Chung (1976). For Gamow-Teller transitions not covered by either the two-particle approximation or Wildenthal's calculations, we use an appropriate mean log ft, determined from averages of experimentally determined Gamow-Teller matrix elements in the *sd*-shell and all of the available Wildenthal calculations used for the six decays considered. The sensitivity of rates to uncertainties in the matrix element assignments are estimated, as are uncertainties in the rates caused by unknown Gamow-Teller strength which may lie beyond the last discrete levels considered in parent and daughter nucleus. The remainder of this section will describe this matrix element assignment procedure, but briefly, we will find that the experimentally determined transitions along with the Fermi and mirror decay matrix elements dominate the rates in most cases. Even in regimes of temperature and density where the unmeasured Gamow-Teller transitions are important, we feel that the rates are well determined. Regimes in which the uncertainty in matrix elements makes the rates uncertain will be explicitly mentioned for each decay.

The isospin purity and symmetry of the nuclear energy levels in *sd*-shell nuclei allows considerable simplification and accuracy in the assignment of some matrix elements. In particular, the Fermi matrix element depends only on the nuclear isospin, T, and its projection $T_z=(Z-N)/2$ for the parent or daughter nucleus, and may be written for

positron emission or electron capture as

$$|M_F|^2 = \frac{1}{2J_1+1}\sum_{m_i}\sum_{m_f}\left|\langle\psi_f m_f|\sum_N \tau_N^-|\psi_i m_i\rangle\right|^2$$
$$= T(T+1) - T_z^i(T_z^i - 1), \tag{11}$$

where T_z^i is the z projection of the parent isospin, $|\psi_i m_i\rangle$ is the initial parent state, $|\psi_f m_f\rangle$ the final daughter state, and the matrix element is averaged over initial and summed over final nuclear spins. Note that the sum on nucleons $\Sigma_N \tau_N^-$ is the minus component of an isovector, spatial scalar operator T^- which commutes with the total isospin T^2, a good quantum number in these nuclei, implying the selection rules $\Delta\Pi = 0$; $\Delta J = 0$; $\Delta T = 0$; $T_z^f = T_z^i - 1$, which have been applied in the second equality of equation (11). In ^{26}Al$\rightarrow^{26}$Mg Fermi transitions, for instance, $|M_F|^2 = 2$, and so from equation (2) $\log(ft)_F = 3.49$. This is very fast compared to the average Gamow-Teller matrix element corresponding to about log $ft = 5.0$ (see discussion later in this section). In addition, essentially all of this Fermi strength is concentrated in the isobaric analog state. Fortunately, in this mass range ($17 \leq A \leq 40$) several analog states occur within 5 MeV of the ground state and are accessible in the precollapse environment. For example, several Fermi transitions can be seen for the decays ^{26}Al$\rightarrow^{26}$Mg and ^{30}P$\rightarrow^{30}$Si in Tables 1 and 2, respectively.

Isospin symmetry allows assignment of matrix elements for some unmeasured transitions in particular decays. If a measured matrix element is available for a transition in the mirror system, then it can be taken over directly for the appropriate transition in the original decay, after correcting for initial and final spin degeneracy. For example, several matrix elements are measured in the ^{26}Si$\rightarrow^{26}$Al decay; these can be taken over with spin degeneracy corrections into the ^{26}Al$\rightarrow^{26}$Mg decay, and are included in Table 1. The mirror systems of all six decays were examined, and many important matrix elements were obtained in this way.

After the above procedure is completed, there are still many Gamow-Teller transitions without assigned matrix elements. Since Gamow-Teller matrix elements are observed to vary over three or four orders of magnitude, it is important to obtain a good handle on their behavior in this mass range. To this end we have used (1) results of the large-scale shell model calculations of Wildenthal (1979), (2) a simple two-particle approximation to the nuclear wave functions, and (3) averages based on shell model calculations and measured decays in the *sd*-shell. The two-particle approximation was used for the decays ^{26}Al$\rightarrow^{26}$Mg and ^{30}P$\rightarrow^{30}$Si because the very simple shell model picture was most appropriate there.

The shell model indicates that the primary configuration of the ^{26}Al ground state is one neutron hole and one proton hole in a filled $1d5/2$ shell, and of ^{26}Mg is two proton holes in the same shell. Similarly, the primary configuration of the ^{30}P ground state is one proton and one neutron outside a closed $1d5/2$ shell, while for ^{30}Si it is two neutrons outside the same closed shell. This suggests that the low-lying states of these systems may be predominantly described in terms of two-particle (two-hole) wave functions, where only the angular momenta of the valence particles are coupled to give the total angular momentum. The possible values of J^π; T (spin, parity; isospin) are constructed for each two-particle *sd*-shell configuration forming a "bank" of states for each nucleus. Since the low-lying states of these nuclei have well measured excitation energies and spins and parities, it is possible to identify physical states with states in the J^π bank, taking into account the energy orderings of the simple shell model configurations. We note that the first 16 states of ^{26}Al exhaust 13 of the 14 possible $T=0$ two-particle *sd*-shell states and three of the expected low-lying $T=1$ states, before a state of ^{26}Al is encountered which cannot be understood in this simple model. Similarly, in ^{26}Mg the lowest 12 states are well accounted for; states 13 and 15 apparently have large many-particle components, but states 14 and 16 match well the remaining $T=1$ states in our ^{26}Mg J^π bank. The first 14 states of ^{30}P exhaust 12 of the 14 possible $T=0$ two-particle states and two of the expected $T=1$ states before an obvious many-particle state is found. Similarly, in ^{30}Si the lowest 10 states are well accounted for, and four others match up with the $T=1$ states remaining in the J^π bank for ^{30}Si. The pure two-particle configuration assignments are displayed for ^{26}Al$\rightarrow^{26}$Mg in Table 1, and for ^{30}P$\rightarrow^{30}$Si in Table 2, the notation being, e.g., for ^{26}Al, $55 \equiv p(1d5/2)n(1d5/2)$, $51 \equiv p(1d5/2)n(2s1/2)$, etc., where p denotes the proton configuration and n the neutron configuration.

The weak interaction matrix elements are calculated using the assigned two-particle *sd*-shell wave functions. The Fermi matrix element is done as above. The Gamow-Teller matrix element is given by

$$|M_{GT}|^2 = \frac{1}{2J_i+1}\sum_{m_i}\sum_{m_f}\left|\langle\psi_f m_f|\sum_N \tau_N^-\sigma_N|\psi_i m_i\rangle\right|^2, \tag{12}$$

TABLE I

LOG *ft*-VALUES FOR $^{26}Al \rightarrow {}^{26}Mg$

STATE	ENERGY	$J^{\pi};T$	^{26}Al	1	2	3	4	5	6	7	8
				0.000	0.228	0.417	1.058	1.759	1.851	2.069	2.070
				5^+	$0^+;1$	3^+	1^+	2^+	1^+	4^+	$2^+;1$
^{26}Mg			CONF	55	55	55	55	51	53	53	55
1	0	$0^+;1$	55		EF 3.48		S 4.01 P 3.63 M 4.58 W 3.85		S 4.29 P 3.87 M 4.58 W 4.34		
2	1.809	$2^+;1$	55	E14.18		P 3.63 M 4.66 W 5.17	P 3.36 M 4.63 W 3.63	M 4.46	P 3.72 M 4.63 W 4.40		FP 3.34 FM 3.45
3	2.938	$2^+;1$	51	E13.35		M 4.66 W 4.07	M 4.63 W 5.49	P 3.31 M 4.46	M 4.63 W 4.47		M 4.90
4	3.588	$0^+;1$	11				M 4.58 W 5.72		M 4.58 W 5.36		
5	3.941	$3^+;1$	51			M 4.98		P 3.37 M 4.43			M 4.58
6	4.320	$4^+;1$	55	P 3.99 M 4.10		P 3.63 M 4.34				P 3.99 M 3.84	
7	4.332	$2^+;1$	53			P 3.68 M 4.66 W 4.97	P 3.91 M 4.63 W 5.22	M 4.46	M 4.63 W 7.57		P 3.61 M 4.90
8	4.350	$3^+;1$	53			P 3.74 M 4.98		M 4.43			P 4.31 M 4.58
9	4.835	$2^+;1$	31			M 4.66 W 4.78	M 4.63 W 4.87	P 4.69 M 4.46	M 4.63 W 6.16		M 4.90
10	4.901	$4^+;1$	53	P 3.39 M 4.10		P 4.84 M 4.34				P 3.09 M 3.84	
11	4.972	$0^+;1$	33				M 4.58 W 7.50		P 3.69 M 4.58 W 4.53		
12	5.291	$2^+;1$	33			M 4.66 W 4.94	M 4.63 W 6.34	M 4.46	P 4.69 M 4.63 W 6.57		M 4.90
13	5.474	$4^+;1$	—								
14	5.690	$1^+;1$	53		P 3.39 M 4.19		P 3.55 M 4.83	M 4.79	M 4.83		P 3.94 M 4.03
15	5.715	$4^+;1$	—								
16	6.127	$1^+;1$	31				M 4.83	P 3.74 M 4.79	M 4.83		M 4.03
	$LOG(ft)_i$			3.29	3.39	3.06	2.97	2.95	3.26	3.04	3.28

TABLE 1–*Continued*

9	10	11	12	13	14	15	16	22	24	ANLG	ANLG
2.072	2.365	2.545	2.661	2.739	2.913	3.074	3.159	3.719	3.745	5.9184	6.3534
1^+	3^+	3^+	2^+	1^+	2^+	3^+	$2^+;1$	1^+	$0^+;1$	$1^+;1$	$1^+;1$
11	51	53	53	31	31	33	51	33	11	53	31
S 4.98											
M 4.08 W 4.28				W 4.77				W 4.77			
		P 4.46	P 3.61							P 3.72	
M 4.63 W 4.96	M 4.66 W 4.99	M 4.66 W 5.79	M 4.46	M 4.63 W 5.22	M 4.46	M 4.66 W 4.36	M 4.90	M 4.63 W 5.05		M 4.25	M 4.25
	P 3.52			P 3.52	P 4.69		FP 3.47				P 3.52
M 4.63 W 5.35	M 4.66 W 4.82	M 4.66 W 4.50	M 4.46	M 4.63 W 6.81	M 4.46	M 4.66 W 6.35	FM 3.45	M 4.63 W 5.18		M 4.25	M 4.25
P 3.30 M 4.58 W 5.57				M 4.58 W 4.90				M 4.58 W 5.24	F 3.49	M 4.75	M 4.75
					P 3.55		P 3.72				
	M 4.98	M 4.98	M 4.43		M 4.43	M 4.98	M 4.58				
		P 3.41									
	M 4.34	M 4.34				M 4.34					
			P 3.61			P 5.24		P 3.37		P 3.37	
M 4.63 W 5.25	M 4.66 W 4.99	M 4.66 W 5.72	M 4.46	M 4.63 W 4.68	M 4.46	M 4.66 W 5.20	M 4.90	M 4.63 W 5.31		M 4.25	M 4.25
						P 4.09					
	M 4.98	M 4.98	M 4.43		M 4.43	M 4.98	M 4.58				
	P 3.69			P 3.69	P 3.31		P 4.69				P 3.34
M 4.63 W 6.31	M 4.66 W 5.43	M 4.66 W 5.13	M 4.46	M 4.63 W 5.03	M 4.46	M 4.66 W 4.91	M 4.90	M 4.63 W 9.24		M 4.25	M 4.25
						P 3.28					
	M 4.34	M 4.34				M 4.34					
								P 3.99		P 3.69	
M 4.58 W 4.79				M 4.58 W 9.65				M 4.58 W 4.36		M 4.75	M 4.75
		P 3.34	P 3.85			P 4.22		P 3.79		P 4.69	
M 4.63 W 5.85	M 4.66 W 5.88	M 4.66 W 6.12	M 4.46	M 4.63 W 6.06	M 4.46	M 4.66 W 7.60	M 4.90	M 4.63 W 4.78		M 4.25	M 4.25
								P 3.74		FP 3.49	
M 4.83			M 4.79	M 4.83	M 4.79		M 4.03	M 4.83	M 4.19	FM 3.44	M 4.70
					P 3.91		P 3.74				FP 3.23
M 4.83			M 4.79	M 4.83	M 4.79		M 4.03	M 4.83		M 4.70	FM 3.46
3.29	3.29	3.12	3.20	3.29	3.04	3.17	3.39	3.06	∞	3.01	2.99

where σ is the Pauli spin operator and the rest of the notation is as for the Fermi matrix element above (eq. [11]). Since $\sum_N \tau_N{}^- \sigma_N$ is a spatial vector and an isovector, we get the Gamow-Teller selection rules, $\Delta\Pi = 0$; $\Delta T = 0, \pm 1$, no $0 \rightarrow 0$; $\Delta J = 0, \pm 1$, no $0 \rightarrow 0$. Note that the Gamow-Teller operator has no dependence on the radial coordinate and hence cannot change the orbital angular momentum of the decaying state. Making the two-particle approximation, we find

$$|M_{\rm GT}|^2 = \frac{1}{2J_i+1} \sum_{m_i} \sum_{m_f} |\langle \psi_f m_f | \tau_1{}^- \sigma_1 + \tau_2{}^- \sigma_2 | \psi_i m_i \rangle|^2. \quad (13)$$

For example, in the transition of a $(T=0,55)$ configuration in ^{26}Al to a $(T=1,55)$ configuration in ^{26}Mg we can

TABLE 2

LOG *ft*-VALUES FOR $^{30}P \rightarrow {}^{30}Si$

STATE			^{30}P	1	2	3	4	5	6	7	8	9	10
	ENERGY			0.0	0.6772	0.7090	1.454	1.973	2.538	2.7232	2.8388	2.9378	3.0186
		$J^\pi;T$		1^+	$0^+;1$	1^+	2^+	3^+	3^+	2^+	3^+	$2^+;1$	1^+
^{30}Si			CONF	11	11	13	13	33	51	51	55	13	33
1	0	$0^+;1$	11	E 4.83 P 3.30 M 4.61 W 5.53	EF 3.49	E 6.18 M 4.61 W 5.35							S 3.99 M 4.61 W 3.71
2	2.2354	$2^+;1$	31	E 5.80 M 4.62 W 4.83		P 3.69 M 4.62 W 4.58	P 3.31 M 4.46	M 4.63 W 5.31	P 3.69 M 4.63 W 5.19	P 4.69 M 4.46	M 4.63 W 5.92	FP 3.45	M 4.62 W 6.02
3	3.4987	$2^+;1$	33	M 4.62 W 4.17		M 4.62 W 5.98	M 4.46	P 4.22 M 4.63 W 5.10	M 4.63 W 4.69	M 4.46	M 4.63 W 6.95	M 5.00	P 3.79 M 4.62 W 4.73
4	3.7697	$1^+;1$	31	M 4.83		M 4.83	P 3.91 M 4.80			P 3.74 M 4.80		M 4.66	M 4.83
5	3.7879	$0^+;1$	33	M 4.61 W 5.01		M 4.61 W 4.58							P 3.99 M 4.61 W 5.53
6	4.8092	$2^+;1$	51	M 4.62 W 5.33		P 3.52 M 4.62 W 4.43	P 4.69 M 4.46	M 4.63 W 4.62	P 3.52 M 4.63 W 6.70	P 3.31 M 4.46	M 4.63 W 6.32	P 4.69 M 5.00	M 4.62 W 5.65
7	4.8307	$3^+;1$	51				P 3.55 M 4.43	M 4.98	M 4.98	P 3.37 M 4.43	M 4.98	P 3.54 M 4.23	
8	5.2306	$3^+;1$	53				M 4.43	P 4.09 M 4.98	M 4.98	M 4.43	P 3.74 M 4.98	M 4.23	
9	5.2795	$4^+;1$	53					P 3.28 M 4.45	M 4.45		P 4.84 M 4.45		
10	5.3720	$0^+;1$	55	M 4.61 W 4.43		M 4.61 W 4.83							M 4.61 W 5.88

DESIGNATIONS FOR LOG ft-VALUES IN TABLES 1 AND 2: S ≡ CALCULATED FROM ISOBARIC SYMMETRY; P ≡ PURE TWO-PARTICLE GAMOW-TELLER VALUE; M ≡ MIXED TWO-PARTICLE GAMOW-TELLER VALUE + 0.5; W ≡ CALCULATED FROM WILDENTHAL RESULTS; E ≡ EXPERIMENTAL VALUE; F ≡ CALCULATED FERMI VALUE; EF ≡ EXPERIMENTAL FERMI VALUE; FP ≡ CALCULATED FERMI AND PURE G-T VALUE; FM ≡ CALCULATED FERMI AND MIXED G-T VALUE + 0.5. CONF = TWO-PARTICLE CONFIGURATION; ANLG = ANALOGUE STATE.

evaluate the isospin matrix element and, in spherical tensor notation, we find

$$|M_{GT}|^2 = \frac{1}{2J_1+1} \cdot \frac{1}{2} \cdot \sum_{m_i} \sum_{m_f} \sum_{k} (-1)^k \langle m_f | -\sigma_1{}^k + \sigma_2{}^k | m_i \rangle \cdot \langle m_i | -\sigma_1{}^{-k} + \sigma_2{}^{-k} | m_f \rangle . \tag{14}$$

We have used the shorthand notation for the matrix elements

$$\langle m_f | \sigma_1{}^k | m_i \rangle = \langle J_f (j_1' j_2)(l_1 l_2)(\tfrac{1}{2}\tfrac{1}{2}) m_f | \sigma_1{}^k | J_i (j_1 j_2)(l_1 l_2)(\tfrac{1}{2}\tfrac{1}{2}) m_i \rangle , \tag{15}$$

where j_1 is the initial j-shell angular momentum of particle one, j_1' is the final j-shell angular momentum of particle one, l_1 the corresponding orbital angular momentum, and $1/2$ the spin, and similarly for particle two. Using the Wigner-Eckart theorem, the above expression becomes, after some tedious angular momentum algebra,

$$\cdot \langle m_f | \sigma_i{}^k | m_i \rangle = (-1)^{1/2 + m_f + l_1 + j_1 + j_1' + j_2 + J_i + J_f}$$

$$\cdot \left[6\,(2J_f+1)\,(2J_1+1)\,(2j_1+1)\,(2j_1'+1) \right]^{1/2} \tag{16}$$

$$\cdot \begin{pmatrix} J_f & 1 & J_i \\ -m_f & k & m_i \end{pmatrix} \begin{Bmatrix} \frac{1}{2} & j_1' & l_1 \\ j_1 & \frac{1}{2} & 1 \end{Bmatrix} \begin{Bmatrix} j_1' & J_f & j_2 \\ J_i & j_1 & 1 \end{Bmatrix} .$$

A similar expression can be derived for $\langle m_f|\sigma_2{}^k|m_i\rangle$, and the orthogonality property of the 3-j symbols exploited to give equation (13) in terms of 6-j symbols which are easily evaluated. This calculation was carried out for allowed transitions between all two-particle *sd*-shell configurations and all possible J^π corresponding to those configurations.

Given the complicated nature of the expression for $|M_{GT}|^2$, it is useful to check against an explicit calculation of the two-particle sum rule. The sum rule is the total amount of Gamow-Teller strength available for an initial state (Takahashi, Yamada, and Kondoh 1973), and is here given by summing over a complete set of final states in $|M_{GT}|^2$ to yield

$$S_i{}^{GT}=\frac{1}{2J_i+1}\sum_{m_i}\langle\psi_i m_i|\Big(\sum_N \tau_N{}^-\boldsymbol{\sigma}_N\Big)^\dagger\Big(\sum_N \tau_N{}^-\boldsymbol{\sigma}_N\Big)|\psi_i m_i\rangle. \tag{17}$$

Considering just the two valence nucleons results in the expression

$$S_i{}^{GT}=3\langle\psi_i{}^{iso}|\tau_1{}^-\tau_1{}^+ +\tau_2{}^-\tau_2{}^+|\psi_i{}^{iso}\rangle+\langle\psi_i{}^{iso}|\tau_1{}^-\tau_2{}^+ +\tau_1{}^-\tau_2{}^+|\psi_i^{iso}\rangle\cdot\Sigma^{GT}, \tag{18}$$

where $\psi_i{}^{iso}$ is the isospin part of the two-particle wave function, and Σ^{GT} is spatial expectation value which can be shown to be

$$\begin{aligned}\Sigma^{GT}&=\frac{1}{2J_i+1}\sum_{m_i}\langle\psi_i m_i|\boldsymbol{\sigma}_1\cdot\boldsymbol{\sigma}_2|\psi_i m_i\rangle\\ &=-2\Big[\frac{3}{4}+j_2(j_2+1)-l_2(l_2+1)\Big]\cdot\Big[\frac{3}{4}+j_1(j_1+1)-l_1(l_1+1)\Big]\cdot\frac{j_1(j_1+1)+j_2(j_2+1)-J_i(J_i+1)}{j_1j_2(2j_1+2)(2j_2+2)}.\end{aligned} \tag{19}$$

The strength due to the interaction with core nucleons in the above analysis is assumed to be at nuclear excitation energies high enough to be irrelevant to the astrophysical rates. Since we have identified all of the two-particle *sd*-shell states in, for instance, daughter ^{26}Mg, each state of parent ^{26}Al explicitly saturates the two-particle sum rule. To the extent that the nuclear wave functions are well represented by the two-particle configurations, this sum rule gives a rough idea of the total Gamow-Teller strength in the range of stellar energies to be expected for each state of the parents ^{26}Al and ^{30}P. The approximate validity of the two-particle assignments in these decays is demonstrated by the way hindered values (unusually large *ft* values for allowed transitions) of the pure configuration matrix elements track fairly well the hindered values of Wildenthal's calculation (see below).

Configuration mixing resulting from the residual interaction between valence nucleons is an important aspect of the wave functions of *sd*-shell nuclei. Its major effects will be to "smear out" the two-particle strength in parent and daughter and to mix many-particle configurations into low-lying states, thus spreading the two-particle strength to higher energies. In the two-particle picture, we treat the first effect by an averaging procedure: We completely mix states of a given $J_P{}^\pi$ in the parent and completely mix states of a given $J_d{}^\pi$ in the daughter, add up the pure configuration strength for all the $J_p{}^\pi\rightarrow J_d{}^\pi$ transitions, and divide by the total number of such transitions. Then each such transition is assigned this average matrix element. This result is termed the mixed configuration matrix element set. The effect on the rate of the distribution of Gamow-Teller strength can be tested by first computing the stellar rate with the pure configuration set of matrix elements and then with the mixed configuration set. In both calculations the measured, mirror-decay, and Fermi-transition log *ft* values were employed. We find that the rates calculated in these two cases are substantially the same for the temperatures and densities considered here, indicating that the stellar rates are relatively insensitive to the placement of the low-lying unmeasured Gamow-Teller strength in the range of excitation energy covered in parent and daughter nuclei. However, the second effect of configuration mixing, the admixture of high-lying configurations and the true many-body nature of the wave functions, results in a decrease in Gamow-Teller matrix elements, especially at the higher excitation energies in parent and daughter. This trend is seen in the results of the large-scale shell model calculations of Gamow-Teller matrix elements done by Wildenthal, and is treated here by slowing down the mixed configuration transition rates by adding 0.5 in log *ft*.

Wildenthal's calculations employ a full *sd*-shell basis and a realistic residual interaction. The wave functions are then the result of an iterative calculation which fits the energies of 199 levels for nuclei between masses 18 and 24. The results obtained for Gamow-Teller transitions in the *sd*-shell agree quite well with experiments where comparison is possible (Brown, Chung, and Wildenthal 1978). Matrix elements from these calculations were available for many, but not all transitions in the decays considered. Where a calculated matrix element exists, two values are provided: one corresponding to the value of the axial vector coupling constant C_A relevant for free nucleon decay (the so-called "free" value), and one corresponding to the value of C_A renormalized by mesonic exchange currents and the effects of truncation of the basis to just the *sd*-shell configurations. The latter result was obtained by fitting

to measuared Gamow-Teller transitions in the *sd*-shell and hence is termed the "fit" value. The fit values are a better representation of the matrix elements over the entire *sd*-shell, and in general the fit matrix elements are slightly smaller (log *ft* is somewhat larger) than the corresponding free values. However, we have adopted the free values because they seem to give slightly better agreement with experimentally measured matrix elements and with those determined from mirror decays in the transitions considered.

Table 1 presents all the experimental, mirror symmetry, pure, mixed (plus 0.5) and free Wildenthal log *ft* values used in the calculations for the $^{26}Al \rightarrow ^{26}Mg$ decay. Table 2 presents the log *ft* values used for the states of lowest excitation considered in the $^{30}P \rightarrow ^{30}Si$ decay. The actual calculations involved states up to 4.3 MeV in ^{30}P and up to 7.5 MeV in ^{30}Si. In these tables, entries with an E are experimentally observed, those with an S are observed in the mirror decays, while entries with an F have a Fermi component. Also appearing in the tables are the log *ft* values from the pure configuration, denoted by a P, and the mixed configuration, denoted by an M. The small and vanishing pure configuration matrix elements are a result of *l*-forbiddenness and two-particle interference effects. Where no entry denoted by P or M exists, the matrix element is zero in the two-particle model. Note that in the $^{26}Al \rightarrow ^{26}Mg$ decay the hindered transitions of Wildenthal roughly track the small matrix element transitions of the two-particle approximation. This effect is not as pronounced in the $^{30}P \rightarrow ^{30}Si$ decay, probably due to less domination by two-particle configurations in the actual nuclear wave functions. The numbers at the bottom of the tables are the effective log *ft* corresponding to the two-particle Gamow-Teller sum rule for each of the parent states of ^{26}Al and are given by

$$\log(ft)_i \equiv -\log \sum_j 1/(ft)_{ij} = 3.596 - \log S_i^{GT}.$$

These numbers give an estimate of the total Gamow-Teller strength to be expected for each parent state. Finally, the free Wildenthal log *ft* are denoted by W. All the decays considered in this paper have available roughly similar numbers of log *ft* values calculated from the results of Wildenthal.

For $^{26}Al \rightarrow ^{26}Mg$ the log *ft* calculated on the basis of the two-particle approximation do well in the two cases where comparison with experiment is possible. The $4 \rightarrow 1$ transition (Table 1: state 4 of ^{26}Al to state 1 of ^{26}Mg) is measured in the mirror system and when corrected for spin-degeneracy factors yields log $ft = 4.01$. (Hereafter we will just refer to such a log *ft* value as "measured.") This measured value is bracketed by the pure, log $ft = 3.63$, and mixed (plus 0.5), log $ft = 4.58$, results. The $6 \rightarrow 1$ transition is measured as log $ft = 4.29$, and is approximated by the pure result as log $ft = 3.87$ and by the mixed (plus 0.5) result as log $ft = 4.58$. In the $^{30}P \rightarrow ^{30}Si$ decay the $1 \rightarrow 1$ transition is measured as log $ft = 4.83$ and is approximated by the pure configuration result as log $ft = 3.30$ and by the mixed configuration (plus 0.5) result as log $ft = 4.61$. The Wildenthal calculation gives log $ft = 5.34$ (free) for this transition. The $1 \rightarrow 2$ transition in this decay is measured as log $ft = 5.8$, and is approximated by the pure result as log $ft = \infty$ (zero matrix element) and by the mixed (plus 0.5) result as log $ft = 4.89$. Here the Wildenthal calculation gives log $ft = 4.83$ (free) and log $ft = 5.17$ (fit). In general, the Wildenthal calculations agree very well with experimental data in the six decays considered, and only very rarely differ by as much as an order of magnitude. For instance, the worst case occurs in the decay $^{32}S \rightarrow ^{32}P$. The $1 \rightarrow 1$ transition is measured to be log $ft = 7.42$ and is calculated by Wildenthal to be log $ft = 4.90$ (free) and log $ft = 5.43$ (fit). However, the other measured transitions in this decay are reproduced very well by Wildenthal's results: transition $2 \rightarrow 1$ measured as log $ft = 4.74$ (Wildenthal free log $ft = 4.68$); transition $3 \rightarrow 1$ measured as log $ft = 5.03$ (Wildenthal free log $ft = 5.05$); transition $4 \rightarrow 1$ measured as log $ft = 5.52$ (Wildenthal free log $ft = 5.78$); transition $9 \rightarrow 1$ measured as log $ft = 5.01$ (Wildenthal free log $ft = 5.06$); transition $15 \rightarrow 1$ measured as log $ft = 4.97$ (Wildenthal free log $ft = 4.65$).

Finally, we distill from this information an average Gamow-Teller matrix element, appropriate for the *sd*-shell, which is to be used for unmeasured Gamow-Teller transitions not covered by Wildenthal's calculations or, in the case of $^{26}Al \rightarrow ^{26}Mg$ and $^{30}P \rightarrow ^{30}Si$, a two-particle calculation. Averages of all Wildenthal calculated matrix elements used in the rate computations were taken for each of the six decays considered. The average Gamow-Teller log *ft* for each decay is remarkably consistent: $^{26}Al \rightarrow ^{26}Mg$ (free log $ft = 4.80 \pm 0.4$), $^{30}P \rightarrow ^{30}Si$ (free log $ft = 4.86 \pm 0.4$), $^{32}S \rightarrow ^{32}P$ (free log $ft = 4.78 \pm 0.5$), $^{31}S \rightarrow ^{31}P$ (free log $ft = 4.84 \pm 0.4$), $^{33}S \rightarrow ^{33}P$ (free log $ft = 5.05 \pm 0.4$), $^{35}Cl \rightarrow ^{35}S$ (free log $ft = 4.93 \pm 0.4$). The overall average for all Wildenthal calculated Gamow-Teller transitions is log *ft* (free) $= 4.86 \pm 0.5$ and log *ft* (fit) $= 5.09 \pm 0.5$. This mean includes roughly 400 matrix elements for transitions between states usually lying at or below excitation energies of 6 MeV. An average of experimentally determined Gamow-Teller transitions in the *sd*-shell taken from Endt and van der Leun (1978) gives log $ft = 4.8 \pm 0.6$. This average is taken only for decays with large nuclear *Q*-values ($\gtrsim 3$ MeV), wherein many Gamow-Teller transitions could be sampled at excitation energies near those required for parent state sum rule saturation. In light of these results, we choose log $ft = 5.0$ for use in otherwise undetermined Gamow-Teller transitions. This is to be compared with log $ft = 5.7$ used by Hansen (1966) in his survey of these nuclei which, though it looks much slower, makes little difference in the

stellar rates except at the higher temperatures and densities due to the dominant role of more accurately determined transitions. Our best stellar rates are computed using, in order of priority, experimental matrix elements and those determined by isospin symmetry (Fermi and mirror transitions), Gamow-Teller values from Wildenthal results, two-particle Gamow-Teller calculations (mixed values plus 0.5), and finally the average Gamow-Teller value of log $ft = 5.0$. This order of priority reflects the associated rank of confidence in each type of matrix element determination and, fortunately, also reflects in general the level of contribution of each type to the rates.

The contribution of each matrix element type to the rates and the sensitivity of these rates to errors in the matrix elements are determined by assigning an uncertainty to each of the matrix element types. Experimentally determined values are assigned a formal uncertainty of zero in log ft, as are those log ft values determined by isospin symmetry. The Wildenthal and two-particle matrix elements are assigned an error of ± 0.4 in log ft, reflecting the average deviation of these numbers from experimentally determined values seen in these decays and in the rest of the *sd*-shell. The average value of $ft = 10^5$ used for the remaining undetermined Gamow-Teller transitions is taken to be uncertain by a factor of 10 (± 1.0 in log ft). The values of log $ft = 4$, 5, 6 correspond to fast, intermediate, and relatively hindered Gamow-Teller matrix elements. This uncertainty is about twice the standard deviation for the average Gamow-Teller transition. A rough rate uncertainty is estimated by the following scheme: The slowest rates are computed using the assigned log ft values with their uncertainties added; likewise, the fastest rates are computed using the assigned log ft values with their uncertainties subtracted. In addition, for the fastest rates, "continuum" states are assigned at energies slightly beyond the last state of parent and daughter nucleus employed and each transition into and out of these states is assigned log $ft = 3.5$, enough strength to take account of possible undetected high-lying Gamow-Teller strength. This latter computational device overestimates the uncertainty by oversaturating the Gamow-Teller sum rule in many cases and by putting all of this strength at the lowest possible excitation energy. The "rate uncertainty" Δ is then computed as the greater of the ratio of the fast rate to our best stellar rate and the ratio of our best stellar rate to the slow rate at each temperature and density point. Log Δ is tabulated in the rate tables, and shows for any temperature and density roughly which matrix element types contribute most to the rate and how much the rate could change due to matrix element errors and undetected high-lying strength. Note that where calculated or average-value Gamow-Teller transitions dominate the rate, Δ is a true measure of the matrix element induced uncertainty only if many such matrix elements contribute to the rate. This is because the assigned uncertainty in these cases reflects the standard deviation of a large ensemble of matrix elements, and any given individual assignment may be in error by a considerably larger factor. However, where Gamow-Teller transitions are important, many usually contribute, except at very low temperatures and high densities where a few Gamow-Teller electron capture channels can contribute (e.g., the $1 \rightarrow 6$ and $1 \rightarrow 10$ transitions in $^{26}\mathrm{Al} \rightarrow {}^{26}\mathrm{Mg}$ have log $ft = 4.10$ and make the substantial contribution to the rate for $\rho/\mu_e > 10^6$ and $T_9 < 1$; *cf.* § IV). In addition, the contribution of the different matrix element types is checked by computing the rate first with just the experimental and mirror decays and Fermi transitions, and then with the calculated Gamow-Teller transitions. Comparison of these rates gives a clear indication of where in temperature and density each matrix element type dominates. Furthermore, examination of the summations (10a) and (10b) term by term gives an explicit measure of the contributions of each individual parent and daughter state.

In summary, we conclude that over most of the range of temperature and density considered the rates are dominated by the most accurately determined matrix elements (experimental, Fermi, and mirror decays), and the rates are fairly well determined even at the highest temperatures and densities where unmeasured Gamow-Teller transitions dominate.

IV. APPLICATIONS AND DISCUSSION

In this section the stellar rates for the decays $^{26}\mathrm{Al} \rightarrow {}^{26}\mathrm{Mg}$ ($Q_n = 3.494$ MeV), $^{30}\mathrm{P} \rightarrow {}^{30}\mathrm{Si}$ ($Q_n = 3.716$ MeV), $^{31}\mathrm{S} \rightarrow {}^{31}\mathrm{P}$ ($Q_n = 4.884$ MeV), $^{32}\mathrm{S} \rightarrow {}^{32}\mathrm{P}$ ($Q_n = -2.221$ MeV), $^{33}\mathrm{S} \rightarrow {}^{33}\mathrm{P}$ ($Q_n = -0.760$ MeV), and $^{35}\mathrm{Cl} \rightarrow {}^{35}\mathrm{S}$ ($Q_n = -0.678$ MeV) are presented as functions of temperature and density. The first three columns of Tables 3, and 5–10, give the temperature $T_9 = T/10^9$ K, the Brigg's logarithm of ρ/μ_e where ρ is the density in g cm^{-3}, and μ_e is the mean molecular weight per electron in g mole^{-1}, and the electron chemical potential U_F in MeV, calculated for a perfect Fermi gas electron equation of state. U_F is the Fermi kinetic energy at high density. In the remaining columns the tables present log β^+, where β^+ designates positron emission rates (all rates in s^{-1}); log ε^- where ε^- designates the electron capture rate; log Σ where Σ is the total weak interaction rate $= \beta^+ + \varepsilon^-$; log Δ, where Δ is the multiplicative uncertainty in Σ; and log ν, where ν is the total neutrino energy loss rate in MeV s^{-1} corresponding to Σ. The level of uncertainty in the neutrino energy loss rates can be gauged by log Δ for the associated weak decay rate Σ. A number of the decay rates are plotted in Figures 2 to 7.

At sufficiently high temperatures all parent $^{26}\mathrm{Al}$ states are in thermal equilibrium and the stellar rate is given by equation (8) with statistical weighting factors (9). These rates are shown in Table 3. As we see in Figure 2*a*, the

TABLE 3

DECAY RATES FOR $^{26}Al \rightarrow ^{26}Mg$

T_9	log ρ/μ_e	U_f	log β^+	log ε^-	log Σ	log Δ	log ν
0.01	1.0	−0.003	−13.558	−17.022	−13.558	0.000	−13.722
0.02	1.0	−0.007	−13.558	−17.176	−13.558	0.000	−13.722
0.03	1.0	−0.013	−13.558	−17.261	−13.558	0.000	−13.722
0.05	1.0	−0.024	−13.558	−17.367	−13.558	0.000	−13.722
0.07	1.0	−0.037	−13.558	−17.437	−13.558	0.000	−13.722
0.10	1.0	−0.058	−13.235	−17.496	−13.235	0.000	−13.137
0.20	1.0	−0.134	−7.760	−13.573	−7.760	0.000	−7.511
0.30	1.0	−0.218	−5.841	−11.718	−5.841	0.000	−5.592
0.50	1.0	−0.398	−4.306	−10.247	−4.306	0.000	−4.057
0.70	1.0	−0.503	−3.649	−8.984	−3.649	0.001	−3.400
1.00	1.0	−0.511	−3.159	−7.196	−3.159	0.001	−2.911
2.00	1.0	−0.511	−2.602	−4.781	−2.599	0.005	−2.346
3.00	1.0	−0.511	−2.402	−3.748	−2.383	0.020	−2.104
5.00	1.0	−0.511	−2.158	−2.560	−2.013	0.139	−1.596
7.00	1.0	−0.511	−1.977	−1.780	−1.566	0.335	−0.986
10.00	1.0	−0.511	−1.785	−0.964	−0.903	0.509	−0.161
0.01	2.0	−0.001	−13.558	−16.043	−13.556	0.000	−13.719
0.02	2.0	−0.003	−13.558	−16.185	−13.557	0.000	−13.720
0.03	2.0	−0.007	−13.558	−16.271	−13.557	0.000	−13.720
0.05	2.0	−0.014	−13.558	−16.369	−13.557	0.000	−13.720
0.07	2.0	−0.023	−13.558	−16.436	−13.557	0.000	−13.721
0.10	2.0	−0.038	−13.235	−16.496	−13.235	0.000	−13.137
0.20	2.0	−0.095	−7.760	−12.574	−7.760	0.000	−7.511
0.30	2.0	−0.158	−5.841	−10.718	−5.841	0.000	−5.592
0.50	2.0	−0.299	−4.306	−9.249	−4.306	0.000	−4.057
0.70	2.0	−0.446	−3.649	−8.571	−3.649	0.001	−3.400
1.00	2.0	−0.506	−3.159	−7.174	−3.159	0.001	−2.911
2.00	2.0	−0.511	−2.602	−4.780	−2.599	0.005	−2.346
3.00	2.0	−0.511	−2.402	−3.748	−2.383	0.020	−2.104
5.00	2.0	−0.511	−2.158	−2.560	−2.013	0.139	−1.596
7.00	2.0	−0.511	−1.977	−1.780	−1.566	0.335	−0.986
10.00	2.0	−0.511	−1.785	−0.964	−0.903	0.509	−0.161
0.01	3.0	0.003	−13.558	−15.141	−13.547	0.000	−13.698
0.02	3.0	0.002	−13.558	−15.225	−13.548	0.000	−13.702
0.03	3.0	0.000	−13.558	−15.303	−13.550	0.000	−13.705
0.05	3.0	−0.004	−13.558	−15.388	−13.551	0.000	−13.708
0.07	3.0	−0.009	−13.558	−15.449	−13.552	0.000	−13.710
0.10	3.0	−0.018	−13.235	−15.501	−13.233	0.000	−13.134
0.20	3.0	−0.055	−7.760	−11.575	−7.760	0.000	−7.511
0.30	3.0	−0.099	−5.841	−9.719	−5.841	0.000	−5.592
0.50	3.0	−0.200	−4.306	−8.250	−4.306	0.000	−4.057
0.70	3.0	−0.314	−3.649	−7.624	−3.649	0.001	−3.400
1.00	3.0	−0.465	−3.159	−6.969	−3.159	0.001	−2.910
2.00	3.0	−0.510	−2.602	−4.777	−2.599	0.005	−2.345
3.00	3.0	−0.511	−2.402	−3.747	−2.383	0.020	−2.104
5.00	3.0	−0.511	−2.158	−2.560	−2.013	0.139	−1.596
7.00	3.0	−0.511	−1.977	−1.780	−1.566	0.335	−0.986
10.00	3.0	−0.511	−1.785	−0.964	−0.903	0.509	−0.161
0.01	4.0	0.012	−13.558	−14.466	−13.507	0.000	−13.618
0.02	4.0	0.012	−13.558	−14.465	−13.507	0.000	−13.617
0.03	4.0	0.011	−13.558	−14.481	−13.509	0.000	−13.621
0.05	4.0	0.010	−13.558	−14.502	−13.511	0.000	−13.625
0.07	4.0	0.009	−13.558	−14.521	−13.513	0.000	−13.629
0.10	4.0	0.005	−13.235	−14.551	−13.215	0.000	−13.112
0.20	4.0	−0.013	−7.760	−10.592	−7.759	0.000	−7.510
0.30	4.0	−0.037	−5.841	−8.727	−5.840	0.000	−5.591
0.50	4.0	−0.100	−4.306	−7.253	−4.305	0.000	−4.056
0.70	4.0	−0.174	−3.649	−6.626	−3.648	0.000	−3.399
1.00	4.0	−0.302	−3.159	−6.151	−3.158	0.001	−2.910
2.00	4.0	−0.497	−2.602	−4.748	−2.598	0.004	−2.345
3.00	4.0	−0.507	−2.402	−3.742	−2.383	0.020	−2.103
5.00	4.0	−0.510	−2.158	−2.559	−2.013	0.139	−1.596
7.00	4.0	−0.511	−1.977	−1.779	−1.566	0.336	−0.986
10.00	4.0	−0.511	−1.785	−0.964	−0.903	0.509	−0.161
0.01	5.0	0.053	−13.558	−13.706	−13.325	0.000	−13.310
0.02	5.0	0.053	−13.558	−13.706	−13.325	0.000	−13.310
0.03	5.0	0.053	−13.558	−13.705	−13.324	0.000	−13.310
0.05	5.0	0.053	−13.558	−13.704	−13.324	0.000	−13.309
0.07	5.0	0.053	−13.558	−13.706	−13.325	0.000	−13.310
0.10	5.0	0.052	−13.235	−13.703	−13.108	0.000	−12.982
0.20	5.0	0.047	−7.760	−9.679	−7.754	0.000	−7.499
0.30	5.0	0.038	−5.841	−7.779	−5.836	0.000	−5.580
0.50	5.0	0.011	−4.306	−6.276	−4.301	0.000	−4.046
0.70	5.0	−0.026	−3.649	−5.637	−3.644	0.000	−3.390
1.00	5.0	−0.098	−3.159	−5.159	−3.154	0.001	−2.900
2.00	5.0	−0.383	−2.601	−4.464	−2.595	0.005	−2.338
3.00	5.0	−0.476	−2.402	−3.690	−2.380	0.021	−2.097
5.00	5.0	−0.502	−2.158	−2.551	−2.010	0.140	−1.592
7.00	5.0	−0.507	−1.977	−1.777	−1.564	0.335	−0.983
10.00	5.0	−0.509	−1.785	−0.963	−0.902	0.509	−0.160
0.01	6.0	0.215	−13.558	−12.801	−12.731	0.000	−12.565
0.02	6.0	0.215	−13.558	−12.801	−12.731	0.000	−12.565
0.03	6.0	0.215	−13.558	−12.801	−12.731	0.000	−12.565
0.05	6.0	0.215	−13.558	−12.801	−12.731	0.000	−12.564
0.07	6.0	0.215	−13.558	−12.800	−12.730	0.000	−12.564
0.10	6.0	0.214	−13.235	−12.751	−12.628	0.044	−12.470
0.20	6.0	0.213	−7.760	−8.785	−7.720	0.001	−7.423
0.30	6.0	0.211	−5.841	−6.875	−5.802	0.000	−5.504
0.50	6.0	0.202	−4.306	−5.341	−4.267	0.001	−3.969
0.70	6.0	0.189	−3.649	−4.680	−3.610	0.001	−3.311
1.00	6.0	0.161	−3.159	−4.181	−3.119	0.003	−2.820
2.00	6.0	0.001	−2.601	−3.575	−2.557	0.012	−2.254
3.00	6.0	−0.212	−2.401	−3.270	−2.346	0.032	−2.026
5.00	6.0	−0.420	−2.156	−2.472	−1.985	0.147	−1.550
7.00	6.0	−0.469	−1.975	−1.750	−1.547	0.336	−0.962
10.00	6.0	−0.491	−1.784	−0.954	−0.894	0.508	−0.151
0.01	6.5	0.402	−13.558	−6.454	−6.454	0.400	−7.627
0.02	6.5	0.402	−13.558	−6.453	−6.453	0.400	−7.625
0.03	6.5	0.402	−13.558	−6.450	−6.450	0.400	−7.620
0.05	6.5	0.402	−13.558	−6.443	−6.443	0.400	−7.606
0.07	6.5	0.402	−13.558	−6.439	−6.439	0.400	−7.595
0.10	6.5	0.402	−13.235	−6.416	−6.416	0.400	−7.552
0.20	6.5	0.401	−7.760	−6.307	−6.292	0.388	−7.017
0.30	6.5	0.399	−5.841	−5.970	−5.599	0.147	−5.353
0.50	6.5	0.394	−4.306	−4.819	−4.190	0.014	−3.824
0.70	6.5	0.386	−3.649	−4.179	−3.537	0.008	−3.165
1.00	6.5	0.368	−3.159	−3.682	−3.045	0.010	−2.671
2.00	6.5	0.266	−2.601	−3.068	−2.474	0.029	−2.093
3.00	6.5	0.101	−2.400	−2.805	−2.256	0.056	−1.860
5.00	6.5	−0.234	−2.153	−2.295	−1.918	0.164	−1.445
7.00	6.5	−0.377	−1.973	−1.688	−1.506	0.339	−0.910
10.00	6.5	−0.449	−1.782	−0.934	−0.876	0.508	−0.132
0.01	7.0	0.711	−13.558	−4.268	−4.268	0.400	−4.778
0.02	7.0	0.711	−13.558	−4.268	−4.268	0.400	−4.778
0.03	7.0	0.711	−13.558	−4.268	−4.268	0.400	−4.778
0.05	7.0	0.711	−13.558	−4.268	−4.268	0.400	−4.777
0.07	7.0	0.711	−13.558	−4.267	−4.267	0.400	−4.775
0.10	7.0	0.711	−13.235	−4.265	−4.265	0.400	−4.773
0.20	7.0	0.711	−7.760	−4.257	−4.257	0.400	−4.756
0.30	7.0	0.710	−5.841	−4.236	−4.225	0.388	−4.567
0.50	7.0	0.706	−4.306	−3.971	−3.806	0.203	−3.492
0.70	7.0	0.701	−3.649	−3.557	−3.299	0.086	−2.853
1.00	7.0	0.689	−3.159	−3.123	−2.840	0.050	−2.360
2.00	7.0	0.622	−2.601	−2.532	−2.264	0.067	−1.771
3.00	7.0	0.510	−2.400	−2.278	−2.034	0.105	−1.529
5.00	7.0	0.187	−2.150	−1.910	−1.712	0.203	−1.164
7.00	7.0	−0.107	−1.966	−1.504	−1.375	0.345	−0.750
10.00	7.0	−0.315	−1.777	−0.869	−0.819	0.507	−0.069
0.01	7.5	1.197	−13.558	−2.945	−2.945	0.400	−3.113
0.02	7.5	1.197	−13.558	−2.945	−2.945	0.400	−3.112
0.03	7.5	1.197	−13.558	−2.945	−2.945	0.400	−3.112
0.05	7.5	1.197	−13.558	−2.945	−2.945	0.400	−3.112
0.07	7.5	1.197	−13.558	−2.944	−2.944	0.400	−3.112
0.10	7.5	1.197	−13.235	−2.944	−2.944	0.400	−3.111
0.20	7.5	1.197	−7.760	−2.942	−2.942	0.400	−3.108
0.30	7.5	1.196	−5.841	−2.936	−2.936	0.399	−3.088
0.50	7.5	1.194	−4.306	−2.873	−2.857	0.359	−2.784
0.70	7.5	1.190	−3.649	−2.707	−2.660	0.268	−2.302
1.00	7.5	1.182	−3.159	−2.433	−2.359	0.176	−1.855
2.00	7.5	1.137	−2.601	−1.933	−1.849	0.138	−1.276
3.00	7.5	1.062	−2.400	−1.700	−1.621	0.168	−1.036
5.00	7.5	0.825	−2.148	−1.380	−1.312	0.251	−0.693
7.00	7.5	0.507	−1.958	−1.104	−1.047	0.359	−0.377
10.00	7.5	0.082	−1.764	−0.681	−0.646	0.504	0.116
0.01	8.0	1.936	−13.558	−1.771	−1.771	0.405	−1.695
0.02	8.0	1.936	−13.558	−1.771	−1.771	0.404	−1.695
0.03	8.0	1.936	−13.558	−1.771	−1.771	0.404	−1.695
0.05	8.0	1.936	−13.558	−1.771	−1.771	0.404	−1.695
0.07	8.0	1.936	−13.558	−1.771	−1.771	0.404	−1.695
0.10	8.0	1.936	−13.235	−1.771	−1.771	0.405	−1.695
0.20	8.0	1.935	−7.760	−1.770	−1.770	0.404	−1.694
0.30	8.0	1.935	−5.841	−1.769	−1.769	0.404	−1.690
0.50	8.0	1.933	−4.306	−1.751	−1.749	0.394	−1.617
0.70	8.0	1.931	−3.649	−1.696	−1.691	0.365	−1.429
1.00	8.0	1.925	−3.159	−1.571	−1.560	0.308	−1.135
2.00	8.0	1.895	−2.601	−1.234	−1.216	0.234	−0.635
3.00	8.0	1.844	−2.400	−1.043	−1.024	0.241	−0.411
5.00	8.0	1.681	−2.148	−0.774	−0.756	0.298	−0.099
7.00	8.0	1.441	−1.955	−0.551	−0.534	0.378	0.172
10.00	8.0	0.982	−1.750	−0.270	−0.255	0.502	0.528
0.01	8.5	3.037	−13.558	−0.710	−0.710	0.449	−0.405
0.02	8.5	3.038	−13.558	−0.709	−0.709	0.449	−0.404
0.03	8.5	3.038	−13.558	−0.710	−0.710	0.449	−0.405
0.05	8.5	3.038	−13.558	−0.710	−0.710	0.450	−0.405
0.07	8.5	3.038	−13.558	−0.710	−0.710	0.450	−0.405
0.10	8.5	3.038	−13.235	−0.710	−0.710	0.450	−0.405
0.20	8.5	3.038	−7.760	−0.709	−0.709	0.449	−0.404
0.30	8.5	3.037	−5.841	−0.709	−0.709	0.450	−0.403
0.50	8.5	3.036	−4.306	−0.702	−0.702	0.446	−0.384
0.70	8.5	3.035	−3.649	−0.681	−0.681	0.435	−0.323
1.00	8.5	3.031	−3.159	−0.627	−0.626	0.407	−0.188
2.00	8.5	3.010	−2.601	−0.432	−0.429	0.344	0.154
3.00	8.5	2.978	−2.400	−0.297	−0.293	0.333	0.339
5.00	8.5	2.864	−2.148	−0.093	−0.089	0.355	0.602
7.00	8.5	2.698	−1.954	0.083	0.087	0.410	0.828
10.00	8.5	2.352	−1.743	0.299	0.303	0.510	1.115
0.01	9.0	4.671	−13.558	0.271	0.271	0.531	0.791
0.02	9.0	4.671	−13.558	0.271	0.271	0.531	0.791
0.03	9.0	4.671	−13.558	0.271	0.271	0.531	0.791
0.05	9.0	4.671	−13.558	0.271	0.271	0.531	0.791
0.07	9.0	4.671	−13.558	0.271	0.271	0.531	0.791
0.10	9.0	4.671	−13.235	0.271	0.271	0.531	0.791
0.20	9.0	4.671	−7.760	0.271	0.271	0.531	0.792
0.30	9.0	4.671	−5.841	0.272	0.272	0.531	0.792
0.50	9.0	4.671	−4.306	0.275	0.275	0.529	0.799
0.70	9.0	4.665	−3.649	0.282	0.283	0.523	0.819
1.00	9.0	4.665	−3.159	0.310	0.310	0.508	0.878
2.00	9.0	4.650	−2.601	0.423	0.424	0.459	1.076
3.00	9.0	4.625	−2.400	0.513	0.514	0.437	1.208
5.00	9.0	4.551	−2.148	0.658	0.659	0.430	1.408
7.00	9.0	4.438	−1.954	0.787	0.788	0.456	1.584
10.00	9.0	4.197	−1.741	0.948	0.949	0.529	1.807

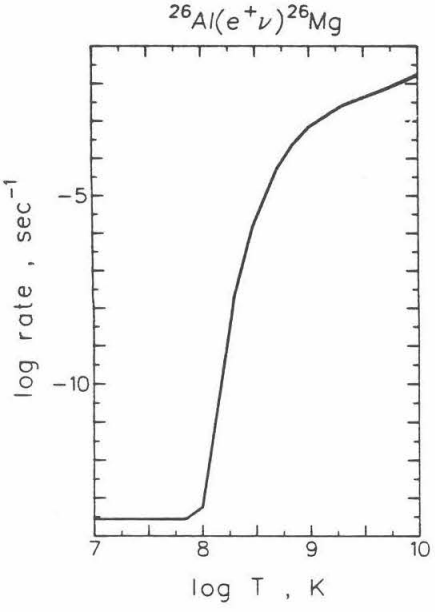

FIG. 2a

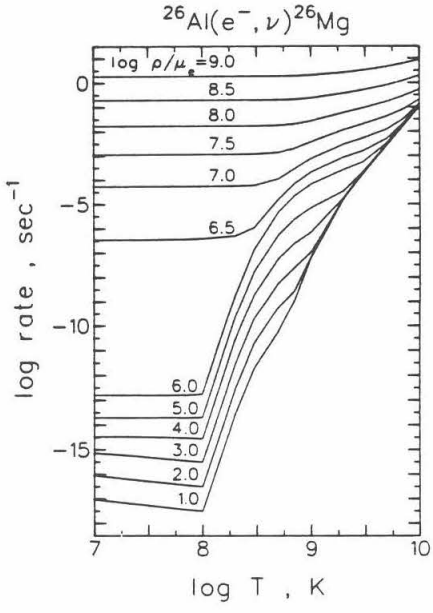

FIG. 2b

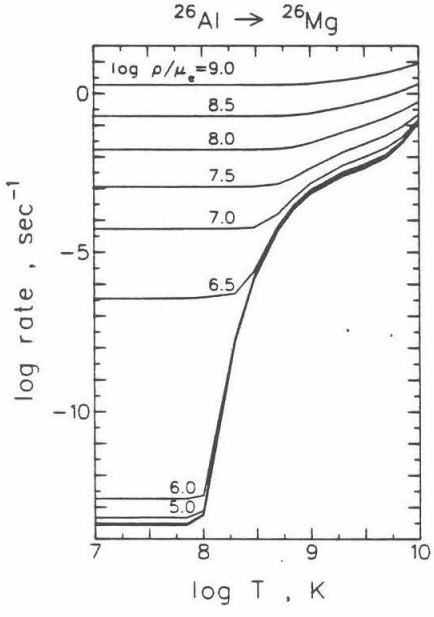

FIG. 2c

FIG. 2.—(*a*) Positron emission rate for $^{26}Al \rightarrow {}^{26}Mg$ with all ^{26}Al states assumed to be in thermal equilibrium. The values of log β^+ from Table 3 are displayed for the temperature and density grid of Fig. 1. The density dependence of positron emission is negligible in most cases of interest. The rate is dominated by the changeover from the laboratory rate determined by the ground state decay to the much faster decays accessible from the metastable isomeric state at 0.228 MeV as it becomes thermally populated. (*b*) Electron capture rate for $^{26}Ag \rightarrow {}^{26}Mg$ with all ^{26}Al states assumed to be in thermal equilibrium. The values of log ε^- from Table 3 are displayed as a function of temperature and density. The dramatic increase of more than six orders of magnitude from log $\rho/\mu_e = 6.0$ to 6.5 at low temperature is due to the opening up of fast (allowed) upward transitions from the parent ground state (5^+) as the electron chemical potential becomes sufficiently large to overcome the energy interval. The equality of the rates at different density points for high temperature is the result of the similar behavior of U_F in Fig. 1. (*c*) Total decay rate (positron emission plus electron capture) for $^{26}Al \rightarrow {}^{26}Mg$ assuming all ^{26}Al states to be in thermal equilibrium. Log Σ from Table 3 is displayed as a function of temperature and density. Positron emission dominates below about log $\rho/\mu_e = 6.0$, electron capture above.

positron emission rate is dominated by the very slow ground state transitions at low temperatures, but the much faster decay from the isomeric state takes over quickly with increasing temperature above $T_9=0.1$. This decay, transition 2→1 in Table 1, is a Fermi transition with log $ft=3.49$. The large available decay phase space and small log ft-value of the isomeric state transition is difficult competition for other transitions to match. A rate based on the ground state and the isomeric state alone would match our curve well until very high temperatures are reached. The electron capture rate (Fig. 2*b*) is slower than the positron emission rate until log $\rho/\mu_e \gtrsim 6$; above this value the electron capture component dominates the total rate (Fig. 2*c*). The electron capture rate for a given transition generally tends to increase smoothly as the density of electrons at the nucleus and the phase space integral, equation (3b), increase. The large increase in the ^{26}Al electron capture rate (Fig. 2*b*) from log $\rho/\mu_e=6.0$ to 6.5 at low temperature is due to the opening up of the intrinsically fast (log $ft\approx 4.1$) but energetically unfavorable upward transitions from the ground state 1→6 and 1→10. Above log $\rho/\mu_e=6.0$ the chemical potential U_F (cf. Fig. 1) becomes large enough for the electrons in the tail of the Fermi-Dirac distribution to become sufficiently energetic to overcome the threshold kinetic energy, which is 0.313 MeV for 1→6 and 0.895 MeV for 1→10. These values result from subtracting the ^{26}Al–^{26}Mg atomic Q-value, 4.005 MeV, from the excitation energies, 4.318 MeV for state 6 in Mg and 4.900 MeV for state 10.

Although the Fermi transition from the 0.228 MeV isomeric state of ^{26}Al dominates the equilibrium rate at even moderate temperatures, communication between the isomeric state and the ground state by electromagnetic transitions is poor, and at sufficiently low temperatures it is not a good assumption that this first excited state is in thermal equilibrium with the ground state. Ward and Fowler (1979) estimate that the time required for the 0.228 MeV state to equilibrate exceeds its lifetime against positron emission for $T_9<0.4$. Therefore, we have calculated positron emission and electron capture rates separately for the metastable state and those that communicate with it (the mestastable state system $^{26}Al_m$) and the ground state and those that communicate with it (the ground state system $^{26}Al_g$). Several states are members of both systems; the gamma-ray branching (Table 26.13 of Endt and van der Leun (1978) has been used to make the fractional assignments of Table 4. Decay rates for the ground state and isomeric state systems are given in Tables 5*a* and 5*b*.

We have seen that the weak destruction rate by electron capture and positron emission of ^{26}Al becomes a sensitive function of temperature and density varying over many orders of magnitude for the more extreme conditions. Since the well studied isomeric state dominates at all but the highest temperatures considered, the positron emission rate agrees well with that of Hansen (1966) until $T_9>3$, at which point the fast transitions (4→1, 6→1, and 9→1 in Table 1) with log ft values given accurately by the mirror decays in ^{26}Si–^{26}Al, increase the rate by a factor of 2–3 faster than Hansen's rates. However, this increase falls within the factor of 5 fitting error quoted by Hansen. At $T_9=2$, our electron capture rate ranges from a factor of 6 slower than Hansen at $\rho/\mu_e=10^2$ (a value outside the range of

TABLE 4

RESOLUTION OF ^{26}Al STATES INTO GROUND STATE ($^{26}Al_g$) AND METASTABLE STATE ($^{26}Al_m$) SYSTEMS

State	E_x (MeV)	g	m
1.....	0	1.	0.
2.....	0.228	0.	1.
3.....	0.417	1.	0.
4.....	1.058	0.	1.
5.....	1.759	0.98	0.02
6.....	1.851	0.	1.
7.....	2.069	1.	0.
8.....	2.070	0.23	0.77
9.....	2.072	0.	1.
10.....	2.365	0.46	0.54
11.....	2.545	0.49	0.51
12.....	2.661	0.67	0.33
13.....	2.739	0.	1.
14.....	2.913	0.53	0.47
15.....	3.074	0.20	0.80
16.....	3.159	0.82	0.18
22.....	3.179	0.06	0.94
24.....	3.745	0.	1.
ANLG	5.918	0.5	0.5
ANLG	6.353	0.5	0.5

TABLE 5A

DECAY RATES FOR $^{26}Al_g \rightarrow {}^{26}Mg$

T_9	log ρ/μ_e	U_r	log β^+	log ε^-	log Σ	log Δ	log ν
0.01	1.0	-0.003	-13.558	-17.022	-13.558	0.000	-13.722
0.02	1.0	-0.007	-13.558	-17.176	-13.558	0.000	-13.722
0.03	1.0	-0.013	-13.558	-17.261	-13.558	0.000	-13.722
0.05	1.0	-0.024	-13.558	-17.367	-13.558	0.000	-13.722
0.07	1.0	-0.037	-13.558	-17.437	-13.558	0.000	-13.722
0.10	1.0	-0.058	-13.558	-17.504	-13.558	0.000	-13.722
0.20	1.0	-0.134	-13.524	-17.585	-13.524	0.046	-13.680
0.30	1.0	-0.218	-11.149	-15.349	-11.149	0.399	-11.211
0.50	1.0	-0.398	-8.350	-12.635	-8.350	0.400	-8.411
0.70	1.0	-0.503	-7.150	-10.824	-7.150	0.400	-7.211
1.00	1.0	-0.511	-6.251	-8.614	-6.249	0.400	-6.309
2.00	1.0	-0.511	-5.207	-5.658	-5.078	0.404	-5.023
3.00	1.0	-0.511	-4.625	-4.405	-4.200	0.454	-3.957
5.00	1.0	-0.511	-3.450	-2.992	-2.862	0.586	-2.452
7.00	1.0	-0.511	-2.790	-2.093	-2.013	0.656	-1.475
10.00	1.0	-0.511	-2.282	-1.184	-1.151	0.708	-0.458
0.01	2.0	-0.001	-13.558	-16.043	-13.556	0.000	-13.719
0.02	2.0	-0.003	-13.558	-16.185	-13.557	0.000	-13.720
0.03	2.0	-0.007	-13.558	-16.271	-13.557	0.000	-13.720
0.05	2.0	-0.014	-13.558	-16.369	-13.557	0.000	-13.720
0.07	2.0	-0.023	-13.558	-16.436	-13.557	0.000	-13.721
0.10	2.0	-0.038	-13.558	-16.504	-13.557	0.000	-13.721
0.20	2.0	-0.095	-13.524	-16.585	-13.524	0.047	-13.679
0.30	2.0	-0.158	-11.149	-14.348	-11.149	0.399	-11.210
0.50	2.0	-0.299	-8.350	-11.637	-8.350	0.400	-8.411
0.70	2.0	-0.446	-7.150	-10.411	-7.149	0.400	-7.211
1.00	2.0	-0.506	-6.251	-8.592	-6.249	0.400	-6.309
2.00	2.0	-0.511	-5.207	-5.658	-5.078	0.404	-5.023
3.00	2.0	-0.511	-4.625	-4.405	-4.200	0.454	-3.957
5.00	2.0	-0.511	-3.450	-2.992	-2.862	0.586	-2.452
7.00	2.0	-0.511	-2.790	-2.093	-2.013	0.656	-1.475
10.00	2.0	-0.511	-2.282	-1.184	-1.151	0.708	-0.458
0.01	3.0	0.003	-13.558	-15.141	-13.547	0.000	-13.698
0.02	3.0	0.002	-13.558	-15.225	-13.548	0.000	-13.702
0.03	3.0	0.000	-13.558	-15.303	-13.550	0.000	-13.705
0.05	3.0	-0.004	-13.558	-15.388	-13.551	0.000	-13.708
0.07	3.0	-0.009	-13.558	-15.449	-13.552	0.000	-13.710
0.10	3.0	-0.018	-13.558	-15.509	-13.553	0.000	-13.711
0.20	3.0	-0.055	-13.524	-15.586	-13.520	0.046	-13.672
0.30	3.0	-0.099	-11.149	-13.349	-11.146	0.399	-11.206
0.50	3.0	-0.200	-8.350	-10.637	-8.348	0.400	-8.407
0.70	3.0	-0.314	-7.150	-9.464	-7.148	0.400	-7.207
1.00	3.0	-0.465	-6.251	-8.386	-6.248	0.400	-6.307
2.00	3.0	-0.510	-5.207	-5.655	-5.075	0.404	-5.022
3.00	3.0	-0.511	-4.625	-4.405	-4.200	0.454	-3.956
5.00	3.0	-0.511	-3.450	-2.992	-2.862	0.586	-2.452
7.00	3.0	-0.511	-2.790	-2.093	-2.013	0.656	-1.475
10.00	3.0	-0.511	-2.282	-1.184	-1.151	0.708	-0.458
0.01	4.0	0.012	-13.558	-14.466	-13.507	0.000	-13.618
0.02	4.0	0.012	-13.558	-14.465	-13.507	0.000	-13.617
0.03	4.0	0.011	-13.558	-14.481	-13.509	0.000	-13.621
0.05	4.0	0.010	-13.558	-14.502	-13.511	0.000	-13.625
0.07	4.0	0.009	-13.558	-14.521	-13.513	0.000	-13.629
0.10	4.0	0.005	-13.558	-14.559	-13.516	0.000	-13.636
0.20	4.0	-0.013	-13.524	-14.600	-13.489	0.047	-13.609
0.30	4.0	-0.037	-11.149	-12.351	-11.123	0.399	-11.167
0.50	4.0	-0.100	-8.350	-9.639	-8.328	0.400	-8.372
0.70	4.0	-0.174	-7.150	-8.464	-7.129	0.400	-7.173
1.00	4.0	-0.302	-6.251	-7.568	-6.231	0.400	-6.274
2.00	4.0	-0.497	-5.207	-5.623	-5.066	0.403	-5.008
3.00	4.0	-0.507	-4.625	-4.399	-4.197	0.454	-3.952
5.00	4.0	-0.510	-3.450	-2.991	-2.862	0.586	-2.451
7.00	4.0	-0.511	-2.790	-2.092	-2.013	0.656	-1.474
10.00	4.0	-0.511	-2.282	-1.184	-1.151	0.708	-0.458
0.01	5.0	0.053	-13.558	-13.706	-13.325	0.000	-13.310
0.02	5.0	0.053	-13.558	-13.706	-13.325	0.000	-13.310
0.03	5.0	0.053	-13.558	-13.705	-13.324	0.000	-13.310
0.05	5.0	0.053	-13.558	-13.704	-13.324	0.000	-13.309
0.07	5.0	0.053	-13.558	-13.706	-13.325	0.000	-13.310
0.10	5.0	0.052	-13.558	-13.711	-13.327	0.000	-13.313
0.20	5.0	0.047	-13.524	-13.639	-13.277	0.071	-13.283
0.30	5.0	0.038	-11.149	-11.331	-10.930	0.399	-10.918
0.50	5.0	0.011	-8.350	-8.645	-8.172	0.400	-8.130
0.70	5.0	-0.026	-7.150	-7.466	-6.979	0.400	-6.933
1.00	5.0	-0.098	-6.251	-6.570	-6.081	0.400	-6.030
2.00	5.0	-0.383	-5.206	-5.339	-4.967	0.403	-4.864
3.00	5.0	-0.476	-4.624	-4.347	-4.163	0.451	-3.915
5.00	5.0	-0.502	-3.449	-2.983	-2.855	0.584	-2.445
7.00	5.0	-0.507	-2.790	-2.090	-2.011	0.656	-1.472
10.00	5.0	-0.509	-2.282	-1.183	-1.150	0.708	-0.458
0.01	6.0	0.215	-13.558	-12.801	-12.731	0.000	-12.565
0.02	6.0	0.215	-13.558	-12.801	-12.731	0.000	-12.565
0.03	6.0	0.215	-13.558	-12.801	-12.731	0.000	-12.565
0.05	6.0	0.215	-13.558	-12.801	-12.731	0.000	-12.564
0.07	6.0	0.215	-13.558	-12.800	-12.730	0.000	-12.564
0.10	6.0	0.214	-13.558	-12.758	-12.694	0.051	-12.564
0.20	6.0	0.213	-13.524	-10.359	-10.358	0.399	-11.576
0.30	6.0	0.211	-11.149	-8.987	-8.984	0.400	-9.851
0.50	6.0	0.202	-8.350	-7.402	-7.355	0.400	-7.397
0.70	6.0	0.189	-7.150	-6.389	-6.319	0.400	-6.206
1.00	6.0	0.161	-6.251	-5.532	-5.457	0.400	-5.292
2.00	6.0	0.001	-5.205	-4.431	-4.363	0.401	-4.150
3.00	6.0	-0.212	-4.621	-3.919	-3.841	0.427	-3.569
5.00	6.0	-0.420	-3.448	-2.903	-2.794	0.569	-2.380
7.00	6.0	-0.469	-2.789	-2.063	-1.988	0.650	-1.448
10.00	6.0	-0.491	-2.282	-1.174	-1.142	0.707	-0.449
0.01	6.5	0.402	-13.558	-6.454	-6.454	0.400	-7.627
0.02	6.5	0.402	-13.558	-6.453	-6.453	0.400	-7.625
0.03	6.5	0.402	-13.558	-6.450	-6.450	0.400	-7.620
0.05	6.5	0.402	-13.558	-6.443	-6.443	0.400	-7.606
0.07	6.5	0.402	-13.558	-6.439	-6.439	0.400	-7.595
0.10	6.5	0.402	-13.558	-6.416	-6.416	0.400	-7.552
0.20	6.5	0.401	-13.524	-6.311	-6.311	0.400	-7.360
0.30	6.5	0.399	-11.149	-6.173	-6.173	0.400	-7.123
0.50	6.5	0.394	-8.350	-5.865	-5.863	0.400	-6.470
0.70	6.5	0.386	-7.150	-5.471	-5.462	0.400	-5.603
1.00	6.5	0.368	-6.251	-4.877	-4.859	0.400	-4.750
2.00	6.5	0.266	-5.205	-3.880	-3.860	0.401	-3.629
3.00	6.5	0.101	-4.620	-3.434	-3.406	0.413	-3.120
5.00	6.5	-0.234	-3.445	-2.722	-2.647	0.537	-2.227
7.00	6.5	-0.377	-2.787	-2.000	-1.934	0.638	-1.390
10.00	6.5	-0.449	-2.280	-1.154	-1.122	0.704	-0.429
0.01	7.0	0.711	-13.558	-4.268	-4.268	0.400	-4.778
0.02	7.0	0.711	-13.558	-4.268	-4.268	0.400	-4.778
0.03	7.0	0.711	-13.558	-4.268	-4.268	0.400	-4.778
0.05	7.0	0.711	-13.558	-4.268	-4.268	0.400	-4.777
0.07	7.0	0.711	-13.558	-4.267	-4.267	0.400	-4.775
0.10	7.0	0.711	-13.558	-4.265	-4.265	0.400	-4.773
0.20	7.0	0.711	-13.524	-4.258	-4.258	0.400	-4.758
0.30	7.0	0.710	-11.149	-4.246	-4.246	0.400	-4.736
0.50	7.0	0.706	-8.350	-4.209	-4.209	0.400	-4.660
0.70	7.0	0.701	-7.150	-4.139	-4.139	0.400	-4.467
1.00	7.0	0.689	-6.251	-3.935	-3.933	0.400	-3.988
2.00	7.0	0.622	-5.205	-3.241	-3.236	0.400	-3.013
3.00	7.0	0.510	-4.619	-2.854	-2.847	0.408	-2.553
5.00	7.0	0.187	-3.441	-2.323	-2.291	0.490	-1.860
7.00	7.0	-0.107	-2.781	-1.812	-1.768	0.606	-1.216
10.00	7.0	-0.315	-2.276	-1.089	-1.061	0.696	-0.365
0.01	7.5	1.197	-13.558	-2.945	-2.945	0.400	-3.113
0.02	7.5	1.197	-13.558	-2.945	-2.945	0.400	-3.112
0.03	7.5	1.197	-13.558	-2.945	-2.945	0.400	-3.112
0.05	7.5	1.197	-13.558	-2.945	-2.945	0.400	-3.112
0.07	7.5	1.197	-13.558	-2.944	-2.944	0.400	-3.112
0.10	7.5	1.197	-13.558	-2.944	-2.944	0.400	-3.111
0.20	7.5	1.197	-13.524	-2.942	-2.942	0.400	-3.108
0.30	7.5	1.196	-11.149	-2.938	-2.938	0.400	-3.102
0.50	7.5	1.194	-8.350	-2.927	-2.927	0.400	-3.083
0.70	7.5	1.190	-7.150	-2.906	-2.906	0.400	-3.040
1.00	7.5	1.182	-6.251	-2.838	-2.838	0.401	-2.885
2.00	7.5	1.137	-5.205	-2.462	-2.461	0.402	-2.250
3.00	7.5	1.062	-4.619	-2.175	-2.173	0.409	-1.868
5.00	7.5	0.825	-3.440	-1.756	-1.747	0.462	-1.303
7.00	7.5	0.507	-2.775	-1.400	-1.382	0.561	-0.816
10.00	7.5	0.082	-2.266	-0.897	-0.879	0.679	-0.176
0.01	8.0	1.936	-13.558	-1.771	-1.771	0.405	-1.695
0.02	8.0	1.936	-13.558	-1.771	-1.771	0.404	-1.695
0.03	8.0	1.936	-13.558	-1.771	-1.771	0.404	-1.695
0.05	8.0	1.936	-13.558	-1.771	-1.771	0.404	-1.695
0.07	8.0	1.936	-13.558	-1.771	-1.771	0.404	-1.695
0.10	8.0	1.936	-13.558	-1.771	-1.771	0.405	-1.695
0.20	8.0	1.935	-13.524	-1.770	-1.770	0.404	-1.694
0.30	8.0	1.935	-11.149	-1.769	-1.769	0.404	-1.692
0.50	8.0	1.933	-8.350	-1.766	-1.766	0.405	-1.686
0.70	8.0	1.931	-7.150	-1.758	-1.758	0.405	-1.672
1.00	8.0	1.925	-6.251	-1.734	-1.734	0.406	-1.622
2.00	8.0	1.895	-5.205	-1.556	-1.556	0.412	-1.303
3.00	8.0	1.844	-4.619	-1.379	-1.379	0.420	-1.037
5.00	8.0	1.681	-3.439	-1.085	-1.083	0.460	-0.611
7.00	8.0	1.441	-2.772	-0.818	-0.813	0.537	-0.227
10.00	8.0	0.982	-2.254	-0.478	-0.470	0.654	0.246
0.01	8.5	3.037	-13.558	-0.710	-0.710	0.449	-0.405
0.02	8.5	3.038	-13.558	-0.709	-0.709	0.449	-0.404
0.03	8.5	3.038	-13.558	-0.710	-0.710	0.449	-0.405
0.05	8.5	3.038	-13.558	-0.710	-0.710	0.450	-0.405
0.07	8.5	3.038	-13.558	-0.710	-0.710	0.450	-0.405
0.10	8.5	3.038	-13.558	-0.710	-0.710	0.450	-0.405
0.20	8.5	3.038	-13.524	-0.709	-0.709	0.449	-0.404
0.30	8.5	3.037	-11.149	-0.709	-0.709	0.449	-0.404
0.50	8.5	3.036	-8.350	-0.707	-0.707	0.449	-0.401
0.70	8.5	3.035	-7.150	-0.705	-0.705	0.451	-0.396
1.00	8.5	3.031	-6.251	-0.694	-0.694	0.451	-0.377
2.00	8.5	3.010	-5.205	-0.606	-0.606	0.454	-0.227
3.00	8.5	2.976	-4.619	-0.506	-0.506	0.460	-0.070
5.00	8.5	2.864	-3.439	-0.322	-0.322	0.484	0.210
7.00	8.5	2.698	-2.771	-0.137	-0.136	0.538	0.491
10.00	8.5	2.352	-2.248	0.111	0.113	0.641	0.855
0.01	9.0	4.671	-13.558	0.271	0.271	0.531	0.791
0.02	9.0	4.671	-13.558	0.271	0.271	0.531	0.791
0.03	9.0	4.671	-13.558	0.271	0.271	0.531	0.791
0.05	9.0	4.671	-13.558	0.271	0.271	0.531	0.791
0.07	9.0	4.671	-13.558	0.271	0.271	0.531	0.791
0.10	9.0	4.671	-13.558	0.271	0.271	0.531	0.791
0.20	9.0	4.671	-13.524	0.271	0.271	0.531	0.792
0.30	9.0	4.671	-11.149	0.272	0.272	0.531	0.792
0.50	9.0	4.671	-8.350	0.272	0.272	0.532	0.793
0.70	9.0	4.665	-7.150	0.272	0.272	0.531	0.793
1.00	9.0	4.665	-6.251	0.278	0.278	0.532	0.803
2.00	9.0	4.650	-5.205	0.329	0.329	0.527	0.881
3.00	9.0	4.625	-4.619	0.388	0.388	0.525	0.970
5.00	9.0	4.551	-3.439	0.502	0.502	0.530	1.141
7.00	9.0	4.438	-2.771	0.620	0.620	0.560	1.324
10.00	9.0	4.197	-2.247	0.791	0.791	0.639	1.584

TABLE 5B

DECAY RATES FOR $^{26}Al_m \rightarrow {}^{26}Mg$

T_9	log ρ/μ_e	U_f	log β^+	log ε^-	log Σ	log Δ	log ν
0.01	1.0	−0.003	−0.962	−6.166	−0.962	0.000	−0.713
0.02	1.0	−0.007	−0.962	−6.321	−0.962	0.000	−0.713
0.03	1.0	−0.013	−0.962	−6.406	−0.962	0.000	−0.713
0.05	1.0	−0.024	−0.962	−6.513	−0.962	0.000	−0.713
0.07	1.0	−0.037	−0.962	−6.584	−0.962	0.000	−0.713
0.10	1.0	−0.058	−0.962	−6.652	−0.962	0.000	−0.713
0.20	1.0	−0.134	−0.962	−6.775	−0.962	0.000	−0.713
0.30	1.0	−0.218	−0.962	−6.839	−0.962	0.000	−0.713
0.50	1.0	−0.398	−0.962	−6.904	−0.962	0.000	−0.713
0.70	1.0	−0.503	−0.962	−6.303	−0.962	0.000	−0.713
1.00	1.0	−0.511	−0.962	−5.015	−0.961	0.000	−0.713
2.00	1.0	−0.511	−0.962	−3.201	−0.960	0.003	−0.706
3.00	1.0	−0.511	−0.965	−2.412	−0.950	0.016	−0.670
5.00	1.0	−0.511	−0.986	−1.563	−0.884	0.137	−0.463
7.00	1.0	−0.511	−1.023	−1.053	−0.737	0.338	−0.140
10.00	1.0	−0.511	−1.073	−0.513	−0.407	0.541	0.369
0.01	2.0	−0.001	−0.962	−5.187	−0.961	0.000	−0.713
0.02	2.0	−0.003	−0.962	−5.330	−0.962	0.000	−0.713
0.03	2.0	−0.007	−0.962	−5.416	−0.962	0.000	−0.713
0.05	2.0	−0.014	−0.962	−5.515	−0.962	0.000	−0.713
0.07	2.0	−0.023	−0.962	−5.583	−0.962	0.000	−0.713
0.10	2.0	−0.038	−0.962	−5.653	−0.962	0.000	−0.713
0.20	2.0	−0.095	−0.962	−5.776	−0.962	0.000	−0.713
0.30	2.0	−0.158	−0.962	−5.839	−0.962	0.000	−0.713
0.50	2.0	−0.299	−0.962	−5.907	−0.962	0.000	−0.713
0.70	2.0	−0.446	−0.962	−5.890	−0.962	0.000	−0.713
1.00	2.0	−0.506	−0.962	−4.994	−0.961	0.000	−0.713
2.00	2.0	−0.511	−0.962	−3.200	−0.960	0.003	−0.706
3.00	2.0	−0.511	−0.965	−2.412	−0.950	0.016	−0.670
5.00	2.0	−0.511	−0.986	−1.563	−0.884	0.137	−0.463
7.00	2.0	−0.511	−1.023	−1.053	−0.737	0.338	−0.140
10.00	2.0	−0.511	−1.073	−0.513	−0.407	0.541	0.369
0.01	3.0	0.003	−0.962	−4.286	−0.961	0.000	−0.713
0.02	3.0	0.002	−0.962	−4.370	−0.961	0.000	−0.713
0.03	3.0	0.000	−0.962	−4.448	−0.961	0.000	−0.713
0.05	3.0	−0.004	−0.962	−4.534	−0.961	0.000	−0.713
0.07	3.0	−0.009	−0.962	−4.596	−0.961	0.000	−0.713
0.10	3.0	−0.018	−0.962	−4.658	−0.961	0.000	−0.713
0.20	3.0	−0.055	−0.962	−4.777	−0.961	0.000	−0.713
0.30	3.0	−0.099	−0.962	−4.840	−0.961	0.000	−0.713
0.50	3.0	−0.200	−0.962	−4.907	−0.961	0.000	−0.713
0.70	3.0	−0.314	−0.962	−4.943	−0.961	0.000	−0.713
1.00	3.0	−0.465	−0.962	−4.788	−0.961	0.000	−0.713
2.00	3.0	−0.510	−0.962	−3.197	−0.960	0.003	−0.706
3.00	3.0	−0.511	−0.965	−2.412	−0.950	0.016	−0.670
5.00	3.0	−0.511	−0.986	−1.563	−0.884	0.137	−0.463
7.00	3.0	−0.511	−1.023	−1.053	−0.737	0.338	−0.140
10.00	3.0	−0.511	−1.073	−0.513	−0.407	0.541	0.369
0.01	4.0	0.012	−0.962	−3.613	−0.961	0.000	−0.711
0.02	4.0	0.012	−0.962	−3.611	−0.961	0.000	−0.711
0.03	4.0	0.011	−0.962	−3.628	−0.961	0.000	−0.711
0.05	4.0	0.010	−0.962	−3.649	−0.961	0.000	−0.711
0.07	4.0	0.009	−0.962	−3.670	−0.961	0.000	−0.711
0.10	4.0	0.005	−0.962	−3.708	−0.961	0.000	−0.711
0.20	4.0	−0.013	−0.962	−3.794	−0.961	0.000	−0.712
0.30	4.0	−0.037	−0.962	−3.848	−0.961	0.000	−0.712
0.50	4.0	−0.100	−0.962	−3.910	−0.961	0.000	−0.712
0.70	4.0	−0.174	−0.962	−3.945	−0.961	0.000	−0.712
1.00	4.0	−0.302	−0.962	−3.970	−0.961	0.000	−0.712
2.00	4.0	−0.497	−0.962	−3.166	−0.959	0.002	−0.705
3.00	4.0	−0.507	−0.965	−2.407	−0.950	0.016	−0.669
5.00	4.0	−0.510	−0.986	−1.562	−0.884	0.138	−0.463
7.00	4.0	−0.511	−1.023	−1.053	−0.737	0.339	−0.140
10.00	4.0	−0.511	−1.073	−0.513	−0.407	0.541	0.369
0.01	5.0	0.053	−0.962	−2.863	−0.956	0.000	−0.700
0.02	5.0	0.053	−0.962	−2.863	−0.956	0.000	−0.700
0.03	5.0	0.053	−0.962	−2.862	−0.956	0.000	−0.700
0.05	5.0	0.053	−0.962	−2.861	−0.956	0.000	−0.700
0.07	5.0	0.053	−0.962	−2.864	−0.956	0.000	−0.700
0.10	5.0	0.052	−0.962	−2.869	−0.956	0.000	−0.700
0.20	5.0	0.047	−0.962	−2.881	−0.956	0.000	−0.701
0.30	5.0	0.038	−0.962	−2.900	−0.957	0.000	−0.701
0.50	5.0	0.011	−0.962	−2.934	−0.957	0.000	−0.702
0.70	5.0	−0.026	−0.962	−2.957	−0.957	0.000	−0.703
1.00	5.0	−0.098	−0.962	−2.978	−0.957	0.000	−0.703
2.00	5.0	−0.383	−0.962	−2.884	−0.957	0.003	−0.699
3.00	5.0	−0.476	−0.965	−2.355	−0.948	0.017	−0.664
5.00	5.0	−0.502	−0.986	−1.554	−0.882	0.137	−0.459
7.00	5.0	−0.507	−1.023	−1.050	−0.735	0.338	−0.138
10.00	5.0	−0.509	−1.073	−0.512	−0.406	0.541	0.370
0.01	6.0	0.215	−0.962	−2.000	−0.923	0.000	−0.625
0.02	6.0	0.215	−0.962	−2.000	−0.923	0.000	−0.625
0.03	6.0	0.215	−0.962	−2.000	−0.923	0.000	−0.625
0.05	6.0	0.215	−0.962	−2.000	−0.923	0.000	−0.625
0.07	6.0	0.215	−0.962	−1.999	−0.923	0.000	−0.625
0.10	6.0	0.214	−0.962	−2.000	−0.924	0.000	−0.625
0.20	6.0	0.213	−0.962	−1.999	−0.923	0.000	−0.625
0.30	6.0	0.211	−0.962	−1.999	−0.923	0.000	−0.625
0.50	6.0	0.202	−0.962	−2.001	−0.924	0.000	−0.625
0.70	6.0	0.189	−0.962	−2.001	−0.924	0.000	−0.624
1.00	6.0	0.161	−0.962	−2.003	−0.924	0.000	−0.624
2.00	6.0	0.001	−0.962	−1.998	−0.924	0.003	−0.619
3.00	6.0	−0.212	−0.964	−1.937	−0.920	0.017	−0.598
5.00	6.0	−0.420	−0.984	−1.476	−0.863	0.138	−0.422
7.00	6.0	−0.469	−1.022	−1.024	−0.722	0.337	−0.118
10.00	6.0	−0.491	−1.073	−0.503	−0.400	0.541	0.378
0.01	6.5	0.402	−0.962	−1.518	−0.855	0.000	−0.482
0.02	6.5	0.402	−0.962	−1.518	−0.855	0.000	−0.482
0.03	6.5	0.402	−0.962	−1.518	−0.855	0.000	−0.482
0.05	6.5	0.402	−0.962	−1.517	−0.855	0.000	−0.482
0.07	6.5	0.402	−0.962	−1.518	−0.855	0.000	−0.482
0.10	6.5	0.402	−0.962	−1.518	−0.855	0.000	−0.482
0.20	6.5	0.401	−0.962	−1.518	−0.855	0.000	−0.482
0.30	6.5	0.399	−0.962	−1.517	−0.855	0.000	−0.481
0.50	6.5	0.394	−0.962	−1.516	−0.855	0.000	−0.480
0.70	6.5	0.386	−0.962	−1.515	−0.854	0.000	−0.479
1.00	6.5	0.368	−0.962	−1.512	−0.854	0.000	−0.477
2.00	6.5	0.266	−0.962	−1.499	−0.851	0.003	−0.465
3.00	6.5	0.101	−0.963	−1.478	−0.847	0.020	−0.444
5.00	6.5	−0.234	−0.981	−1.302	−0.812	0.138	−0.328
7.00	6.5	−0.377	−1.019	−0.962	−0.689	0.333	−0.070
10.00	6.5	−0.449	−1.071	−0.483	−0.383	0.539	0.397
0.01	7.0	0.711	−0.962	−1.004	−0.681	0.000	−0.180
0.02	7.0	0.711	−0.962	−1.004	−0.681	0.000	−0.180
0.03	7.0	0.711	−0.962	−1.003	−0.681	0.000	−0.180
0.05	7.0	0.711	−0.962	−1.003	−0.681	0.000	−0.180
0.07	7.0	0.711	−0.962	−1.003	−0.681	0.000	−0.180
0.10	7.0	0.711	−0.962	−1.003	−0.681	0.000	−0.180
0.20	7.0	0.711	−0.962	−1.003	−0.681	0.000	−0.179
0.30	7.0	0.710	−0.962	−1.002	−0.680	0.000	−0.179
0.50	7.0	0.706	−0.962	−1.002	−0.680	0.000	−0.178
0.70	7.0	0.701	−0.962	−1.001	−0.680	0.000	−0.177
1.00	7.0	0.689	−0.962	−0.998	−0.678	0.000	−0.173
2.00	7.0	0.622	−0.962	−0.984	−0.672	0.005	−0.155
3.00	7.0	0.510	−0.963	−0.968	−0.664	0.025	−0.132
5.00	7.0	0.187	−0.978	−0.924	−0.649	0.137	−0.068
7.00	7.0	−0.107	−1.013	−0.781	−0.581	0.323	0.079
10.00	7.0	−0.315	−1.066	−0.419	−0.331	0.534	0.458
0.01	7.5	1.197	−0.962	−0.456	−0.338	0.000	0.295
0.02	7.5	1.197	−0.962	−0.456	−0.338	0.000	0.295
0.03	7.5	1.197	−0.962	−0.456	−0.338	0.000	0.295
0.05	7.5	1.197	−0.962	−0.456	−0.338	0.000	0.295
0.07	7.5	1.197	−0.962	−0.456	−0.338	0.000	0.295
0.10	7.5	1.197	−0.962	−0.456	−0.338	0.000	0.295
0.20	7.5	1.197	−0.962	−0.456	−0.338	0.000	0.295
0.30	7.5	1.196	−0.962	−0.455	−0.337	0.000	0.296
0.50	7.5	1.194	−0.962	−0.455	−0.337	0.000	0.296
0.70	7.5	1.190	−0.962	−0.454	−0.336	0.000	0.298
1.00	7.5	1.182	−0.962	−0.452	−0.335	0.000	0.301
2.00	7.5	1.137	−0.962	−0.442	−0.327	0.006	0.316
3.00	7.5	1.062	−0.963	−0.431	−0.319	0.032	0.336
5.00	7.5	0.825	−0.976	−0.416	−0.311	0.140	0.377
7.00	7.5	0.507	−1.005	−0.391	−0.296	0.306	0.433
10.00	7.5	0.082	−1.054	−0.233	−0.172	0.523	0.637
0.01	8.0	1.936	−0.962	0.125	0.160	0.000	0.889
0.02	8.0	1.936	−0.962	0.125	0.159	0.000	0.889
0.03	8.0	1.936	−0.962	0.125	0.159	0.000	0.889
0.05	8.0	1.936	−0.962	0.125	0.159	0.000	0.889
0.07	8.0	1.936	−0.962	0.125	0.159	0.000	0.889
0.10	8.0	1.936	−0.962	0.125	0.160	0.000	0.889
0.20	8.0	1.935	−0.962	0.125	0.159	0.000	0.889
0.30	8.0	1.935	−0.962	0.125	0.160	0.000	0.889
0.50	8.0	1.933	−0.962	0.126	0.160	0.000	0.890
0.70	8.0	1.931	−0.962	0.126	0.161	0.000	0.891
1.00	8.0	1.925	−0.962	0.128	0.162	0.000	0.893
2.00	8.0	1.895	−0.962	0.134	0.168	0.007	0.903
3.00	8.0	1.844	−0.963	0.140	0.173	0.037	0.916
5.00	8.0	1.681	−0.976	0.141	0.173	0.145	0.936
7.00	8.0	1.441	−1.002	0.136	0.167	0.298	0.957
10.00	8.0	0.982	−1.041	0.169	0.195	0.509	1.038
0.01	8.5	3.037	−0.962	0.741	0.749	0.003	1.558
0.02	8.5	3.038	−0.962	0.741	0.749	0.003	1.558
0.03	8.5	3.038	−0.962	0.741	0.749	0.003	1.558
0.05	8.5	3.038	−0.962	0.741	0.749	0.003	1.558
0.07	8.5	3.038	−0.962	0.741	0.749	0.003	1.558
0.10	8.5	3.038	−0.962	0.741	0.749	0.003	1.558
0.20	8.5	3.038	−0.962	0.741	0.749	0.003	1.558
0.30	8.5	3.037	−0.962	0.741	0.749	0.003	1.558
0.50	8.5	3.036	−0.962	0.741	0.750	0.002	1.559
0.70	8.5	3.035	−0.962	0.741	0.750	0.003	1.560
1.00	8.5	3.031	−0.962	0.742	0.751	0.003	1.561
2.00	8.5	3.010	−0.962	0.746	0.754	0.012	1.567
3.00	8.5	2.978	−0.963	0.748	0.757	0.045	1.573
5.00	8.5	2.864	−0.976	0.739	0.748	0.157	1.575
7.00	8.5	2.698	−1.001	0.721	0.729	0.304	1.574
10.00	8.5	2.352	−1.035	0.716	0.723	0.506	1.605
0.01	9.0	4.671	−0.962	1.391	1.393	0.019	2.287
0.02	9.0	4.671	−0.962	1.391	1.393	0.019	2.287
0.03	9.0	4.671	−0.962	1.391	1.393	0.019	2.287
0.05	9.0	4.671	−0.962	1.391	1.393	0.019	2.287
0.07	9.0	4.671	−0.962	1.391	1.393	0.019	2.287
0.10	9.0	4.671	−0.962	1.391	1.393	0.019	2.287
0.20	9.0	4.671	−0.962	1.391	1.393	0.019	2.287
0.30	9.0	4.671	−0.962	1.392	1.394	0.019	2.287
0.50	9.0	4.671	−0.962	1.392	1.394	0.019	2.288
0.70	9.0	4.665	−0.962	1.391	1.393	0.019	2.287
1.00	9.0	4.665	−0.962	1.392	1.394	0.019	2.289
2.00	9.0	4.650	−0.962	1.394	1.396	0.029	2.292
3.00	9.0	4.625	−0.963	1.394	1.396	0.064	2.293
5.00	9.0	4.551	−0.976	1.380	1.382	0.179	2.284
7.00	9.0	4.438	−1.001	1.353	1.355	0.321	2.265
10.00	9.0	4.197	−1.033	1.327	1.329	0.513	2.263

validity of Hansen's fit to his calculated rates) to a factor of 6 faster at $\rho/\mu_e = 10^9$ g cm^{-3}. At higher temperatures our electron capture rates are faster by factors of 5–100, as a result of the many relatively fast electron capture channels which open up at higher temperatures and densities. (Note that in these cases the uncertainty in our rate is roughly a factor of 3.) Any detailed calculation of the production and destruction of ^{26}Al in stellar environments should take into account these results.

The remaining decays $^{30}\text{P}\rightarrow{}^{30}\text{Si}$, $^{31}\text{S}\rightarrow{}^{31}\text{P}$, $^{32}\text{S}\rightarrow{}^{32}\text{P}$, $^{33}\text{S}\rightarrow{}^{33}\text{P}$, and $^{35}\text{Cl}\rightarrow{}^{35}\text{S}$ are most important in influencing neutronization of the core material prior to and during the initial phase of silicon burning in massive stars preceding the collapse which initiates the supernova event. In particular, Weaver, Woosley, and Zimmerman (1978) find that the ratio of ^{28}Si to ^{30}Si abundance at silicon ignition is determined partly by neutronization via these five decays, which were chosen as being most important on the basis of the product of rate and abundance. In turn, the composition of core and mantle material resulting from silicon burning depends on this ratio with interesting consequences for subsequent nucleosynthesis.

We find that our overall weak destruction rates agree well with the Hansen parametrized fits (1966, p. A-41) in most cases at low temperature and intermediate densities, but do differ significantly in some cases at temperatures and densities relevant to the neutronization-nucleosynthesis problem, motivating our detailed tabulation of these rates.

The decay $^{30}\text{P}\rightarrow{}^{30}\text{Si}$ (Table 6) is similar to that of $^{26}\text{Al}\rightarrow{}^{26}\text{Mg}$. There is a comparable $Q_n = 3.72$ MeV of available phase space in the ground state to ground state transition, and there is an isomeric state at 680 keV in ^{30}P. In contrast, the ground state to ground state transition $1\rightarrow1$ is relatively fast in this case ($\log ft = 4.83$). The fast Fermi transition ($2\rightarrow1$, $\log ft = 3.49$) from the isomeric state dominates the rates for temperatures higher than $T_9 \approx 1$. At still higher temperatures the fast decay ($10\rightarrow1$, $\log ft = 3.99$ from the mirror decay) becomes important. The positron emission rate agrees with the Hansen fit to within a factor of 2. The electron capture rate, on the other hand, is influenced partly by the relatively fast Gamow-Teller transitions at low excitation energy ($1\rightarrow2$, $1\rightarrow3$, $3\rightarrow2$, $3\rightarrow5$, and $3\rightarrow6$ of Table 2) and accessible at intermediate temperatures and densities, resulting in a rate 6 times faster than Hansen at $T_9 = 2$, $\rho/\mu_e = 10^8$. There is no dramatic density dependence due to upward transitions at low temperature in this case (Fig. 3); they do not compete well with the fast energetically favored transitions. At higher temperatures even faster Gamow-Teller channels open up at high density to give rates a factor of 4 to 40 times faster than Hansen's. The concurrent uncertainty in our rates is a factor of 3 at $T_9 = 10$, $\rho/\mu_e = 10^9$, showing that at even these extreme conditions, transitions with experimental, mirror, and calculated Gamow-Teller $\log ft$ values make the major contribution to the rate.

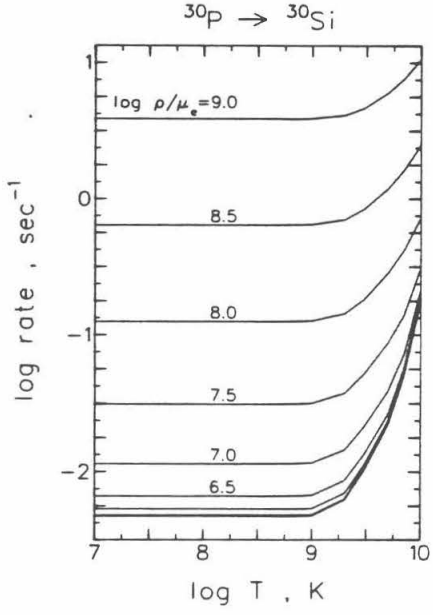

FIG. 3.—Total decay rate for $^{30}\text{P}\rightarrow{}^{30}\text{S}_i$; log Σ from Table 6. The ground state decay is fairly rapid, and the enhancement due to continuum electron capture at high densities shows only the smooth increase of U_F with log ρ/μ_e (cf., Fig. 1).

TABLE 6

DECAY RATES FOR $^{30}P \rightarrow {}^{30}Si$

T_9	log ρ/μ_e	U_f	log β^+	log ε^-	log Σ	log Δ	log ν
0.01	1.0	-0.003	-2.323	-7.370	-2.323	0.000	-2.074
0.02	1.0	-0.007	-2.323	-7.525	-2.323	0.000	-2.074
0.03	1.0	-0.013	-2.323	-7.611	-2.323	0.000	-2.074
0.05	1.0	-0.024	-2.323	-7.719	-2.323	0.000	-2.074
0.07	1.0	-0.037	-2.323	-7.791	-2.323	0.000	-2.074
0.10	1.0	-0.058	-2.323	-7.861	-2.323	0.000	-2.074
0.20	1.0	-0.134	-2.323	-7.989	-2.323	0.000	-2.074
0.30	1.0	-0.218	-2.323	-8.055	-2.323	0.000	-2.074
0.50	1.0	-0.398	-2.323	-8.122	-2.323	0.000	-2.074
0.70	1.0	-0.503	-2.323	-7.521	-2.323	0.000	-2.074
1.00	1.0	-0.511	-2.320	-6.228	-2.320	0.000	-2.071
2.00	1.0	-0.511	-2.205	-4.335	-2.202	0.002	-1.929
3.00	1.0	-0.511	-2.007	-3.407	-1.990	0.010	-1.677
5.00	1.0	-0.511	-1.757	-2.321	-1.653	0.094	-1.221
7.00	1.0	-0.511	-1.583	-1.621	-1.300	0.269	-0.715
10.00	1.0	-0.511	-1.369	-0.859	-0.742	0.456	0.011
0.01	2.0	-0.001	-2.323	-6.391	-2.323	0.000	-2.074
0.02	2.0	-0.003	-2.323	-6.534	-2.323	0.000	-2.074
0.03	2.0	-0.007	-2.323	-6.621	-2.323	0.000	-2.074
0.05	2.0	-0.014	-2.323	-6.721	-2.323	0.000	-2.074
0.07	2.0	-0.023	-2.323	-6.790	-2.323	0.000	-2.074
0.10	2.0	-0.038	-2.323	-6.862	-2.323	0.000	-2.074
0.20	2.0	-0.095	-2.323	-6.989	-2.323	0.000	-2.074
0.30	2.0	-0.158	-2.323	-7.054	-2.323	0.000	-2.074
0.50	2.0	-0.299	-2.323	-7.125	-2.323	0.000	-2.074
0.70	2.0	-0.446	-2.323	-7.108	-2.323	0.000	-2.074
1.00	2.0	-0.506	-2.320	-6.207	-2.320	0.000	-2.071
2.00	2.0	-0.511	-2.205	-4.335	-2.202	0.002	-1.929
3.00	2.0	-0.511	-2.007	-3.407	-1.990	0.010	-1.677
5.00	2.0	-0.511	-1.757	-2.321	-1.653	0.094	-1.221
7.00	2.0	-0.511	-1.583	-1.621	-1.300	0.269	-0.715
10.00	2.0	-0.511	-1.369	-0.859	-0.742	0.456	0.011
0.01	3.0	0.003	-2.323	-5.490	-2.323	0.000	-2.074
0.02	3.0	0.002	-2.323	-5.575	-2.323	0.000	-2.074
0.03	3.0	0.000	-2.323	-5.653	-2.323	0.000	-2.074
0.05	3.0	-0.004	-2.323	-5.741	-2.323	0.000	-2.074
0.07	3.0	-0.009	-2.323	-5.803	-2.323	0.000	-2.074
0.10	3.0	-0.018	-2.323	-5.867	-2.323	0.000	-2.074
0.20	3.0	-0.055	-2.323	-5.991	-2.323	0.000	-2.074
0.30	3.0	-0.099	-2.323	-6.056	-2.323	0.000	-2.074
0.50	3.0	-0.200	-2.323	-6.125	-2.323	0.000	-2.074
0.70	3.0	-0.314	-2.323	-6.160	-2.323	0.000	-2.074
1.00	3.0	-0.465	-2.320	-6.001	-2.320	0.000	-2.071
2.00	3.0	-0.510	-2.205	-4.331	-2.202	0.002	-1.929
3.00	3.0	-0.511	-2.007	-3.406	-1.990	0.010	-1.677
5.00	3.0	-0.511	-1.757	-2.321	-1.652	0.093	-1.221
7.00	3.0	-0.511	-1.583	-1.621	-1.300	0.269	-0.715
10.00	3.0	-0.511	-1.369	-0.859	-0.742	0.456	0.011
0.01	4.0	0.012	-2.323	-4.820	-2.322	0.000	-2.071
0.02	4.0	0.012	-2.323	-4.819	-2.322	0.000	-2.071
0.03	4.0	0.011	-2.323	-4.836	-2.322	0.000	-2.071
0.05	4.0	0.010	-2.323	-4.858	-2.322	0.000	-2.072
0.07	4.0	0.009	-2.323	-4.879	-2.322	0.000	-2.072
0.10	4.0	0.005	-2.323	-4.919	-2.322	0.000	-2.072
0.20	4.0	-0.013	-2.323	-5.008	-2.322	0.000	-2.072
0.30	4.0	-0.037	-2.323	-5.064	-2.322	0.000	-2.073
0.50	4.0	-0.100	-2.323	-5.128	-2.322	0.001	-2.073
0.70	4.0	-0.174	-2.323	-5.162	-2.322	0.001	-2.073
1.00	4.0	-0.302	-2.320	-5.183	-2.320	0.000	-2.070
2.00	4.0	-0.497	-2.205	-4.300	-2.202	0.002	-1.928
3.00	4.0	-0.507	-2.007	-3.401	-1.989	0.010	-1.677
5.00	4.0	-0.510	-1.757	-2.320	-1.652	0.094	-1.221
7.00	4.0	-0.511	-1.583	-1.621	-1.300	0.269	-0.715
10.00	4.0	-0.511	-1.369	-0.859	-0.742	0.456	0.011
0.01	5.0	0.053	-2.323	-4.081	-2.316	0.002	-2.059
0.02	5.0	0.053	-2.323	-4.080	-2.316	0.002	-2.059
0.03	5.0	0.053	-2.323	-4.080	-2.316	0.002	-2.059
0.05	5.0	0.053	-2.323	-4.078	-2.316	0.002	-2.059
0.07	5.0	0.053	-2.323	-4.081	-2.316	0.002	-2.059
0.10	5.0	0.052	-2.323	-4.087	-2.316	0.002	-2.059
0.20	5.0	0.047	-2.323	-4.099	-2.316	0.002	-2.059
0.30	5.0	0.038	-2.323	-4.119	-2.316	0.001	-2.060
0.50	5.0	0.011	-2.323	-4.152	-2.317	0.002	-2.061
0.70	5.0	-0.026	-2.323	-4.174	-2.317	0.001	-2.061
1.00	5.0	-0.098	-2.320	-4.191	-2.315	0.002	-2.059
2.00	5.0	-0.383	-2.205	-4.018	-2.198	0.003	-1.921
3.00	5.0	-0.476	-2.006	-3.349	-1.987	0.011	-1.672
5.00	5.0	-0.502	-1.757	-2.312	-1.650	0.094	-1.218
7.00	5.0	-0.507	-1.583	-1.618	-1.299	0.270	-0.713
10.00	5.0	-0.509	-1.369	-0.858	-0.741	0.456	0.012
0.01	6.0	0.215	-2.323	-3.218	-2.271	0.012	-1.971
0.02	6.0	0.215	-2.323	-3.218	-2.271	0.012	-1.971
0.03	6.0	0.215	-2.323	-3.218	-2.271	0.012	-1.971
0.05	6.0	0.215	-2.323	-3.218	-2.271	0.012	-1.971
0.07	6.0	0.215	-2.323	-3.218	-2.271	0.012	-1.971
0.10	6.0	0.214	-2.323	-3.218	-2.271	0.012	-1.971
0.20	6.0	0.213	-2.323	-3.217	-2.271	0.013	-1.971
0.30	6.0	0.211	-2.323	-3.216	-2.271	0.013	-1.971
0.50	6.0	0.202	-2.323	-3.216	-2.271	0.013	-1.971
0.70	6.0	0.189	-2.323	-3.215	-2.271	0.014	-1.970
1.00	6.0	0.161	-2.320	-3.211	-2.268	0.014	-1.967
2.00	6.0	0.001	-2.205	-3.129	-2.156	0.016	-1.838
3.00	6.0	-0.212	-2.005	-2.930	-1.956	0.020	-1.611
5.00	6.0	-0.420	-1.756	-2.233	-1.631	0.099	-1.184
7.00	6.0	-0.469	-1.582	-1.592	-1.286	0.270	-0.694
10.00	6.0	-0.491	-1.369	-0.849	-0.735	0.456	0.019
0.01	6.5	0.402	-2.323	-2.722	-2.177	0.037	-1.810
0.02	6.5	0.402	-2.323	-2.722	-2.177	0.037	-1.810
0.03	6.5	0.402	-2.323	-2.722	-2.177	0.037	-1.810
0.05	6.5	0.402	-2.323	-2.722	-2.177	0.037	-1.810
0.07	6.5	0.402	-2.323	-2.723	-2.178	0.037	-1.810
0.10	6.5	0.402	-2.323	-2.722	-2.177	0.036	-1.810
0.20	6.5	0.401	-2.323	-2.722	-2.177	0.037	-1.810
0.30	6.5	0.399	-2.323	-2.721	-2.177	0.037	-1.809
0.50	6.5	0.394	-2.323	-2.718	-2.176	0.038	-1.808
0.70	6.5	0.386	-2.323	-2.715	-2.175	0.038	-1.806
1.00	6.5	0.368	-2.320	-2.707	-2.171	0.040	-1.801
2.00	6.5	0.266	-2.205	-2.620	-2.064	0.043	-1.677
3.00	6.5	0.101	-2.005	-2.466	-1.876	0.044	-1.466
5.00	6.5	-0.234	-1.754	-2.058	-1.578	0.109	-1.096
7.00	6.5	-0.377	-1.580	-1.530	-1.253	0.271	-0.649
10.00	6.5	-0.449	-1.367	-0.829	-0.719	0.456	0.038
0.01	7.0	0.711	-2.323	-2.177	-1.943	0.091	-1.477
0.02	7.0	0.711	-2.323	-2.177	-1.943	0.091	-1.477
0.03	7.0	0.711	-2.323	-2.177	-1.943	0.091	-1.477
0.05	7.0	0.711	-2.323	-2.177	-1.943	0.091	-1.477
0.07	7.0	0.711	-2.323	-2.177	-1.943	0.091	-1.477
0.10	7.0	0.711	-2.323	-2.177	-1.943	0.091	-1.477
0.20	7.0	0.711	-2.323	-2.176	-1.943	0.091	-1.476
0.30	7.0	0.710	-2.323	-2.176	-1.942	0.091	-1.476
0.50	7.0	0.706	-2.323	-2.174	-1.941	0.092	-1.474
0.70	7.0	0.701	-2.323	-2.171	-1.940	0.093	-1.472
1.00	7.0	0.689	-2.320	-2.164	-1.934	0.094	-1.465
2.00	7.0	0.622	-2.205	-2.085	-1.840	0.095	-1.354
3.00	7.0	0.510	-2.005	-1.944	-1.672	0.090	-1.181
5.00	7.0	0.187	-1.751	-1.676	-1.411	0.139	-0.847
7.00	7.0	-0.107	-1.575	-1.347	-1.145	0.275	-0.506
10.00	7.0	-0.315	-1.363	-0.765	-0.667	0.454	0.097
0.01	7.5	1.197	-2.323	-1.578	-1.506	0.160	-0.960
0.02	7.5	1.197	-2.323	-1.578	-1.506	0.160	-0.960
0.03	7.5	1.197	-2.323	-1.578	-1.506	0.160	-0.960
0.05	7.5	1.197	-2.323	-1.578	-1.506	0.160	-0.960
0.07	7.5	1.197	-2.323	-1.578	-1.506	0.160	-0.960
0.10	7.5	1.197	-2.323	-1.578	-1.506	0.160	-0.960
0.20	7.5	1.197	-2.323	-1.577	-1.506	0.161	-0.960
0.30	7.5	1.196	-2.323	-1.577	-1.505	0.160	-0.959
0.50	7.5	1.194	-2.323	-1.576	-1.504	0.161	-0.958
0.70	7.5	1.190	-2.323	-1.574	-1.502	0.161	-0.956
1.00	7.5	1.182	-2.320	-1.568	-1.498	0.163	-0.950
2.00	7.5	1.137	-2.205	-1.503	-1.424	0.157	-0.856
3.00	7.5	1.062	-2.005	-1.381	-1.288	0.148	-0.688
5.00	7.5	0.825	-1.749	-1.156	-1.058	0.179	-0.408
7.00	7.5	0.507	-1.569	-0.952	-0.858	0.285	-0.160
10.00	7.5	0.082	-1.354	-0.577	-0.510	0.452	0.274
0.01	8.0	1.936	-2.323	-0.919	-0.902	0.220	-0.306
0.02	8.0	1.936	-2.323	-0.919	-0.902	0.220	-0.306
0.03	8.0	1.936	-2.323	-0.919	-0.902	0.220	-0.306
0.05	8.0	1.936	-2.323	-0.919	-0.902	0.220	-0.306
0.07	8.0	1.936	-2.323	-0.919	-0.902	0.220	-0.306
0.10	8.0	1.936	-2.323	-0.919	-0.902	0.220	-0.306
0.20	8.0	1.935	-2.323	-0.919	-0.902	0.220	-0.306
0.30	8.0	1.935	-2.323	-0.919	-0.902	0.220	-0.306
0.50	8.0	1.933	-2.323	-0.918	-0.901	0.220	-0.305
0.70	8.0	1.931	-2.323	-0.917	-0.900	0.221	-0.303
1.00	8.0	1.925	-2.320	-0.913	-0.896	0.221	-0.298
2.00	8.0	1.895	-2.205	-0.863	-0.843	0.213	-0.224
3.00	8.0	1.844	-2.005	-0.763	-0.739	0.199	-0.083
5.00	8.0	1.681	-1.749	-0.574	-0.546	0.216	0.161
7.00	8.0	1.441	-1.566	-0.411	-0.381	0.301	0.367
10.00	8.0	0.982	-1.343	-0.170	-0.142	0.453	0.673
0.01	8.5	3.037	-2.323	-0.198	-0.195	0.268	0.453
0.02	8.5	3.038	-2.323	-0.198	-0.195	0.269	0.453
0.03	8.5	3.038	-2.323	-0.198	-0.195	0.268	0.453
0.05	8.5	3.038	-2.323	-0.198	-0.195	0.268	0.453
0.07	8.5	3.038	-2.323	-0.198	-0.195	0.268	0.453
0.10	8.5	3.038	-2.323	-0.198	-0.195	0.268	0.453
0.20	8.5	3.038	-2.323	-0.198	-0.195	0.269	0.453
0.30	8.5	3.037	-2.323	-0.198	-0.195	0.269	0.453
0.50	8.5	3.036	-2.323	-0.197	-0.194	0.269	0.454
0.70	8.5	3.035	-2.323	-0.196	-0.193	0.269	0.455
1.00	8.5	3.031	-2.320	-0.194	-0.191	0.269	0.459
2.00	8.5	3.010	-2.205	-0.158	-0.154	0.261	0.515
3.00	8.5	2.976	-2.005	-0.082	-0.077	0.246	0.626
5.00	8.5	2.864	-1.749	0.070	0.076	0.256	0.828
7.00	8.5	2.698	-1.565	0.202	0.210	0.327	0.999
10.00	8.5	2.352	-1.338	0.389	0.397	0.462	1.245
0.01	9.0	4.671	-2.323	0.587	0.588	0.316	1.308
0.02	9.0	4.671	-2.323	0.587	0.588	0.316	1.308
0.03	9.0	4.671	-2.323	0.587	0.588	0.316	1.308
0.05	9.0	4.671	-2.323	0.587	0.588	0.316	1.308
0.07	9.0	4.671	-2.323	0.587	0.588	0.316	1.308
0.10	9.0	4.671	-2.323	0.587	0.588	0.316	1.308
0.20	9.0	4.671	-2.323	0.587	0.588	0.316	1.308
0.30	9.0	4.671	-2.323	0.587	0.588	0.317	1.308
0.50	9.0	4.671	-2.323	0.588	0.589	0.316	1.309
0.70	9.0	4.665	-2.323	0.587	0.587	0.317	1.308
1.00	9.0	4.665	-2.320	0.589	0.590	0.317	1.311
2.00	9.0	4.650	-2.205	0.613	0.614	0.311	1.349
3.00	9.0	4.625	-2.005	0.665	0.666	0.299	1.430
5.00	9.0	4.551	-1.749	0.779	0.780	0.307	1.588
7.00	9.0	4.438	-1.565	0.880	0.882	0.366	1.724
10.00	9.0	4.197	-1.337	1.024	1.026	0.481	1.919

TABLE 7

· DECAY RATES FOR $^{31}S \rightarrow {}^{31}P$

T_9	log ρ/μ_e	U_r	log β^+	log ε^-	log Σ	log Δ	log ν
0.01	1.0	-0.003	-0.559	-6.007	-0.559	0.000	-0.182
0.02	1.0	-0.007	-0.559	-6.162	-0.559	0.000	-0.182
0.03	1.0	-0.013	-0.559	-6.249	-0.559	0.000	-0.182
0.05	1.0	-0.024	-0.559	-6.357	-0.559	0.000	-0.182
0.07	1.0	-0.037	-0.559	-6.430	-0.559	0.000	-0.182
0.10	1.0	-0.058	-0.559	-6.502	-0.559	0.000	-0.182
0.20	1.0	-0.134	-0.559	-6.634	-0.559	0.000	-0.182
0.30	1.0	-0.218	-0.559	-6.704	-0.559	0.000	-0.182
0.50	1.0	-0.398	-0.559	-6.778	-0.559	0.000	-0.182
0.70	1.0	-0.503	-0.559	-6.183	-0.559	0.000	-0.182
1.00	1.0	-0.511	-0.559	-4.902	-0.559	0.000	-0.182
2.00	1.0	-0.511	-0.560	-3.099	-0.558	0.001	-0.179
3.00	1.0	-0.511	-0.561	-2.310	-0.553	0.007	-0.166
5.00	1.0	-0.511	-0.567	-1.432	-0.511	0.066	-0.061
7.00	1.0	-0.511	-0.563	-0.872	-0.390	0.214	0.192
10.00	1.0	-0.511	-0.524	-0.268	-0.076	0.430	0.695
0.01	2.0	-0.001	-0.559	-5.028	-0.559	0.000	-0.182
0.02	2.0	-0.003	-0.559	-5.172	-0.559	0.000	-0.182
0.03	2.0	-0.007	-0.559	-5.259	-0.559	0.000	-0.182
0.05	2.0	-0.014	-0.559	-5.360	-0.559	0.000	-0.182
0.07	2.0	-0.023	-0.559	-5.430	-0.559	0.000	-0.182
0.10	2.0	-0.038	-0.559	-5.502	-0.559	0.000	-0.182
0.20	2.0	-0.095	-0.559	-5.634	-0.559	0.000	-0.182
0.30	2.0	-0.158	-0.559	-5.703	-0.559	0.000	-0.182
0.50	2.0	-0.299	-0.559	-5.780	-0.559	0.000	-0.182
0.70	2.0	-0.446	-0.559	-5.770	-0.559	0.000	-0.182
1.00	2.0	-0.506	-0.559	-4.881	-0.559	0.000	-0.182
2.00	2.0	-0.511	-0.560	-3.099	-0.558	0.001	-0.179
3.00	2.0	-0.511	-0.561	-2.310	-0.553	0.007	-0.166
5.00	2.0	-0.511	-0.567	-1.432	-0.511	0.066	-0.061
7.00	2.0	-0.511	-0.563	-0.872	-0.390	0.214	0.192
10.00	2.0	-0.511	-0.524	-0.268	-0.076	0.430	0.695
0.01	3.0	0.003	-0.559	-4.127	-0.559	0.000	-0.181
0.02	3.0	0.002	-0.559	-4.212	-0.559	0.000	-0.181
0.03	3.0	0.000	-0.559	-4.291	-0.559	0.000	-0.181
0.05	3.0	-0.004	-0.559	-4.379	-0.559	0.000	-0.181
0.07	3.0	-0.009	-0.559	-4.442	-0.559	0.000	-0.182
0.10	3.0	-0.018	-0.559	-4.508	-0.559	0.000	-0.182
0.20	3.0	-0.055	-0.559	-4.635	-0.559	0.000	-0.182
0.30	3.0	-0.099	-0.559	-4.704	-0.559	0.000	-0.182
0.50	3.0	-0.200	-0.559	-4.781	-0.559	0.000	-0.182
0.70	3.0	-0.314	-0.559	-4.823	-0.559	0.000	-0.182
1.00	3.0	-0.485	-0.559	-4.675	-0.559	0.000	-0.182
2.00	3.0	-0.510	-0.560	-3.095	-0.558	0.001	-0.179
3.00	3.0	-0.511	-0.561	-2.310	-0.553	0.007	-0.166
5.00	3.0	-0.511	-0.567	-1.432	-0.511	0.066	-0.061
7.00	3.0	-0.511	-0.563	-0.872	-0.390	0.214	0.192
10.00	3.0	-0.511	-0.524	-0.268	-0.076	0.430	0.695
0.01	4.0	0.012	-0.559	-3.459	-0.559	0.001	-0.180
0.02	4.0	0.012	-0.559	-3.458	-0.559	0.001	-0.180
0.03	4.0	0.011	-0.559	-3.475	-0.559	0.001	-0.180
0.05	4.0	0.010	-0.559	-3.498	-0.559	0.001	-0.181
0.07	4.0	0.009	-0.559	-3.520	-0.559	0.001	-0.181
0.10	4.0	0.005	-0.559	-3.561	-0.559	0.000	-0.181
0.20	4.0	-0.013	-0.559	-3.654	-0.559	0.000	-0.181
0.30	4.0	-0.037	-0.559	-3.713	-0.559	0.000	-0.181
0.50	4.0	-0.100	-0.559	-3.784	-0.559	0.000	-0.181
0.70	4.0	-0.174	-0.559	-3.825	-0.559	0.000	-0.181
1.00	4.0	-0.302	-0.559	-3.857	-0.559	0.000	-0.181
2.00	4.0	-0.497	-0.560	-3.084	-0.558	0.001	-0.179
3.00	4.0	-0.507	-0.561	-2.305	-0.553	0.007	-0.166
5.00	4.0	-0.510	-0.567	-1.431	-0.511	0.067	-0.060
7.00	4.0	-0.511	-0.563	-0.872	-0.390	0.215	0.192
10.00	4.0	-0.511	-0.524	-0.268	-0.076	0.430	0.695
0.01	5.0	0.053	-0.559	-2.729	-0.556	0.001	-0.175
0.02	5.0	0.053	-0.559	-2.729	-0.556	0.001	-0.175
0.03	5.0	0.053	-0.559	-2.728	-0.556	0.001	-0.175
0.05	5.0	0.053	-0.559	-2.727	-0.556	0.001	-0.175
0.07	5.0	0.053	-0.559	-2.730	-0.556	0.001	-0.175
0.10	5.0	0.052	-0.559	-2.736	-0.556	0.001	-0.175
0.20	5.0	0.047	-0.559	-2.750	-0.556	0.001	-0.176
0.30	5.0	0.038	-0.559	-2.772	-0.557	0.001	-0.176
0.50	5.0	0.011	-0.559	-2.811	-0.557	0.001	-0.176
0.70	5.0	-0.026	-0.559	-2.839	-0.557	0.001	-0.177
1.00	5.0	-0.098	-0.559	-2.867	-0.557	0.000	-0.177
2.00	5.0	-0.383	-0.559	-2.782	-0.557	0.001	-0.178
3.00	5.0	-0.476	-0.561	-2.253	-0.552	0.007	-0.163
5.00	5.0	-0.502	-0.567	-1.423	-0.510	0.067	-0.058
7.00	5.0	-0.507	-0.563	-0.869	-0.389	0.215	0.194
10.00	5.0	-0.509	-0.524	-0.267	-0.076	0.431	0.696
0.01	6.0	0.215	-0.559	-1.891	-0.540	0.003	-0.139
0.02	6.0	0.215	-0.559	-1.891	-0.540	0.003	-0.139
0.03	6.0	0.215	-0.559	-1.891	-0.539	0.002	-0.139
0.05	6.0	0.215	-0.559	-1.891	-0.539	0.002	-0.139
0.07	6.0	0.215	-0.559	-1.890	-0.539	0.002	-0.139
0.10	6.0	0.214	-0.559	-1.891	-0.540	0.003	-0.139
0.20	6.0	0.213	-0.559	-1.890	-0.539	0.002	-0.139
0.30	6.0	0.211	-0.559	-1.890	-0.539	0.002	-0.139
0.50	6.0	0.202	-0.559	-1.893	-0.540	0.003	-0.139
0.70	6.0	0.189	-0.559	-1.895	-0.540	0.002	-0.139
1.00	6.0	0.161	-0.559	-1.899	-0.540	0.002	-0.139
2.00	6.0	0.001	-0.559	-1.899	-0.540	0.003	-0.139
3.00	6.0	-0.212	-0.560	-1.836	-0.538	0.009	-0.131
5.00	6.0	-0.420	-0.566	-1.345	-0.499	0.069	-0.035
7.00	6.0	-0.469	-0.562	-0.843	-0.379	0.215	0.210
10.00	6.0	-0.491	-0.523	-0.258	-0.070	0.431	0.703
0.01	6.5	0.402	-0.559	-1.418	-0.503	0.006	-0.064
0.02	6.5	0.402	-0.559	-1.418	-0.503	0.006	-0.064
0.03	6.5	0.402	-0.559	-1.418	-0.503	0.006	-0.064
0.05	6.5	0.402	-0.559	-1.418	-0.503	0.006	-0.064
0.07	6.5	0.402	-0.559	-1.419	-0.503	0.006	-0.064
0.10	6.5	0.402	-0.559	-1.419	-0.503	0.006	-0.064
0.20	6.5	0.401	-0.559	-1.419	-0.503	0.006	-0.064
0.30	6.5	0.399	-0.559	-1.418	-0.503	0.006	-0.064
0.50	6.5	0.394	-0.559	-1.417	-0.503	0.006	-0.064
0.70	6.5	0.386	-0.559	-1.416	-0.503	0.006	-0.063
1.00	6.5	0.368	-0.559	-1.415	-0.503	0.007	-0.062
2.00	6.5	0.266	-0.559	-1.402	-0.501	0.008	-0.057
3.00	6.5	0.101	-0.560	-1.378	-0.498	0.015	-0.048
5.00	6.5	-0.234	-0.564	-1.171	-0.468	0.076	0.026
7.00	6.5	-0.377	-0.560	-0.781	-0.356	0.220	0.248
10.00	6.5	-0.449	-0.522	-0.238	-0.056	0.431	0.721
0.01	7.0	0.711	-0.559	-0.912	-0.400	0.017	0.126
0.02	7.0	0.711	-0.559	-0.912	-0.400	0.017	0.126
0.03	7.0	0.711	-0.559	-0.912	-0.400	0.017	0.126
0.05	7.0	0.711	-0.559	-0.912	-0.400	0.017	0.126
0.07	7.0	0.711	-0.559	-0.911	-0.400	0.017	0.126
0.10	7.0	0.711	-0.559	-0.911	-0.400	0.017	0.126
0.20	7.0	0.711	-0.559	-0.911	-0.399	0.016	0.126
0.30	7.0	0.710	-0.559	-0.910	-0.399	0.017	0.126
0.50	7.0	0.706	-0.559	-0.910	-0.399	0.017	0.127
0.70	7.0	0.701	-0.559	-0.909	-0.399	0.017	0.128
1.00	7.0	0.689	-0.559	-0.906	-0.398	0.018	0.130
2.00	7.0	0.622	-0.559	-0.891	-0.393	0.020	0.141
3.00	7.0	0.510	-0.560	-0.870	-0.387	0.031	0.157
5.00	7.0	0.187	-0.562	-0.794	-0.362	0.097	0.216
7.00	7.0	-0.107	-0.556	-0.601	-0.277	0.231	0.372
10.00	7.0	-0.315	-0.518	-0.175	-0.012	0.433	0.777
0.01	7.5	1.197	-0.559	-0.368	-0.152	0.043	0.497
0.02	7.5	1.197	-0.559	-0.368	-0.152	0.043	0.497
0.03	7.5	1.197	-0.559	-0.368	-0.152	0.043	0.497
0.05	7.5	1.197	-0.559	-0.368	-0.152	0.043	0.497
0.07	7.5	1.197	-0.559	-0.368	-0.152	0.043	0.497
0.10	7.5	1.197	-0.559	-0.368	-0.152	0.043	0.497
0.20	7.5	1.197	-0.559	-0.368	-0.152	0.043	0.497
0.30	7.5	1.198	-0.559	-0.367	-0.152	0.043	0.498
0.50	7.5	1.194	-0.559	-0.367	-0.151	0.043	0.498
0.70	7.5	1.190	-0.559	-0.366	-0.151	0.044	0.499
1.00	7.5	1.182	-0.559	-0.364	-0.150	0.044	0.502
2.00	7.5	1.137	-0.559	-0.352	-0.143	0.048	0.514
3.00	7.5	1.062	-0.560	-0.335	-0.132	0.061	0.534
5.00	7.5	0.825	-0.561	-0.288	-0.102	0.133	0.592
7.00	7.5	0.507	-0.551	-0.211	-0.048	0.257	0.687
10.00	7.5	0.082	-0.510	0.011	0.125	0.438	0.945
0.01	8.0	1.936	-0.559	0.213	0.281	0.084	1.033
0.02	8.0	1.936	-0.559	0.213	0.281	0.084	1.033
0.03	8.0	1.936	-0.559	0.213	0.281	0.084	1.033
0.05	8.0	1.936	-0.559	0.213	0.281	0.084	1.033
0.07	8.0	1.936	-0.559	0.213	0.281	0.084	1.033
0.10	8.0	1.936	-0.559	0.213	0.281	0.084	1.033
0.20	8.0	1.935	-0.559	0.213	0.281	0.084	1.033
0.30	8.0	1.935	-0.559	0.213	0.281	0.084	1.033
0.50	8.0	1.933	-0.559	0.214	0.282	0.083	1.034
0.70	8.0	1.931	-0.559	0.214	0.282	0.084	1.035
1.00	8.0	1.925	-0.559	0.216	0.283	0.085	1.037
2.00	8.0	1.895	-0.559	0.224	0.290	0.089	1.047
3.00	8.0	1.844	-0.560	0.236	0.300	0.102	1.064
5.00	8.0	1.681	-0.561	0.269	0.329	0.173	1.112
7.00	8.0	1.441	-0.549	0.313	0.369	0.287	1.182
10.00	8.0	0.982	-0.500	0.411	0.461	0.447	1.329
0.01	8.5	3.037	-0.559	0.835	0.852	0.133	1.677
0.02	8.5	3.038	-0.559	0.835	0.852	0.133	1.677
0.03	8.5	3.038	-0.559	0.835	0.852	0.133	1.677
0.05	8.5	3.038	-0.559	0.835	0.852	0.133	1.677
0.07	8.5	3.038	-0.559	0.835	0.852	0.133	1.677
0.10	8.5	3.038	-0.559	0.835	0.852	0.133	1.677
0.20	8.5	3.038	-0.559	0.835	0.852	0.133	1.677
0.30	8.5	3.037	-0.559	0.835	0.852	0.133	1.677
0.50	8.5	3.036	-0.559	0.835	0.853	0.132	1.677
0.70	8.5	3.035	-0.559	0.836	0.853	0.133	1.678
1.00	8.5	3.031	-0.559	0.837	0.854	0.133	1.679
2.00	8.5	3.010	-0.559	0.842	0.859	0.136	1.687
3.00	8.5	2.976	-0.560	0.849	0.866	0.147	1.698
5.00	8.5	2.864	-0.561	0.869	0.885	0.212	1.731
7.00	8.5	2.698	-0.548	0.896	0.911	0.315	1.781
10.00	8.5	2.352	-0.495	0.952	0.967	0.459	1.881
0.01	9.0	4.671	-0.559	1.500	1.503	0.186	2.397
0.02	9.0	4.671	-0.559	1.499	1.503	0.186	2.397
0.03	9.0	4.671	-0.559	1.499	1.503	0.186	2.397
0.05	9.0	4.671	-0.559	1.500	1.503	0.186	2.397
0.07	9.0	4.671	-0.559	1.500	1.503	0.186	2.397
0.10	9.0	4.671	-0.559	1.500	1.503	0.186	2.397
0.20	9.0	4.671	-0.559	1.500	1.503	0.187	2.397
0.30	9.0	4.671	-0.559	1.500	1.504	0.186	2.397
0.50	9.0	4.671	-0.559	1.500	1.504	0.186	2.398
0.70	9.0	4.665	-0.559	1.499	1.503	0.186	2.397
1.00	9.0	4.665	-0.559	1.500	1.504	0.187	2.399
2.00	9.0	4.650	-0.559	1.503	1.507	0.188	2.403
3.00	9.0	4.625	-0.560	1.506	1.510	0.197	2.409
5.00	9.0	4.551	-0.561	1.515	1.519	0.254	2.429
7.00	9.0	4.438	-0.548	1.527	1.531	0.344	2.459
10.00	9.0	4.197	-0.494	1.557	1.561	0.473	2.524

The decay $^{31}S \rightarrow {}^{31}P$ (Table 7) is a self-mirror system, with the result that all transitions along the diagonal ($1 \rightarrow 1$, $2 \rightarrow 2$, $3 \rightarrow 3$, etc.) have fast Fermi components. With its Gamow-Teller component included, the ground state to ground state transition has $\log ft = 3.69$ and $Q_n = 4.88$ MeV of available electron-capture phase space, yielding a very fast rate even at low temperatures (Fig. 4). The first excited state in ^{31}S lies at an excitation energy of 1.25 MeV, so that the ground state transition dominates the low density rate at all but the highest temperatures considered. However, at high temperature and density a large number of relatively fast Gamow-Teller electron capture channels open up. For instance, the $1 \rightarrow 15$ decay has $\log ft = 4.29$; $1 \rightarrow 17$, $\log ft = 4.028$; and $1 \rightarrow 20$, $\log ft = 4.30$ (all determined from calculations of Wildenthal [1979]). The diagonal Fermi transitions dominate the positron emission rate with the result that our $^{31}S \rightarrow {}^{31}P$ rate agrees very well with that given by the parametrized fit of Hansen (1966). However, at higher densities, where electron capture dominates the total weak destruction rate, our rates are somewhat faster than those of Hansen. At $T_9 = 2$ and $\rho/\mu_e = 10^8$, our rate is within a factor of 2 of the Hansen value, but at $T_9 = 10$ and $\rho/\mu_e = 10^6$ we are roughly 60 times faster, and at $T_9 = 10$ and $\rho/\mu_e = 10^9$ we are 4 times faster with an uncertainty of a factor of 2.5.

The decay $^{32}S \rightarrow {}^{32}P$ (Table 8) is extremely slow at any but the highest temperatures and densities considered, but as a result of the large abundance of ^{32}S at the end of oxygen burning it becomes an important neutronizer. The slow nature of the rate is a reflection of the fact that ^{32}S is stable in the laboratory ($Q_n = -2.221$ MeV) and of the very small matrix element for the ground state to ground state transition ($\log ft = 7.42$). Furthermore, the first excited state of ^{32}S lies at 2.23 MeV, although the transition from this state to the ground state of ^{32}P ($2 \rightarrow 1$) has a somewhat faster than average matrix element ($\log ft = 4.74$ as determined by mirror symmetry from the $^{32}Cl \rightarrow {}^{32}S$ positron decay). At lower temperatures the positron emission rate is very slow, since there is no contribution from the ground state, but a very steep temperature dependence develops as the first excited state begins to become populated around $T_9 = 3.0$. This results in positron emission rates 100 times faster than Hansen's at $T_9 = 3$. The electron capture rates at intermediate temperatures and higher densities are influenced by several relatively fast Gamow-Teller transitions upward from the ground state of ^{32}Si (Fig. 5): transition $1 \rightarrow 4$, $\log ft = 3.99$; $1 \rightarrow 9$, $\log ft = 4.20$; $1 \rightarrow 20$, $\log ft = 4.17$, all accessible for Fermi energies larger than 1 MeV; and finally, transition $1 \rightarrow 25$, $\log ft = 3.56$, accessible

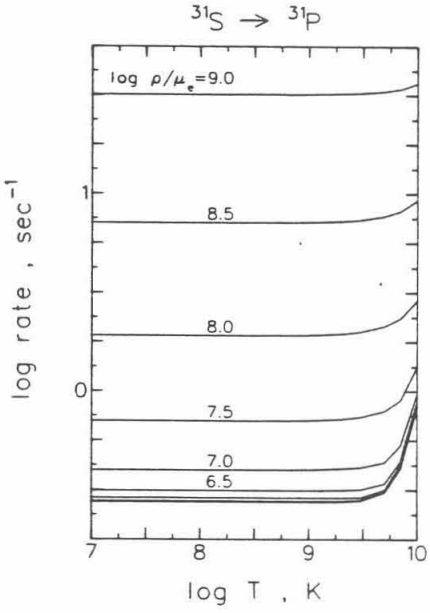

FIG. 4

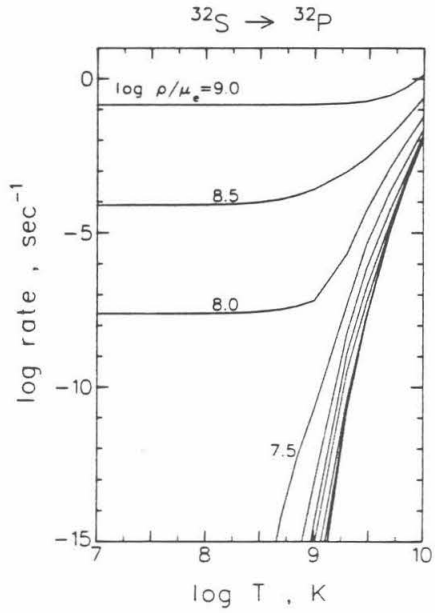

FIG. 5

FIG. 4.—Total decay rate for $^{31}S \rightarrow {}^{31}P$; $\log \Sigma$ from Table 7. This self-mirror system is dominated by the large number of fast Fermi transitions (cf., § III), and shows no dramatic temperature or density dependence. Electron capture dominates above $\log \rho/\mu_e = 6.0$.

FIG. 5.—Total decay rate for $^{32}S \rightarrow {}^{32}P$; $\log \Sigma$ from Table 8. since ^{32}S is stable in the laboratory, the rate of this decay is very slow at low densities until the temperature is high enough for significant thermal population of parent excited states. However, at $\log \rho/\mu_e \gtrsim 8.0$, U_F is large enough to allow upward transitions from the ground state, and a dramatic change in the low-temperature rate is observed.

TABLE 8

DECAY RATES FOR $^{32}S \rightarrow {}^{32}P$

T_9	log ρ/μ_e	U_r	log β^+	log ε^-	log Σ	log Δ	log ν
0.01	1.0	−0.003	−99.999	−99.999	−99.999	0.000	−99.999
0.02	1.0	−0.007	−99.999	−99.999	−99.999	0.000	−99.999
0.03	1.0	−0.013	−99.999	−99.999	−99.999	0.000	−99.999
0.05	1.0	−0.024	−99.999	−99.999	−99.999	0.000	−99.999
0.07	1.0	−0.037	−99.999	−99.999	−99.999	0.000	−99.999
0.10	1.0	−0.058	−99.999	−99.999	−99.999	0.000	−99.999
0.20	1.0	−0.134	−99.862	−56.705	−56.705	0.000	−57.985
0.30	1.0	−0.218	−68.124	−42.079	−42.079	0.000	−43.180
0.50	1.0	−0.398	−42.734	−30.239	−30.239	0.000	−31.054
0.70	1.0	−0.503	−31.851	−24.216	−24.216	0.000	−24.626
1.00	1.0	−0.511	−23.671	−18.339	−18.339	0.001	−18.530
2.00	1.0	−0.511	−13.773	−10.723	−10.723	0.057	−10.738
3.00	1.0	−0.511	−10.069	−7.782	−7.779	0.173	−7.682
5.00	1.0	−0.511	−6.375	−4.937	−4.922	0.382	−4.628
7.00	1.0	−0.511	−4.476	−3.397	−3.362	0.553	−2.899
10.00	1.0	−0.511	−3.090	−1.962	−1.931	0.709	−1.272
0.01	2.0	−0.001	−99.999	−99.999	−99.999	0.000	−99.999
0.02	2.0	−0.003	−99.999	−99.999	−99.999	0.000	−99.999
0.03	2.0	−0.007	−99.999	−99.999	−99.999	0.000	−99.999
0.05	2.0	−0.014	−99.999	−99.999	−99.999	0.000	−99.999
0.07	2.0	−0.023	−99.999	−99.999	−99.999	0.000	−99.999
0.10	2.0	−0.038	−99.999	−99.245	−99.245	0.000	−99.999
0.20	2.0	−0.095	−99.862	−55.704	−55.704	0.000	−56.984
0.30	2.0	−0.158	−68.124	−41.078	−41.078	0.000	−42.179
0.50	2.0	−0.299	−42.734	−29.241	−29.241	0.000	−30.056
0.70	2.0	−0.446	−31.851	−23.803	−23.803	0.000	−24.213
1.00	2.0	−0.506	−23.671	−18.317	−18.317	0.001	−18.509
2.00	2.0	−0.511	−13.773	−10.723	−10.723	0.057	−10.738
3.00	2.0	−0.511	−10.069	−7.782	−7.779	0.173	−7.682
5.00	2.0	−0.511	−6.375	−4.937	−4.922	0.382	−4.628
7.00	2.0	−0.511	−4.476	−3.397	−3.362	0.553	−2.899
10.00	2.0	−0.511	−3.090	−1.962	−1.931	0.709	−1.272
0.01	3.0	0.003	−99.999	−99.999	−99.999	0.000	−99.999
0.02	3.0	0.002	−99.999	−99.999	−99.999	0.000	−99.999
0.03	3.0	0.000	−99.999	−99.999	−99.999	0.000	−99.999
0.05	3.0	−0.004	−99.999	−99.999	−99.999	0.000	−99.999
0.07	3.0	−0.009	−99.999	−99.999	−99.999	0.000	−99.999
0.10	3.0	−0.018	−99.999	−98.228	−98.228	0.000	−99.812
0.20	3.0	−0.055	−99.862	−54.698	−54.698	0.000	−55.978
0.30	3.0	−0.099	−68.124	−40.076	−40.076	0.000	−41.176
0.50	3.0	−0.200	−42.734	−28.240	−28.240	0.000	−29.055
0.70	3.0	−0.314	−31.851	−22.855	−22.855	0.000	−23.265
1.00	3.0	−0.465	−23.671	−18.111	−18.111	0.001	−18.303
2.00	3.0	−0.510	−13.773	−10.720	−10.720	0.057	−10.735
3.00	3.0	−0.511	−10.069	−7.781	−7.779	0.174	−7.681
5.00	3.0	−0.511	−6.375	−4.937	−4.922	0.382	−4.628
7.00	3.0	−0.511	−4.476	−3.397	−3.362	0.553	−2.899
10.00	3.0	−0.511	−3.090	−1.962	−1.931	0.709	−1.272
0.01	4.0	0.012	−99.999	−99.999	−99.999	0.000	−99.999
0.02	4.0	0.012	−99.999	−99.999	−99.999	0.000	−99.999
0.03	4.0	0.011	−99.999	−99.999	−99.999	0.000	−99.999
0.05	4.0	0.010	−99.999	−99.999	−99.999	0.000	−99.999
0.07	4.0	0.009	−99.999	−99.999	−99.999	0.000	−99.999
0.10	4.0	0.005	−99.999	−97.072	−97.072	0.000	−98.656
0.20	4.0	−0.013	−99.862	−53.644	−53.644	0.000	−54.924
0.30	4.0	−0.037	−68.124	−39.047	−39.047	0.000	−40.148
0.50	4.0	−0.100	−42.734	−27.229	−27.229	0.000	−28.045
0.70	4.0	−0.174	−31.851	−21.852	−21.852	0.000	−22.264
1.00	4.0	−0.302	−23.671	−17.292	−17.292	0.001	−17.483
2.00	4.0	−0.497	−13.773	−10.689	−10.688	0.056	−10.704
3.00	4.0	−0.507	−10.069	−7.776	−7.773	0.173	−7.676
5.00	4.0	−0.510	−6.375	−4.936	−4.921	0.382	−4.627
7.00	4.0	−0.511	−4.476	−3.396	−3.362	0.553	−2.899
10.00	4.0	−0.511	−3.090	−1.962	−1.931	0.709	−1.272
0.01	5.0	0.053	−99.999	−99.999	−99.999	0.000	−99.999
0.02	5.0	0.053	−99.999	−99.999	−99.999	0.000	−99.999
0.03	5.0	0.053	−99.999	−99.999	−99.999	0.000	−99.999
0.05	5.0	0.053	−99.999	−99.999	−99.999	0.000	−99.999
0.07	5.0	0.053	−99.999	−99.999	−99.999	0.000	−99.999
0.10	5.0	0.052	−99.999	−94.728	−94.728	0.000	−96.312
0.20	5.0	0.047	−99.862	−52.137	−52.137	0.000	−53.417
0.30	5.0	0.038	−68.124	−37.775	−37.775	0.000	−38.875
0.50	5.0	0.011	−42.734	−26.115	−26.115	0.000	−26.944
0.70	5.0	−0.026	−31.851	−20.816	−20.816	0.000	−21.242
1.00	5.0	−0.098	−23.671	−16.289	−16.289	0.001	−16.478
2.00	5.0	−0.383	−13.772	−10.404	−10.404	0.057	−10.418
3.00	5.0	−0.476	−10.068	−7.723	−7.721	0.173	−7.623
5.00	5.0	−0.502	−6.374	−4.928	−4.913	0.382	−4.619
7.00	5.0	−0.507	−4.476	−3.394	−3.359	0.552	−2.897
10.00	5.0	−0.509	−3.090	−1.961	−1.930	0.709	−1.272
0.01	6.0	0.215	−99.999	−99.999	−99.999	0.000	−99.999
0.02	6.0	0.215	−99.999	−99.999	−99.999	0.000	−99.999
0.03	6.0	0.215	−99.999	−99.999	−99.999	0.000	−99.999
0.05	6.0	0.215	−99.999	−99.999	−99.999	0.000	−99.999
0.07	6.0	0.215	−99.999	−99.999	−99.999	0.000	−99.999
0.10	6.0	0.214	−99.999	−86.538	−86.538	0.000	−88.122
0.20	6.0	0.213	−99.862	−47.952	−47.952	0.000	−49.232
0.30	6.0	0.211	−68.124	−34.882	−34.882	0.000	−35.982
0.50	6.0	0.202	−42.734	−24.205	−24.205	0.000	−25.071
0.70	6.0	0.189	−31.851	−19.414	−19.414	0.000	−19.963
1.00	6.0	0.161	−23.671	−15.208	−15.208	0.002	−15.387
2.00	6.0	0.001	−13.771	−9.485	−9.485	0.063	−9.487
3.00	6.0	−0.212	−10.064	−7.290	−7.290	0.175	−7.188
5.00	6.0	−0.420	−6.372	−4.847	−4.834	0.380	−4.540
7.00	6.0	−0.469	−4.474	−3.367	−3.334	0.553	−2.871
10.00	6.0	−0.491	−3.089	−1.952	−1.922	0.709	−1.263
0.01	6.5	0.402	−99.999	−99.999	−99.999	0.000	−99.999
0.02	6.5	0.402	−99.999	−99.999	−99.999	0.000	−99.999
0.03	6.5	0.402	−99.999	−99.999	−99.999	0.000	−99.999
0.05	6.5	0.402	−99.999	−99.999	−99.999	0.000	−99.999
0.07	6.5	0.402	−99.999	−99.999	−99.999	0.000	−99.999
0.10	6.5	0.402	−99.999	−77.087	−77.087	0.000	−78.671
0.20	6.5	0.401	−99.862	−43.226	−43.226	0.000	−44.506
0.30	6.5	0.399	−68.124	−31.714	−31.714	0.000	−32.815
0.50	6.5	0.394	−42.734	−22.270	−22.270	0.000	−23.142
0.70	6.5	0.386	−31.851	−18.067	−18.067	0.000	−18.745
1.00	6.5	0.368	−23.671	−14.470	−14.470	0.002	−14.686
2.00	6.5	0.266	−13.771	−8.917	−8.917	0.077	−8.897
3.00	6.5	0.101	−10.063	−6.791	−6.791	0.182	−6.682
5.00	6.5	−0.234	−6.369	−4.663	−4.655	0.378	−4.359
7.00	6.5	−0.377	−4.472	−3.302	−3.274	0.553	−2.809
10.00	6.5	−0.449	−3.087	−1.931	−1.902	0.709	−1.243
0.01	7.0	0.711	−99.999	−99.999	−99.999	0.000	−99.999
0.02	7.0	0.711	−99.999	−99.999	−99.999	0.000	−99.999
0.03	7.0	0.711	−99.999	−99.999	−99.999	0.000	−99.999
0.05	7.0	0.711	−99.999	−99.999	−99.999	0.000	−99.999
0.07	7.0	0.711	−99.999	−83.521	−83.521	0.000	−85.261
0.10	7.0	0.711	−99.999	−61.479	−61.479	0.000	−63.064
0.20	7.0	0.711	−99.862	−35.410	−35.410	0.000	−36.690
0.30	7.0	0.710	−68.124	−26.495	−26.495	0.000	−27.595
0.50	7.0	0.706	−42.734	−19.123	−19.123	0.000	−19.996
0.70	7.0	0.701	−31.851	−15.814	−15.814	0.000	−16.533
1.00	7.0	0.689	−23.671	−13.139	−13.139	0.005	−13.566
2.00	7.0	0.622	−13.771	−8.246	−8.246	0.123	−8.195
3.00	7.0	0.510	−10.062	−6.178	−6.178	0.207	−6.054
5.00	7.0	0.187	−6.365	−4.251	−4.248	0.376	−3.950
7.00	7.0	−0.107	−4.467	−3.112	−3.093	0.552	−2.626
10.00	7.0	−0.315	−3.083	−1.866	−1.840	0.710	−1.179
0.01	7.5	1.197	−99.999	−99.999	−99.999	0.000	−99.999
0.02	7.5	1.197	−99.999	−99.999	−99.999	0.000	−99.999
0.03	7.5	1.197	−99.999	−98.871	−98.871	0.000	−99.999
0.05	7.5	1.197	−99.999	−63.742	−63.742	0.000	−65.629
0.07	7.5	1.197	−99.999	−48.532	−48.532	0.000	−50.272
0.10	7.5	1.197	−99.999	−36.987	−36.987	0.000	−38.571
0.20	7.5	1.197	−99.862	−23.164	−23.164	0.000	−24.443
0.30	7.5	1.196	−68.124	−18.322	−18.322	0.000	−19.422
0.50	7.5	1.194	−42.734	−14.209	−14.209	0.000	−15.082
0.70	7.5	1.190	−31.851	−12.290	−12.290	0.000	−13.010
1.00	7.5	1.182	−23.671	−10.707	−10.707	0.006	−11.260
2.00	7.5	1.137	−13.771	−7.323	−7.323	0.242	−7.301
3.00	7.5	1.062	−10.062	−5.409	−5.409	0.267	−5.275
5.00	7.5	0.825	−6.363	−3.647	−3.646	0.382	−3.342
7.00	7.5	0.507	−4.460	−2.686	−2.679	0.550	−2.207
10.00	7.5	0.082	−3.072	−1.672	−1.655	0.713	−0.988
0.01	8.0	1.936	−99.999	−7.608	−7.608	0.000	−8.374
0.02	8.0	1.936	−99.999	−7.611	−7.611	0.000	−8.378
0.03	8.0	1.936	−99.999	−7.610	−7.610	0.000	−8.377
0.05	8.0	1.936	−99.999	−7.609	−7.609	0.000	−8.375
0.07	8.0	1.936	−99.999	−7.607	−7.607	0.000	−8.372
0.10	8.0	1.936	−99.999	−7.604	−7.604	0.000	−8.365
0.20	8.0	1.935	−99.862	−7.586	−7.586	0.000	−8.329
0.30	8.0	1.935	−68.124	−7.556	−7.556	0.000	−8.272
0.50	8.0	1.933	−42.734	−7.471	−7.471	0.000	−8.117
0.70	8.0	1.931	−31.851	−7.367	−7.367	0.001	−7.937
1.00	8.0	1.925	−23.671	−7.190	−7.190	0.009	−7.654
2.00	8.0	1.895	−13.771	−5.681	−5.681	0.359	−5.852
3.00	8.0	1.844	−10.062	−4.312	−4.312	0.358	−4.231
5.00	8.0	1.681	−6.362	−2.876	−2.875	0.401	−2.565
7.00	8.0	1.441	−4.457	−2.062	−2.060	0.544	−1.584
10.00	8.0	0.982	−3.060	−1.243	−1.236	0.713	−0.562
0.01	8.5	3.037	−99.999	−4.109	−4.109	0.369	−4.729
0.02	8.5	3.038	−99.999	−4.102	−4.102	0.369	−4.723
0.03	8.5	3.038	−99.999	−4.104	−4.104	0.368	−4.726
0.05	8.5	3.038	−99.999	−4.103	−4.103	0.369	−4.724
0.07	8.5	3.038	−99.999	−4.101	−4.101	0.369	−4.721
0.10	8.5	3.038	−99.999	−4.096	−4.096	0.369	−4.716
0.20	8.5	3.038	−99.862	−4.069	−4.069	0.372	−4.685
0.30	8.5	3.037	−68.124	−4.029	−4.029	0.373	−4.637
0.50	8.5	3.036	−42.734	−3.919	−3.919	0.379	−4.499
0.70	8.5	3.035	−31.851	−3.790	−3.790	0.384	−4.325
1.00	8.5	3.031	−23.671	−3.593	−3.593	0.390	−4.047
2.00	8.5	3.010	−13.771	−3.024	−3.024	0.397	−3.229
3.00	8.5	2.978	−10.062	−2.579	−2.579	0.398	−2.581
5.00	8.5	2.864	−6.362	−1.843	−1.843	0.422	−1.545
7.00	8.5	2.698	−4.456	−1.269	−1.269	0.531	−0.788
10.00	8.5	2.352	−3.054	−0.624	−0.622	0.705	0.062
0.01	9.0	4.671	−99.999	−0.855	−0.855	0.400	−0.718
0.02	9.0	4.671	−99.999	−0.855	−0.855	0.399	−0.718
0.03	9.0	4.671	−99.999	−0.855	−0.855	0.399	−0.718
0.05	9.0	4.671	−99.999	−0.855	−0.855	0.399	−0.718
0.07	9.0	4.671	−99.999	−0.855	−0.855	0.399	−0.718
0.10	9.0	4.671	−99.999	−0.855	−0.855	0.400	−0.718
0.20	9.0	4.671	−99.862	−0.855	−0.855	0.400	−0.717
0.30	9.0	4.671	−68.124	−0.854	−0.854	0.400	−0.715
0.50	9.0	4.671	−42.734	−0.851	−0.851	0.400	−0.711
0.70	9.0	4.665	−31.851	−0.851	−0.851	0.400	−0.709
1.00	9.0	4.665	−23.671	−0.842	−0.842	0.400	−0.695
2.00	9.0	4.650	−13.771	−0.803	−0.803	0.400	−0.628
3.00	9.0	4.625	−10.062	−0.742	−0.742	0.401	−0.523
5.00	9.0	4.551	−6.362	−0.541	−0.541	0.420	−0.188
7.00	9.0	4.438	−4.456	−0.273	−0.273	0.503	0.231
10.00	9.0	4.197	−3.053	0.138	0.138	0.680	0.838

only for Fermi energies near 5 MeV ($\rho/\mu_e \approx 10^9$). This structure contributes to our rates being 10 times faster than Hansen's at $T_9=2$, $\rho/\mu_e=10^6$, 10 times slower at $\rho/\mu_e=10^8$ and the same temperature, and then, as the 1→25 transition becomes accessible, 200 times faster at $\rho/\mu_e=10^9$. At $T_9=10$ and densities between $\rho/\mu_e=10^6$ and 10^9, our rates are between a factor of 15 and 60 times faster than Hansen's, with matrix element induced uncertainties between factors of 2.5 and 5.

The decay $^{33}S \rightarrow {}^{33}P$ (Table 9) is again characterized by a relatively slow rate and a large abundance of laboratory stable ^{33}S in the presupernova neutronization regime, but here the nuclear Q_n-value is only -0.76 MeV. The ground state to ground state decay is measured to have the relatively slow matrix element log $ft=5.33$. However, here the first excited state of parent ^{33}S is at only 0.841 MeV and is accompanied by the relatively fast 2→1 transition of log $ft=4.44$ (determined from the mirror positron decay $^{33}Ar \rightarrow {}^{33}Cl$, and determined from calculations by Wildenthal to be log $ft=4.32$). Again, the positron decay rate is very slow until the first excited state begins to become thermally populated at around $T_9=0.5$, at which point it rises steeply. This rate is much slower than Hansen's until about $T_9 \approx 0.5-1$, at which point it rises to become 100 times faster between $T_9 \approx 2$ and 6, and then begins to converge on the Hansen rate at $T_9=10$ as the fast 2→1 decay becomes relatively less important than the Fermi and Gamow-Teller transition from the analogue of the daughter ground state at 5.47 MeV (30→1, log $ft=3.34$.) The electron capture rates are influenced by many average Gamow-Teller channels, with only a few fast channels available, and these at only very high daughter excitation energy (1→9, log $ft=4.17$, 4.19 MeV excitation; 1→1, log $ft=4.48$, 4.86 MeV excitation). Consequently, our rates agree well with those of Hansen at $T_9=2$, and are faster by a factor of 5 at $T_9=10$, where many unmeasured and uncalculated Gamow-Teller channels contribute; the factor of 5 reflects the difference between Hansen's average log $ft=5.7$ and our average log $ft=5.0$, and at $T_9=10.0$, $\rho/\mu_e=10^9$, for instance, the uncertainty is about a factor of 7, reflecting the order of magnitude uncertainty assigned to the average Gamow-Teller value. The total rate for the $^{33}S \rightarrow {}^{33}P$ decay is shown in Figure 6.

Finally, the $^{35}Cl \rightarrow {}^{35}S$ decay (Table 10) again reflects the slow decay of a relatively abundant laboratory-stable species. Here the ground state to ground state matrix element is measured to be log $ft=5.01$ and the nuclear Q-value is only -0.68 MeV. The first excited state of parent ^{35}Cl is at 1.219 MeV, and its population begins to affect the rate at intermediate temperatures (Fig. 7). The transition from the first excited state to the ground state of ^{35}S (2→1) is determined from calculations by Wildenthal to be a very slow log $ft=6.43$, but the 2→2 transition is calculated to

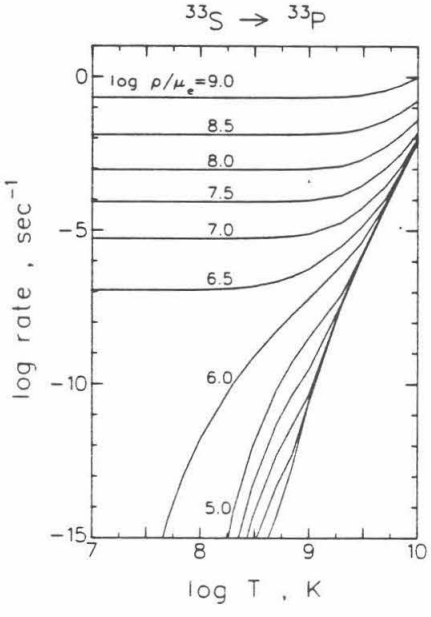

FIG. 6

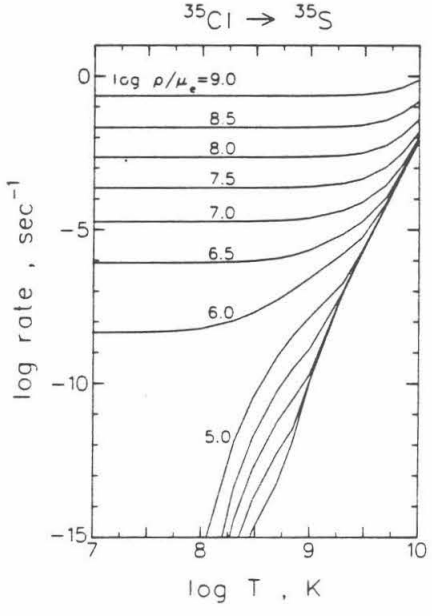

FIG. 7

FIG. 6.—Total decay rate for $^{33}S \rightarrow {}^{33}P$; log Σ from Table 9. As in Fig. 5, but in stable ^{33}S lower temperatures are required for significant population of low-lying parent levels, and upward transitions from the ground state begin to be important for log $\rho/\mu_e \geq 6.5$.

FIG. 7.—Total decay rate for $^{35}Cl \rightarrow {}^{35}S$; log Σ from Table 10. As in Figs. 5 and 6, except that still lower temperatures and densities are sufficient to achieve a significant weak interaction rate for the decay of laboratory-stable ^{35}Cl.

TABLE 9

DECAY RATES FOR $^{33}S \rightarrow {}^{33}P$

T_9	log ρ/μ_e	U_T	log β^+	log ε^-	log Σ	log Δ	log ν
0.01	1.0	-0.003	-99.999	-99.999	-99.999	0.000	-99.999
0.02	1.0	-0.007	-99.999	-78.751	-78.751	0.000	-79.035
0.03	1.0	-0.013	-99.999	-55.569	-55.569	0.000	-57.676
0.05	1.0	-0.024	-99.999	-38.500	-38.500	0.000	-40.383
0.07	1.0	-0.037	-99.999	-31.109	-31.109	0.000	-32.843
0.10	1.0	-0.058	-99.999	-25.491	-25.491	0.000	-27.067
0.20	1.0	-0.134	-63.543	-18.744	-18.744	0.000	-20.009
0.30	1.0	-0.218	-44.118	-16.369	-16.369	0.000	-17.449
0.50	1.0	-0.398	-28.578	-14.324	-14.324	0.000	-15.165
0.70	1.0	-0.503	-21.919	-12.716	-12.716	0.000	-13.393
1.00	1.0	-0.511	-16.924	-10.568	-10.568	0.000	-11.055
2.00	1.0	-0.511	-11.097	-7.386	-7.386	0.003	-7.487
3.00	1.0	-0.511	-8.985	-5.913	-5.913	0.040	-5.821
5.00	1.0	-0.511	-6.067	-4.263	-4.256	0.290	-3.941
7.00	1.0	-0.511	-4.569	-3.213	-3.194	0.556	-2.730
10.00	1.0	-0.511	-3.477	-2.116	-2.098	0.795	-1.465
0.01	2.0	-0.001	-99.999	-99.999	-99.999	0.000	-99.999
0.02	2.0	-0.003	-99.999	-75.734	-75.734	0.000	-78.018
0.03	2.0	-0.007	-99.999	-54.565	-54.565	0.000	-56.672
0.05	2.0	-0.014	-99.999	-37.496	-37.496	0.000	-39.379
0.07	2.0	-0.023	-99.999	-30.105	-30.105	0.000	-31.839
0.10	2.0	-0.038	-99.999	-24.489	-24.489	0.000	-26.066
0.20	2.0	-0.095	-63.543	-17.744	-17.744	0.000	-19.008
0.30	2.0	-0.158	-44.118	-15.368	-15.368	0.000	-16.448
0.50	2.0	-0.299	-28.578	-13.326	-13.326	0.000	-14.167
0.70	2.0	-0.446	-21.919	-12.303	-12.303	0.000	-12.980
1.00	2.0	-0.506	-16.924	-10.547	-10.547	0.000	-11.034
2.00	2.0	-0.511	-11.097	-7.386	-7.386	0.003	-7.486
3.00	2.0	-0.511	-8.985	-5.913	-5.913	0.040	-5.820
5.00	2.0	-0.511	-6.067	-4.263	-4.256	0.290	-3.941
7.00	2.0	-0.511	-4.569	-3.213	-3.194	0.556	-2.730
10.00	2.0	-0.511	-3.477	-2.116	-2.098	0.795	-1.465
0.01	3.0	0.003	-99.999	-99.999	-99.999	0.000	-99.999
0.02	3.0	0.002	-99.999	-74.510	-74.510	0.000	-76.794
0.03	3.0	0.000	-99.999	-53.458	-53.458	0.000	-55.564
0.05	3.0	-0.004	-99.999	-36.450	-36.450	0.000	-38.333
0.07	3.0	-0.009	-99.999	-29.078	-29.078	0.000	-30.812
0.10	3.0	-0.018	-99.999	-23.472	-23.472	0.000	-25.048
0.20	3.0	-0.055	-63.543	-16.738	-16.738	0.000	-18.003
0.30	3.0	-0.099	-44.118	-14.366	-14.366	0.000	-15.445
0.50	3.0	-0.200	-28.578	-12.325	-12.325	0.000	-13.166
0.70	3.0	-0.314	-21.919	-11.354	-11.354	0.000	-12.032
1.00	3.0	-0.465	-16.924	-10.341	-10.341	0.000	-10.828
2.00	3.0	-0.510	-11.097	-7.383	-7.383	0.003	-7.483
3.00	3.0	-0.511	-8.985	-5.912	-5.912	0.039	-5.820
5.00	3.0	-0.511	-6.067	-4.263	-4.256	0.290	-3.941
7.00	3.0	-0.511	-4.569	-3.213	-3.194	0.556	-2.730
10.00	3.0	-0.511	-3.477	-2.116	-2.098	0.795	-1.465
0.01	4.0	0.012	-99.999	-99.999	-99.999	0.000	-99.999
0.02	4.0	0.012	-99.999	-71.935	-71.935	0.000	-74.219
0.03	4.0	0.011	-99.999	-51.560	-51.560	0.000	-53.667
0.05	4.0	0.010	-99.999	-35.013	-35.013	0.000	-36.896
0.07	4.0	0.009	-99.999	-27.801	-27.801	0.000	-29.536
0.10	4.0	0.005	-99.999	-22.316	-22.316	0.000	-23.892
0.20	4.0	-0.013	-63.543	-15.683	-15.683	0.000	-16.948
0.30	4.0	-0.037	-44.118	-13.337	-13.337	0.000	-14.417
0.50	4.0	-0.100	-28.578	-11.313	-11.313	0.000	-12.154
0.70	4.0	-0.174	-21.919	-10.348	-10.348	0.000	-11.026
1.00	4.0	-0.302	-16.924	-9.519	-9.519	0.000	-10.006
2.00	4.0	-0.497	-11.097	-7.351	-7.351	0.003	-7.452
3.00	4.0	-0.507	-8.984	-5.907	-5.907	0.040	-5.815
5.00	4.0	-0.510	-6.067	-4.262	-4.256	0.291	-3.940
7.00	4.0	-0.511	-4.569	-3.213	-3.194	0.556	-2.730
10.00	4.0	-0.511	-3.477	-2.116	-2.098	0.795	-1.465
0.01	5.0	0.053	-99.999	-99.999	-99.999	0.000	-99.999
0.02	5.0	0.053	-99.999	-61.504	-61.504	0.000	-63.789
0.03	5.0	0.053	-99.999	-44.521	-44.521	0.000	-46.628
0.05	5.0	0.053	-99.999	-30.687	-30.687	0.000	-32.569
0.07	5.0	0.053	-99.999	-24.637	-24.637	0.000	-26.372
0.10	5.0	0.052	-99.999	-19.972	-19.972	0.000	-21.548
0.20	5.0	0.047	-63.543	-14.177	-14.177	0.000	-15.441
0.30	5.0	0.038	-44.118	-12.065	-12.065	0.000	-13.144
0.50	5.0	0.011	-28.578	-10.195	-10.195	0.000	-11.036
0.70	5.0	-0.026	-21.919	-9.282	-9.282	0.000	-9.960
1.00	5.0	-0.098	-16.924	-8.489	-8.489	0.000	-8.977
2.00	5.0	-0.383	-11.095	-7.064	-7.064	0.002	-7.184
3.00	5.0	-0.476	-8.983	-5.854	-5.854	0.039	-5.762
5.00	5.0	-0.502	-6.066	-4.254	-4.247	0.290	-3.932
7.00	5.0	-0.507	-4.569	-3.210	-3.192	0.557	-2.727
10.00	5.0	-0.509	-3.477	-2.115	-2.097	0.795	-1.464
0.01	6.0	0.215	-99.999	-30.383	-30.383	0.000	-32.969
0.02	6.0	0.215	-99.999	-20.813	-20.813	0.000	-23.097
0.03	6.0	0.215	-99.999	-17.393	-17.393	0.000	-19.500
0.05	6.0	0.215	-99.999	-14.410	-14.410	0.000	-16.293
0.07	6.0	0.215	-99.999	-12.975	-12.975	0.000	-14.709
0.10	6.0	0.214	-99.999	-11.783	-11.783	0.000	-13.359
0.20	6.0	0.213	-63.543	-9.998	-9.998	0.000	-11.259
0.30	6.0	0.211	-44.118	-9.182	-9.182	0.000	-10.256
0.50	6.0	0.202	-28.578	-8.287	-8.287	0.000	-9.122
0.70	6.0	0.189	-21.919	-7.747	-7.747	0.000	-8.420
1.00	6.0	0.161	-16.924	-7.205	-7.205	0.000	-7.695
2.00	6.0	0.001	-11.094	-6.119	-6.119	0.003	-6.216
3.00	6.0	-0.212	-8.977	-5.420	-5.420	0.039	-5.325
5.00	6.0	-0.420	-6.065	-4.173	-4.167	0.288	-3.851
7.00	6.0	-0.469	-4.568	-3.183	-3.166	0.557	-2.701
10.00	6.0	-0.491	-3.476	-2.107	-2.088	0.795	-1.456
0.01	6.5	0.402	-99.999	-6.942	-6.942	0.000	-7.874
0.02	6.5	0.402	-99.999	-6.942	-6.942	0.000	-7.873
0.03	6.5	0.402	-99.999	-6.941	-6.941	0.000	-7.871
0.05	6.5	0.402	-99.999	-6.938	-6.938	0.000	-7.866
0.07	6.5	0.402	-99.999	-6.939	-6.939	0.000	-7.864
0.10	6.5	0.402	-99.999	-6.930	-6.930	0.000	-7.848
0.20	6.5	0.401	-63.543	-6.889	-6.889	0.000	-7.770
0.30	6.5	0.399	-44.118	-6.827	-6.827	0.000	-7.655
0.50	6.5	0.394	-28.578	-6.668	-6.668	0.000	-7.380
0.70	6.5	0.386	-21.919	-6.498	-6.498	0.000	-7.100
1.00	6.5	0.368	-16.924	-6.248	-6.248	0.000	-6.706
2.00	6.5	0.266	-11.093	-5.499	-5.499	0.003	-5.588
3.00	6.5	0.101	-8.975	-4.917	-4.917	0.039	-4.815
5.00	6.5	-0.234	-6.062	-3.990	-3.986	0.285	-3.669
7.00	6.5	-0.377	-4.566	-3.119	-3.104	0.557	-2.638
10.00	6.5	-0.449	-3.475	-2.086	-2.068	0.796	-1.435
0.01	7.0	0.711	-99.999	-5.274	-5.274	0.000	-5.716
0.02	7.0	0.711	-99.999	-5.274	-5.274	0.000	-5.716
0.03	7.0	0.711	-99.999	-5.274	-5.274	0.000	-5.715
0.05	7.0	0.711	-99.999	-5.274	-5.274	0.000	-5.715
0.07	7.0	0.711	-99.999	-5.273	-5.273	0.000	-5.714
0.10	7.0	0.711	-99.999	-5.272	-5.272	0.000	-5.711
0.20	7.0	0.711	-63.543	-5.266	-5.266	0.000	-5.701
0.30	7.0	0.710	-44.118	-5.257	-5.257	0.000	-5.683
0.50	7.0	0.706	-28.578	-5.230	-5.230	0.000	-5.632
0.70	7.0	0.701	-21.919	-5.193	-5.193	0.000	-5.563
1.00	7.0	0.689	-16.924	-5.119	-5.119	0.000	-5.429
2.00	7.0	0.622	-11.093	-4.742	-4.742	0.003	-4.800
3.00	7.0	0.510	-8.974	-4.300	-4.300	0.042	-4.178
5.00	7.0	0.187	-6.059	-3.582	-3.581	0.283	-3.257
7.00	7.0	-0.107	-4.561	-2.929	-2.919	0.558	-2.450
10.00	7.0	-0.315	-3.470	-2.020	-2.005	0.798	-1.370
0.01	7.5	1.197	-99.999	-4.073	-4.073	0.000	-4.195
0.02	7.5	1.197	-99.999	-4.073	-4.073	0.000	-4.195
0.03	7.5	1.197	-99.999	-4.073	-4.073	0.000	-4.195
0.05	7.5	1.197	-99.999	-4.073	-4.073	0.000	-4.195
0.07	7.5	1.197	-99.999	-4.073	-4.073	0.000	-4.195
0.10	7.5	1.197	-99.999	-4.073	-4.073	0.000	-4.194
0.20	7.5	1.197	-63.543	-4.071	-4.071	0.000	-4.191
0.30	7.5	1.196	-44.118	-4.069	-4.069	0.000	-4.186
0.50	7.5	1.194	-28.578	-4.062	-4.062	0.000	-4.173
0.70	7.5	1.190	-21.919	-4.051	-4.051	0.000	-4.153
1.00	7.5	1.182	-16.924	-4.028	-4.028	0.000	-4.110
2.00	7.5	1.137	-11.093	-3.860	-3.860	0.007	-3.823
3.00	7.5	1.062	-8.974	-3.567	-3.567	0.052	-3.397
5.00	7.5	0.825	-6.057	-2.995	-2.994	0.285	-2.653
7.00	7.5	0.507	-4.555	-2.506	-2.502	0.558	-2.026
10.00	7.5	0.082	-3.460	-1.825	-1.815	0.801	-1.177
0.01	8.0	1.936	-99.999	-3.029	-3.029	0.008	-2.899
0.02	8.0	1.936	-99.999	-3.029	-3.029	0.008	-2.899
0.03	8.0	1.936	-99.999	-3.029	-3.029	0.008	-2.899
0.05	8.0	1.936	-99.999	-3.029	-3.029	0.008	-2.899
0.07	8.0	1.936	-99.999	-3.029	-3.029	0.008	-2.899
0.10	8.0	1.936	-99.999	-3.029	-3.029	0.008	-2.899
0.20	8.0	1.935	-63.543	-3.028	-3.028	0.008	-2.898
0.30	8.0	1.935	-44.118	-3.027	-3.027	0.008	-2.897
0.50	8.0	1.933	-28.578	-3.024	-3.024	0.011	-2.892
0.70	8.0	1.931	-21.919	-3.018	-3.018	0.012	-2.884
1.00	8.0	1.925	-16.924	-3.007	-3.007	0.017	-2.868
2.00	8.0	1.895	-11.093	-2.910	-2.910	0.048	-2.730
3.00	8.0	1.844	-8.974	-2.713	-2.713	0.098	-2.482
5.00	8.0	1.681	-6.057	-2.281	-2.281	0.299	-1.903
7.00	8.0	1.441	-4.552	-1.894	-1.893	0.559	-1.401
10.00	8.0	0.982	-3.448	-1.393	-1.389	0.806	-0.743
0.01	8.5	3.037	-99.999	-1.887	-1.887	0.186	-1.629
0.02	8.5	3.038	-99.999	-1.886	-1.886	0.186	-1.629
0.03	8.5	3.038	-99.999	-1.886	-1.886	0.185	-1.629
0.05	8.5	3.038	-99.999	-1.886	-1.886	0.185	-1.629
0.07	8.5	3.038	-99.999	-1.886	-1.886	0.185	-1.629
0.10	8.5	3.038	-99.999	-1.886	-1.886	0.185	-1.629
0.20	8.5	3.038	-63.543	-1.886	-1.886	0.186	-1.628
0.30	8.5	3.037	-44.118	-1.885	-1.885	0.186	-1.627
0.50	8.5	3.036	-28.578	-1.883	-1.883	0.187	-1.624
0.70	8.5	3.035	-21.919	-1.879	-1.879	0.188	-1.620
1.00	8.5	3.031	-16.924	-1.872	-1.872	0.190	-1.610
2.00	8.5	3.010	-11.093	-1.818	-1.818	0.199	-1.533
3.00	8.5	2.978	-8.974	-1.709	-1.709	0.208	-1.374
5.00	8.5	2.864	-6.057	-1.430	-1.430	0.333	-0.995
7.00	8.5	2.698	-4.551	-1.149	-1.148	0.565	-0.623
10.00	8.5	2.352	-3.442	-0.770	-0.769	0.811	-0.109
0.01	9.0	4.671	-99.999	-0.682	-0.682	0.304	-0.269
0.02	9.0	4.671	-99.999	-0.682	-0.682	0.303	-0.269
0.03	9.0	4.671	-99.999	-0.682	-0.682	0.303	-0.269
0.05	9.0	4.671	-99.999	-0.682	-0.682	0.304	-0.269
0.07	9.0	4.671	-99.999	-0.682	-0.682	0.304	-0.269
0.10	9.0	4.671	-99.999	-0.682	-0.682	0.304	-0.269
0.20	9.0	4.671	-63.543	-0.681	-0.681	0.303	-0.268
0.30	9.0	4.671	-44.118	-0.681	-0.681	0.303	-0.268
0.50	9.0	4.671	-28.578	-0.679	-0.679	0.303	-0.266
0.70	9.0	4.665	-21.919	-0.680	-0.680	0.303	-0.266
1.00	9.0	4.665	-16.924	-0.675	-0.675	0.304	-0.260
2.00	9.0	4.650	-11.093	-0.651	-0.651	0.304	-0.225
3.00	9.0	4.625	-8.974	-0.599	-0.599	0.302	-0.149
5.00	9.0	4.551	-6.057	-0.443	-0.443	0.384	0.073
7.00	9.0	4.438	-4.551	-0.266	-0.266	0.582	0.318
10.00	9.0	4.197	-3.441	-0.015	-0.015	0.820	0.679

TABLE 10

DECAY RATES FOR $^{35}Cl \rightarrow {}^{35}S$

T_9	$\log \rho/\mu_e$	U_r	$\log \beta^+$	$\log \varepsilon^-$	$\log \Sigma$	$\log \Delta$	$\log \nu$
0.01	1.0	-0.003	-99.999	-98.605	-98.605	0.000	-99.999
0.02	1.0	-0.007	-99.999	-55.976	-55.976	0.000	-58.259
0.03	1.0	-0.013	-99.999	-41.648	-41.648	0.000	-43.754
0.05	1.0	-0.024	-99.999	-30.061	-30.061	0.000	-31.942
0.07	1.0	-0.037	-99.999	-25.018	-25.018	0.000	-26.751
0.10	1.0	-0.058	-74.322	-21.161	-21.161	0.000	-22.735
0.20	1.0	-0.134	-43.596	-16.464	-16.464	0.000	-17.725
0.30	1.0	-0.218	-33.346	-14.769	-14.769	0.000	-15.844
0.50	1.0	-0.398	-23.234	-13.263	-13.263	0.000	-14.098
0.70	1.0	-0.503	-18.161	-11.883	-11.883	0.000	-12.558
1.00	1.0	-0.511	-14.352	-9.918	-9.918	0.000	-10.420
2.00	1.0	-0.511	-9.807	-7.061	-7.060	0.003	-7.221
3.00	1.0	-0.511	-7.812	-5.757	-5.753	0.036	-5.703
5.00	1.0	-0.511	-5.557	-4.236	-4.216	0.292	-3.886
7.00	1.0	-0.511	-4.207	-3.214	-3.172	0.679	-2.665
10.00	1.0	-0.511	-3.160	-2.132	-2.093	1.004	-1.405
0.01	2.0	-0.001	-99.999	-97.548	-97.548	0.000	-99.999
0.02	2.0	-0.003	-99.999	-54.958	-54.958	0.000	-57.242
0.03	2.0	-0.007	-99.999	-40.643	-40.643	0.000	-42.749
0.05	2.0	-0.014	-99.999	-29.057	-29.057	0.000	-30.938
0.07	2.0	-0.023	-99.999	-24.014	-24.014	0.000	-25.746
0.10	2.0	-0.038	-74.322	-20.159	-20.159	0.000	-21.733
0.20	2.0	-0.095	-43.596	-15.464	-15.464	0.000	-16.725
0.30	2.0	-0.158	-33.346	-13.768	-13.768	0.000	-14.843
0.50	2.0	-0.299	-23.234	-12.265	-12.265	0.000	-13.100
0.70	2.0	-0.446	-18.161	-11.470	-11.470	0.000	-12.145
1.00	2.0	-0.506	-14.352	-9.896	-9.896	0.000	-10.398
2.00	2.0	-0.511	-9.807	-7.061	-7.060	0.004	-7.221
3.00	2.0	-0.511	-7.812	-5.757	-5.753	0.036	-5.703
5.00	2.0	-0.511	-5.557	-4.236	-4.216	0.292	-3.886
7.00	2.0	-0.511	-4.207	-3.214	-3.172	0.679	-2.665
10.00	2.0	-0.511	-3.160	-2.132	-2.093	1.004	-1.405
0.01	3.0	0.003	-99.999	-95.926	-95.926	0.000	-98.512
0.02	3.0	0.002	-99.999	-53.735	-53.735	0.000	-56.019
0.03	3.0	0.000	-99.999	-39.536	-39.536	0.000	-41.642
0.05	3.0	-0.004	-99.999	-28.011	-28.011	0.000	-29.892
0.07	3.0	-0.009	-99.999	-22.987	-22.987	0.000	-24.720
0.10	3.0	-0.018	-74.322	-19.142	-19.142	0.000	-20.716
0.20	3.0	-0.055	-43.596	-14.458	-14.458	0.000	-15.719
0.30	3.0	-0.099	-33.346	-12.765	-12.765	0.000	-13.840
0.50	3.0	-0.200	-23.234	-11.264	-11.264	0.000	-12.099
0.70	3.0	-0.314	-18.161	-10.522	-10.522	0.000	-11.196
1.00	3.0	-0.465	-14.352	-9.690	-9.690	0.000	-10.192
2.00	3.0	-0.510	-9.806	-7.058	-7.057	0.004	-7.218
3.00	3.0	-0.511	-7.812	-5.756	-5.753	0.036	-5.702
5.00	3.0	-0.511	-5.557	-4.236	-4.216	0.292	-3.886
7.00	3.0	-0.511	-4.207	-3.214	-3.172	0.679	-2.665
10.00	3.0	-0.511	-3.160	-2.132	-2.093	1.004	-1.405
0.01	4.0	0.012	-99.999	-91.290	-91.290	0.000	-93.876
0.02	4.0	0.012	-99.999	-51.160	-51.160	0.000	-53.443
0.03	4.0	0.011	-99.999	-37.639	-37.639	0.000	-39.745
0.05	4.0	0.010	-99.999	-26.574	-26.574	0.000	-28.455
0.07	4.0	0.009	-99.999	-21.711	-21.711	0.000	-23.443
0.10	4.0	0.005	-74.322	-17.985	-17.985	0.000	-19.559
0.20	4.0	-0.013	-43.596	-13.403	-13.403	0.000	-14.664
0.30	4.0	-0.037	-33.346	-11.737	-11.737	0.000	-12.812
0.50	4.0	-0.100	-23.234	-10.252	-10.252	0.000	-11.087
0.70	4.0	-0.174	-18.161	-9.516	-9.516	0.000	-10.190
1.00	4.0	-0.302	-14.352	-8.868	-8.868	0.000	-9.370
2.00	4.0	-0.497	-9.806	-7.026	-7.025	0.003	-7.186
3.00	4.0	-0.507	-7.812	-5.751	-5.747	0.035	-5.697
5.00	4.0	-0.510	-5.557	-4.235	-4.215	0.292	-3.885
7.00	4.0	-0.511	-4.207	-3.214	-3.172	0.679	-2.665
10.00	4.0	-0.511	-3.160	-2.132	-2.093	1.004	-1.404
0.01	5.0	0.053	-99.999	-70.429	-70.429	0.000	-73.015
0.02	5.0	0.053	-99.999	-40.729	-40.729	0.000	-43.013
0.03	5.0	0.053	-99.999	-30.599	-30.599	0.000	-32.705
0.05	5.0	0.053	-99.999	-22.247	-22.247	0.000	-24.129
0.07	5.0	0.053	-99.999	-18.546	-18.546	0.000	-20.279
0.10	5.0	0.052	-74.322	-15.642	-15.642	0.000	-17.216
0.20	5.0	0.047	-43.596	-11.897	-11.897	0.000	-13.158
0.30	5.0	0.038	-33.346	-10.465	-10.465	0.000	-11.540
0.50	5.0	0.011	-23.234	-9.135	-9.135	0.000	-9.969
0.70	5.0	-0.026	-18.161	-8.451	-8.451	0.000	-9.124
1.00	5.0	-0.098	-14.352	-7.838	-7.838	0.000	-8.339
2.00	5.0	-0.383	-9.804	-6.738	-6.738	0.003	-6.898
3.00	5.0	-0.476	-7.811	-5.698	-5.694	0.035	-5.644
5.00	5.0	-0.502	-5.557	-4.227	-4.207	0.291	-3.877
7.00	5.0	-0.507	-4.207	-3.211	-3.169	0.678	-2.662
10.00	5.0	-0.509	-3.160	-2.131	-2.092	1.004	-1.404
0.01	6.0	0.215	-99.999	-8.352	-8.352	0.000	-9.797
0.02	6.0	0.215	-99.999	-8.347	-8.347	0.000	-9.788
0.03	6.0	0.215	-99.999	-8.339	-8.339	0.000	-9.773
0.05	6.0	0.215	-99.999	-8.314	-8.314	0.000	-9.727
0.07	6.0	0.215	-99.999	-8.280	-8.280	0.000	-9.664
0.10	6.0	0.214	-74.322	-8.226	-8.226	0.000	-9.561
0.20	6.0	0.213	-43.596	-7.964	-7.964	0.000	-9.123
0.30	6.0	0.211	-33.346	-7.710	-7.710	0.000	-8.723
0.50	6.0	0.202	-23.234	-7.282	-7.282	0.000	-8.084
0.70	6.0	0.189	-18.161	-6.946	-6.946	0.000	-7.597
1.00	6.0	0.161	-14.352	-6.563	-6.563	0.000	-7.050
2.00	6.0	0.001	-9.801	-5.781	-5.781	0.002	-5.937
3.00	6.0	-0.212	-7.805	-5.260	-5.258	0.031	-5.206
5.00	6.0	-0.420	-5.554	-4.146	-4.129	0.292	-3.798
7.00	6.0	-0.469	-4.206	-3.184	-3.145	0.681	-2.637
10.00	6.0	-0.491	-3.159	-2.122	-2.084	1.005	-1.395
0.01	6.5	0.402	-99.999	-6.074	-6.074	0.000	-6.815
0.02	6.5	0.402	-99.999	-6.074	-6.074	0.000	-6.815
0.03	6.5	0.402	-99.999	-6.073	-6.073	0.000	-6.814
0.05	6.5	0.402	-99.999	-6.072	-6.072	0.000	-6.811
0.07	6.5	0.402	-99.999	-6.073	-6.073	0.000	-6.812
0.10	6.5	0.402	-74.322	-6.069	-6.069	0.000	-6.804
0.20	6.5	0.401	-43.596	-6.050	-6.050	0.000	-6.768
0.30	6.5	0.399	-33.346	-6.019	-6.019	0.000	-6.710
0.50	6.5	0.394	-23.234	-5.933	-5.933	0.000	-6.552
0.70	6.5	0.386	-18.161	-5.828	-5.828	0.000	-6.369
1.00	6.5	0.368	-14.352	-5.658	-5.658	0.000	-6.085
2.00	6.5	0.266	-9.801	-5.146	-5.148	0.002	-5.286
3.00	6.5	0.101	-7.803	-4.747	-4.746	0.028	-4.689
5.00	6.5	-0.234	-5.550	-3.963	-3.952	0.292	-3.619
7.00	6.5	-0.377	-4.203	-3.120	-3.086	0.685	-2.576
10.00	6.5	-0.449	-3.158	-2.102	-2.065	1.007	-1.375
0.01	7.0	0.711	-99.999	-4.745	-4.745	0.000	-5.113
0.02	7.0	0.711	-99.999	-4.745	-4.745	0.000	-5.112
0.03	7.0	0.711	-99.999	-4.745	-4.745	0.000	-5.112
0.05	7.0	0.711	-99.999	-4.744	-4.744	0.000	-5.112
0.07	7.0	0.711	-99.999	-4.744	-4.744	0.000	-5.111
0.10	7.0	0.711	-74.322	-4.743	-4.743	0.000	-5.109
0.20	7.0	0.711	-43.596	-4.738	-4.738	0.000	-5.101
0.30	7.0	0.710	-33.346	-4.732	-4.732	0.000	-5.088
0.50	7.0	0.706	-23.234	-4.711	-4.711	0.000	-5.049
0.70	7.0	0.701	-18.161	-4.683	-4.683	0.000	-4.996
1.00	7.0	0.689	-14.352	-4.626	-4.626	0.000	-4.892
2.00	7.0	0.622	-9.801	-4.377	-4.377	0.001	-4.464
3.00	7.0	0.510	-7.802	-4.110	-4.110	0.028	-4.033
5.00	7.0	0.187	-5.544	-3.554	-3.550	0.293	-3.212
7.00	7.0	-0.107	-4.198	-2.932	-2.909	0.695	-2.394
10.00	7.0	-0.315	-3.154	-2.037	-2.005	1.012	-1.312
0.01	7.5	1.197	-99.999	-3.644	-3.644	0.000	-3.727
0.02	7.5	1.197	-99.999	-3.644	-3.644	0.000	-3.728
0.03	7.5	1.197	-99.999	-3.644	-3.644	0.000	-3.727
0.05	7.5	1.197	-99.999	-3.644	-3.644	0.000	-3.727
0.07	7.5	1.197	-99.999	-3.644	-3.644	0.000	-3.727
0.10	7.5	1.197	-74.322	-3.643	-3.643	0.000	-3.726
0.20	7.5	1.197	-43.596	-3.642	-3.642	0.000	-3.724
0.30	7.5	1.196	-33.346	-3.640	-3.640	0.000	-3.720
0.50	7.5	1.194	-23.234	-3.634	-3.634	0.000	-3.708
0.70	7.5	1.190	-18.161	-3.624	-3.624	0.000	-3.691
1.00	7.5	1.182	-14.352	-3.605	-3.605	0.000	-3.654
2.00	7.5	1.137	-9.801	-3.502	-3.502	0.002	-3.469
3.00	7.5	1.062	-7.802	-3.356	-3.356	0.024	-3.220
5.00	7.5	0.825	-5.542	-2.965	-2.964	0.296	-2.612
7.00	7.5	0.507	-4.191	-2.513	-2.504	0.712	-1.981
10.00	7.5	0.082	-3.144	-1.845	-1.823	1.024	-1.123
0.01	8.0	1.936	-99.999	-2.647	-2.647	0.001	-2.491
0.02	8.0	1.936	-99.999	-2.647	-2.647	0.001	-2.491
0.03	8.0	1.936	-99.999	-2.647	-2.647	0.001	-2.491
0.05	8.0	1.936	-99.999	-2.647	-2.647	0.001	-2.491
0.07	8.0	1.936	-99.999	-2.647	-2.647	0.001	-2.491
0.10	8.0	1.936	-74.322	-2.647	-2.647	0.001	-2.491
0.20	8.0	1.935	-43.596	-2.647	-2.647	0.001	-2.490
0.30	8.0	1.935	-33.346	-2.646	-2.646	0.001	-2.489
0.50	8.0	1.933	-23.234	-2.643	-2.643	0.001	-2.485
0.70	8.0	1.931	-18.161	-2.640	-2.640	0.002	-2.478
1.00	8.0	1.925	-14.352	-2.632	-2.632	0.003	-2.464
2.00	8.0	1.895	-9.801	-2.587	-2.587	0.010	-2.387
3.00	8.0	1.844	-7.802	-2.511	-2.511	0.035	-2.263
5.00	8.0	1.681	-5.541	-2.257	-2.257	0.319	-1.867
7.00	8.0	1.441	-4.187	-1.915	-1.913	0.740	-1.374
10.00	8.0	0.982	-3.132	-1.423	-1.414	1.048	-0.702
0.01	8.5	3.037	-99.999	-1.677	-1.677	0.046	-1.326
0.02	8.5	3.038	-99.999	-1.677	-1.677	0.046	-1.325
0.03	8.5	3.038	-99.999	-1.677	-1.677	0.046	-1.325
0.05	8.5	3.038	-99.999	-1.677	-1.677	0.046	-1.325
0.07	8.5	3.038	-99.999	-1.677	-1.677	0.046	-1.325
0.10	8.5	3.038	-74.322	-1.677	-1.677	0.046	-1.325
0.20	8.5	3.038	-43.596	-1.677	-1.677	0.047	-1.325
0.30	8.5	3.037	-33.346	-1.676	-1.676	0.046	-1.324
0.50	8.5	3.036	-23.234	-1.675	-1.675	0.047	-1.322
0.70	8.5	3.035	-18.161	-1.673	-1.673	0.047	-1.319
1.00	8.5	3.031	-14.352	-1.669	-1.669	0.048	-1.313
2.00	8.5	3.010	-9.801	-1.646	-1.646	0.058	-1.278
3.00	8.5	2.976	-7.802	-1.602	-1.602	0.095	-1.215
5.00	8.5	2.864	-5.541	-1.439	-1.439	0.404	-0.978
7.00	8.5	2.698	-4.187	-1.200	-1.199	0.796	-0.626
10.00	8.5	2.352	-3.126	-0.825	-0.823	1.086	-0.092
0.01	9.0	4.671	-99.999	-0.644	-0.644	0.263	-0.153
0.02	9.0	4.671	-99.999	-0.645	-0.645	0.264	-0.153
0.03	9.0	4.671	-99.999	-0.644	-0.644	0.263	-0.153
0.05	9.0	4.671	-99.999	-0.645	-0.645	0.264	-0.153
0.07	9.0	4.671	-99.999	-0.644	-0.644	0.263	-0.153
0.10	9.0	4.671	-74.322	-0.644	-0.644	0.263	-0.153
0.20	9.0	4.671	-43.596	-0.644	-0.644	0.264	-0.152
0.30	9.0	4.671	-33.346	-0.644	-0.644	0.265	-0.152
0.50	9.0	4.671	-23.234	-0.643	-0.643	0.268	-0.150
0.70	9.0	4.665	-18.161	-0.644	-0.644	0.270	-0.151
1.00	9.0	4.665	-14.352	-0.640	-0.640	0.277	-0.146
2.00	9.0	4.650	-9.801	-0.626	-0.628	0.316	-0.128
3.00	9.0	4.625	-7.802	-0.602	-0.602	0.386	-0.093
5.00	9.0	4.551	-5.541	-0.510	-0.510	0.633	0.044
7.00	9.0	4.438	-4.187	-0.370	-0.370	0.909	0.264
10.00	9.0	4.197	-3.125	-0.121	-0.120	1.147	0.648

have log $ft = 4.46$. The analog of the ^{35}S ground state lies at the very high excitation energy of 5.65 MeV and the Fermi transition from this state (with an average Gamow-Teller component of log $ft = 5.0$) has log $ft = 3.30$. The result is that the rates again exhibit a steep temperature dependence which tracks the Hansen parametrized fits well for both positron emission and electron capture until relatively high temperatures. At a temperature of $T_9 = 10$ and $\rho/\mu_e = 10^6$, our rates are a factor of 6 faster than Hansen's, dropping to a factor of 3 faster at $\rho/\mu_e = 10^8$. At the most extreme temperature and density point considered ($T_9 = 10$ and $\rho/\mu_e = 10^9$), our rates are almost six orders of magnitude faster than Hansen's, with a rate uncertainty well over an order of magnitude, indicating the importance of unknown high lying Gamow-Teller strength at these conditions.

In conclusion, the nuclear weak interaction rates of the decays $^{26}\text{Al} \rightarrow ^{26}\text{Mg}$, $^{30}\text{P} \rightarrow ^{30}\text{Si}$, $^{31}\text{S} \rightarrow ^{31}\text{P}$, $^{32}\text{S} \rightarrow ^{32}\text{P}$, $^{33}\text{S} \rightarrow ^{33}\text{P}$, and $^{35}\text{Cl} \rightarrow ^{35}\text{S}$ become sensitive functions of temperature and density in the stellar enviornment. These rates are for the most part determined by experimentally measured matrix elements and matrix elements derived from isospin symmetry, but where unmeasured Gamow-Teller transitions are important the rates can be computed with some confidence utilizing the detailed shell model calculations and nuclear systematics considered here. Our rates roughly agree with those of Hansen (1966) over a large range of conditions, but potentially important differences in the rates exist at temperatures and densities relevant for the production and destruction of ^{26}Al and for the neutronization-neutrino loss problem of presupernova evolution. Uncertainties in the rates have been estimated as a function of temperature and density, and the improved rates are presented in a form which should make them convenient to incorporate into detailed nucleosynthesis calculations involving these key species.

We are grateful to professor B. H. Wildenthal for providing us with nuclear matrix elements derived from the detailed nuclear shell model calculations into which he and his colleagues have put so much effort over the years, to H. S. Wilson and R. W. Kavanagh for making available to us their unpublished log ft measurements, to S. E. Koonin for helpful discussions on many aspects of the problem, and to S. E. Woosley and T. Weaver for many interesting discussions o the effects of weak-interaction processes in the late stages of presupernova stellar evolution, and especially for providing a list of the weak decays of great importance to the supernova problem.

REFERENCES

Arnett, W. D., and Wefel, J. P. 1978, *Ap. J. (Letters)*, **224**, L139.
Arnould, M., Hillebrandt, W., and Thielemann, F. K. 1978, Max-Planck-Institut, preprint.
Bahcall, J. N. 1961, *Phys. Rev.*, **124**, 495.
_____. 1962*a*, *Phys. Rev.*, **126**, 1143.
_____. 1962*b*, *Phys. Rev.*, **128**, 1297.
_____. 1962*c*, *Ap. J.*, **136**, 445.
_____. 1964, *Ap. J.*, **139**, 318.
Bethe, H. A., Brown, G. E., Applegate, J., and Lattimer, J. M. 1979, *Nucl. Phys. A.*
Brown, B. A., Chung, W., and Wildenthal, B. H. 1978, *Phys. Rev. Letters*, **40**, 1631.
Cameron, A. G. W. 1959, *Ap. J.*, **130**, 453.
Chung, W. 1976, Ph.D. thesis, Michigan State University.
Egawa, Y., Koichi, Y., and Yamada, M. 1975, *Progr. Theor. Phys.*, **54**, 1339.
Endt, P. M., and van der Leun, C. 1973, *Nucl. Phys.*, **214A**, 1.
_____. 1978, *Nucl. Phys.*, **310A**, 1.
Fowler, W. A., and Hoyle, F. 1964, *Ap. J. Suppl.*, **9**, 201.
Gove, N. B., and Martin, M. J. 1971, *Nuclear Data Tables*, **10**, 205.
Gray, C. M., and Compston, W. 1974, *Nature*, **251**, 495.
Hansen, C. J. 1966, Ph.D. thesis, Yale University.
Iben, I. 1978, *Ap. J.*, **219**, 213.
Lee, T., and Papanastassiou, D. A. 1974, *Geophys. Res. Letters*, **1**, 225.
Lee, T., Papanastassiou, D. A., and Wasserburg, G. J. 1976, *Geophys. REs. Letters*, **3**, 109.
Mazurek, T. J., Truran, J. W., and Cameron, A. G. W. 1974, *Ap. Space Sci.*, **27**, 261.
Peterson, V. L., and Bahcall, J. N. 1963, *Ap. J.*, **138**, 437.
Takahashi, K. 1971, *Progr. Theor. Phys.*, **45**, 1466.
Takahashi, K., and Yamada, J. 1969, *Progr. Theor. Phys.*, **41**, 1470.
Takahashi, K., Yamada, M., and Kondoh, T. 1973, *Atomic Data and Nuclear Data Tables*, **12**, 101.
Takahashi, K., El Eid, M. F., and Hillebrandt, W. 1978, *Astr. Ap.*, **67**, 185.
Truran, J. W., and Cameron, A. G. W. 1978, *Ap. J.*, **219**, 226.
Tubbs, D. L., and Koonin, S. E. 1979, *Ap. J. (Letters)*, **232**, L59.
Ward, R. A., and Fowler, W. A. 1979, preprint.
Weaver, T. A., Woosley, S. E., and Zimmerman, G. B. 1978, *Ap. J.*, **225**, 1021.
Weaver, T. A., and Woosley, S. E. 1979, private communication.
Wildenthal, B. H. 1977, *Elementary Modes of Excitation in Nuclei*, vol. **69**, (Corso: Soc. Italiana di Fisica-Bologna-Italy).
_____. 1979, private communication.
Wilson, H. S., and Kavanagh, R. W. 1978, private communication.
Woosley, S. E., Arnett, W. D., and Clayton, D. D. 1972, *Ap. J.*, **175**, 731.

GEORGE M. FULLER and WILLIAM A. FOWLER: W. K. Kellogg Radiation Laboratory 106-38, California Institute of Technology, Pasadena, CA 91125

MICHAEL J. NEWMAN: T-DOT, Mail Stop 288, Los Alamos Scientific Laboratory, University of California, P.O. Box 1663, Los Alamos, NM 87545

III. NUCLEAR WEAK INTERACTION RATE CALCULATIONS AND THE FERMI AND GAMOW-TELLER RESONANCES

STELLAR WEAK INTERACTION RATES[1] FOR INTERMEDIATE MASS NUCLEI II: A = 21 TO A = 60

GEORGE M. FULLER[2] and WILLIAM A. FOWLER

W. K. Kellogg Radiation Laboratory

California Institute of Technology, Pasadena, California 91125

and

MICHAEL J. NEWMAN

Theoretical Applications Division

Los Alamos National Scientific Laboratory

University of California, Los Alamos, New Mexico 87544

[1]Supported in part by the National Science Foundation [PHY79-23638] at the California Institute of Technology, and by the U.S. Department of Energy.

[2]Fannie and John Hertz Foundation Fellow.

ABSTRACT

Astrophysical electron and positron emission, continuum electron and positron capture rates as well as the associated neutrino energy loss rates are calculated for free nucleons and 226 nuclei with masses between A = 21 and 60. Measured nuclear level information and matrix elements are used where available. Unmeasured matrix elements for allowed transitions are assigned as in Paper I. Simple shell model arguments are used to estimate Gamow-Teller sum rules and collective state resonance excitation energies. The discrete state contribution to the rates, dominated by experimental information and the Fermi transitions, determines the nuclear rates in the regime of temperatures and densities characteristic of the hydrostatic phases of presupernova stellar evolution. At the higher temperatures and densities characteristic of the supernova collapse phase, the nuclear rates are dominated by the Fermi and the Gamow-Teller collective resonance contributions. Also included is the important effect of neutron shell closure blocking of electron capture on neutron-rich nuclei. Uncertainties in the rate calculation are discussed. Reference is made to other treatments of the problem. Results of the calculations on a detailed temperature-density grid are available in computer readable form on magnetic tape upon request to MJN.

I. INTRODUCTION

The problem of nuclear beta decay in the stellar environment has been discussed in Paper I of this series (Fuller, Fowler, and Newman 1980, hereafter referred to as F^2N I). In that work the positron emission, continuum electron capture and neutrino energy loss rates were calculated for $^{26}Al \rightarrow {}^{26}Mg$, $^{30}P \rightarrow {}^{30}Si$, $^{31}S \rightarrow {}^{31}P$, $^{32}S \rightarrow {}^{32}P$, $^{33}S \rightarrow {}^{33}P$, and $^{35}Cl \rightarrow {}^{35}S$. These rates are important in determining nucleosynthesis, neutronization, and neutrino cooling during the phases of presupernova evolution corresponding to core carbon, oxygen, and silicon burning. The temperatures and densities most relevant to these stellar environments are $0.1 \leq T_9 \leq 5$ and $10^5 \leq \rho/\mu_e \leq 10^9$, encompassing conditions from mild degeneracy up to electron Fermi energies near 5 MeV.

In this work the set of nuclei considered is extended to include free neutrons and protons and 226 nuclei between mass 21 and 60 inclusive. The present calculation includes positron emission, continuum electron capture, electron emission, and continuum positron capture rates, as well as ν and $\bar{\nu}$ energy loss rates for all nuclei considered. The reaction rates are calculated on an extended grid of temperatures and densities: $0.01 \leq T_9 \leq 100$ and $10 \leq \rho/\mu_e \leq 10^{11}$. This extended thermodynamic regime includes the conditions most appropriate for precollapse hydrostatic stellar evolution as well as the extreme environment of stellar core collapse, wherein temperatures in excess of 1 MeV and densities corresponding to electron Fermi energies near 25 MeV may be encountered before neutrino trapping. In the case of precollapse conditions, the nuclear weak interaction rates are dominated by discrete transitions; whereas in the extreme temperature and density environment of the stellar core collapse the rates are dominated by

the collective Gamow-Teller resonances.

The discrete state calculations performed in this work proceed as in F^2N I. The procedure is very closely tied to experimentally measured nuclear properties. Measured nuclear energy levels, spins, and parities are used to define the discrete states. Experimentally measured weak matrix elements are used where available. Unknown Fermi transitions can be calculated with precision (cf. F^2N I). Unknown Gamow-Teller transition matrix elements are assigned an average value appropriate to this nuclear mass range [log ft = 5.0, F^2N I; Gleit, Tang, and Coryell (1968)]. Forbidden transitions are neglected, but see Fuller (1981).

The work of Bethe, Brown, Applegate, and Lattimer (1979, hereafter BBAL) points the way to solving the problem of extreme high density, high temperature electron capture. In the present paper Gamow-Teller collective state strengths and excitation energies are calculated based on a simple shell model picture fashioned after the work of BBAL, Klapdor (1976, 1979), and Gaarde and collaborators (Gaarde et al. 1972, Gaarde et al. 1980), and guided by the growing volume of experimental data from (p,n) and (t,^{3}He) reactions and conventional delayed proton, neutron, and gamma decay experiments. Also included is the important effect of neutron shell closure blocking of electron capture for neutron-rich nuclei (Fuller 1981).

As the temperature and density rise in the collapsing stellar core, parent nucleus excited states are thermally populated, and many otherwise unattainable electron capture channels are opened among daughter nucleus excited states due to the increasing electron Fermi energy. Eventually the weak interaction rates are dominated by the Gamow-Teller collective resonances as pointed out by BBAL. In the present paper the

Gamow-Teller collective resonances in both parent and daughter are treated as discrete states; one discrete resonance state in the daughter (parent) for each energy level considered in the parent (daughter) nucleus. The energies of these discrete resonance states are estimated using single particle energies from Seeger and Howard (1975), also Seeger and Perisho (1967) and employing an average particle-hole repulsion energy as in BBAL. The collective state transition matrix elements are estimated with a simple shell model sum rule and subtraction of measured strength.

Since the Gamow-Teller resonances are approximated as discrete states, the calculational apparatus employed in F^2N I can be used directly. All of the equations governing the decay rate of nuclei in the stellar environment derived in § II of F^2N I apply here, with the exception that the occupation index P_i in Paper I, equation (9a) is handled differently for resonance state transitions (see § V, this paper).

The importance of obtaining accurate nuclear weak rates during both the hydrostatic phases of stellar evolution (Couch and Arnett 1973; Woosley, Arnett, and Clayton 1972; Weaver and Woosley 1979) and during the collapse phases is a well known problem. Neutronization resulting from electron capture during the phases of stellar evolution up through silicon burning has been treated statistically, utilizing the relatively long time scales associated with the various burning phases (Arnett 1977, 1980). Ultimately detailed neutronization, neutrino loss rates, and nucleosynthesis yields during presupernova evolution as well as the testing of statistical schemes require a detailed treatment of weak interaction rates. Reliable electron capture rates are required to compute the dynamics of the core infall epoch (Van Riper and Lattimer 1981). The initiation of the collapse in electron-capture

supernova depends on the detailed electron capture rates of intermediate mass nuclei (Couch and Arnett 1967, Nomoto 1980). The very high density electron capture rates determine to some extent the entropy and lepton-to-baryon ratio evolution in the collapsing stellar core, and hence are required for an understanding of the explosion mechanism.

The rates calculated in this work are available in a detailed temperature-density grid in computer readable form on magnetic tape upon request to MJN, and will subsequently be published on an abbreviated temperature and density grid in the Astrophysical Journal Supplement Series (Fuller, Fowler, and Newman 1981; hereafter F^2N III). The remainder of the present paper (hereafter F^2N II) describes the nuclear transition matrix element calculations, the uncertainties in the rates, and the results for a few interesting nuclei as examples.

II. NUCLEAR MATRIX ELEMENTS

The rate of decay from the i^{th} state of the parent nucleus to the j^{th} state of the daughter is given by

$$\lambda_{ij} = \ell n\ 2\ \frac{f_{ij}(T,\rho,U_F)}{(ft)_{ij}} \qquad (1)$$

The $(ft)_{ij}$ are the comparative half lives and are related to the allowed weak interaction matrix elements by equations (I-2a) and (I-2b), where equations denoted I are found in F^2N I. The phase space factors f_{ij} are given as integrals over the lepton distribution functions (I-3a) and (I-3b) and hence are sensitive functions of the temperature and density in the stellar interior. Similar expressions hold for the associated neutrino energy loss rates (I-6a) and (I-6b). The total decay or neutrino energy loss rate for a nucleus in the star is given by summing over all transitions between parent and daughter states.

The double sum over these discrete state transitions involves weighting nuclear parent levels with a Boltzmann population factor, introducing further temperature sensitivity in the total decay rate. To compute the weak interaction rates for a parent-daughter nucleus pair, discrete state excitation energies, spins, and parities are required for both nuclei, as well as weak interaction transition amplitudes connecting these states.

There has been a vast increase in the amount of measured nuclear level information since the weak rate surveys of Hansen (1966) and Mazurek, Truran, and Cameron (1974) were undertaken. In order to exploit these data and keep the rate calculations close to experiment, measured nuclear level information is used wherever possible. Typically, about 20 discrete states are included in each nucleus; resonance states will be discussed below. The nuclear level excitation energies, spins, and parities are taken from the latest nuclear information tabulations of Endt and van der Leun (1978) and Lederer et al. (1978) where available. For some proton- or neutron-rich nuclei the measured level information may be incomplete. In these cases, the nuclear level data can be supplemented by adroit attention to valence neutron and proton numbers and the shell model. For example, where excitation energies are known, but spins and parities are lacking, a zero order shell model for the valence nucleons can be used to generate a "bank" of J^{π} values which can then be assigned to the experimental states as needed. Where the measurement of spin for a given nuclear level is uncertain and several values are possible, the largest value is chosen in this work.

Finally, it is sometimes necessary to make estimates of excitation

energies of levels as well as spins and parities. This is accomplished here by using nuclear level information from a well measured isotope, isotone or isobar closer to the valley of beta-stability which has its valence nucleons filling the same j-subshells as the unmeasured nucleus. Further, the measured nucleus must be even-even, odd-odd, odd-even, or even-odd, just as for the unmeasured nucleus. For instance in $^{33}_{14}Si_{19}$, no excitation energies, spins or parities are known. The isotone $^{35}_{16}S_{19}$ is used to supply the missing information. In very neutron- or proton-rich nuclei, not even the masses are known accurately. In addition to the above techniques to fill out the unknown level information, theoretical nuclear mass values are taken from the calculations of Møller and Nix (1980) where necessary.

In principle, weak interaction matrix elements are required for all transitions between parent and daughter states. Matrix elements for forbidden transitions are not calculated in this work, since we are mainly interested in the weak rates of intermediate mass nuclei in temperature and density environments encountered during the collapse before neutrino trapping sets in. In these conditions allowed transitions and/or experimentally observed transitions, which may be forbidden, dominate the weak interaction rates. In the regime of stellar conditions beyond neutrino trapping [$\rho \gtrsim 5 \times 10^{11}$ g cm^{-3}, Arnett (1977)] most of the transitions are at least partially blocked, the electron captures go through hindered or forbidden transitions, and the bulk of the neutronization is carried by electron capture on free protons (Arnett 1977, 1980; Fuller 1981). In this work then, only allowed transitions between discrete states are considered except where rates for forbidden or hindered transitions are known experimentally.

The treatment of allowed matrix elements proceeds as in § III of F^2N I. Briefly, isospin symmetry is exploited to calculate accurately the Fermi transition matrix element and the energies of the isobaric analog states which carry this Fermi strength. Isospin symmetry is also used to extend the set of measured log ft values by extracting matrix elements measured in the mirror system, corresponding to the pair of nuclei of interest, after correcting for spin degeneracy factors. After the Fermi and mirror transitions are included in the calculation of a particular reaction, there are typically still many unmeasured Gamow-Teller transitions which can contribute to the weak decay rate. A mean log ft = 5.0 is taken for these transitions when allowed. This mean reflects the general trend of Gamow-Teller matrix elements in intermediate mass nuclei and is the result of an extensive survey of measured and calculated values done in F^2N I. As concluded in that work, the experimental and calculated Gamow-Teller and Fermi transitions serve to dominate weak decay calculations and yield a reliable rate for well studied intermediate mass nuclei over most of the range of temperature and density of interest in the hydrostatic phases of stellar evolution. The extension of reliability of these rate calculations to the regime of extreme temperature and density requires a knowledge of the beta-strength function over a large range of nuclear excitation energy. In particular, the Gamow-Teller strength function is needed as well as a way to handle large numbers of thermally populated isobaric analog states carrying Fermi strength.

III. FERMI AND GAMOW-TELLER COLLECTIVE MODES

The Gamow-Teller strength distribution has been a problem of increasing concern to nuclear experimentalists because the details of this

distribution are very sensitive to the central isovector spin and tensor components of the nuclear force. However, an increasing amount of experimental and theoretical lore points to the existence of a giant Gamow-Teller resonance which contains much of the collective Gamow-Teller strength in a broad peak (Goodman et al. 1980).

The Fermi transitions are illustrative of the resonance collective state phenomena. To each state of a $T^{>}$-parent nucleus ($T \equiv |Z - N|/2$), there corresponds a $T^{>}$ isobaric analog state (IAS) in the $T^{<}$-daughter nucleus. These analog states can be generated by acting on the associated parent states with the isospin raising or lowering operator

$$T_{\pm} = \sum_{n} \tau_{\pm}(n) \qquad (2)$$

given by a sum over nucleons. The selection rules for the Fermi operator are $\Delta\pi = 0$; $\Delta T = 0$; $\Delta J = 0$. This operator commutes with all parts of the nuclear Hamiltonian save the Coulomb force. As a result the analog state is pushed up in excitation by the difference in Coulomb energy between parent and daughter nuclei. Furthermore, the off-diagonal matrix elements of the Coulomb interaction serve to mix the isospin quantum number. In practice the resultant mixing is very small, isospin is a good quantum number, and hence all of the Fermi strength is concentrated in the analog states (Soper 1969, deShalit and Feshbach 1974). There is, of course, no Fermi resonance for a transition from a $T^{<}$-parent state to a $T^{>}$-daughter state. The important point here is that isospin is a good quantum number and the Fermi strength is narrowly concentrated even though the isospin operator generates only an approximate symmetry for the nuclear system.

The situation for the Gamow-Teller operator and its associated resonance is somewhat more involved, though qualitatively similar to the Fermi isobaric analog problem. Consider again the decay of a $T^>$ parent nucleus to states in the $T^<$ daughter, but now via the Gamow-Teller operator,

$$GT = \sum_n \vec{\sigma}(n)\ \tau_{\pm}(n) \tag{3}$$

given as a sum over nucleons. The τ_+ and the τ_- are the isospin raising and lowering operators for individual nucleons, and $\vec{\sigma}$ is the Pauli spin operator. Note that since GT is a spatial vector and an isovector, the Wigner-Eckart theorem implies the selection rules $\Delta\pi = 0$; $\Delta T = 0, \pm 1$, no $0 \rightarrow 0$; $\Delta J = 0, \pm 1$, no $0 \rightarrow 0$. GT then connects to both $T^<$ and $T^>$ states and can change the spin of a nucleon but cannot change either its orbital angular momentum or its principle quantum number in allowed transitions. Like the Fermi operator GT does not commute with the total nuclear Hamiltonian.

Unfortunately, the Gamow-Teller operator does not commute with the strong spin-dependent parts of the nuclear interaction, whereas the force responsible for isospin symmetry breaking is the relatively weaker electromagnetic interaction. As a result, the "isobaric state" corresponding to the collective Gamow-Teller mode is expected to be badly split among the nuclear daughter levels as compared to the Fermi isobaric-analog state resonance.

The strictly nuclear part of the nucleon-nucleon potential can be represented as a sum of central, tensor, and spin-orbit terms. For the most general Hamiltonian invariant under rotations generated by total spin ($\vec{J} = \vec{L} + \vec{S}$) and isospin ($\vec{T}$), we have the terms

$$H^{\text{central}} = V^{c} + V^{c}_{\sigma}\,\vec{\sigma}_1\cdot\vec{\sigma}_2 + V^{c}_{\tau}\,\vec{\tau}_1\cdot\vec{\tau}_2 + V^{c}_{\sigma\tau}\,(\vec{\sigma}_1\cdot\vec{\tau}_1)(\vec{\sigma}_2\cdot\vec{\tau}_2) \qquad (4)$$

$$H^{\text{tensor}} = (V^{t} + V^{t}_{\tau}\,\vec{\tau}_1\cdot\vec{\tau}_2)(3(\vec{\sigma}_1\cdot\hat{r})(\vec{\sigma}_2\cdot\hat{r}) - \vec{\sigma}_1\cdot\vec{\sigma}_2) \qquad (5)$$

$$H^{\text{spin orbit}} = (V^{so} + V^{so}_{\tau}\,\vec{\tau}_1\cdot\vec{\tau}_2)\,(\vec{L}\cdot\vec{S}) \qquad (6)$$

where all of the potentials, V, are functions of r and where $\hat{r} = (\vec{r}_1 - \vec{r}_2)/|\vec{r}_1 - \vec{r}_2|$ is the normalized nucleon coordinate difference. The coefficients are taken to be the sums of Yukawa potentials in the usual phenomenological effective interaction studies (e.g., Austin 1980). The strengths and ranges of these forces can be found from DWBA analyses of scattering data as well as modeling nuclear spectra, though the parameters of some forces are known better than others. In particular V^{c}_{σ}, $V^{c}_{\sigma\tau}$, and V^{t}_{τ} are comparatively not well known, and these are just the forces most responsible for shaping the Gamow-Teller strength distribution (Halbleib and Sorensen 1967, Fujita and Ikeda 1965).

These forces not only introduce mixing among daughter states, but also can produce particle-hole correlations in the parent nucleus wave functions. The particle-hole forces in the spin-flip isospin-flip mode (i.e., pn^{-1} or $p^{-1}n$) are determined by $V^{c}_{\sigma\tau}$. The studies by Gaarde et al. (1972) and Martinsen and Randrup (1972) show that the effect of this force is to push the Gamow-Teller spin-flip mode strength up in daughter excitation energy, while weakening the no-spin-flip mode strength and spreading it out in excitation energy. This will be developed in more detail below, where a simple shell model is discussed.

As emphasized above, however, even though a nuclear symmetry is

only very approximate, it may still be a useful description of the nucleus. In the case of the Fermi operator, the approximation of an isospin-independent interaction insures concentration of all Fermi strength in an isobaric analog state. In the Gamow-Teller case, approximation of a spin and isospin independent nuclear force would insure concentration of the GT-strength in an isobaric resonance state. Specifically, an assumption of a spin and isospin independent nuclear Hamiltonian would result in the Fermi and Gamow-Teller collective strengths being concentrated in a single degenerate daughter nucleus eigenstate: the Wigner supermultiplet state. Gaponov and Lyutostanskii (1974) have shown from a finite Fermi system model that the degenerate supermultiplet state is split by $V^{c}_{\sigma\tau}$ in such a manner as to concentrate the Gamow-Teller strength in a collective state a few MeV above the analog state in most intermediate mass nuclei. The picture of the Gamow-Teller transition for the ground state of a $T^{>}$-nucleus to a $T^{<}$-nucleus then, is that the collective GT strength is contained in a broad peak centered well above the first analog state, with the no-spin-flip strength relatively more spread out than the concentrated spin-flip strength.

The growing volume of experimental data seems to support this conclusion for the $T^{>} \rightarrow T^{<}$ transitions of neutron-rich intermediate mass nuclei, whereas the $T^{<} \rightarrow T^{>}$ transition characteristics are much different. The Gamow-Teller strength distribution can be examined experimentally either in gamma-decay branching or in delayed neutron, e.g., ^{31}Na, and proton, e.g., ^{33}Ar, experiments. The results are available as log ft values tabulated in Endt and van der Leun (1978) or Lederer et al. (1980), as discussed above. The problem with these

techniques is that there are no nuclei whose decays have a large enough Q-value to reach the main part of the beta-strength in the daughter nucleus. The $^{33}Ar \rightarrow {}^{33}Cl$ positron-decay has a large Q-value (11.618 MeV) and even in this case only about 12% of the expected strength is observed. This decay has been analyzed in terms of the simple shell model by Klapdor (1976) in some detail and tends to confirm the trends in the strength function mentioned above.

Another experimental technique which has met with some success involves charged particle reactions to excite the IAS in a nucleus resulting from electron-emission. The spin part of the electromagnetic M1 operator corresponds very closely to the Gamow-Teller operator and so the M1 decay from the excited IAS populates the same states as would the electron emission from the parent nucleus ground state. Gaarde et al. (1972) have used $^{48}Ca(p,\gamma)$ to populate the IAS in ^{49}Sc corresponding to the ground state of ^{49}Ca, with results which confirm the theoretical conclusion discussed above that the spin-flip strength is pushed up and strengthened by $V^{c}_{\sigma\tau}$, while the no-spin-flip strength is weakened and spread out in daughter excitation energy.

By far, however, the most dramatic confirmation of the position of the GT resonance comes from recent change-exchange experiments, notably (p,n) and (^{3}He, t). These reactions mimic electron emission by creating a neutron-hole and proton-particle state in the residual nucleus and hence are especially useful for studying $T^{>} \rightarrow T^{<}$ decays. The advantage of this technique lies with the relative lack of Q-value restrictions on the daughter excitation energy region explored, allowing complete resolution of the high lying Gamow-Teller strength. The incident proton or ^{3}He energy must be high enough to insure a

predominantly direct component in the scattering amplitude. In this case the scattering amplitude is related in the usual manner to the DWBA T-matrix element, given by

$$T_{FI} = \int \chi_F^{\dagger} \quad \langle \Psi_f | V^c_{\sigma\tau} | \Psi_i \rangle \quad \chi_I \; d^3r \qquad (7)$$
$$\propto \langle \Psi_f \; | \vec{\sigma} \quad \tau_{\pm} | \Psi_i \rangle$$

where the χ_F and χ_I are the appropriately advanced and retarded distorted waves and $\langle \Psi_f | V^c_{\sigma\tau} | \Psi_i \rangle$ is the matrix element of the effective nucleon-nucleon potential between initial and final nuclear wave functions Ψ_i and Ψ_f (Austin 1980). Measuring the cross section for a charge exchange reaction in the forward direction assures the dominance of low-ℓ, even partial waves which in turn determine, through the selection rules, which part of the nuclear interaction contributes.

For example, in the (p,n) reaction, for relative s-wave scattering, isospin must change, and spin can change by 0 or 1 unit of angular momentum. The interactions V^c_{τ}, $V^c_{\sigma\tau}$, V^t_{τ} can then contribute, where V^c_{τ} is responsible for the "Fermi" transition to the IAS and where $V^c_{\sigma\tau}$ is predominantly responsible for the Gamow-Teller spin-flip and no-spin-flip transitions. V^t_{τ} is not as important, since this force is known to be weak in the lower partial waves, dominating only for high momentum transfer (Austin 1980). The IAS and the associated Fermi strength were first discovered with the (p,n) reaction by Anderson and Wong (1961), while the Gamow-Teller peak was unambiguously identified in the $^{90}Zr(p,n)^{90}Nb$ experiment by Doering et al. (1975)., Bainum et al. (1980), Goodman et al. (1980) and Sterrenburg et al. (1980).

The results for the $^{90}Zr(p,n)^{90}Nb$ experiment tend to confirm the overall features discussed above for the $T^{>} \rightarrow T^{<}$ transitions: a broad

Gamow-Teller resonance lies roughly 5 MeV above the first IAS in ^{90}Nb. (Bainum et al. 1980). In general the results for ^{90}Zr(p,n)^{90}Nb agree well with a simple shell model prediction, though not all of the predicted strength is seen. Such charge exchange experiments have been performed for other Zr isotopes with results in general similar to the ^{90}Zr(p,n)^{90}Nb case but with details which change in a complicated manner with increasing Zr mass number (Sterrenburg et al. 1980, Galonsky 1980). The description of Gamow-Teller resonance behavior for lighter nuclei is better understood as higher resolution (p,n) experiments have been done, for example, in ^{26}Mg(p,n)^{26}Al by Goodman et al. (1980) and in ^{48}Ca(p,n)^{48}Sc by Anderson et al. (1980). The simple-shell model systematics of Klapdor (1976) and others provides the basis for a very simple, compelling explanation for the Gamow-Teller resonance characteristics in this mass range for the $T^{>} \rightarrow T^{<}$ transitions and will be discussed below.

The experimental observations are much less complete for the Gamow-Teller resonance systematics in the $T^{<} \rightarrow T^{>}$ transitions, e.g., $^{56}Fe + e^{-} \rightarrow {}^{56}Mn + \nu$. The conventional measurements of log ft values for discrete state transitions are hindered in the $T^{<} \rightarrow T^{>}$ direction by the nuclear Q-values. The $T^{>}$-daughter ground state usually lies higher in energy than the $T^{<}$-parent ground state by at least the Coulomb energy difference, which is considerable in intermediate and heavy mass nuclei. There are some lighter nuclei where weak transition matrix elements have been measured for $T^{<} \rightarrow T^{>}$, but these measured matrix elements do not exhaust the Gamow-Teller sum rule. The work of Flynn et al. (1974) using the (t,^{3}He) reaction has identified $0^{+} \rightarrow 1^{+}$ transitions in ^{28}Si(t,^{3}He)^{28}Al and ^{58}Ni(t,^{3}He)^{58}Co, among

others, which seem to be related to pieces of the giant M1-GT collective modes. A promising experimental technique which has so far not been employed in searches for Gamow-Teller strength is the (n,p) reaction. Though this reaction suffers in resolution (Brady and Needham 1980), it has the advantage over (t,^{3}He) in not being inhibited strongly by Coulomb-barrier penetration.

Some indication of the Gamow-Teller resonance characteristics for ^{56}Fe are given by the detailed shell model calculations of Bloom and Fuller (1981). In that work, the Gamow-Teller strength for the ^{56}Fe (ground state) → ^{56}Mn (continuum) is seen to lie in a broad peak centered at 2.7 MeV in ^{56}Mn, while the ^{56}Fe(1st excited state) → ^{56}Mn (continuum) is located in a broad feature at 4.6 MeV. This calculation is a good confirmation of the simple estimate of the ^{56}Fe Gamow-Teller peak energy done by BBAL, and it appears that shell model systematics suffice to predict the trend of strength and excitation energy for the Gamow-Teller resonance in the $T^{<} \rightarrow T^{>}$ direction, which is just the isospin change direction most important in neutronization and neutrino loss processes in the late stages of stellar evolution.

IV. SHELL MODEL INTERPRETATION OF GT-RESONANCE CHARACTERISTICS

A shell-model description of nuclear beta decay processes based on the ideas of Gaarde et al. (1972), Klapdor (1976) and BBAL is used in the rate calculations presented in this work to give (1) an approximate collective Gamow-Teller ground state sum rule, and (2) an approximate daughter nucleus excitation energy for this collective state. The Gamow-Teller resonance and its strength, together with the allowed

discrete state transitions serve to outline the β-strength distribution and provide a reliable weak interaction rate at high temperature and density. The differing characteristics of the $T^{<} \rightarrow T^{>}$ and the $T^{>} \rightarrow T^{<}$ Gamow-Teller strength functions emerge naturally from this procedure, as do important predictions about the variation of collective state strengths with increasing neutron richness.

Consider first the $T^{<} \rightarrow T^{>}$ Gamow-Teller strength distribution for transitions from the ground state of an intermediate mass nucleus, e.g., $^{33}S(e^{-},\nu_{e})^{33}P$. The contribution to the stellar rates from the collective resonances for each of the parent excited states will be discussed below. A possible zero-order shell model configuration for the ground state of ^{33}S, for example, is represented in Figure 1. The valence nucleons are filling the sd-shell, the $1d_{5/2}$ and $2s_{1/2}$ orbits are closed for both protons and neutrons and there is one unpaired neutron in the $1d_{3/2}$ orbit. The Gamow-Teller selection rules derived above allow both spin-flip and no-spin-flip transition modes but it is clear from Figure 1 for this $T^{<} \rightarrow T^{>}$ case (i.e., continuum electron capture or positron emission) that the no-spin-flip transitions are not possible, while only one type of spin-flip mode contributes, one of six $1d_{5/2}$ protons transforming into one of three $1d_{3/2}$ neutron holes. In reality, the ground state nuclear wave function for ^{33}S will be an admixture of many such simple shell model configurations since the residual nuclear forces polarize the $2s_{1/2}$-$1d_{5/2}$ closed shells. The resulting holes in the $1d_{5/2}$ neutron shell could allow a no-spin-flip transition of a $1d_{5/2}$ proton into a $1d_{5/2}$ neutron hole. However, in this work it is argued that the ground state wave function is predominantly given by the zero-order model, the more complicated configurations tending to be concentrated in highly

excited states due to the substantial single particle energy difference penalty required to excite particles out of closed shells.

For the purposes of these stellar rate calculations it is sufficient to estimate the Gamow-Teller spin-flip mode excitation energy in ^{33}P, since as discussed above, experiment shows that the spin-flip mode is relatively concentrated, the no-spin-flip mode being spread out in daughter nucleus excitation energy when it can occur. The Gamow-Teller collective spin-flip mode is given by

$$|\Psi\rangle_{CGT} = \sum_{ij} \langle i|\vec{\sigma}\tau_-|j\rangle \quad a_i^\dagger a_j |\Psi(^{33}S^{gs})\rangle \tag{8}$$

where $a_i^\dagger$ creates a neutron in single particle orbit i, a_j destroys a proton in single particle orbit j, and gs indicates ground state. With a simple zero-order shell model like the one shown for ^{33}S one can solve for the collective state excitation energy relative to the ^{33}P ground state. This collective spin-flip configuration (shown in Fig. 2) differs from the ^{33}P ground state by the excitation of a $1d_{5/2}$ proton to the $2s_{1/2}$ proton orbit. The equation for the collective resonance energies E_n (n = 1, 2, ...) will be

$$\{\varepsilon_a - \varepsilon_b - E_n\}\psi^{(n)}(a\ b) + \sum_{\ell m} \langle ab|V_{ph}|\ell m\rangle \psi^{(n)}(\ell m) = 0 \tag{9}$$

where ε_a, in the case of ^{33}P, is the single particle energy of the $2s_{1/2}$ proton orbit, ε_b is the energy of the $1d_{5/2}$ proton orbit, V_{ph} is the component of the nucleon-nucleon force which acts in the particle-hole channel, and the $\psi^{(n)}(a\ b)$ are the coefficients of the particle-hole configurations in $|\Psi\rangle_{CGT}$, i.e., for some n

$$|\Psi\rangle_{CGT} \simeq \left(\sum_{ij} \psi^{(n)}(ij)\ a_i^\dagger a_j \right) |\Psi(^{33}P^{gs})\rangle \quad . \tag{10}$$

If there are n_p particles in the upper orbit of the final nucleus (e.g., n_p^f = 2 protons in $2s_{1/2}$ in $^{33}P^{sf}$ indicates spin-flip) and if there are n_h^f holes in the lower orbit (e.g., n_h^f = 1 proton hole in $1d_{5/2}$ in $^{33}P^{sf}$), then the problem reduces to finding the eigenvectors and eigenvalues of an $n_p^f n_h^f \times n_p^f n_h^f$ matrix.

Although the residual force acting between nucleons is generally attractive, in the particle-hole channel it is usually repulsive, as can be seen by applying the Pandya relations (Schiffer and True 1976, Koonin 1978). Further, as is implicit in the discussion of beta decay in BBAL, this particle-hole repulsion energy is taken as constant in this work, and in particular

$$\langle ab|V_{ph}|\ell m\rangle \simeq \nu_{ph} \tag{11}$$

If the sum on particle-hole pairs (a b) is taken over just the orbits relevant for the spin-flip excitation (e.g., two $2s_{1/2}$ proton particles and one $1d_{5/2}$ proton hole in the $^{33}P^{sf}$ case) and the equation (11) approximation is employed, then equation (9) becomes

$$\left(\varepsilon(2s_{1/2}) - \varepsilon(1d_{5/2}) - E_n\right)\cdot\begin{pmatrix}\psi_1^n\\ \psi_2^n\\ \vdots\end{pmatrix} = \begin{pmatrix}1 & 1\ldots & \\ 1 & 1 & \ddots \\ \vdots & & \ddots\end{pmatrix}\begin{pmatrix}\psi_1^n\\ \psi_2^n\\ \vdots\end{pmatrix} \tag{12}$$

The eigenvalues of an $n_p^f n_h^f \times n_p^f n_h^f$ matrix of 1's are zero and $n_p^f n_h^f$, so that the collective mode eigenstate is the coherent sum of the equally weighted ψ^n(a b)'s

$$|\Psi\rangle_{CGT} = \frac{1}{(n_p n_h)^{\frac{1}{2}}}\sum_{ij} a_i^\dagger a_j \,|\Psi(^{33}P^{gs})\rangle \tag{13}$$

corresponding to the excitation energy eigenvalue

$$E(^{33}P^{sf}) = \varepsilon(2s_{1/2}) - \varepsilon(1d_{5/2}) + n_p^f n_h^f \cdot \nu_{ph} \qquad (14)$$

$$= 7.80 \text{ MeV}.$$

This is similar to the calculation made in BBAL to arrive at the prediction of $\Delta_n = 3$ MeV in the $^{56}Fe \rightarrow {}^{56}Mn$ transition, which agrees very well with the detailed shell model value of 2.7 MeV from Bloom and Fuller (1981). In this work the value of $n_p^f n_h^f \cdot \nu_{ph}$ for each nucleus is approximated as 2.0 MeV (Bertsch 1980) and this agrees with the shell model calculations and experimental data fairly well.

The total Gamow-Teller strength in the collective mode can be estimated from equation (13). In principle, for a collective state which corresponds to an eigenstate of the daughter nucleus, the total Gamow-Teller strength from the ground state of the parent is defined to be,

$$|M_{GT}|^2 = \frac{1}{2J_1 + 1} \sum_{m_{CGT}} \sum_{m_i} \sum_k |\langle \Psi_{CGT}\, m_{CGT} | \sigma_\kappa \tau_\pm | \Psi_i m_i \rangle|^2 \qquad (15)$$

In practice, and as experiment shows, the collective Gamow-Teller state is split among many daughter nucleus eigenstates. In this case, the collective strength is given as an incoherent sum of the strengths from each daughter state. From the expression for the collective Gamow-Teller wave function and from equation (15) it can be shown that the incoherent strength is

$$|M_{GT}|^2 = \sum_{if} \frac{n_p^i \; n_h^f}{2j_f + 1} \; |M_{GT}^{sp}|^2_{if} \qquad (16)$$

where the sum is over initial orbits i, and final orbits f. The number of particles in orbit i is n_p^i, n_h^f is the number of holes in orbit f, and $2j_f + 1$ is the degeneracy of the final orbit. $|M_{GT}^{sp}|^2_{if}$ is the single particle Gamow-Teller matrix element connecting particle state i and

hole state f. $|M_{GT}^{sp}|^2$ for $j_i = \ell \pm \frac{1}{2}$ and $j_f = \ell \pm \frac{1}{2}$ is given by

$$|M_{GT}^{sp}|_{if}^2 = 6(2j_f + 1) \begin{Bmatrix} 1/2 & 1/2 & 1 \\ j_i & j_f & \ell \end{Bmatrix}^2 . \qquad (17)$$

As shown in deShalit and Feshbach (1974), the six-j symbol is easily evaluated to yield the table of $|M_{GT}^{sp}|^2$ shown in Table 1. For instance, the single particle matrix element table gives $|M_{GT}^{sp}|^2 = 12/7$ for $f_{7/2} \rightarrow f_{5/2}$. In general for each particle orbit j_i, there are two possible final hole orbits, corresponding to no-spin-flip (nsf), $j_f = j_i$, and spin-flip (sf), $j_f = j_i \pm 1/2$. The single valence particle orbit case then gives, from equation (16),

$$|M_{GT}|^2 = \frac{n_p n_h^{nsf}}{2j_f^{nsf} + 1} |M_{GT}^{sp}|_{nsf}^2 + \frac{n_p n_h^{sf}}{2j_f^{sf} + 1} |M_{GT}^{sp}|_{sf}^2 \qquad (18)$$

Note that the ratio $n_h/(2j_f+1)$ is the fractional number of holes available in the parent nucleus. For positron emission and electron capture decay, each term in equation (18) is the number of protons in the valence orbit times the fractional number of holes in the neutron orbit, times the characteristic single particle matrix element. In the case of electron emission or positron capture the roles of neutrons and protons are reversed.

An example of the application of the expression in equation (16) is given by the zero-order shell model picture for ^{33}S presented in Figure 1. Consider first $^{33}S(e^-, \nu_e)^{33}P$. There are six valence protons in the $1d_{5/2}$ orbit, and two in the $2s_{1/2}$ orbit. Deeper lying proton orbits need not be considered, as these give zero beta strength;

that is, all corresponding neutron orbits are filled (blocked), the Gamow-Teller operator cannot change principal quantum number, and hence cannot allow particle transitions between major shells. Likewise, the no-spin-flip transition is not allowed for the six $1d_{5/2}$ protons in ^{33}S as there are no neutron holes in $1d_{5/2}$. Since the Gamow-Teller operator cannot change orbital angular momentum, the two protons in $2s_{1/2}$ can only transform into $2s_{1/2}$ neutron holes, of which there are none in ^{33}S. These two protons give zero beta strength. This is an example of neutron blocking, which occurs whenever all final allowed orbits for valence protons are completely filled by neutrons. A similar blocking can occur in electron emission or positron capture when there are no allowed proton-hole slots for valence neutron transitions. In the example of ^{33}S, the only unblocked transition is for $1d_{5/2}$ protons transforming into neutron holes in the $1d_{3/2}$ orbital, a spin-flip transition. The single particle matrix element for $1d_{5/2} \rightarrow 1d_{3/2}$ is $|M_{GT}^{sp}|^2 = 8/5$, so that with $n_p = 6$ and $n_h/2j_f + 1 = 3/4$ one has

$$|M_{GT}|^2 = 6 \cdot 3/4 \cdot 8/5 = 36/5 \qquad (19)$$

which, from equation (I-2a) gives log ft = 2.739. For the reverse transition $^{33}P(e^- \bar{\nu}_e)^{33}S$, the spin-flip decay of six $1d_{5/2}$ neutrons to four $1d_{3/2}$ proton holes contributes, as do two no-spin-flip transitions: two $1d_{3/2}$ neutrons into four $1d_{3/2}$ proton holes, and two $2s_{1/2}$ neutrons in one $2s_{1/2}$ proton hole. Applying equation (16) and equation (I-2a) gives a total $|M_{GT}|^2 = 69/5$ so that log ft = 2.456. This is faster than the log ft = 2.739 for the positron emission, electron capture transitions because ^{33}P is a neutron-rich nucleus and therefore has more unblocked neutron particles than ^{33}S has unblocked proton

particles. In the case of large neutron excess, where both spin-flip and no-spin-flip proton orbits corresponding to the filled or partially filled neutron orbits are empty, then $n_h^f/(2j_f+1) = 1$, and equation (16) reduces to

$$|M_{GT}|^2 = \sum_i n_p^i \{|M_{GT}^{sp}|^2_{isf} + |M_{GT}^{sp}|^2_{insf}\}$$
$$= 3 \cdot |N - Z| \qquad (20)$$

where N - Z is the difference in neutron and proton numbers for the parent nucleus. With the use of the absolute value of N - Z, equation (20) is generalized to the case of unblocked proton orbits for Z > N. This is the expression for $|M_{GT}|^2$ derived by Gapanov and Lyutostanskii (1974). Equation (20) makes good physical sense, since it states that there are |N - Z| completely unblocked nucleons, and since each free nucleon has an unblocked Gamow-Teller matrix element $|M_{GT}|^2 = 3$, the total Gamow-Teller strength is 3 · |N - Z|. Equation (I-11) for the Fermi transition matrix element can be recast, using $T_z^i = (Z - N)/2$ as

$$|M_F|^2 = |N - Z| \qquad (21)$$

and again, since for a free nucleon $|M_F|^2 = 1$, equation (21) is easily interpreted. The total beta strength possessed by a free nucleon remains the same when placed in a nucleus and only blocking can make this strength unavailable.

In comparing to the moment-method shell model calculations done by Bloom and Fuller (1981) the zero-order shell model result of equation (16) does quite well. The moment-method calculations for electron capture in $^{56}Fe \rightarrow {}^{56}Mn$ yields $|M_{GT}|^2 = 9.125$ (log ft = 2.64) for the total beta strength from the 0^+ ground state of ^{56}Fe, and $|M_{GT}|^2 = 9.656$

(log ft = 2.61) from the 2^+ first excited state of ^{56}Fe. The application of equation (16) to the zero-order shell model ground configuration of ^{56}Fe yields $|M_{GT}|^2 = 72/7 = 10.29$ (log ft = 2.58), which agrees well with the moment-method shell model results. In the present paper the strengths for collective state resonances corresponding to the excited states of the parent nucleus are taken to be the same as for the ground state, i.e., the zero-order shell model result, equation (16). This conjecture will be discussed below, but note that it seems to be borne out in the ^{56}Fe results. For ^{60}Fe$\rightarrow$ ^{60}Mn the zero-order shell model and equation (16) predict $|M_{GT}|^2 = 48/7 = 6.86$ (log ft = 2.76), whereas Bloom and Fuller calculate $|M_{GT}|^2 = 7.33$ (log ft = 2.73) from the ground state and $|M_{GT}|^2 = 7.04$ (log ft = 2.75) from the first excited state of ^{60}Fe, and again good agreement obtains. In the case of electron capture in ^{64}Fe $\rightarrow$ ^{64}Mn the Bloom and Fuller result gives $|M_{GT}|^2 = 1.06$ (log ft = 3.57) from the ^{64}Fe ground state and $|M_{GT}|^2 = 1.05$ (log ft = 3.57) from the ^{64}Fe first excited state. The present paper uses the energy and ordering of the shell model orbits for protons and neutrons given by Seeger and Howard (1975). The $1f_{5/2}$ neutron orbit is then taken to lie lower than the $2p_{1/2}$ neutron orbit. Since there are 38 neutrons in ^{64}Fe, in the zero-order shell model employed here, the $1f_{5/2}$ neutron orbit is completely filled, the ^{64}Fe $\rightarrow$ ^{64}Mn transition is blocked, and the application of equation (16) yields $|M_{GT}|^2 = 0$. The Bloom and Fuller strength result is small but not zero, corresponding to the value of a typical Gamow-Teller transition which reflects the mixing of configurations due to the residual nucleon-nucleon interaction. The Bloom and Fuller ^{64}Fe $\rightarrow$ ^{64}Mn strength is about a factor of 10 less than equation (16) would predict were the $2p_{1/2}$ neutron orbit to lie

lower in energy than the $1f_{5/2}$ neutral orbit in the zero-order model employed here, opening neutron holes in the $1f_{5/2}$ shell.

The ^{54}Fe $(^{3}He,t)^{54}Co$ experiment performed and analyzed by Gaarde et al. (1980) also tends to confirm the validity of equation (16). A two-particle shell model calculation of the total weak interaction strength in the $^{54}Fe \rightarrow {}^{54}Co$ transition made by these authors yields $|M_{GT}|^2 = 13.8$ which agrees well with the total weak interaction strength inferred from the $^{54}Fe(^{3}He,t)^{54}Co$ experiment. In a zero-order shell model picture of ^{54}Fe in which the valence fp-shell has 6 protons in the $1f_{7/2}$ proton orbit, and 8 neutrons in $1f_{7/2}$ nuetron orbit equation (16) yields $|M_{GT}|^2 = 114/7 = 16.3$ (note that Gaarde et al. also quote $|M_{GT}|^2 = 16.3$ derived from an expression similar to eq. [20]). The sum rule expression employed in the present paper and given by equation (16) then seems to give good agreement with theoretical and experimental results.

The simple shell model utilized in this work serves to provide a weak interaction sum rule for $T^{<} \rightleftarrows T^{>}$ as outlined above and, in addition, gives a simple interpretation for the location of the $T^{<} \rightarrow T^{>}$ Gamow-Teller resonance. In particular the shell model procedure predicts the daughter nucleus excitation energy of the Gamow-Teller collective state resonance in $T^{<} \rightarrow T^{>}$ in terms of single particle energy differences for spin-flip and an average particle-hole repulsion energy. The accuracy of these predicted excitation energies will be examined below, but first the application of the shell model to the characteristics of the $T^{>} \rightarrow T^{<}$ Gamow-Teller strength distribution must be addressed.

The $T^{>} \rightarrow T^{<}$ and $T^{<} \rightarrow T^{>}$ Gamow-Teller strength distributions differ

markedly, as the experimental data and theoretical results outlined previously indicate. The principal difference between these distributions reflects the fact that in the $T^{>} \rightarrow T^{<}$ transition both $T^{<}$ and $T^{>}$ states in the $T^{<}$-daughter nucleus may be populated by the Gamow-Teller operator. To understand how these differences arise in the context of the simple shell model requires a discussion of the so-called M1-method for determining the resonance excitation energies for both $T^{<} \rightarrow T^{>}$ and $T^{>} \rightarrow T^{<}$ transitions.

Following Klapdor, the M1-method for $T^{>} \rightarrow T^{<}$ nuclear transitions is best explained in terms of a doubly-magic, neutron-rich parent nucleus. A schematic shell model diagram for such a nucleus is shown in Figure 3a. In Figure 3b an excited configuration of this nucleus is shown, wherein a neutron is promoted from a completely filled $j = \ell + \frac{1}{2}$ single particle orbit to the higher-lying $j = \ell - \frac{1}{2}$ orbit. This is the M1 excitation and the configuration in Figure 3b represents the giant M1-configuration. Another such giant M1-configuration could be constructed by promoting a proton in a single particle orbit up to its unfilled spin-orbit partner. Such proton M1-configurations will be discussed below in connection with $T^{<} \rightarrow T^{>}$ transitions of neutron rich nuclei.

Returning to the neutron M1-configuration in the doubly-magic neutron-rich nucleus, note that the excitation energy of this configuration relative to the Figure 3a ground state could be calculated via an expression involving single particle energy differences and a particle-hole repulsion as in equation (12). In this case the excitation would amount to the difference in energy between the filled $j = \ell + \frac{1}{2}$ neutron orbital and its empty $j = \ell - \frac{1}{2}$ spin-orbit partner,

plus the particle-hole repulsion energy and a pairing energy if a neutron pair must be broken in the excitation. Thus, the excitation energy of this neutron M1-configuration can be found in the $T^{>}$-parent nucleus and, furthermore, its isospin must be equal to $T^{>}$.

The neutron M1-configuration in Figure 3b can now be operated on with the isospin raising operator $T_+ = \sum_i \tau_+^i$ (in this work, $\tau_3^n = -\frac{1}{2}$, $\tau_3^p = +\frac{1}{2}$), where the sum on i is over all neutrons. The operator τ_+ acting on a neutron creates a proton in the same orbit with a factor 1; hence acting on the Figure 3b configuration with T_+ creates the $T = T^{>}$ configuration mixture shown in Figure 4a, the coefficients multiplying each component configuration following from the number of neutrons in each orbit with appropriate normalization. (T_o is defined such that $2T_o + 1 = |N - Z|$ for the original $T^{>}$ nucleus shown in Fig. 3). The result shown in Figure 4a is the isobaric analog state (IAS) in the $T^{<}$-daughter corresponding to the neutron M1-excitation in the $T^{>}$-parent. For very neutron-rich nuclei, where T_o is large but with the $j = \ell - 1/2$ orbit empty, the analog of the M1-configuration will clearly consist predominantly of the second of the two configurations shown in Figure 4a.

The anti-isobaric-analog state (AIAS) corresponding to the M1-analog in Figure 4a can be constructed from the same basis configurations by using orthogonality. Interchanging the coefficients and reversing the sign between the configurations in Figure 4a results in the orthogonal AIAS configuration shown in Figure 4b, which must have isospin $T = T^{<}$. Because of the reversal of coefficients, the M1-AIAS will be predominantly the first configuration in Figure 4b for very neutron-rich nuclei.

Note that the first, predominant configuration in the Figure 4b M1-AIAS is just the spin-flip configuration generated from the $T^{>}$-parent ground state configuration, Figure 3a, by transforming a neutron with $j = \ell + 1/2$ into an empty proton orbit with $j = \ell - 1/2$. As discussed in § IIIa, the experimental and theoretical results point to this spin-flip configuration as the carrier of most of the relatively concentrated Gamow-Teller strength. Therefore, for this doubly-magic neutron-rich nucleus, the Gamow-Teller resonance could be expected to lie near the excitation energy of the AIAS of the M1-excitation, since for large T_o the M1-AIAS contains most of the spin-flip configuration.

The excitation energy of the M1-AIAS can be estimated in the following way. The excitation energy of the M1 configuration in the $T^{>}$-parent is calculated as previously discussed. The IAS of this M1-excitation in the $T^{<}$-daughter has an excitation energy which is the energy of the first analog state plus the M1-excitation energy in the $T^{>}$-parent. The M1-AIAS differs from the M1-IAS only in total isospin; other than that both states contain the same configurations. In the absence of an isospin-dependent residual interaction, the M1-IAS and M1-AIAS would be degenerate in energy. In fact, the nucleon-nucleon force in equation (4) contains a $\tau_1 \cdot \tau_2$ term and Lane (1962) has shown that this results in an isospin potential, the Lane potential, which splits otherwise identical states differing in isospin. The form of the Lane potential used here is

$$V = \frac{V_\tau^c (2T_o + 1)}{2A} \simeq \frac{50}{A} |N - Z| \qquad (22)$$

and the M1-AIAS lies lower than the M1-IAS by the value of this potential.

To summarize the proposed method for finding the excitation energy of the Gamow-Teller resonance in the $T^<$-daughter, the $T^>$-parent M1-excitation energy is added to the first-IAS energy in the $T^<$-daughter, yielding the M1-IAS excitation energy, from which is subtracted the Lane potential, to finally yield the excitation energy of the M1-AIAS containing the greater part of the Gamow-Teller strength. As will be made clear in the example below, this is not quite the procedure adopted for $T^> \rightarrow T^<$ transitions in this paper.

The method for computing the parameters of the $T^> \rightarrow T^<$ Gamow-Teller resonance adopted later will, however, require the first analog state excitation energy in the $T^<$ nucleus. The first analog state energy is taken from experiment where available, or else calculated using the parametrized formulae of Fowler and Woosley (1980). For a nucleus with Z_A protons, N_A neutrons, and mass excess ΔM_A, which has an analog state in a nucleus with Z_C protons, N_C neutrons, and mass excess ΔM_C, the expression for the analog state excitation energy E_{IAS} for $N_C \geq Z_C$ and $Z_A = Z_C - 1$, $N_A = N_C + 1$

$$E_{IAS} = \Delta M_A - \Delta M_C - 0.7824 + \frac{1.728(Z_C - 1)}{R} \text{ MeV} \qquad (23)$$

where $(6/5)e^2 = 1.728$ MeV-fermis and the nuclear radius R (for both nuclei) is in fermis. Fowler and Woosley (1980) give $R = 1.12\ A^{1/3} + 0.78$ fermis. This is the customary way to calculate E_{IAS}. However, in some cases ΔM_A is known for a proton-rich nucleus across the Z = N line which can yield the energy of the $T^>$-analog in the $T^<$-nucleus. In this case $N_C \geq Z_C$ and $Z_A = N_C + 1$ so that

$$E_{IAS} = \Delta M_A - \Delta M_C + 0.7824\ (Z_A - Z_C) - 0.864\ \frac{[N_C(N_C + 1) - Z_C(Z_C - 1)]}{R} \text{ MeV} \qquad (24)$$

For $N_C \leq Z_C$ and $Z_A = Z_C + 1$ the result is

$$E_{IAS} = \Delta M_A - \Delta M_C + 0.7824 - \frac{1.728\ Z_C}{R}\ \text{MeV} \qquad (25)$$

and, finally, for $N_C \leq Z_C$ and $Z_A = N_C - 1$ the result is

$$E_{IAS} = \Delta M_A - \Delta M_C - 0.7824\ (Z_C - Z_A) + 0.864\ \frac{[Z_C(Z_C - 1) - (N_C - 1)(N_C - 2)]}{R}\ \text{MeV} \qquad (26)$$

In the application of the M1-method to the neutron-rich nucleus discussed above, it was clear that most of the Gamow-Teller spin-flip configuration was concentrated in the M1-AIAS. For less neutron-rich nuclei, including many of those encountered in this survey, this is not always the case and a significant portion of the spin-flip configuration may be contained in the M1-IAS. The M1-IAS lies at a higher excitation energy than the M1-AIAS and so the question of the splitting of the Gamow-Teller strength between them is an important point to resolve in calculating the stellar rates.

The question of M1-IAS/M1-AIAS Gamow-Teller strength splitting in $T^{>} \rightarrow T^{<}$ transitions is best illuminated with an example, ${}^{33}_{18}Ar_{15} \rightarrow {}^{33}_{17}Cl_{16}$. This is a $T^{>} \rightarrow T^{<}$ transition corresponding to positron emission or electron capture, and has a ground state to ground state nuclear mass difference of 11.107 MeV, so that a considerable number of discrete transitions from the ${}^{33}Ar$ ground state have been measured.

The zero-order shell model ground state for ${}^{33}Ar$ is shown in Figure 5. The proton M1-excitation in ${}^{33}Ar$ can be made by promoting a $1d_{5/2}$ proton up to the partially filled $1d_{3/2}$ proton orbit. If now the usual

M1-method is employed, the M1-IAS in ^{33}Cl can be constructed by operating on the ^{33}Ar proton M1-excitation with T^-. This schematic diagram for the M1-IAS is shown in Figure 6. Note that the first configuration in the M1-IAS state in ^{33}Cl corresponds to the spin-flip configuration which can be made from the ^{33}Ar ground state configuration by transforming a $1d_{5/2}$ proton into a $1d_{3/2}$ neutron. Of course the lower-lying M1-AIAS would consist of a mixture of the same configurations, but with the coefficients interchanged and the relative signs reversed. The $^{33}\text{Ar} \rightarrow {}^{33}\text{Cl}$ reaction is an example of one in which most of the Gamow-Teller spin-flip strength is concentrated closer to the M1-IAS, rather than to the M1-AIAS.

The equation (14) result can be used to estimate the excitation energy of the M1-IAS and M1-AIAS in the following manner. First, the proton M1-excitation in ^{33}Ar would have an excitation energy of

$$E^{M1}(^{33}\text{Ar}) = \mathcal{E}(1d_{3/2}) - \mathcal{E}(1d_{5/2}) + \Delta E_{pair} + \Delta E_{ph}$$

$$= \frac{73.6-57.3}{(33)^{1/3}} + \frac{12}{(33)^{1/2}} + 2.0 = 9.1717 \text{ MeV} \qquad (27)$$

where the difference in the proton single particle energies is taken from the tabulation of Seeger and Howard (1975), the particle hole repulsion energy, $\Delta E_{ph} \equiv n_p n_h \nu_{ph}$, is taken as 2.0 MeV and since a proton pair is broken in the proton M1-excitation energy, a pairing energy of $\Delta E_{pair} = 12/A^{1/2}$ is added (Klapdor 1976). Since the first analog state in ^{33}Cl is known to lie at an excitation energy of 5.544 MeV, the M1-IAS will have an excitation energy in ^{33}Cl of $E^{M1}(^{33}\text{Cl}) = 9.1717 + 5.544 = 14.715$; whereas the M1-AIAS will lie at this excitation energy less the value of the Lane potential in equation (22), or $E^{M1}_{AIAS} =$

$14.715 - \frac{50}{A} |N - Z| = 10.169$ MeV. In the simple zero-order shell model applied here, 75% of the Gamow-Teller spin-flip strength should be carried by the M1-IAS, while the other 25% would be concentrated on the M1-AIAS.

If the usual M1-method were employed, all of the strength would be lumped in a resonance near the M1-AIAS at 10.169 MeV excitation. The application of the equation (16) sum rule to the ground state configuration of ^{33}Ar (Fig. 5) yields $|M_{GT}^{sf}|^2 = 48/5 = 9.6$, $|M_{GT}^{nsf}|^2 = 21/5 = 4.2$ and $|M_{GT}|^2 = 69/5 = 13.8$. Since the Gamow-Teller resonance is believed to be very broad, as discussed in the last section, it would be reasonable to expect a considerable amount of strength below the resonance at 10.169 MeV. In contrast, only $\log(\Sigma\ 1/ft)^{-1} = 4.09$ ($|M_{GT}|^2 = 0.321$) is measured from 0 to 5.446 MeV excitation in ^{33}Cl and only $\log(\Sigma\ 1/ft)^{-1} = 3.49$ ($|M_{GT}|^2 = 1.276$) from 5.675 to 8.969 MeV (Endt and van der Leun 1978, Table 33.21). In other words, approximately 12% of the total sum rule strength is located at excitation energies less than 8.969 MeV. This is inconsistent with the broad Gamow-Teller resonance being located near the M1-AIAS and indicates that the zero-order shell model is correct in predicting the Gamow-Teller strength peak nearer the M1-IAS at 14.715 MeV.

The shell structure in the $^{33}\text{Ar} \rightarrow {}^{33}\text{Cl}$ transition which results in the Gamow-Teller strength being concentrated more on the M1-IAS rather than the M1-AIAS is common to many of the $T^{>} \rightarrow T^{<}$ transitions considered in this survey of weak rates. In light of this fact, the following procedure is adopted here for computing the excitation energy of the Gamow-Teller resonance in all $T^{>} \rightarrow T^{<}$ transitions considered in this work. First, a zero-order shell model diagram is constructed for

the ground state of the $T^{>}$-parent. The appropriate Gamow-Teller spin-flip configuration in the $T^{<}$-daughter is constructed as outlined above. The excitation energy of this spin-flip configuration relative to the $T^{<}$-daughter ground state is reckoned in the usual manner using equation (12), with the addition that in the case of $T^{>} \rightarrow T^{<}$ transitions, the first analog state energy is added. The equation (16) sum rule strength is computed for the $T^{>}$-parent ground state, all discrete state transition strength included in the stellar rate computation is subtracted from the sum rule strength, and the remaining strength is lumped into the Gamow-Teller resonance at the calculated energy.

The procedure for the $^{33}Ar \rightarrow {}^{33}Cl$ transition is illustrative of this process. The Gamow-Teller spin-flip configuration generated from the ^{33}Ar ground state is shown in the first configuration in Figure 6. It differs from the zero-order ^{33}Cl ground state by the excitation of a $1d_{5/2}$ proton to the $1d_{3/2}$ proton orbit and a $2s_{1/2}$ neutron to the $1d_{3/2}$ neutron orbit, by the breaking of a $2s_{1/2}$ neutron pair, and by a particle-hole excitation energy, so that the modified equation (12) result will be

$$E(^{33}Cl^{GT}) = E(^{33}Cl^{sf}) = [\varepsilon(1d_{3/2}) - \varepsilon(1d_{5/2})]_p + [\varepsilon(1d_{3/2}) - \varepsilon(2s_{1/2})]_n + \Delta E_{ph} + \Delta E_{pair} + E_{IAS}$$

$$= \frac{16.3}{(33)^{1/3}} + \frac{4.8}{(33)^{1/3}} + 2.0 + 2.089 + 5.544$$

$$= 16.211 \text{ MeV} \qquad (28)$$

where the Seeger and Howard (1975) single particle energies are used along with the usual formula for the pairing energy, and the first analog state energy, 5.544 MeV, is included.

This is the procedure followed in this paper for all $T^{>} \rightarrow T^{<}$ transitions. Adding in the energy of the first IAS yields an estimated Gamow-Teller excitation energy which may be too high relative to the values given by the M1-method. The experimental evidence in the $^{33}Ar \rightarrow {}^{33}Cl$ transition is that most of the Gamow-Teller strength must lie well beyond 9 MeV, and as shown, the shell model estimate predicts most of the strength near the M1-IAS at 14.7 MeV, and so the F^2N II method is still somewhat high compared to the M1-method but is not in disagreement with the limited experimental data which does not reveal the full sum-rule strength. Additional experiments are needed.

Of course for $T^{>} \rightarrow T^{<}$ transitions in very proton or neutron-rich nuclei, most of the Gamow-Teller spin-flip strength will lie closer to the M1-AIAS state than the M1-IAS state, and the F^2N II procedure will be in greater disagreement with the M1-method. In these cases the F^2N II result will lie higher by the first IAS energy or more accurately, by the Lane potential. From the discussion in the last sections it was clear that the Gamow-Teller strength is expected to lie at excitation energies above the first IAS in the $T^{<}$-daughter.

The $^{90}Zr(p,n)^{90}Nb$ data obtained by Bainum et al. (1980) was discussed above in connection with the behavior of the strength distribution in $T^{>} \rightarrow T^{<}$ transitions. These authors observe a broad $T^{<} = 4$ Gamow-Teller spin-flip peak centered at 8.7 MeV in ^{90}Nb, a few MeV above the first IAS at 5.1 MeV and the $T^{>} = 5$ peak at 13.4 MeV. Several smaller Gamow-Teller non-spin-flip features were reported below the main peaks. The application of the equation (16) sum rule to the ^{90}Zr ground state yields a total Gamow-Teller strength of $|M_{GT}|^2 = 30$, yet Bainum et al. observe only 38% of this strength below

20 MeV excitation. The remainder of the strength lies at very high excitation energy as discussed in Bertsch (1981) and Bohr and Mottelson (1981). The F^2N II $T^> \rightarrow T^<$ resonance procedure would put this strength at 11.85 MeV. The M1-method places 53.3% of this strength at 8.938 MeV and 5.3% at 14.493 MeV. The remainder, the non-spin-flip strength, is spread over a large range in energy. It is clear in this case that both methods of calculation are in error. However, the placing of the full strength at a single resonance energy equal to 11.85 MeV compensates approximately for the observed spread from 8.7 MeV to greater than 20 MeV.

In the very neutron or proton-rich $T^> \rightarrow T^<$ transitions in which the F^2N II procedure places the strength too high, the first IAS in the $T^<$-daughter will lie higher in excitation above the transitions available to the $T^>$-parent states, i.e., E_{IAS} (in $T^<$) $> Q_n(T^> - T^<)$. In such circumstances the placement of the Gamow-Teller resonance in the $T^<$-daughter is not crucial; what is crucial is the strength within the range of the nuclear Q-value, and the F^2N II stellar rate computations attempt to take this strength into account with discrete state transitions with observed or calculated log ft values or with log ft = 5 assumed on average for allowed transitions.

An example of a $T^> \rightarrow T^<$ transition treated in this survey in which discrete state transition strength plays an important role is the positron capture transition $^{26}Mg(T = 1) \rightarrow {}^{26}Al(T = 0)$. Of course positron capture is of little interest in the applications of our results. But this example has experimental strength functions from the $^{26}Mg(p,n)^{26}Al$ reaction studies. The zero-order shell model state for ^{26}Mg consists of a filled $1d_{5/2}$ neutron orbit and two holes in the $1d_{5/2}$ proton orbit, and is shown in Figure 7a. Figure 7b shows the excited spin-flip configuration in daughter ^{26}Al; wherein one of six $1d_{5/2}$ neutrons in ^{26}Mg

has transformed into any of four $1d_{3/2}$ proton holes. The ^{26}Al zero-order ground state configuration is shown in Figure 8 and it is clear that the spin-flip configuration differs from it by the excitation of an unpaired $1d_{5/2}$ proton to the $1d_{3/2}$ orbit. In accordance with the F^2N II resonance procedure for $T^> \rightarrow T^<$ transitions, the excitation energy of the Gamow-Teller resonance in ^{26}Al is calculated as

$$E(^{26}\text{Al}^{GT}) = [\varepsilon(1d_{3/2}) - \varepsilon(1d_{5/2})]_p + \Delta E_{ph} + E_{IAS}$$

$$= \frac{73.6 - 57.3}{(26)^{1/3}} + 2.0 + 0.228 = 7.730 \text{ MeV} \qquad (29)$$

where E_{IAS} = 0.228 MeV is the energy of the first 0^+; 1 state in ^{26}Al. Note that ^{26}Al is relatively atypical in having such a low-lying analog state.

The result obtained above in the F^2N II resonance calculation for $^{26}\text{Mg} \rightarrow {}^{26}\text{Al}$ can be compared with the recent results of the $^{26}\text{Mg(p,n)}^{26}\text{Al}$ charge exchange experiment done by Goodman et al. (1980). Their Gamow-Teller strength distribution consists of three broad peaks. The first of these peaks is resolved into three narrow peaks which correspond to the three discrete $J = 1^+$ states in ^{26}Al at 1.058, 1.851, and 2.072 MeV excitation energy, respectively. The log ft and $|M_{GT}|^2$ for the transitions from the ground state of ^{26}Mg to these three ^{26}Al states can be obtained from isospin symmetry from measurements made in the $^{26}\text{Si} \rightarrow {}^{26}\text{Al}$ system (see discussion on p. 453 of F^2N I). The other broad peaks in the Goodman et al. spectrum occur at 5.0 and 10.6 MeV.

In the stellar rate computations for $^{26}\text{Mg} \rightarrow {}^{26}\text{Al}$ in this work the mirror transitions to the three discrete states are, or course, explicitly included. In accordance with the above procedure, the discrete

strength is summed, subtracted from the equation (16) sum rule, and the remaining strength placed at 7.73 MeV. This resonance then should mock-up the two higher-lying strength peaks in the Goodman et al. spectrum. The rough energy centroid of the strength in these peaks is at about 8 MeV, so the agreement with the F^2N II $T^> \rightarrow T^<$ resonance procedure is good. For $T^> \rightarrow T^<$ transitions in which the energy of the first IAS is larger than in this case, the F^2N II procedure will not give such good agreement, but it is argued here that the discrete state transitions will then determine the stellar rates.

It should be noted that the $T^< \rightarrow T^>$ transitions can also be examined with the M1-method. The procedure is to operate on the spin-flip configuration in the $T^>$-parent with $T^\pm$ to generate its analog in the $T^<$-daughter. T^+ operates on nuclei with $N > Z$ and T^- operates on nuclei with $Z > N$. Orthogonality can be used to generate one or more spin-flip-anti-analog states with $T = T^<$. These anti-analog states will contain most of the M1-excitation configuration. The excitation energy of the M1-excitation and hence the anti-analog states can be estimated by the usual techniques and then the Lane potential can be added to yield the energy of the analog state. Subtraction of the first analog state energy from the estimated spin-flip-analog energy yields an estimate of the excitation of the spin-flip configuration in the $T^>$-daughter. The M1-method for studying $T^< \rightarrow T^>$ transitions is discussed in connection with $(t, {}^3He)$ reactions by Flynn and Garrett (1972). Though complicated, this method confirms and illuminates the $T^< \rightarrow T^>$ resonance procedure adopted in this rate survey.

To illustrate both the M1-method and the F^2N II technique for treating $T^< \rightarrow T^>$ transitions, consider the electron capture reaction

$^{56}Fe \rightarrow {}^{56}Mn$ at high electron Fermi-energies. The zero-order shell model ground states for $^{56}Fe(T = 2)$ and $^{56}Mn(T = 3)$ are shown in Figures 9a and 9b. The ^{56}Mn spin-flip configuration can be constructed from the ^{56}Fe ground state configuration by transforming one of six $1f_{7/2}$ protons into a neutron in the empty $1f_{5/2}$ neutron orbital. This spin-flip configuration is shown in Figure 10.

Turning first to the M1-method, the ^{56}Mn spin-flip configuration can be operated on with T^+ in the usual manner to yield the $T^>$-spin-flip analog state in ^{56}Fe, shown in Figure 11, with the subscript 1 coefficients. Two $T^<$-anti-analog states can now be constructed using orthogonality. (In our example $T^> = 3$, $T^< = 2$). These states, designated $T^<_+$ and $T^<_-$, are shown in Figure 11 with the appropriate coefficients multiplying the $|1\rangle$, $|2\rangle$, and $|3\rangle$ basis configurations. The $T^<_-$ spin-flip anti-analog state contains two-thirds of the proton M1-excitation in ^{56}Fe, the $|1\rangle$ configuration. The excitation energies of the $T^<_+$ and $T^<_-$ states can be estimated in the usual manner by comparing the basis configurations to the ^{56}Fe ground state configuration, applying the modified equation (12) result, and weighting the energy for each basis configuration by the appropriate coefficients in $T^<_-$ or $T^<_+$.

Carrying out this procedure with the Seeger and Howard (1975) single particle energies yields the following excitation energies for the spin-flip anti-analog states:

$$E(T^<_+) = 10.756 \text{ MeV}$$

$$E(T^<_-) = 10.037 \text{ MeV} \qquad (30)$$

The $T^>$ spin-flip analog and the $T^<_+$ anti-analog differ only in total

isospin, since both states consist of the same three basis configurations with coefficients of the same magnitude. As a result, these states are separated by the value of the Lane potential, and thus the excitation of the spin-flip analog is

$$E(T^{>}) = 10.756 + \frac{50 \times 6}{56} = 16.113 \text{ MeV}. \quad (31)$$

Subtracting the excitation energy of the first analog state in ^{56}Fe, 11.440 MeV, gives the energy of the ^{56}Mn spin-flip configuration as

$$E(^{56}Mn^{sf}) = 4.673 \text{ MeV}. \quad (32)$$

The technique adopted in this paper for computing the parameters of the Gamow-Teller resonance for $T^{<} \rightarrow T^{>}$ transitions can now be applied to the $^{56}Fe \rightarrow ^{56}Mn$ reaction. In the F^2N II technique, as previously outlined, the spin-flip configuration in the $T^{>}$-daughter is constructed and its excitation energy relative to the $T^{>}$-daughter ground state is estimated as in equation (12). The ^{56}Mn spin-flip configuration in Figure 10 differs from the ^{56}Mn ground state, Figure 9b, by the excitation of a $2p_{3/2}$ neutron to the $1f_{5/2}$ neutron orbit, with no nucleon pair broken, so that

$$E(^{56}Mn^{sf}) = [\varepsilon(1f_{5/2}) - \varepsilon(2p_{3/2})]_n + \Delta E_{ph} = 3.777 \text{ MeV} \quad (33)$$

where the Seeger and Howard (1980) single particle energies have been used. The F^2N II spin-flip mode excitation energy differs from the M1-method result by about 0.9 MeV.

Part of this discrepancy results from the necessity of adding the Lane potential to the excitation energy of $T_+^{<}$ state in the M1-method. The $T^{>}$ spin-flip analog configuration cannot be directly compared with the ^{56}Fe ground state in estimating an excitation energy since these

states differ in total isospin. The Lane potential is parametrized by the strength of the V_τ^c component of the residual interaction, which varies from nucleus to nucleus. On the other hand, some of the discrepancy between the M1-method and the F^2N II technique is a result of using the Seeger and Howard (1975) single particle energies which differ for protons and neutrons. To see the effect of this the calculations can be repeated with the Nilsson single particle energies (cf. Hillman and Grover 1969, Table I) which are the same for protons and neutrons. Repeating first the F^2N II technique in equation (33) yields

$$E(^{56}Mn^{sf}) = 2.810 \text{ MeV} \tag{34}$$

for the spin-flip mode excitation in ^{56}Mn.

The arguments of the M1-method leading to equation (30) can be repeated with the Nilsson single particle energies. In this case the $T_+^<$ and $T_-^<$ spin-flip anti-analog states are found to be degenerate in energy, with

$$E(T_+^<) = E(T_-^<) = 7.876 \text{ MeV}. \tag{35}$$

Adding the Lane potential and then subtracting the first analog state energy yields an estimate of the ^{56}Mn spin-flip excitation energy of

$$E(^{56}Mn^{sf}) = 7.876 + \frac{50 \times 6}{56} - 11.440 = 1.793 \text{ MeV}. \tag{36}$$

The results in equations (34) and (36) should, in principle, agree. That they do not reflects the use of a particular value of the Lane potential. If the Lane potential parameter were chosen as $V_\tau^c/2 = 60$, which is common in many works (Klapdor 1976), then the M1-method employed in equation (36) would give an estimated ^{56}Mn spin-flip mode excitation energy of 2.865 MeV, in good agreement with the F^2N II

result (2.810 MeV) employing the Nilsson energies.

There is an alternative approach to the M1-method for the $^{56}Fe \rightarrow {}^{56}Mn$ transition. The proton $1f_{7/2} \rightarrow 1f_{5/2}$ and neutron $1f_{7/2} \rightarrow 1f_{5/2}$ M1-excitations can be constructed and the resulting configurations can be combined to yield a $T^{<}$ (T = 2) M1-state in ^{56}Fe, whose excitation energy can be estimated in the standard manner. For reasons of simplicity we neglect the M1-excitation of the $2p_{3/2}$-neutrons in ^{56}Fe to the $2p_{1/2}$ state. A $T^{>}$ (T = 3) state can be constructed from the M1 basis states using orthogonality. The excitation energy of this state will be the $T^{<}$ M1-state energy plus the Lane potential. Operating on the $T^{>}$ M1-state with T^{+} yields the T = 3 spin-flip configuration in ^{56}Mn, with excitation energy equal to the difference in energies of the $T^{>}$ M1-state and the first analog state in ^{56}Fe. For the proper choice of the Lane potential parameter this method yields an estimate of the ^{56}Mn spin-flip excitation energy in good agreement with the F^2N II result using the Nilsson energies (eq. [34]).

As discussed previously, the Bloom and Fuller (1981) shell model calculation of the electron capture β-strength distribution for $^{56}Fe \rightarrow {}^{56}Mn$ yields a fairly broad distribution with a centroid at 2.7 MeV, which again is in reasonable agreement with the F^2N II calculation. The resonance energies for the electron capture transitions from the ground state of ^{60}Fe is calculated as 2.0 MeV in ^{60}Mn with the F^2N II technique. The Bloom and Fuller results for Gamow-Teller strength centroid in ^{60}Mn for this transition is 1.5 MeV and again agrees well with the F^2N II results.

In $T^{<} \rightarrow T^{>}$ transitions in which several spin-flip transitions are possible the above procedure is carried out for each spin-flip and

several resonances may be placed in the $T^{>}$-daughter. In contrast, for $T^{>} \rightarrow T^{<}$ transitions in which several spin-flip transitions are possible the resulting resonance excitation energies are averaged and the total sum rule strength lumped in a single resonance at this average excitation energy. This procedure is justified for $T^{>} \rightarrow T^{<}$ transitions because a $T^{>}$-nucleus, which is neutron-rich enough to have several possible spin-flip transitions, will have Gamow-Teller resonances at high excitation energy in the $T^{<}$-daughter.

Finally, a few nuclear transitions in this work have possible back-spin-flip transitions, for example, $1d_{3/2} \rightarrow 1d_{5/2}$ in $^{30}Al(e^{-}\bar{\nu}_{e})^{30}Si$. This Gamow-Teller transition strength is expected to lie at low excitation energy (Klapdor 1976) and thus, as for the no-spin-flip transitions, the discrete state transitions should include most of this strength.

At this point a summary of the Gamow-Teller resonance procedure employed in this work is in order. Typically, some twenty discrete nuclear levels are employed in the calculation for both $T^{<}$ and $T^{>}$ nuclei. Gamow-Teller matrix elements for these $T^{>} \rightleftarrows T^{<}$ discrete state transitions are assigned as in $F^{2}N$ I. A zero-order shell model diagram is constructed for both $T^{<}$ and $T^{>}$ ground states, and equation (16) is employed to give the total Gamow-Teller strength for the $T^{<} \rightarrow T^{>}$ and $T^{>} \rightarrow T^{<}$ transitions. The discrete state transition strength from the ground state of the $T^{<}(T^{>})$-parent to all states of the $T^{>}(T^{<})$-daughter is summed and subtracted from the sum rule result. This remaining Gamow-Teller strength is placed in a collective resonance in the $T^{>}(T^{<})$-daughter which connects to the $T^{<}(T^{>})$-parent ground state. The excitation energy of this resonance is chosen to be the excitation energy of

the spin-flip mode in the $T^{>}(T^{<})$-daughter. The spin-flip mode excitation energy is calculated by the techniques discussed above, differing for $T^{<} \rightarrow T^{>}$ and $T^{>} \rightarrow T^{<}$ transitions.

V. RESONANCE TRANSITIONS FOR EXCITED STATES

The previous discussion reviews the calculations used in this work to estimate Fermi and Gamow-Teller sum rules and resonance excitation energies for transitions from the ground states of the $T^{<}$ and $T^{>}$ nuclei. The rate calculations described in this paper use only these ground-state resonance transitions; resonances corresponding to all of the excited discrete states included in both $T^{<}$ and $T^{>}$ nuclei are taken into account here through the use of a special occupation index for ground-state $\rightleftarrows$ resonance-state transitions. The mathematical manipulations involved in the use of this special occupation index are based on reasonable assumptions about nuclear shell structure.

The basic $T^{<} \rightleftarrows T^{>}$ rate calculation problem is depicted in Figure 12. $E^{<}$ and $E^{>}$ denote the discrete states in the $T^{<}$ and $T^{>}$ nuclei respectively. These symbols will also be used to designate the energy of these states. These discrete states represent those states included in the rate calculation where excitation energies, spins and parities are taken from experimental tabultaions. $R^{>}$ designates Gamow-Teller resonances for each of the $E^{<}$ states, while the $R^{<}$ resonances correspond to the $E^{>}$ discrete states. In the $T^{<} \rightarrow T^{>}$ transition, the $R^{<} \rightarrow E^{>}$ transitions contribute to the stellar rates through the thermal population of the $R^{<}$ collective states. Likewise, in the reverse $T^{>} \rightarrow T^{<}$ transition, the $R^{>} \rightarrow E^{<}$ transitions contribute through the thermal population of the $R^{>}$ collective states. It will be clear that

the $T^{<} \rightarrow T^{>}$ and the $T^{>} \rightarrow T^{<}$ transitions are symmetrical. In what follows the $T^{<} \rightarrow T^{>}$ transitions are discussed in detail. Generalization to $T^{>} \rightarrow T^{<}$ will be obvious.

The resonance problem is simplified by making two assumptions. First, it is assumed here that on the average each $E^{<}$ and $E^{>}$ discrete state has a similar number of valence particles and holes in the same single particle orbits as does the assigned shell model ground state configuration. In this case, from equation (16) for the Gamow-Teller sum rule, all $E^{<} \rightarrow R^{>}$ transitions have equal strengths and all $R^{<} \rightarrow E^{>}$ transitions have equal strengths. The second assumption made here is that the excitation energies of the $R^{<}(R^{>})$ resonances scale just as do their corresponding $E^{>}(E^{<})$ discrete states; for example, if the ground state and first excited state in the $T^{<}$-nucleus differ by 0.847 MeV as in ^{56}Fe, then the first two $R^{>}$ resonances in the $T^{>}$-nucleus, ^{56}Mn in this example, differ in excitation energy by 0.847 MeV. In other words, each $E^{<} \rightarrow R^{>}$ transitions has the same Q-value as does the ground-state $\rightarrow$ resonance transition.

Similarly each $R^{<} \rightarrow E^{>}$ transition has the same Q-value as does the resonance $\rightarrow$ ground state transition. Of course, the residual interaction will produce considerable configuration mixing and these assumptions of constant sum rule and transition Q-value will be only approximately valid. It is argued here, however, that the approximate validity of these assumptions will serve to simulate the effect of excited-discrete-state $\rightleftarrows$ collective-resonance transitions on the stellar rates.

How valid are these assumptions? Weak rates are available only for a few excited states of nuclei (isomers) and therefore comparison

to theoretical shell model calculations must be made for most excited states. The Bloom and Fuller (1981) moment calculations give a strength function centroid of 2.8 MeV and sum rule of $|M_{GT}|^2 = 9.04$ for the ^{56}Fe(ground state) → ^{56}Mn transition. For ^{56}Fe(first-excited-state) → ^{56}Mn transition, those authors calculate a strength centroid of 4.3 MeV and a sum rule of $|M_{GT}|^2 = 9.25$. The agreement of the ground state data with the F^2N II resonance procedure is discussed above, but note that since the first excited state of ^{56}Fe($J^\pi = 2^+$) lies at an excitation energy of 0.847 MeV, the F^2N II scaling assumption would put the corresponding Gamow-Teller resonance at 3.777 + 0.847 = 4.624 MeV in ^{56}Mn with $|M_{GT}|^2 = 72/7 = 10.29$. This is in good agreement with the shell model calculation results. In general, the differences in the shell model structure for each wave function will tend to average out for at least the important low-lying discrete states of the $T^<$ and $T^>$ nuclei, with the result that the Q-value and sum rule strength scaling procedure used here will allow excited-discrete-state ⇄ resonance-state transitions to be taken into account with a special treatment of the occupation index for ground-state ⇄ resonance transitions.

Consider first the $E^< \rightarrow R^>$ transitions; the transitions, $R^< \rightarrow E^>$, which proceed through the thermal population of the states collectively treated as a single resonance state are slightly more complicated and will be discussed later. As illustrated in Figure 12 the discrete states in the $T^<$-nucleus are designated by $E_i^<$ where i = 1, 2. . . while the discrete states in the $T^>$-nucleus are designated by $E_j^>$ where j = 1, 2. . . . Since there is a one-to-one correspondence between the resonance, in the $T^<$-nucleus and the $E^>$ states, these resonances

are designated by $R_j^<$ and similarly the resonances in the $T^>$-nucleus are designated by $R_i^>$.

From equations (I-7) and (I-8) the overall transition rate from $T^<$-nucleus is

$$\lambda^< = \sum_i P_i^< \sum_j \lambda_{ij}^< \tag{37}$$

where the occupation index, $P_i^<$, is defined by

$$P_i^< = G_i^</G^< = (2J_i^< + 1)\ \exp(-E_i^</kT)/G^< \tag{38}$$

and the partition function for the $T^<$-nucleus is given by

$$G^< = \Sigma G_i^< = \sum_i (2J_i^< + 1)\ \exp(-E_i^</kT). \tag{39}$$

For the $E^< \rightarrow R^>$ contribution to $\lambda^<$ it is clear that

$$\sum_j \lambda_{ij}^< = \lambda_{ii}^< \tag{40}$$

If this contribution is designated by λ_{ER} it follows that

$$\lambda_{ER}^< = \sum_i P_i^< \lambda_{ii}^< \tag{41}$$

which is completely general. If it is assumed, in addition, that all of the $\lambda_{ii}^<$ are identical as discussed previously and are equal, say, to $\lambda_{er}^<$ as calculated from the Gamow-Teller matrix elements then

$$\lambda_{ER}^< = \lambda_{er}^< \sum_i P_i^< \tag{42}$$

But

$$\sum_i P_i^< = 1 \tag{43}$$

so that

$$\lambda^{<}_{ER} = \lambda^{<}_{er} \quad . \tag{44}$$

In other words the contribution of the $E^{<} \rightarrow R^{>}$ transitions to the total $T^{<} \rightarrow T^{>}$ transition rate can be calculated by including only the $E^{<}_{1} \rightarrow R^{>}_{1}$ transition and setting the occupation index for the $E^{<}_{1}$ state in this transition equal to unity. The two basic assumptions made in reaching this conclusion were discussed at the beginning of this section. It will be immediately obvious that the errors arising from the use of a finite number of discrete states are magnified by this procedure especially at high temperature. Another source of error in the calculations discussed here is the inclusion of the $R^{<}$ collective states in the calculation of $G^{<}$. At low temperatures the small Boltzmann factors for high lying states make these errors negligible; whereas, at high temperatures (especially $T_9 = 100$), where the errors in the calculation of G may be considerable, the stellar rates are dominated by the resonance transitions and do not depend sensitively on G.

Consider next the $R^{<} \rightarrow E^{>}$ contribution to the transition rate which will be designated by $\lambda^{<}_{RE}$. In these transitions only the $R^{<}_{j}$ resonances in the $T^{<}$-nucleus take part and

$$\sum_{i} \lambda^{<}_{ij} = \lambda^{<}_{jj} \tag{45}$$

so that

$$\lambda^{<}_{RE} = \sum_{j} P^{<}_{j} \lambda^{<}_{jj} \quad . \tag{46}$$

If it is now assumed that all the $\lambda^{<}_{jj}$ are identical and equal, say, to $\lambda^{<}_{re}$ then

$$\lambda^{<}_{RE} = \lambda^{<}_{re} \sum_j P^{<}_j \quad . \tag{47}$$

The calculation of the sum over j is now somewhat more subtle than in equations (42) and (43). The $P^{<}_j$ are given by

$$P^{<}_j = (2J^{<}_j + 1)\ \exp(-R^{<}_j/kT)/G^{<} \quad . \tag{48}$$

The complications involved in the multiplicity in spins (≤ 3) and the corresponding statistical weight factors for $R^{<}_j$ resonances associated with each $E^{>}_j$ state can be treated simply by replacing $J^{<}_j$ in equation (48) with $J^{>}_j$. In addition

$$R^{<}_j = R^{<}_1 + E^{>}_j - E^{>}_1 \quad . \tag{49}$$

One is free to set $E^{>}_1 = 0$ and thus

$$P^{<}_j = (2J^{>}_j + 1)\ \exp(-E^{>}_j/kT)\ \exp(-R^{<}_1/kT)/G^{<} \tag{50}$$

which in turn yields

$$\sum_j P^{<}_j = \frac{\exp(-R^{<}_1/kT)}{G^{<}} \sum_j (2J^{>}_j + 1)\ \exp(-E^{>}_j/kT) \quad . \tag{51}$$

The sum over j will be recognized as $G^{>}$ and thus finally

$$\sum_j P^{<}_j = (G^{>}/G^{<})\ \exp(-R^{<}_1/kT) \tag{52}$$

and

$$\lambda^{<}_{RE} = \lambda^{<}_{re}\ (G^{>}/G^{<})\ \exp(-R^{<}_1/kT) \quad . \tag{53}$$

In other words the contribution of the $R^{<} \rightarrow E^{>}$ transitions to the total $T^{<} \rightarrow T^{>}$ transition rate can be calculated by including only the rate for the $R_1^{<} \rightarrow E_1^{>}$ transition and setting the occupation index for the $R_1^{<}$ resonance equal to the ratio of the partition function for the $T^{>}$-nucleus to that for the $T^{<}$-nucleus multiplied by the Boltzmann factor for the first resonance in the $T^{<}$-nucleus.

Throughout this paper we have referred to ground states whereas the simple shell model gives a lower configuration which yields in general a number of degenerate ground states. This point is particularly relevant to the choice of $G^{>}$ and $G^{<}$ in equation (53). In principle these G's should be calculated by summing over the states arising from the appropriate configurations. This was not done. In the spirit of using experimental information as much as possible, the G's in equation (53) were calculated using spins and energies of known states. Since the ratio of $G^{>}/G^{<}$ occurs in equation (53) the error arising from this procedure is well within the other uncertainties involved.

These occupation index manipulations allow the effect of all the resonances to be taken into account by calculating only the ground-state to resonance transition rate as a representative average value. At very high temperatures where the F^2N II partition function calculation breaks down, the stellar rates will be almost completely dominated by these resonance transtions. It is argued here that the F^2N II occupation index manipulations allow reasonable estimates of the stellar rates even at very high temperature, since the expressions for the occupation indices for the resonances involve only ratios of partition functions and, hence, errors in the partition functions will tend to

cancel. There remains the question whether the matrix elements calculated for transitions involving the lowest shell model configurations are representative for high excitations. In electron capture, for example, neutron shell blocking will not be effective and matrix elements will increase but not by unreasonable factors except perhaps at $T_9 = 100$ where uncertainties of the order of a factor of two from this and other causes must be admitted.

In generalizing to $T^> \rightarrow T^<$ transitions the counterpart of equation (44) will be an identical statement equating the total rate to that for the ground state → resonance rate. The counterpart of equation (53) will contain $(G^</G^>)\ \exp(-R_1^>/kT)$.

To each discrete state in a $T^>$-nucleus there corresponds a $T^>$ analog state in the $T^<$-nucleus. The discrete state ⇄ analog state Fermi transitions precisely obey the Q-value scaling and constancy of the sum rules which were approximations for the Gamow-Teller transitions. Again, the deep similarity between the behavior of the Fermi and Gamow-Teller analog resonances becomes apparent. It would be desirable not to have to include in the stellar rate computations an analog state for every $T^>$ discrete state, and yet still include their effect. The occupation index, partition function manipulations proceed exactly as before and the analog states are handled just like the Gamow-Teller resonances. The ground-state → first-isobaric-analog-state transition is given an occupation index equal to unity, whereas the thermally populated isobaric analog state in the $T^<$-nucleus which transforms to the $T^>$-nucleus ground state is given an occupation index equal to $(G^>/G^<)\ \exp(-A_1^</kT)$ where the G's are the respective nuclear partition functions and $A_1^< \equiv E_{IAS}$ is the excitation energy of the first isobaric analog state in the $T^<$ nucleus. We show $A_1^<$, $A_2^<$, $A_3^<$ ... $A_j^<$ in

Figure 12. The individual transition rates corresponding to the $\lambda_{er}^{<}$ and the $\lambda_{er}^{>}$ will be equal and can be calculated from the appropriate Fermi matrix element.

VI. DISCUSSION OF THE STELLAR RATES

The salient point of the F^2N I discussion of stellar weak rates was the close reliance of the calculations on experimental nuclear data. In this paper the weak rate calculations have been extended to include 226 nuclei up to mass 60 and free protons and neutrons; further, these calculations have been performed on an extended temperature and density grid. The larger variety of nuclei and the considerably more extreme stellar conditions involved in the rate calculations of this paper require a far better coverage of the weak interaction strength distribution than in the F^2N I calculations. In this work the validity of the rate calculations relies on the experimental discrete states to reproduce the detailed, relatively low excitation strength, and on at most a few Fermi and Gamow-Teller resonances to yield the high excitation energy strength function characteristics so important to the regime of extreme temperatures and density. The last section discussed the nuclear physics underlying the Fermi and Gamow-Teller strength distribution in intermediate mass nuclei and on calculations of the Fermi and Gamow-Teller resonance excitation energies and strengths used in the rate calculations presented here. The sensitivity of the stellar weak rates to the parameters of the resonance procedure presented in the last section must be tested, much as the discrete-state transition matrix element assignment procedure introduced in F^2N I was tested in § III of that paper. It will be seen that the resonance procedure used in these rate calculations is adequate in most cases to assure accurate rates in extreme conditions. The central

point of this paper is that the calculated stellar rates should be valid at the lower temperatures and densities characteristic of hydrostatic stellar evolution because of the discrete state transitions, while at the more extreme conditions the Gamow-Teller resonances and Fermi analog transitions should adequately determine the rates.

a) The Temperature and Density Grid

The temperature and density grid on which the rate calculations were performed consists of 143 points: for each of the temperatures (T_9 = 0.01, 0.1, 0.2, 0.4, 0.7, 1.0, 1.5, 2.0, 3.0, 5.0, 10.0, 30.0, 100.0) the rates are computed at the densities $\log(\rho/\mu_e)$ = 1.0, 2.0, 3.0, 4.0, 5.0, 6.0, 7.0, 8.0, 9.0, 10.0, 11.0; where the notation follows F^2N I. Note that this grid covers conditions from electron non-degeneracy up to electron Fermi energies near 25 MeV. Neutrino trapping and hence neutrino blocking of electron capture is expected to set in for densities in excess of 10^{11} g cm^{-3} (Arnett 1977), while many nuclei in nuclear statistical equilibrium at these conditions will have allowed electron capture blocked. This means electron capture on heavy nuclei at densities above $\rho = 10^{11}$ g cm^{-3} may not be very important. Future calculations to extend the present work to nuclear masses in the A = 61 to A = 70 range will be done on a grid of temperatures and densities which includes $\rho = 10^{12}$ g cm^{-3}.

The temperature-density grid used in this work should be adequate to cover most of the conditions of interest in stellar evolution. The rate tables available on magnetic tape and printed in abbreviated form in F^2N III are suitable for interpolation between temperature-density points. The interpolation error in the detailed grid is probably

comparable to the systematic errors due to the approximate nuclear physics in the rate calculations. Note, however, that in this calculation screening effects are neglected (cf. F^2N I, p. 451 for a discussion of the effects of screening). Continuum electron capture is included in the calculation but bound state electron capture is not. A discussion of this point and a table of terrestrial bound state electron capture rates for the nuclei considered here are presented in F^2N III. That table also includes all known terrestrial weak decay rates for the nuclei included in this survey.

At the lower temperatures and densities characteristic of the hydrostatic phases of stellar evolution, the discrete state transitions dominate the stellar electron-capture rates, but as the electron Fermi energy rises above 5 MeV ($\rho/\mu_e \gtrsim 10^9$ g cm^{-3}) or when the temperatures approach $T_9 = 10$ ($kT \sim 1$ MeV), the dominant transitions involve the Gamow-Teller and Fermi resonances. To illustrate this point, consider the electron capture rate of $^{26}Al(e^-,\nu_e)^{26}Mg$. The F^2N I and F^2N II calculations contain the same discrete state information and the same Fermi transitions, but the F^2N II calculations also have Gamow-Teller resonances whose excitation energies and strengths are calculated with the procedure set down in Part IV of this paper. The $^{26}Al(e^-, \nu_e)^{26}Mg$ rate is $\log \varepsilon^- = -3.123$ at $T_9 = 1.0$, $\log (\rho/\mu_e) = 7$ in the F^2N I calculation, while at the same temperature and density the F^2N II result is $\log \varepsilon^- = -3.119$. Clearly, in these typical carbon/oxygen burning conditions the Fermi and discrete state transitions are dominating the rate. For $T_9 = 0.01$ and $\log(\rho/\mu_e) = 9.0$, the electron Fermi energy is, using equation (I-4c), $U_F \simeq 5.0$ MeV, and so electrons do not have quite enough energy to reach the Gamow-Teller resonance in

^{26}Mg at 11.408 MeV excitation which requires an electron energy equal to 11.408 - 4.004 = 7.404 MeV; consequently, the rates are again similar, with log ε^- = 0.271 for F^2N I and log ε^- = 0.282 for F^2N II.

The added effect of the Gamow-Teller resonance can be seen in the electron capture rate $^{56}Co(e^-,\nu_e)^{56}Fe$. The Gamow-Teller resonance lies at 5.380 MeV excitation in ^{56}Fe, while the Q_n for the reaction is -4.056, so that an electron inducing the ^{56}Co(ground state) → ^{56}Fe(resonance state) transition must have total energy equal to at least 5.380 - 4.056 = 1.324 MeV. At T_9 = 0.01 and $\log(\rho/\mu_e)$ = 7.0 the total electron Fermi energy is 1.222 MeV, clearly not high enough to reach the resonance and thus the F^2N II electron capture rate (log ε^- = -4.545) should be dominated by the discrete state transitions. At the same temperature and $\log(\rho/\mu_e)$ = 8.0 the total electron Fermi energy is 2.447 MeV and the Gamow-Teller resonance in ^{56}Fe can be reached. The ^{56}Co(ground state) → ^{56}Fe(resonance state) contribution to the overall electron capture rate can be computed setting the occupation index of the ground state equal to unity and employing the equation (I-3b) phase space factor result for a degenerate electron gas to yield log ε^-(ground state → resonance) = -0.585. The F^2N II calculation yields log ε^- = -0.540 for the overall ^{56}Co electron capture rate, and thus the resonance is beginning to dominate the overall transition rate at this density. At T_9 = 0.01 and $\log(\rho/\mu_e)$ = 11 the total electron Fermi energy is 23.930 MeV and the resonance transition can be expected to completely dominate the rate. Applying the equation (I-3b) result yields log ε^-(ground state → resonance) = 5.168, while the full F^2N II computation gives log ε^- = 5.194 for the overall electron capture rate and thus, indeed, the resonance transition dominates.

Where the resonances dominate, they make substantive differences in the stellar weak rates. The above example is an indication of how much faster the neutronization rate during stellar collapse/silicon burning can be due to low-lying Gamow-Teller resonances, as first pointed out by BBAL. On the other hand, blocked nuclei at these extreme conditions have stellar weak rates characterized only by discrete state Gamow-Teller and Fermi transitions, the lack of resonance transitions implying a relatively less drastic increase in the rates as the temperature and density increase. Unblocking by configuration mixing, thermal excitation and forbidden transitions is discussed by Fuller (1981).

In conclusion, it is clear that the nuclear physics which dominates the rate calculations meshes well with the two regimes of stellar conditions represented in the temperature-density grid used here. At the lower temperatures and densities characteristic of the hydrostatic phases of stellar evolution, very accurate stellar weak rates may be required to determine the nucleosynthesis of nuclear species, the overall neutrino energy loss rates which may affect the temperature, and the detailed lepton/baryon ratio which becomes very important going into stellar collapse. In these conditions the F^2N II rates are dominated by discrete state Gamow-Teller and Fermi transitions which, as pointed out above, are heavily reliant on the best experimental nuclear information available and so serve accurately to determine the stellar rates. In the extreme conditions encountered in the later phases of silicon burning, and on into the collapse phase, overall neutronization rates and neutrino production rates become the most interesting quantities. What is needed there are reliable estimates of the stellar rates based on the total amount of Gamow-Teller strength and how much of it

can be reached in a given nucleus at a given temperature and density. The Gamow-Teller resonance procedure is designed to do this by approximating the high-lying Gamow-Teller strength as one or two narrow resonances.

b) Tests of the Gamow-Teller Resonance Procedure

In principle, of course, the most accurate stellar weak rate calculations require a complete and detailed Gamow-Teller strength distribution in the daughter nucleus for each parent nucleus discrete state. Section III of this paper discussed the underlying nuclear physics of the Gamow-Teller strength distribution as well as how the problem is handled in this calculation. In brief, as many discrete states are included in each nucleus as possible in order to outline accurately the Gamow-Teller distribution out to the excitation energy of the last discrete state. The discrete state strength is summed and subtracted from the zero-order shell model sum rule result, the remaining strength is typically lumped in a discrete Gamow-Teller resonance state at an excitation energy calculated in accordance with the procedure discussed in § III. At higher nuclear excitation energy the state density is very large and as a result the Gamow-Teller strength distribution is nearly continuous. How much error is being made in these rate computations by approximating what is known experimentally to be a broad strength distribution by one or two narrow resonances?

Specifically, there are two major worries regarding this resonance procedure. The first is just how sensitive the rates are to the placement of the strength-distribution centroid and to the total strength, the second involves possible threshold effects. A single narrow

resonance would not contribute to, say, an electron capture reaction until the electron Fermi energy was sufficient to exceed the Q-value. The danger is that the stellar rates might show an unphysical jump just as the electron Fermi energy reaches the resonance Q-value. This latter problem is expected to be ameliorated by three effects. First, discrete state transitions serve to broaden the Gamow-Teller strength distribution, as outlined above. Second, the high temperatures encountered in the typical stellar conditions where Gamow-Teller resonances are important serve to thermally populate many parent states, coupling into the calculation many more decay channels than just the resonance transitions and, thus, helping to effectively smear out any resonance threshold effects. Finally, and most important, these high temperatures smear out the electron Fermi-Dirac distribution function, increasing the length of the high energy exponential tail. Thus some electrons will be energetic enough to reach the Gamow-Teller resonance even though the electron Fermi energy has not reached the resonance Q-value, serving to wash out a threshold effect.

To test the sensitivity of the stellar rates to the resonance procedure, the $^{56}Fe(e^-,\nu_e)^{56}Mn$ reaction was examined in some detail. This reaction is particularly appropriate to test, not only because the nuclear physics underlying its resonance calculation was discussed at length above, but because it is fairly representative of important neutronization reactions in silicon burning, where the Gamow-Teller resonances are becoming important. Briefly, in § III of this paper the resonance calculations for the $^{56}Fe(e^-,\nu_e)^{56}Mn$ decay were discussed with the result that the excitation energy of the Gamow-Teller resonance in ^{56}Mn was found to be at 3.777 MeV with a total strength of

$|M_{GT}|^2 = 10.296$ (log ft = 2.58). The Fermi and Gamow-Teller resonances in ^{56}Fe corresponding to the ground state of ^{56}Mn were calculated to be at 11.440 MeV and 24.719 MeV excitation respectively and thus are not very important in the overall continuum electron capture reaction at low temperature because they are not populated. The reaction rate calculated by this standard technique is shown as a function of temperature for various densities in Figure 13a.

The calculations of Bloom and Fuller (1981) give a detailed strength distribution for the ^{56}Fe (ground state) → ^{56}Mn transition. For purposes of testing, this detailed strength distribution is approximated as four discrete resonances whose excitation energies and strengths are reproduced in Table 2. Note that the total strength in the 4-resonance approximation is $|M_{GT}|^2 = 9.036$ (log ft = 2.64), or 13% less strength than the F^2N II result. The $^{56}Fe(e^-,\nu_e)^{56}Mn$ reaction rate in the 4-resonance approximation was calculated on the standard temperature-density grid and is shown as a function of temperature for various densities in Figure 13b.

A detailed comparison of the ^{56}Fe → ^{56}Mn rates calculated with the single resonance F^2N II method and with the 4-resonance approximation to the Bloom and Fuller strength function serves to illustrate the accuracy of the F^2N II calculations. First, the total electron-emission rate for ^{56}Mn → ^{56}Fe at very high temperature, $T_9 = 100$, differs in the two calculations by just 13%, reflecting the uniform thermal population of the Gamow-Teller resonances in ^{56}Mn and the 13% difference in total strength in the calculations.

The ground state to ground state nuclear mass difference for ^{56}Fe → ^{56}Mn is -4.206 MeV. In the F^2N II calculation, then, the resonance Q-value

is Q_R = 3.777 + 4.206 = 7.983 MeV. That is, the total electron Fermi energy must approach the value of Q_R before electron capture proceeds predominantly through the Gamow-Teller resonance. At $\log(\rho/\mu_e)$ = 9.0 the total electron Fermi energy is 5.182 MeV, while for $\log(\rho/\mu_e)$ = 10 it is 11.119 MeV and so the F^2N II Q_R is reached somewhere between these densities. Similarly, in the 4-resonance calculation the resonance Q_R's are 5.706 MeV, 6.706 MeV, 8.006 MeV, and 9.106 MeV, respectively, and the total electron Fermi energy exceeds all these energies in the range $9.0 < \log(\rho/\mu_e) < 10$. In comparing Figure 13a with Figure 13b it is seen that the rates are identical at $\log(\rho/\mu_e)$ = 9 and 11 and differ only 0.2 in the logarithm at $\log(\rho/\mu_e)$ = 10. No unphysical threshold effects are evident. The F^2N II single resonance procedure reproduces the 4-resonance approximated Bloom-Fuller strength function quite well.

The majority of $T^< \rightarrow T^>$ rates are not very sensitive to small errors in the Gamow-Teller resonance placement, once the electron Fermi energy is larger than Q_R. The $T^> \rightarrow T^<$ rates are even less sensitive to the placement of the $T^<$-resonance, but this is because the resonance usually lies very high in the $T^<$-daughter excitation energy.

c) Trends in Gamow-Teller Resonance Positions and Strengths

In undertaking this survey of 226 nuclei, some important trends in Gamow-Teller peak energies and strengths have become apparent. Here specific examples will be given for some iron group nuclei of importance in neutronization during silicon burning and the onset of core collapse in supernovae models.

In general, as nuclei become more neutron rich, the Gamow-Teller

$T^{<} \rightarrow T^{>}$ resonance strength decreases due to increasing neutron blocking of allowed transitions. Accompanying this effect is a trend of decreasing daughter resonance excitation energy due in part to the smaller number of single particle excitations required to make the spin-flip transition as neutron blocking is approached. The model in which these effects were predicted was discussed in § III. In Table 3 is listed the total Gamow-Teller strength and the excitation energy for A = 56 isobars as calculated by the standard F^2N II resonance procedure. The general trends in strength and excitation energy of the resonances is illustrated, though this A-chain is not carried out to complete blocking.

Where the resonances excitation energies are the same in Table 3 the spin-flip configurations in the $T^{>}$-daughters involve similar particle excitation and nucleon pair breaking. In the cases where the $T^{>}$-daughter resonance excitation energy is 2.0 MeV, the spin-flip configuration is coincident with the zero-order shell model configuration, there are no single particle excitations required, the 2.0 MeV simply reflecting the particle-hole repulsion energy. Though one could conclude from Table 3 that the resonance excitation energy decreases while the strength weakens, it is clear that the Q_R for each reaction increases on the average as blocking is approached. This effect was briefly mentioned in § II and can be seen to aide the neutron blocking at low temperature in lowering the electron capture rates as neutronization proceeds. In the two electron capture reactions $^{56}V \rightarrow {}^{56}Ti$ and $^{56}Ti \rightarrow {}^{56}Sc$ the rates at $T_9 = 0.01$ and $\log(\rho/\mu_e) = 11$ (total electron Fermi energy = 23.930 MeV) differ by almost a factor of 30. This is due in part to the factor of 1.87 decrease in $T^{<} \rightarrow T^{>}$ Gamow-Teller

strength between the two cases; but in the main the large decrease in electron capture rate ongoing from $^{56}V \rightarrow {}^{56}Ti$ to $^{56}Ti \rightarrow {}^{56}Sc$ results from the increase in Q_n from 6.810 MeV in the former reaction to 16.251 MeV in the latter reaction.

The situation for the electron capture rates in Table 3 is much different for the higher temperature case [$T_9 = 100$, $\log(\rho/\mu_e) = 11$)]. The blocking and increasing Q_R effects on the rates are washed out at these temperatures due to the thermal population of the analog and $R^<$ resonances in the parent nuclei. At $\log(\rho/\mu_e) = 11$ and $T_9 = 0.01$ the electron capture rates for $^{56}Ni \rightarrow {}^{56}Co$ and $^{56}Ti \rightarrow {}^{56}Sc$ differ by a factor of almost 300; whereas at the same density and $T_9 = 100$ the rates differ by a little over a factor of 4. In neutron rich nuclei as blocking is approached the $T^< \rightarrow T^>$ Gamow-Teller strength systematically decreases, but the $T^> \rightarrow T^<$ strength increases due to increasing neutron richness, and at extremely high temperature this strength becomes accessible to the $T^< \rightarrow T^>$ electron capture reactions through the thermal populations of the $R^<$ resonances.

Early in supernova core collapse, the overall neutronization should be carried by electron capture on heavy nuclei, but as the mean nucleus becomes more neutron rich and blocking sets in, an increasing share of the neutronization will be carried by electron capture on free protons. The Fermi matrix element for the free nucleon weak transition is $|M_F|^2 = 1$, while the Gamow-Teller matrix element is $|M_{GT}|^2 = 3$. These matrix elements imply, through equations (I-2a) and (I-2b), an overall log ft = 3.035. The rates for the reactions $p(e^-,\nu_e)n$, $n(e^+,\bar{\nu}_e)p$, $n(e^- \bar{\nu}_e)p$ and the associated neutrino energy loss rates were calculated with the numerical techniques outlined in F^{2}N I and are reproduced in

this work with great accuracy on the standard F^2N II temperature-density grid. Note that the $p(e^+ \nu_e)n$ decay is energetically forbidden. At extremely high ambient temperatures and correspondingly high nuclear excitation energies, all nuclear states and configurations become sparsely populated and shell structure blocking cannot occur. As a consequence nucleons in nuclei act more and more like free nucleons and in some limit it is possible to treat all protons and neutrons, in and out of nuclei, as free particles in the sense that they have maximum weak neutron matrix elements $|M_P|^2 = 1$ and $|M_{GT}|^2 = 3$. Although nuclei are still bound at $T_9 = 100$ ($kT \sim 9$ MeV) according to Tubbs and Koonin (1979) we estimate that at this temperature the maximum sum rule limit is approached. Thus at $T_9 \geq 100$ an upper limit on transition rates can be calculated for electron capture and positron emission by using

$$|M_F|^2 = Z; \quad |M_{GT}|^2 = 3Z \tag{54}$$

and for electron emission and positron capture by using

$$|M_F|^2 = N; \quad |M_{GT}|^2 = 3N \tag{55}$$

The electron-capture $^{56}Ni \rightarrow {}^{56}Co$ in Table 3 illustrates the approach to these limits in the rates calculated in this paper. At $(\rho/\mu_e) = 10^{11}$ and $T_9 = 0.1$ the ratio of the rate for this transition to that for electron capture on the free proton is dex(5.234 - 4.409) = 6.68 from Table 3. The ratio of the products of the appropriate coupling constants times the matrix elements is $(1.567 \times 96/7)/(1 + 1.567 \times 3) = 3.77$. Recall that $[C(GT)/C(F)]^2 = 1.567$ from equation (I-2) and $|M_{GT}|^2 = 96/7$ for $E_1^< \rightarrow R_1^>$ in $^{56}Ni \rightarrow {}^{56}Co$. This factor becomes 6.79 when multiplied by the ratio of the Fermi functions ≈ 1.80 for capture

at high electron energy (Rose et al., 1955). The agreement is satisfactory and the ratio ~ 7 is to be compared with the expected limit at low temperature, high density namely $(1.567 \times 3 \times 28)/(1 + 1.567 \times 3) = 23.1$. At $(\rho/\mu_e) = 10^{11}$ and $T_9 = 100$ the ratio of the rate for electron capture on ^{56}Ni to that on the proton is dex(6.181 - 4.982) = 15.81. This is in reasonable agreement with the ratio of the matrix elements we have used assuming that the space factors are the same except for the ratio of the Fermi functions given above. In this case the expected limit at high temperature, high density is Z = 28. In other words, the calculated values for the last entries in the grid exceed 50% of the maximum sum rule limit. This is a very reasonable result. To within a factor of two all neutrons and protons inside and out of nuclei can be treated as free particles in regard to the weak interaction at high temperature, $T_9 \leq 100$ and high density $(\rho/\mu_e) \approx 10^{11}$. Similar analysis shows that at $T_9 = 100$ and low density the protons in ^{56}Ni have electron capture rates $\approx 12\%$ of that for free protons.

VII. CONCLUSION

Stellar electron and positron emission, continuum electron and positron capture rates, and all associated neutrino energy loss have been computed for 226 nuclei with masses between A = 21 and A = 60 as well as for free nucleons. The Fermi and Gamow-Teller strength functions are covered by discrete state transitions at low nuclear excitation energies and by one or two narrow resonances, with the remainder of the sum rule strength, at higher excitation energies. This gives an accurate rate at the lower temperatures and densities characteristic of the hydrostatic phases of stellar evolution where detailed rates are

required for nucleosynthesis calculations and gives a good estimate of the rates at the extreme temperatures and densities characteristic of silicon burning and core collapse.

The uncertainties associated with the Gamow-Teller resonance calculations were discussed in the last section where it was shown that approximating the high excitation strength function as a single narrow resonance does not result in any unphysical threshold effects and reproduces quite well calculations with a broader, more realistic Gamow-Teller strength distribution. The level of uncertainty associated with this resonances procedure can be judged by the results presented in § VI.

The results of the calculations described here are available in computer readable form on magnetic tape upon request to MJN. The stellar rates will be presented in tables on a somewhat abbreviated temperature-density grid in a forthcoming publication in the Astrophysical Journal Supplement Series.

REFERENCES

Anderson, B. D., Knudson, J. N., Tandy, P. C., Watson, J. W., and Madey, R. 1980, Phys. Rev. Lett., 45, 699.

Anderson, B. D., and Wong, C. 1961, Phys. Rev. Lett., 7, 250.

Arnett, W. D. 1977, Ap. J., 218, 815.

_____. 1980, Ann. N.Y. Acad. Sci., 336, 366; and private communication.

Austin, S. M. 1980, in The (p,n) Reaction and the Nucleon-Nucleon Force, eds. Goodman, C. D., Austin, S. M., Bloom, S. D., Rapaport, J., and Satchler, G. R. (New York: Plenum Press).

Bainum, D. E., Rapaport, J., Goodman, C. D., Horen, D. J., Foster, C. C., Greenfield, M. B., and Goulding, C. A. 1980, Phys. Rev. Lett., 44, 1751.

Bertsch, G. F. 1980, private communication.

_____. 1981, Nucl. Phys., A354, 157c.

Bethe, H. A., Brown, G. E., Applegate, J., and Lattimer, J. M. 1979, Nucl. Phys., A324, 487.

Bloom, S. D., and Fuller, G. M. 1981, in preparation.

Bohr, A., and Mottelson, B. R. 1981, Phys. Lett., 100B, 10.

Brady, F. P., and Needham, G. A. 1980, in The (p,n) Reaction and the Nucleon-Nucleon Force, eds. Goodman, C. D., Austin, S. M., Bloom, S. D., Rapaport, J., and Satchler, G. R. (New York: Plenum Press).

Couch, R. G., and Arnett, W. D. 1973, Ap. J. (Letters), 180, L101.

deShalit, A., and Feshbach, H. 1974, Theoretical Nuclear Physics, Volume I: Nuclear Structure (New York: John Wiley and Sons).

Doering, R. R., Galonsky, A., Patterson, D. M., and Bertsch, G. F. 1975, Phys. Rev. Lett., 35, 1691.

Endt, P. M., and van der Leun, C. 1978, Nucl. Phys., A310, 1.

Flynn, E. R., and Garrett, J. D. 1972, Phys. Rev. Lett., 29, 1748.

Flynn, E. R., Sherman, J., and Stein, N. 1974, Phys. Rev. Lett., 32, 846.

Fowler, W. A., and Woosley, S. E. 1980, in preparation.

Fujita, J., and Ikeda, K. 1965, Nucl. Phys., 67, 145.

Fuller, G. M. 1981, preprint.

Fuller, G. M., Fowler, W. A., and Newman, M. J. 1980, Ap. J. Suppl., 42, 447.

_____. 1981, preprint.

Gaarde, G., Kemp, K., Petresch, C., and Folkman, F. 1972, Nucl. Phys., A184, 241.

Gaarde, C., Larsen, J. S., Drentje, A. G., Harakeh, M. N., and Van Der Werf, S. Y. 1980, Nucl. Phys., A346, 497.

Galonsky, A. 1980, in The (p,n) Reaction and the Nucleon-Nucleon Force, eds. Goodman, C. D., Austin, S. M., Bloom, S. D., Rapaport, J., and Satchler, G. R. (New York: Plenum Press).

Gaponov, Yu. V., and Lyutostanskii, Yu. S. 1974, Yad. Fiz., 19, 62.

Gleit, C. E., Tang, C. W., and Coryell, C. D. 1968, Nucl. Data Sheets, 13, 5.

Goodman, C. D., Goulding, C. A., Greenfield, M. B., Rapaport, J., Bainum, D. E., Foster, C. C., Love, W. G., and Petrovich, F. 1980, Phys. Rev. Lett., 44, 1755.

Halbleib, J. A., and Sorensen, R. A. 1967, Nucl. Phys., A98, 542.

Hansen, C. J. 1966, Ph.D. thesis, Yale University.

Hillman, M., and Grover, J. R. 1969, Phys. Rev., 185, 1307.

Klapdor, H. V. 1976, Cern-Report 76-13, Proceedings 3rd International Conference on Nuclei Far From Stability.

Klapdor, H. V. (editor) 1979, Report MPI H-1979-V13.

Koonin, S. E. 1978, Course Notes and references therein.

Lane, A. M. 1962, Nucl. Phys., 35, 676.

Lederer, D. M. et al. 1978, Table of Isotopes, eds. Lederer, C. M. and Shirley, V. S. (New York: Wiley and Sons).

Martinsen, P. O., and Randrup, J. 1972, Nucl. Phys., A195, 26.

Mazurek, T. J., Truran, J. M., and Cameron, A. G. W. 1974, Ap. Space Sci., 27, 261.

Møller, P., and Nix, R. 1980, Los Alamos preprint.

Nomoto, K. 1980, Proceedings of the Texas Workshop on Type-I Supernovae, ed. Wheeler, J. C. (Austin: University of Texas Press).

Rose, M. E., Dismuke, N. M., Perry, C. L., and Bell, P. R. 1955, in Beta and Gamma-Ray Spectroscopy, ed. Siegbahn, K. (Amsterdam: North Holland), p. 875.

Schiffer, J. P., and True, W. W. 1976, Rev. Mod. Phys., 48, 194.

Seeger, P. A., and Howard, W. M. 1975, Nucl. Phys., A238, 491.

Seeger, P. A., and Perisho, R. 1967, Los Alamos Scientific Laboratory Report, LA-3751.

Soper, J. M. 1969, in Isospin in Nuclear Physics, ed. Wilkinson, D. H. (Amsterdam: North Holland), p. 231.

Sterrenberg, W. A., Austin, S. M. DeVito, R. P., and Galonsky, A. 1980, Phys. Rev. Lett., 45, 1839.

Tubbs, D. L., and Koonin, S. E. 1979, Ap. J. (Letters), 232, L59.

Van Riper, K. A., and Lattimer, J. M. 1981, preprint.

Weaver, T. A., and Woosley, S. E. 1979, private communication.

Woosley, S. E., Arnett, W. D., and Clayton, D. D. 1972, Ap. J., 175, 731.

TABLE 1

SINGLE PARTICLE GAMOW-TELLER MATRIX ELEMENTS

$j_i \backslash j_f$	$\ell + 1/2$	$\ell - 1/2$
$\ell + 1/2$	$\frac{j_i + 1}{j_i}$	$\frac{2j_i - 1}{j_i}$
$\ell - 1/2$	$\frac{2j_i + 3}{j_i + 1}$	$\frac{j_i}{j_i + 1}$

TABLE 2

FOUR RESONANCE APPROXIMATIONS TO BLOOM AND FULLER

$^{56}Fe(g.s.) \rightarrow {}^{56}Mn$ GAMOW-TELLER STRENGTH FUNCTION

Excitation Energy in ^{56}Mn(MeV)	Percent of Total Strength	Strength in Each Resonance	
		$\|M_{GT}\|^2$	log ft
1.5	35%	3.083	3.107
2.5	25%	2.259	3.242
3.8	25%	2.259	3.242
4.9	15%	1.355	3.464

TABLE 3

RATES AT $(\rho/\mu_e) = 10^{11}$

Reaction	Resonance Excitation Energy (daughter nucleus) MeV	Resonance Strength $\lvert M_{GT}\rvert^2$	Resonance Strength log ft	Q_R (MeV)	log λ_{ec} Rates (s^{-1}) at $(\rho/\mu_e) = 10^{11}$ $T_9 = 0.01$	$T_9 = 100$
$p(e^-,\nu_e)n$	0	–	3.035	1.293	4.409	4.982
$^{56}Ni(e^-,\nu_e)^{56}Co$	3.777	13.677	2.460	2.153	5.234	6.181
$^{56}Co(e^-,\nu_e)^{56}Fe$	5.381	11.995	2.517	1.324	5.194	6.025
$^{56}Fe(e^-,\nu_e)^{56}Mn$	3.777	10.280	2.584	7.983	4.727	5.791
$^{56}Mn(e^-,\nu_e)^{56}Cr$	5.381	8.570	2.663	7.536	4.685	5.691
$^{56}Cr(e^-,\nu_e)^{56}V$	2.0	7.105	2.744	13.106	4.071	5.224
$^{56}V(e^-,\nu_e)^{56}Ti$	2.0	4.285	2.964	8.801	4.268	5.798
$^{56}Ti(e^-,\nu_e)^{56}Sc$	2.0	2.286	3.237	18.251	2.800	5.557

Figure 1

The zero-order shell model orbit-occupation diagram for the ground state configuration of $^{33}_{16}S_{17}$ is shown. The closed proton and neutron sp-shells (closed at 8 nucleons each) are shown at the bottom of the diagram. Other closed orbits are denoted with circles.

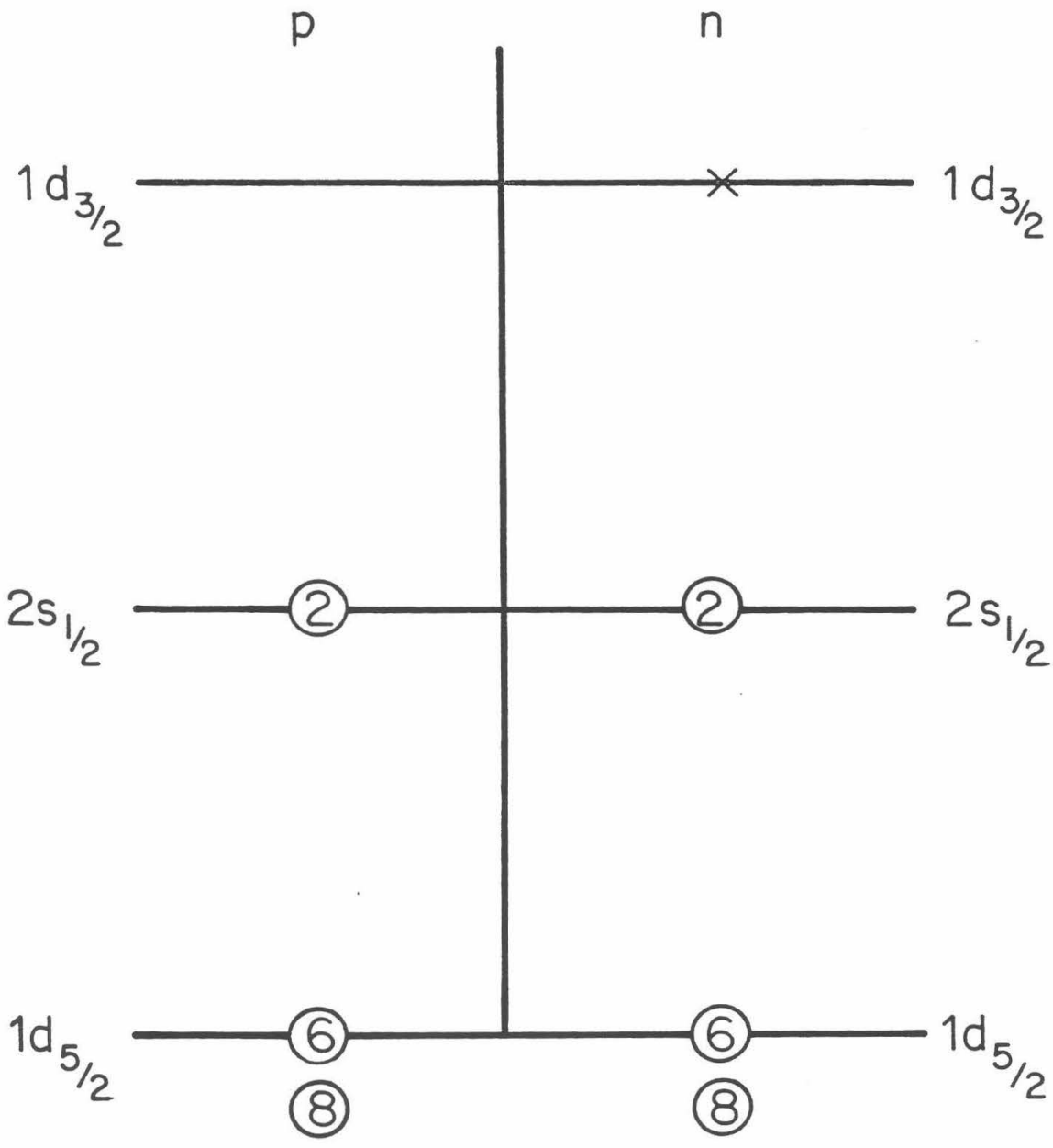

$^{33}_{16}S_{17}$ gs

Fig. 1

Figure 2

The zero-order shell model orbit-occupation diagram for the spin-flip configuration in $^{33}_{15}P_{18}$ is shown. This configuration can be generated from the Figure 1 diagram by transforming a $1d_{5/2}$ proton into a hole in the $1d_{3/2}$ neutron orbit.

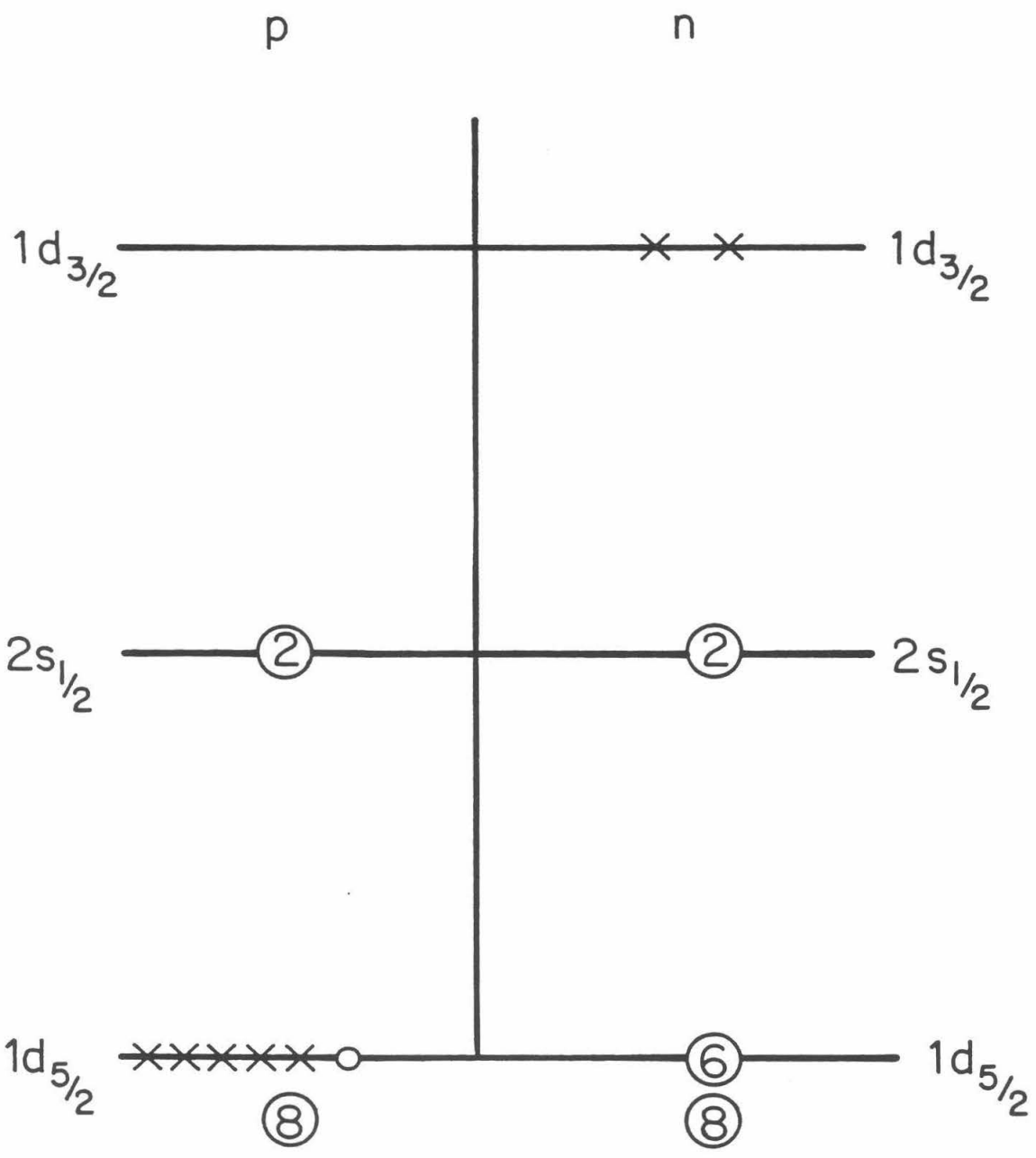

$^{33}_{15}P^{sf}_{18}$

Fig. 2

Figure 3

(a) shows the zero-order ground state configuration diagram for a neutron rich nucleus. (b) depicts an excited configuration for this nucleus wherein a neutron is promoted from a $j = \ell + \frac{1}{2}$ orbit to a higher-lying, empty, $j = \ell - \frac{1}{2}$ orbit.

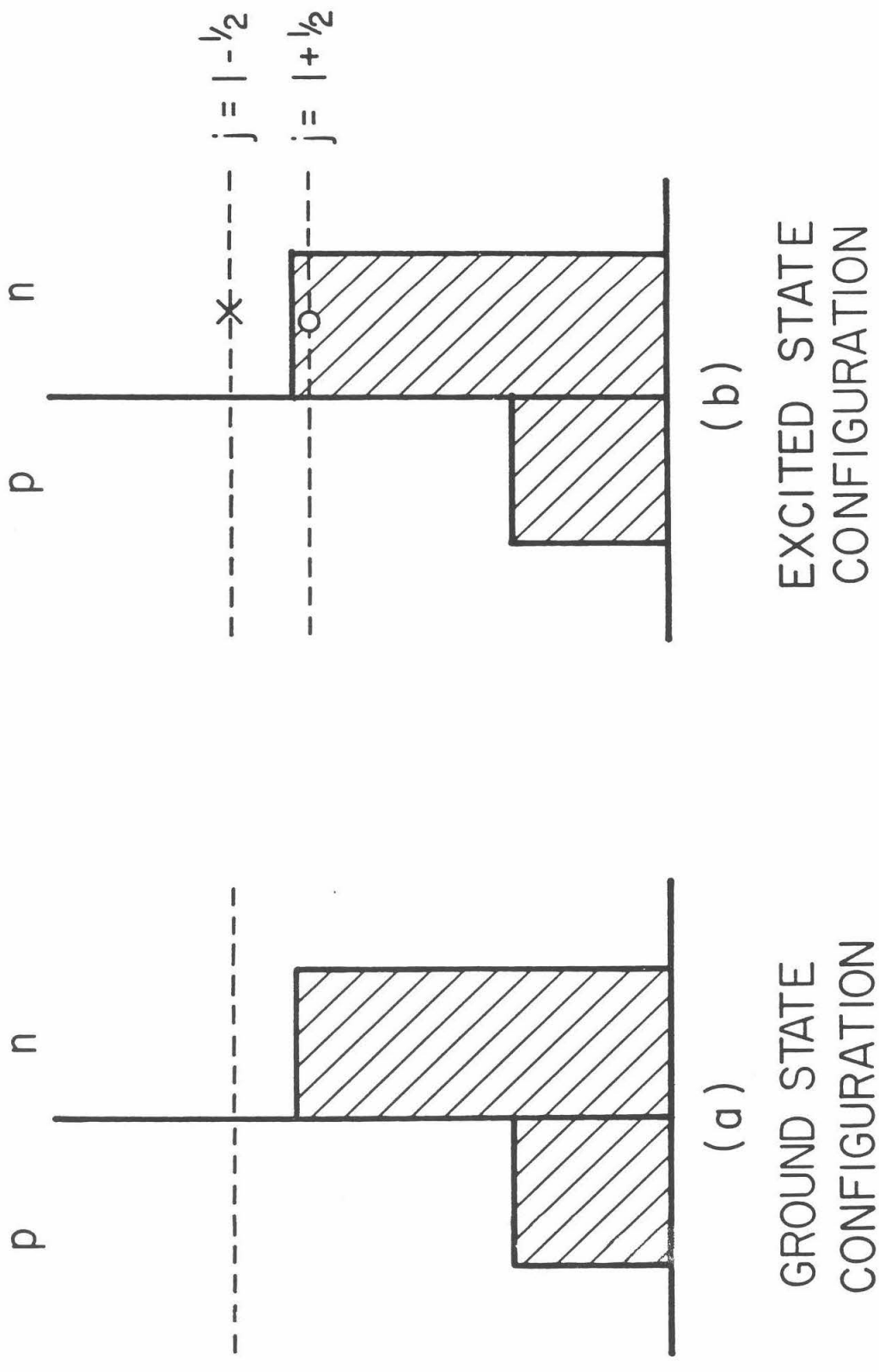
DOUBLY MAGIC NUCLEUS WITH N > Z
GROUND STATE CONFIGURATION
EXCITED STATE CONFIGURATION
(a)
(b)
p
n
p
n
j = l + ½
j = l - ½

Fig. 3

Figure 4a

The neutron M1 analog is shown for a neutron rich nucleus. This configuration can be generated from the excited configuration in Figure 3b by operating with T_+.

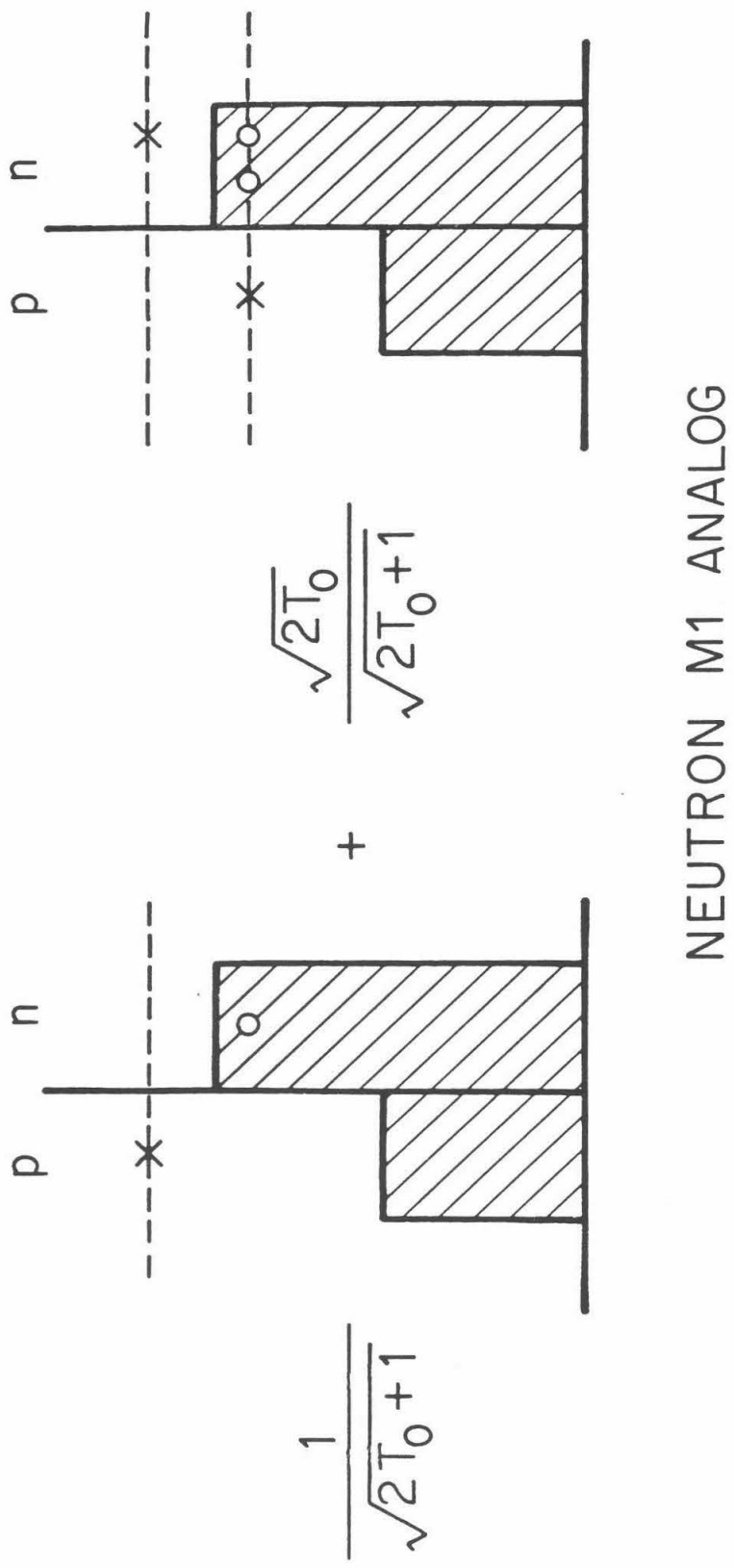
NEUTRON M1 ANALOG
p
n
p
n
+
$\frac{1}{\sqrt{2T_0+1}}$
$\frac{\sqrt{2T_0}}{\sqrt{2T_0+1}}$

Fig. 4a

Figure 4b

The neutron M1 anti-analog corresponding to the M1 analog in Figure 4a is shown. This configuration can be generated from that in Figure 4a by noting that the anti-analog state must be identical to the analog state in all quantum numbers save total isospin T. It is therefore orthogonal to the Figure 4a configuration.

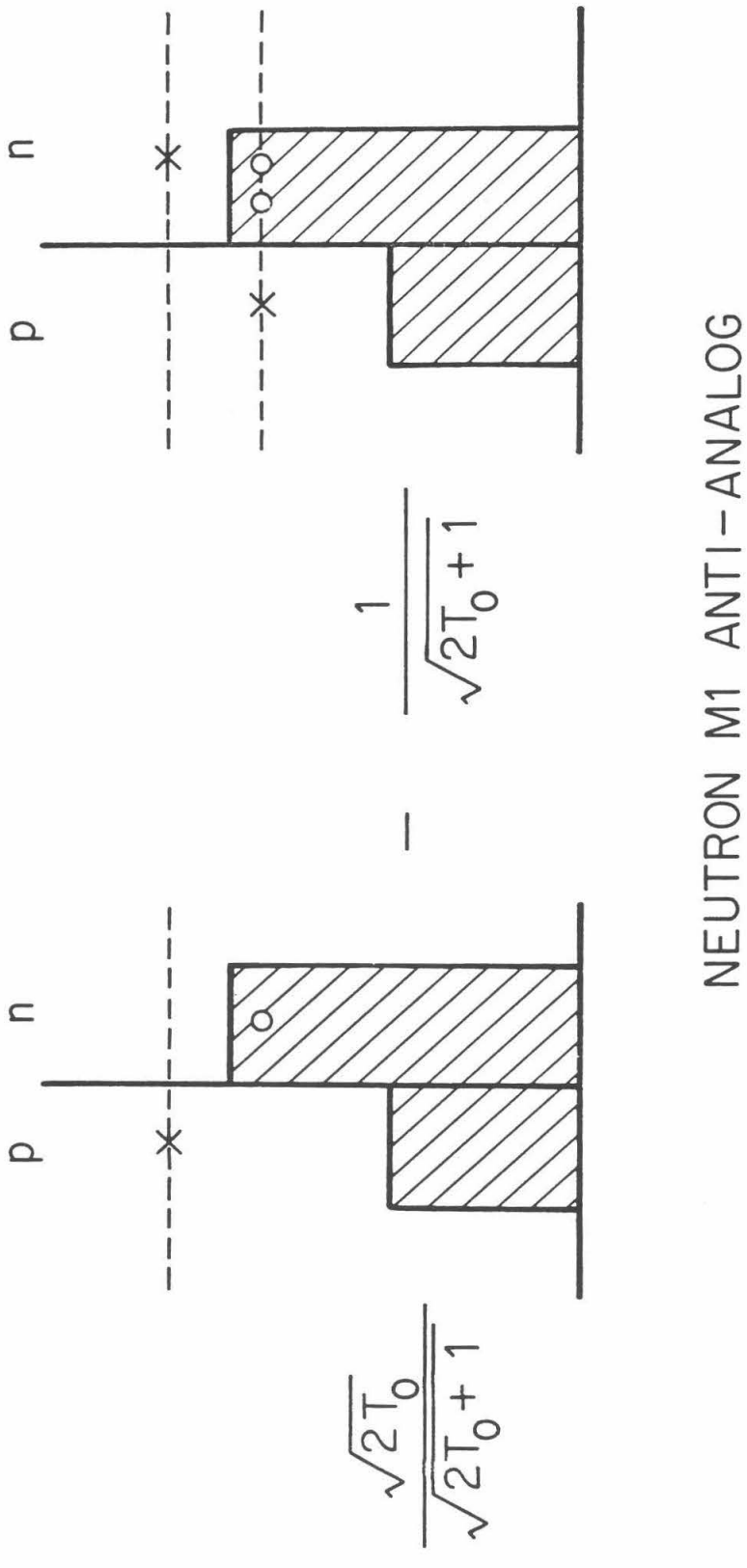
p
n
p
n
$\frac{\sqrt{2T_0}}{\sqrt{2T_0}+1}$
−
$\frac{1}{\sqrt{2T_0}+1}$
NEUTRON M1 ANTI-ANALOG

Fig. 4b

Figure 5

The zero-order orbit-occupation diagram for the ground state configuration of $^{33}_{18}Ar_{15}$ is shown. Notation is as in Figure 1. Note that ^{33}Ar is proton rich.

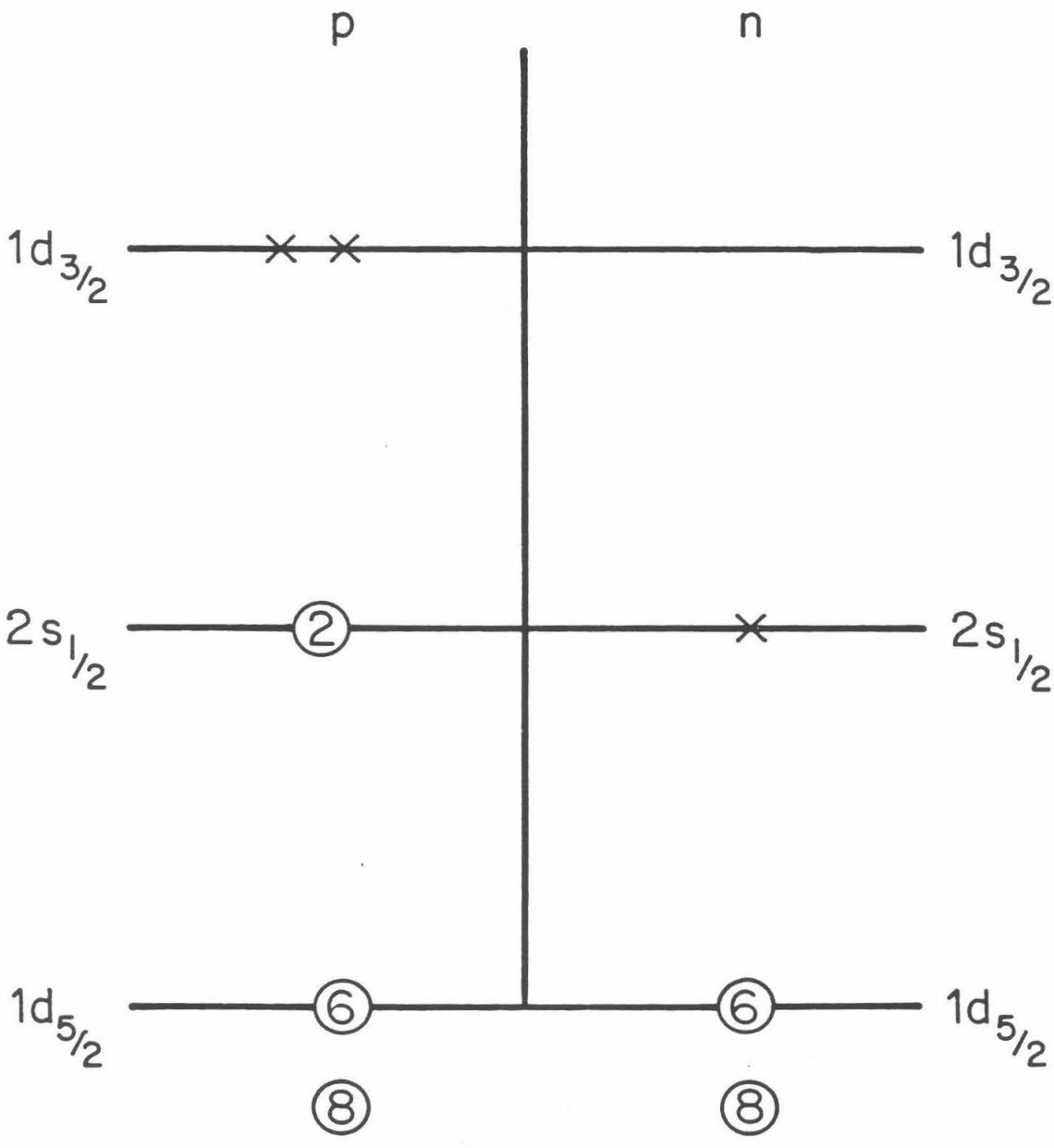

$^{33}_{18}Ar^{gs}_{15}$

Fig. 5

Figure 6

The orbit-occupation diagram for the ^{33}Cl proton M1 analog state, which can be generated from the Figure 5, ^{33}Ar ground state, configuration by the promotion of a proton from $1d_{5/2}$ to $1d_{3/2}$ and the application of T^-.

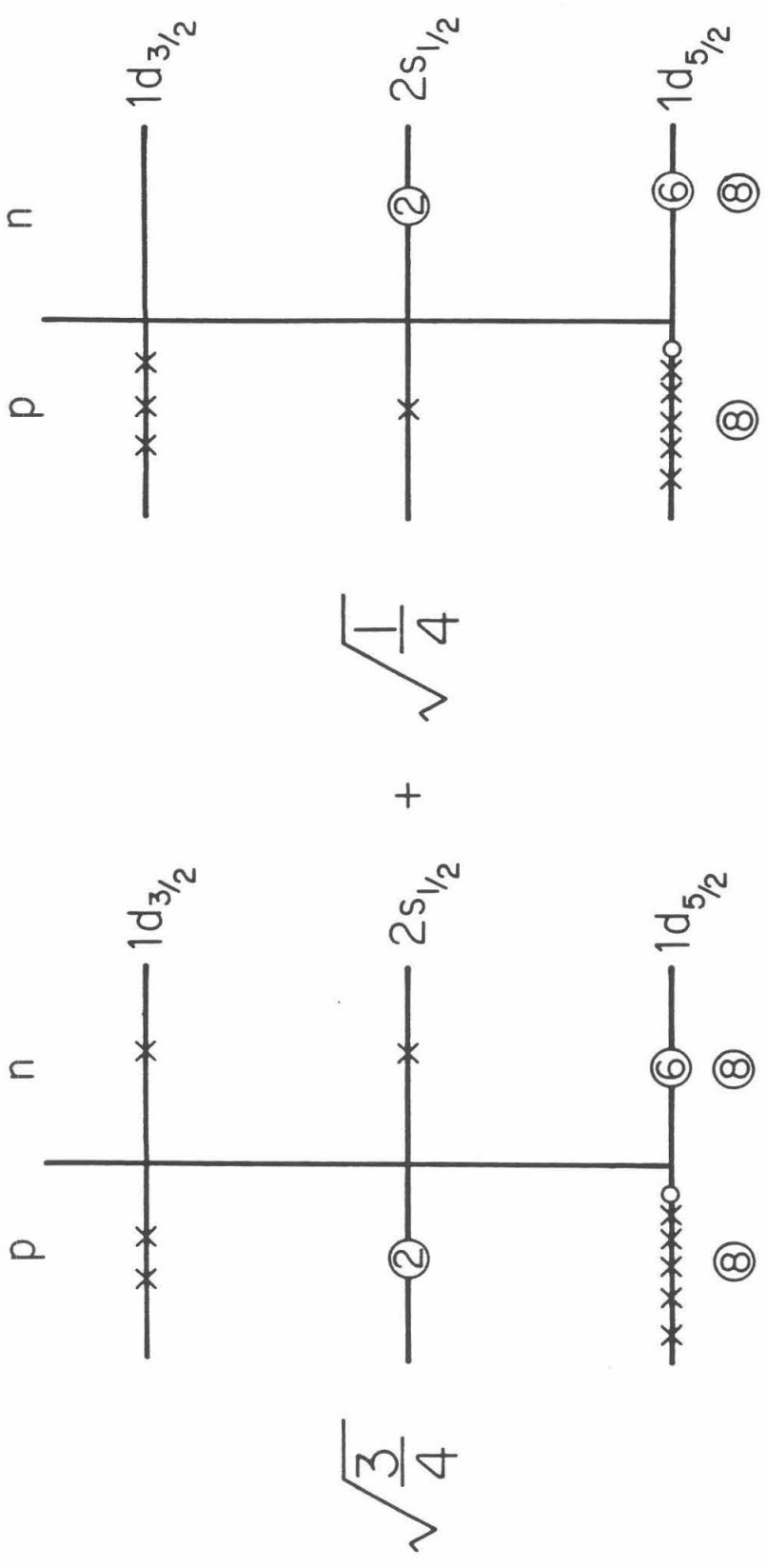

Fig. 6

Figure 7

(a) The zero-order orbit-occupation diagram for the ground state configuration of $^{26}_{12}Mg_{14}$.

(b) The zero-order orbit-occupation diagram of the $^{26}_{13}Al_{13}$ spin-flip configuration generated from (a) by the transformation of a $1d_{5/2}$ neutron into a $1d_{3/2}$ proton hole.

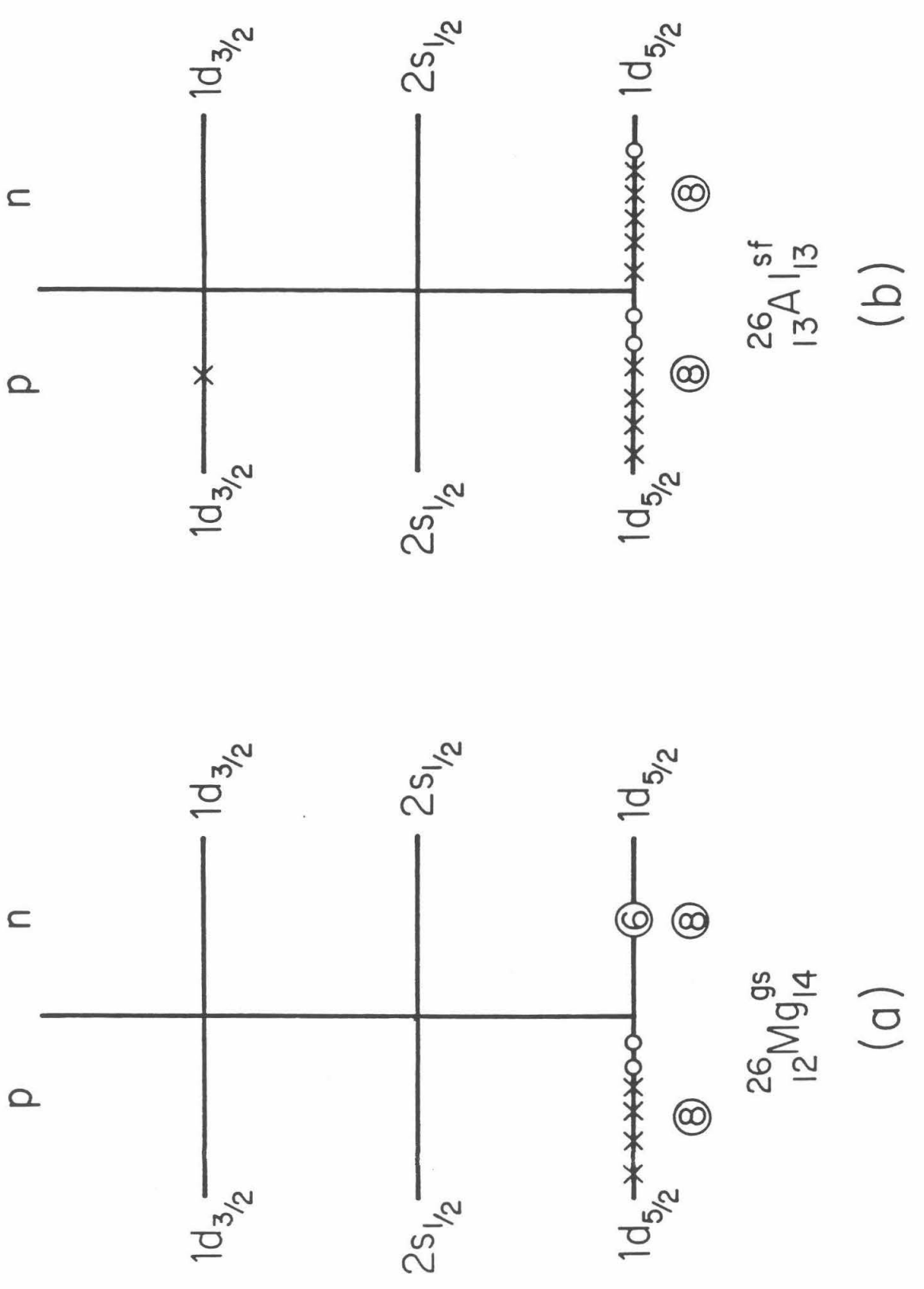

Fig. 7

Figure 8

The zero-order orbit-occupation diagram for the ground state configuration of $^{26}_{13}Al_{13}$.

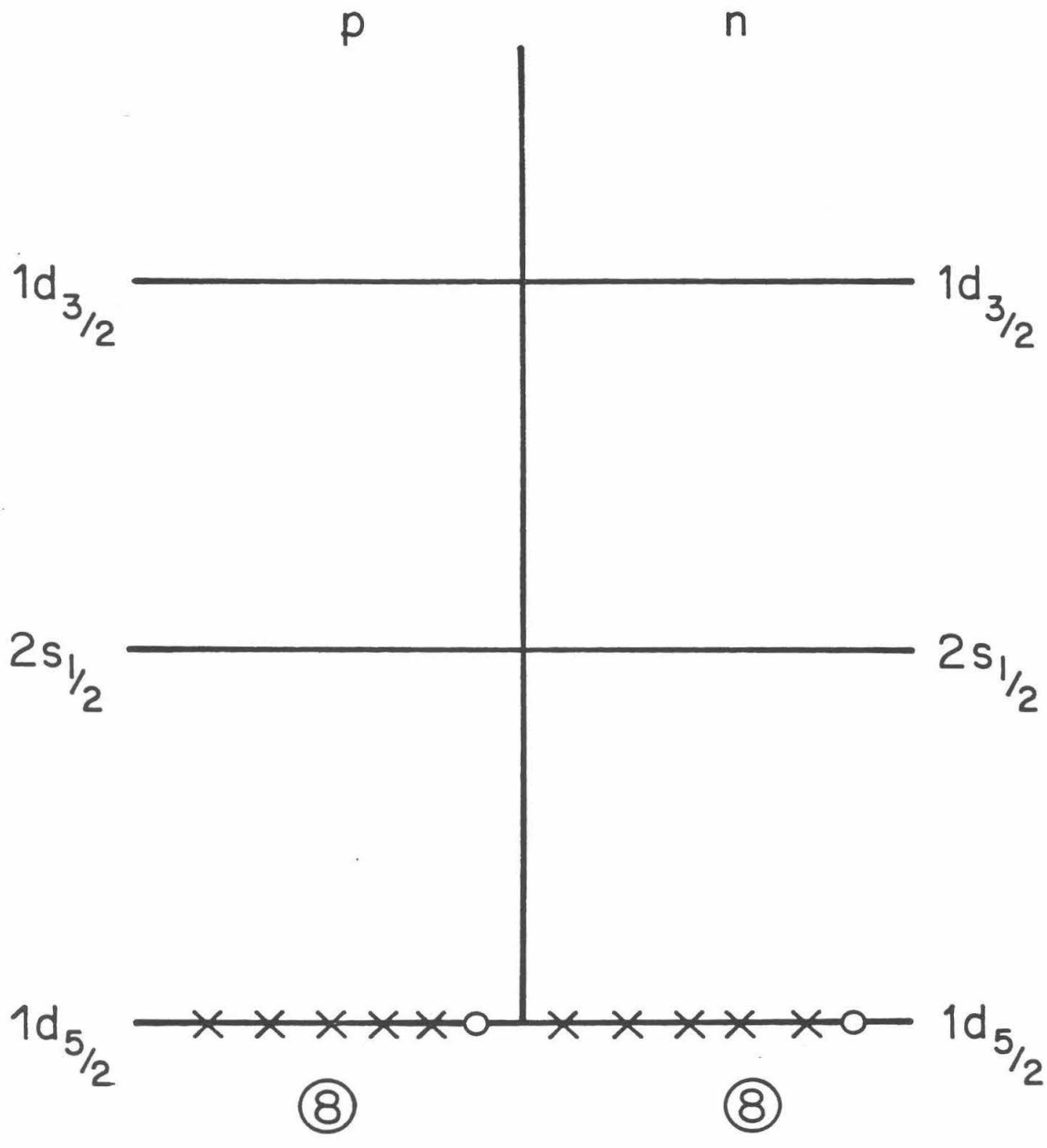

$^{26}_{13}Al^{gs}_{13}$

Fig. 8

Figure 9

(a) The $^{56}_{26}Fe_{30}$ ground state configuration zero-order orbit-occupation diagram. Note the closed proton and neutron sd and sp-shells (closed at 20 nucleons each) indicated at the bottom of the diagram.

(b) The $^{56}_{25}Mn_{31}$ ground state configuration zero-order orbit-occupation diagram.

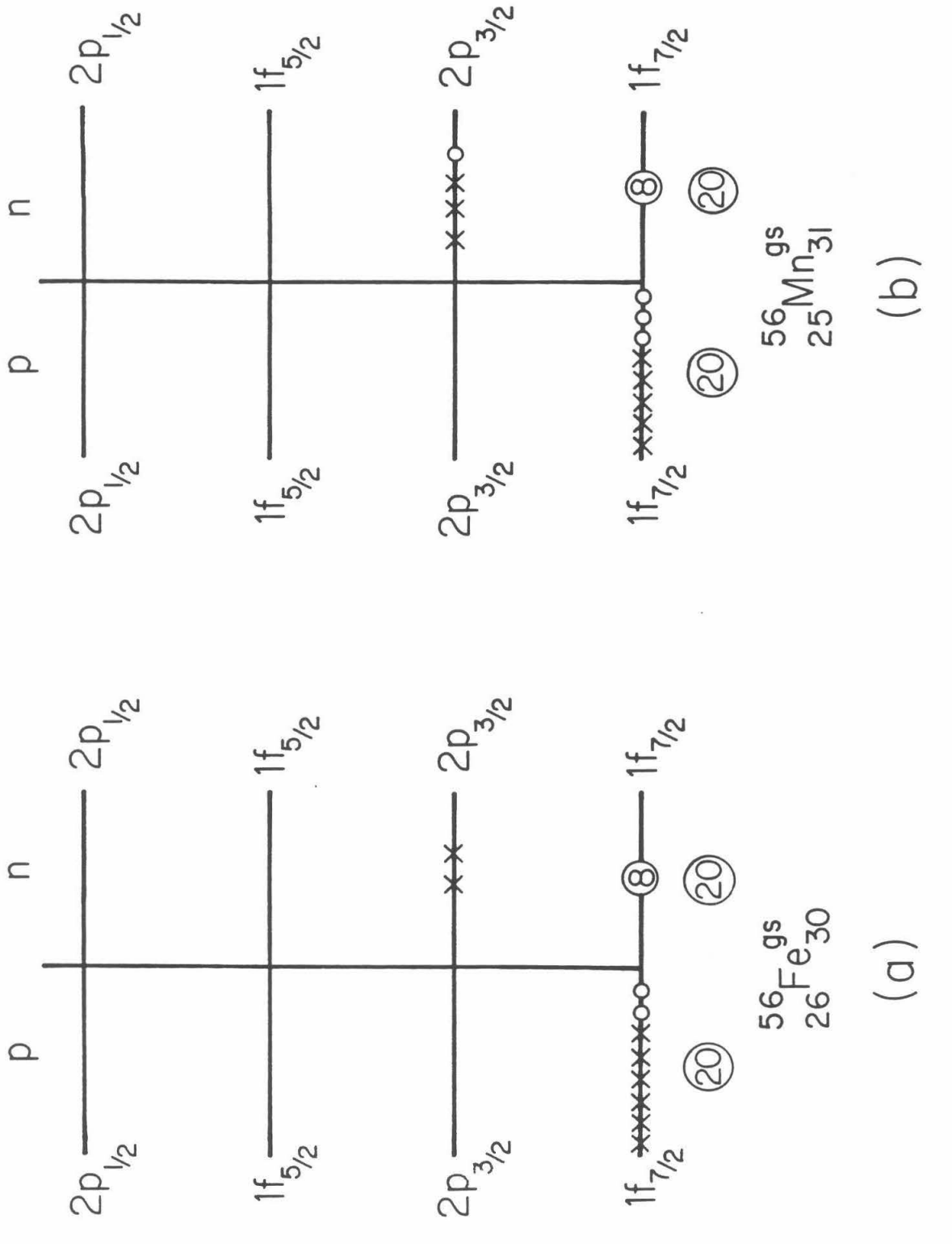

Fig. 9

Figure 10

The zero-order orbit-occupation diagram for the spin-flip configuration in ^{56}Mn is shown. This configuration is generated from that in Figure 9a by the transformation of a $1f_{7/2}$ proton into a $1f_{5/2}$ neutron hole.

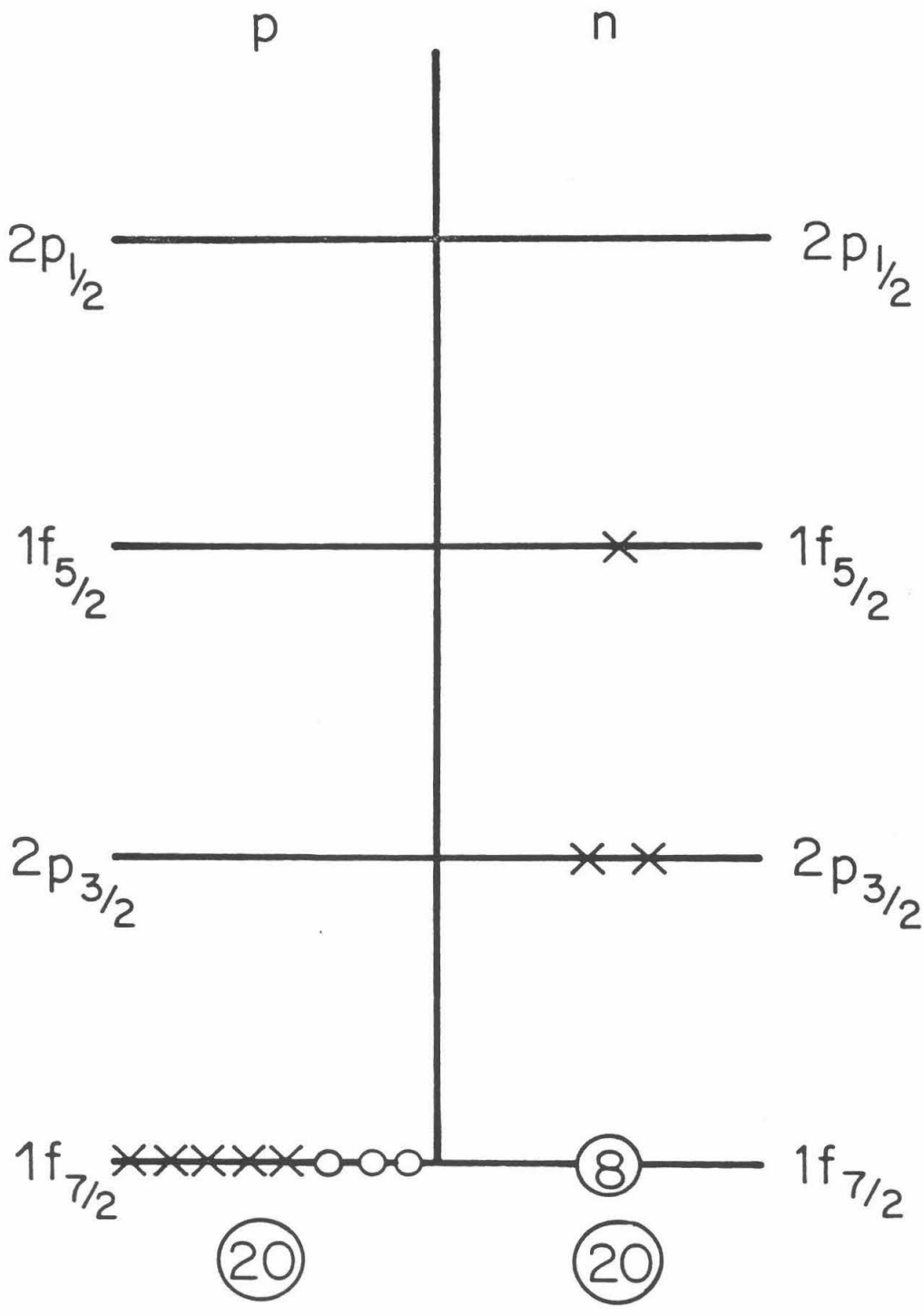

$^{56}_{25}Mn^{sf}_{31}$

Fig. 10

Figure 11

This figure shows the zero-order orbit-occupation diagrams for several states generated from the ^{56}Mn spin-flip configuration by (a) acting with T^{+} to give the $T^{>}$-spin-flip-analog in ^{56}Fe with indicated coefficients α, β, γ for the $|1\rangle$, $|2\rangle$, and $|3\rangle$ coefficients, respectively; (b) and (c) are the $T_{+}^{<}$ and $T_{-}^{<}$-spin-flip anti-analog states generated from the configuration in (a) by orthogonality, with coefficients of the $|1\rangle$, $|2\rangle$, and $|3\rangle$ configurations as indicated.

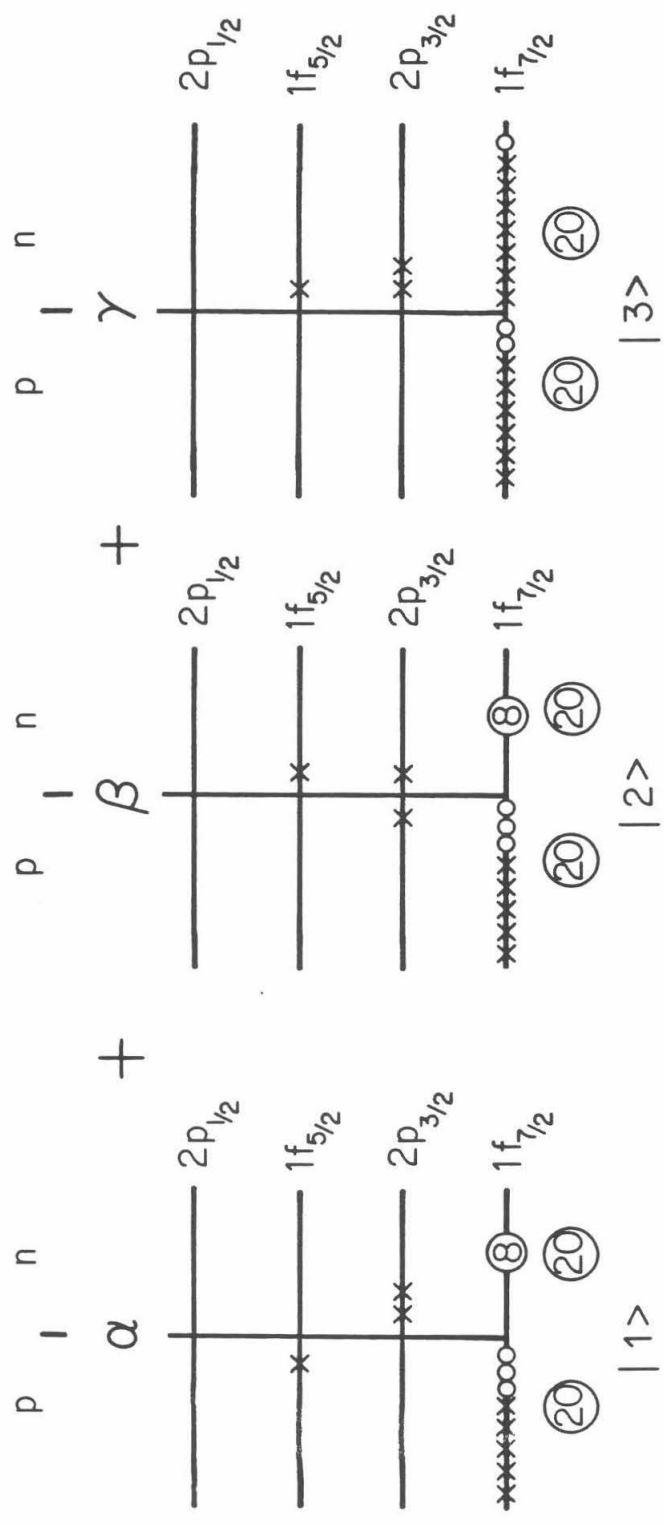

(a) $T^{>}$ - SPIN-FLIP ANALOG IN $^{56}Fe \longrightarrow \alpha_1 = \sqrt{\frac{1}{6}}$ $\beta_1 = \sqrt{\frac{1}{3}}$ $\gamma_1 = \sqrt{\frac{1}{2}}$

(b) $T_+^{<}$ - SPIN-FLIP ANTI-ANALOG IN $^{56}Fe \longrightarrow \alpha_2 = \sqrt{\frac{1}{6}}$ $\beta_2 = \sqrt{\frac{1}{3}}$ $\gamma_2 = -\sqrt{\frac{1}{2}}$

(c) $T_-^{<}$ - SPIN-FLIP ANTI-ANALOG IN $^{56}Fe \longrightarrow \alpha_3 = \sqrt{\frac{2}{3}}$ $\beta_3 = -\sqrt{\frac{1}{3}}$ $\gamma_3 = 0$

Fig. 11

Figure 12

A schematic representation of a typical excited state problem is shown. $E_1^<$, $E_2^<$, ... $E_i^<$ are the discrete states of the $T^<$-nucleus. $E_1^>$, $E_2^>$, ... $E_j^>$ are the discrete states in the $T^>$-nucleus. $A_1^<$, $A_2^<$, ... $A_j^<$ are the analogs of $E_1^>$, $E_2^>$, ... $E_j^>$. Transitions from the discrete states of the $T^<$-nucleus to Gamow-Teller collective resonances ($R_1^>$, $R_2^>$, ... $R_i^>$) in the $T^>$-nucleus, and the reverse transitions, are shown with rates $\lambda_{ii} = \lambda_{er}$. Similarly, transitions from the discrete states of the $T^>$-nucleus to collective Gamow-Teller resonances in the $T^<$-nucleus ($R_1^<$, $R_2^<$, ... $R_j^<$), and the reverse transitions are shown with rates $\lambda_{jj} = \lambda_{re}$. For clarity the Fermi transitions λ^F_{jj} between $E_j^> \rightleftarrows A_j^<$ are not illustrated.

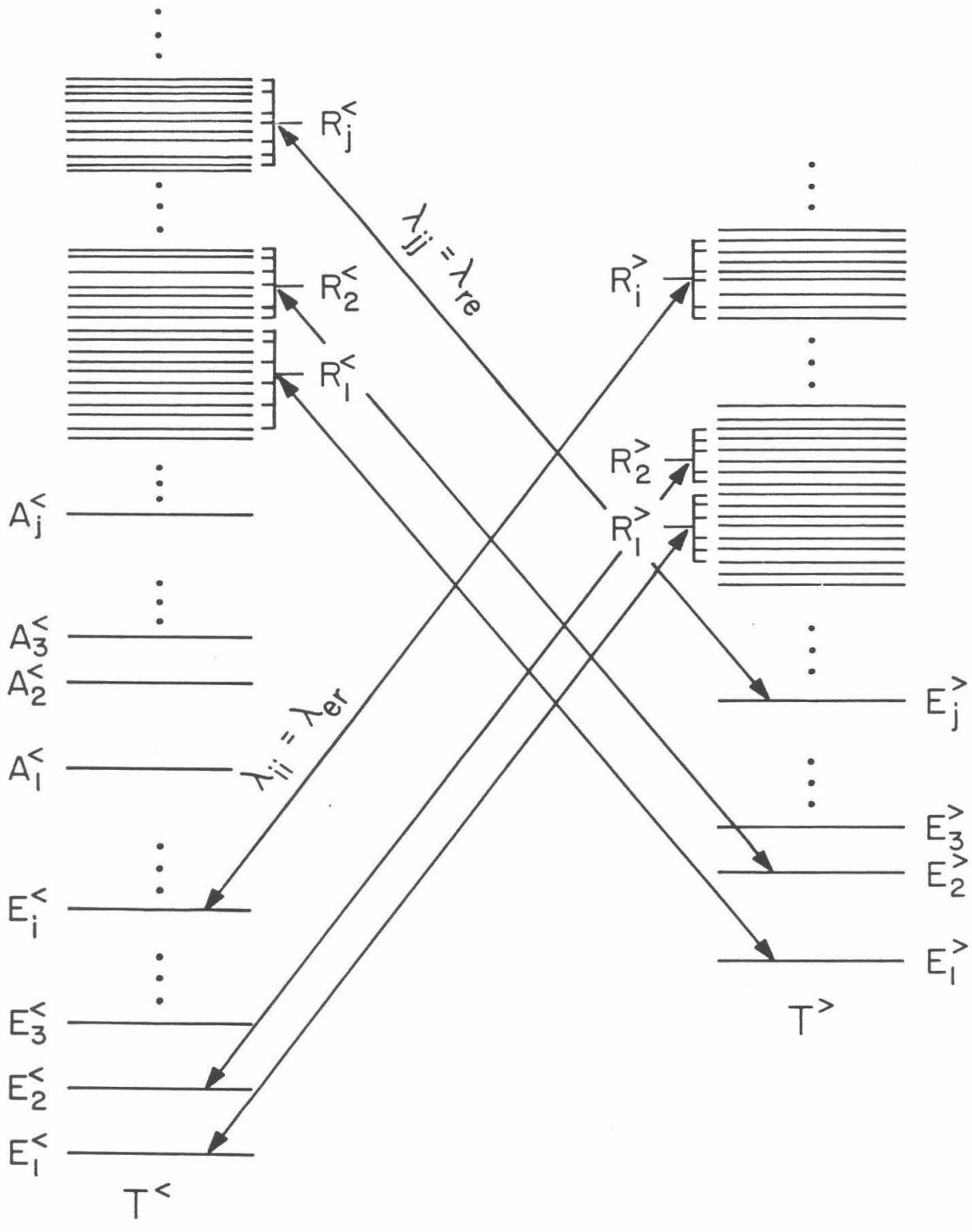
$R_j^<$
$R_2^<$
$R_1^<$
$\lambda_{ij} = \lambda_{re}$
$R_i^>$
$R_2^>$
$R_1^>$
$A_j^<$
$A_3^<$
$A_2^<$
$A_1^<$
$\lambda_{ii} = \lambda_{er}$
$E_j^>$
$E_3^>$
$E_2^>$
$E_1^>$
$E_i^<$
$E_3^<$
$E_2^<$
$E_1^<$
$T^<$
$T^>$

Fig. 12

Figure 13a

The total $^{56}Fe \rightarrow {}^{56}Mn$ weak transition rate is shown for the F^2N II single resonance approximation as a function of temperature T (K) for the densities, $\log(\rho/\mu e) = 7, 8, 9, 10, 11$.

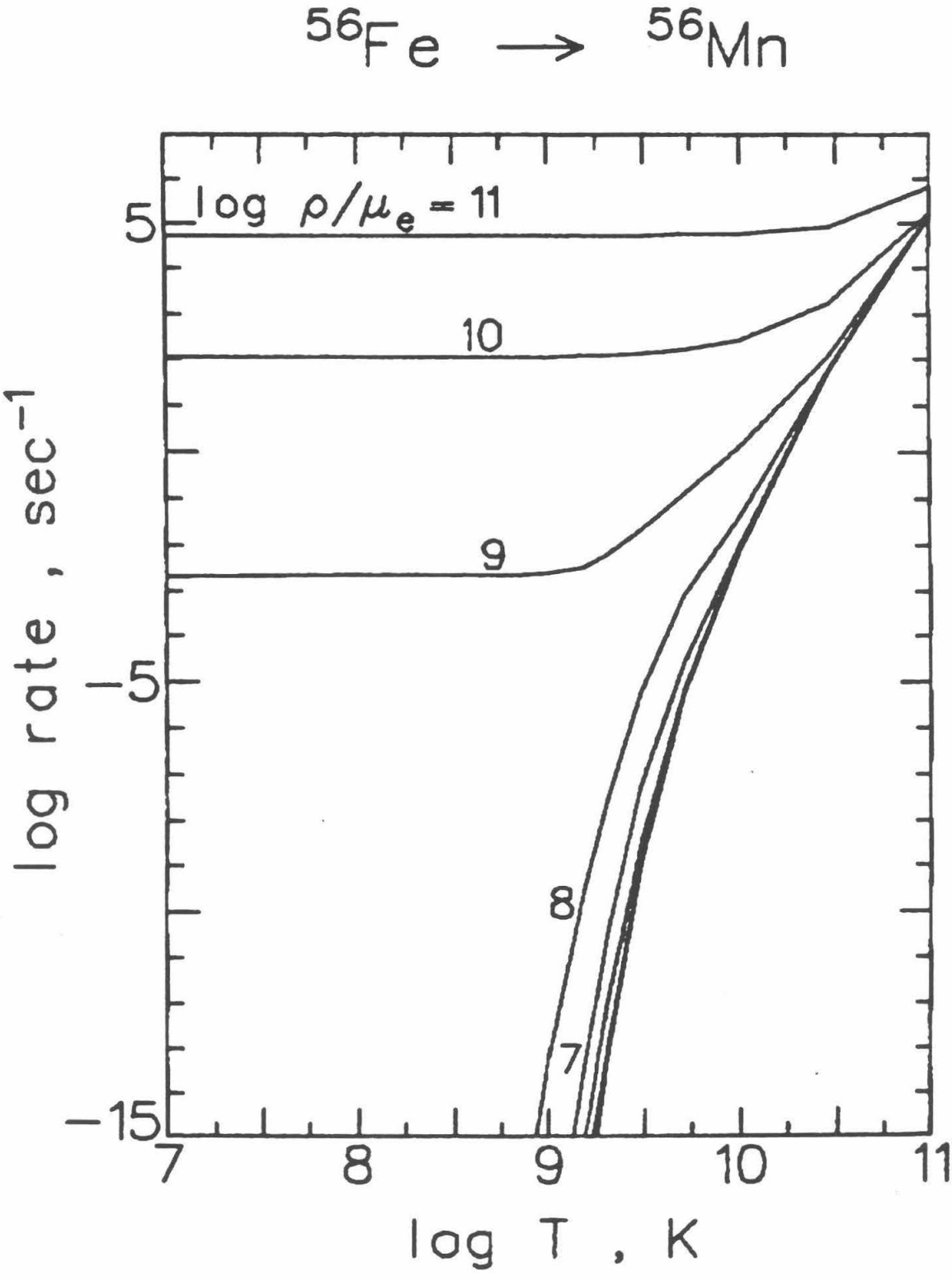
$^{56}Fe \rightarrow {}^{56}Mn$
log $\rho/\mu_e = 11$
10
9
8
7
5
−5
−15
log rate , sec^{-1}
7
8
9
10
11
log T , K

Fig. 13a

Figure 13b

The total $^{56}Fe \rightarrow {}^{56}Mn$ weak transition rate as shown in Figure 13a, but now with the four-resonance approximation to the Bloom and Fuller (1981) strength function. There is very little change in the overall transition rate.

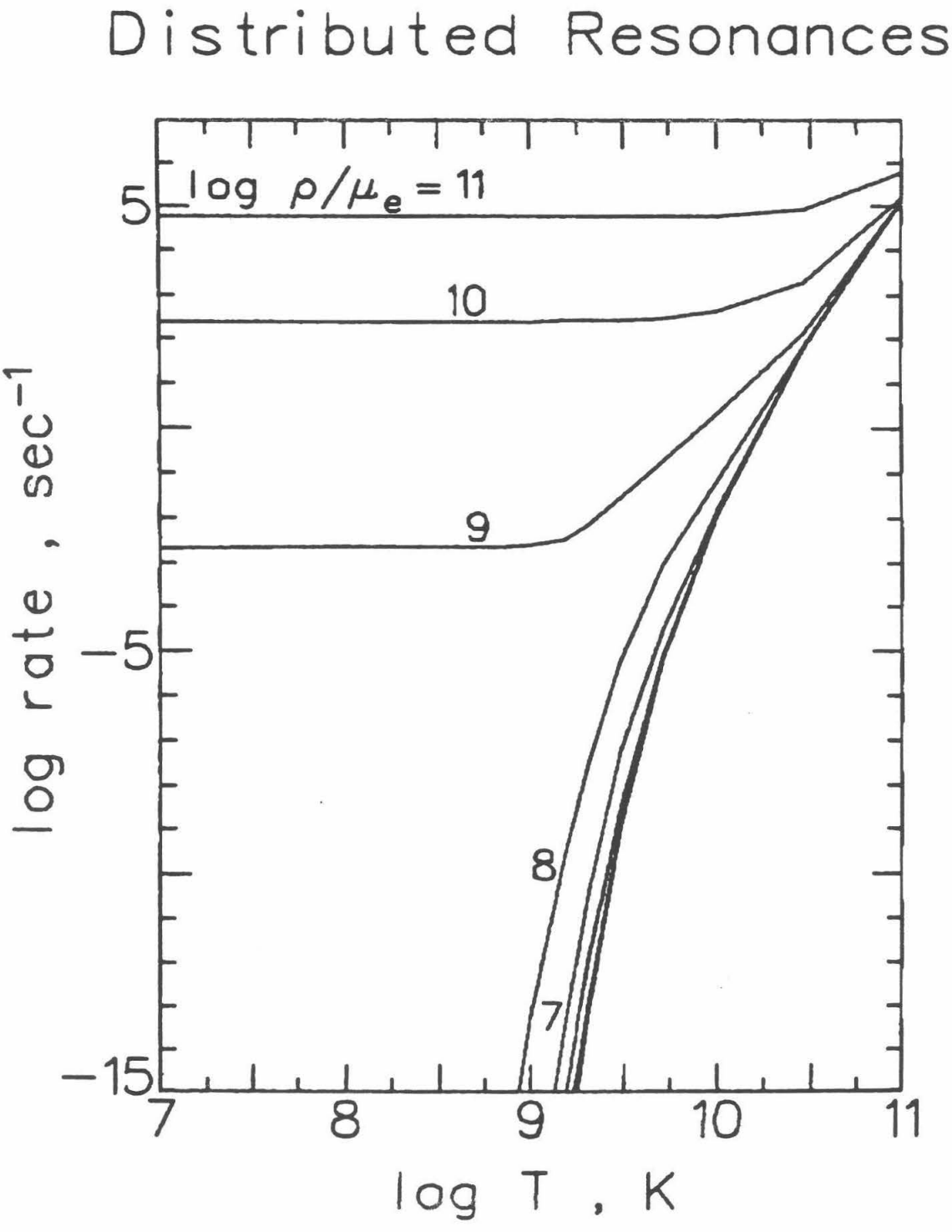
Distributed Resonances
log $\rho/\mu_e = 11$
10
9
8
7
5
−5
−15
log rate , sec^{-1}
7
8
9
10
11
log T , K

Fig. 13b

IV. RESULTS OF THE STELLAR RATE CALCULATIONS AND DISCUSSION

STELLAR WEAK INTERACTION RATES[1] FOR INTERMEDIATE MASS NUCLEI III: RATE TABLES FOR THE FREE NUCLEONS AND A = 21 TO A = 60

GEORGE M. FULLER[2] and WILLIAM A. FOWLER

W. K. Kellogg Radiation Laboratory

California Institute of Technology, Pasadena, California 91125

and

MICHAEL J. NEWMAN

Theoretical Applications Division

Los Alamos National Scientific Laboratory

University of California, Los Alamos, New Mexico 87544

---

[1] Supported in part by the National Science Foundation [PHY79-23638] at Caltech and in part by the U.S. Department of Energy.

[2] Fannie and John Hertz Foundation Fellow.

ABSTRACT

Stellar electron and positron emission rates, and continuum electron and positron capture rates as well as the associated neutrino energy loss rates are tabulated for the free nucleons and 226 nuclei with masses between A = 21 and 60. These rates were calculated in accordance with the procedure described in papers I and II of this series and are presented here in tabular form on an abbreviated temperature and density grid. Results of these calculations on a detailed temperature and density grid are available in computer readable form on magnetic tape upon request to MJN. The stellar weak rate calculation procedure is reviewed and the results are discussed. Comparison of the stellar weak rates to terrestrial decay rates are made where possible.

Subject headings:

I. INTRODUCTION

In this work, electron and positron emission rates in stars, continuum electron and positron capture rates in stars and the associated neutrino energy loss rates are tabulated for free protons and neutrons as well as 226 nuclei with masses between A = 21 and 60. The rate computations were performed following the procedures discussed in papers I and II of this series (Fuller, Fowler, and Newman 1980, hereafter F^2N I, and Fuller, Fowler, and Newman 1981, hereafter F^2N II). The previous papers are concerned with the details of stellar weak rate calculations and the nuclear physics of the Gamow-Teller strength distribution.

The purpose of this paper is to discuss the results of the stellar rate computations in comparison with other work and with known terrestrial decay rates, and to provide ready access to printed rates for active investigations in the fields of stellar evolution and nucleosynthesis. The rates presented here in tabular form are reproduced, by necessity, on an abbreviated temperature and density grid which will allow a fair estimate of stellar rates to be made for most astrophysical environments. Where more accurate stellar rates are required, as in stellar evolution and nucleosynthesis calculations, the reader is urged to write to MJN and request the stellar rate magnetic tape. This tape presents the computation results on a far more detailed temperature and density grid in a computer readable form suitable for interpolation in temperature and density.

The temperature and density grid employed in these calculations covers conditions ranging from the relatively mild environments characteristic of hydrostatic carbon and oxygen burning, through the more

extreme conditions characteristic of silicon burning and the onset and early stages of core collapse. The temperatures cover the range $0.01 \leq T_9 \leq 100.$ (0.862 keV $\leq$ kT ≤ 8.617 MeV) while the densities cover the range $10 \leq \rho/\mu_e$ (g cm^{-3}) $\leq 10^{11}$; thus, the electron gas ranges from non-degenerate to degenerate conditions, with electron Fermi energies approaching 25 MeV for the highest densities.

The nuclear weak rates computed here are important in determining the neutronization and neutrino energy loss rates during stellar evolution and collapse (Weaver and Woosley 1981, Arnett and Thielemann 1981). The outcome of stellar core collapse and bounce calculations depends on the previous neutronization history of the star and on electron capture during the collapse phase (Van Riper and Lattimer 1981, Baym, Bethe, and Brown 1981). Ultimately, the nuclear weak rates presented here will be important in determinations of the nucleosynthesis yields of the elements and their isotopes both during hydrostatic burning regimes and the subsequent collapse and explosive burning phases.

The nuclei whose stellar weak rates are computed here range in mass from A = 21 up to A = 60. These include many nuclei of astrophysical interest in the stellar conditions discussed above. Subsequent work will extend the rate survey presented here to include neutron-rich nuclei in the A = 60 to A = 75 mass range for use in the supernova problem. Concomitant with this extension in mass range will come an extension in the density range to include $\rho/\mu_e = 10^{12}$ g cm^{-3}. Of interest in the r-process and s-process are the weak transition rates of heavy neutron-rich nuclei at temperatures and densities which are relatively low compared to those encountered in the late stages of stellar evolution discussed above. In these less extreme conditions unmeasured

forbidden transitions and bound electron capture may be important. The reader is referred to Cosner and Truran (1981) for the most up-to-date treatment of the problem.

II. REVIEW OF STELLAR RATE COMPUTATION PROCEDURE

The stellar rate computation problem is shown schematically in Figure 1 for $T^<$ and $T^>$ nuclei. The $T^< \rightleftarrows T^>$ stellar transition rates must be computed. Some twenty discrete states are typically included in each nucleus for many of the cases considered here. The discrete state excitation energies, spins, and parities are taken from the experimental tabulations of Lederer et al. (1978) and Endt and van der Leun (1978) wherever possible. Isospin symmetry is used to obtain excitation energies, spins, and parities in unmeasured nuclei whose mirror nuclei are well studied. For very neutron-rich unmeasured nuclei, discrete state energies, spins, and parities are inferred from isotopes with similar shell structure. The discrete states in the $T^<$ ($T^>$) nucleus are denoted by $E^<$ ($E^>$) in Figure 1, while the resonant states are denoted by $R^<$ ($R^>$). The symbols also designate the energies of the discrete and resonant states.

The weak transition rate from the i^{th} state of the parent to the j^{th} state of the daughter nucleus is given by

$$\lambda_{ij} = \ell n\, 2 \frac{f_{ij}(T, \rho, U_F)}{(ft)_{ij}} \qquad (1)$$

where $(ft)_{ij}$ is the comparative half-life, which is related to the allowed weak-interaction matrix elements by equations (I-2a) and (I-2b) (I and II denote equations in papers I and II of this series,

respectively). The $f_{ij}(T,\rho,U_F)$ are the phase space factors for either electron or positron emission (eq. [I-3a]), continuum electron or positron capture (eq. [I-3b]), or the associated neutrino energy loss rates for these processes (eqs. [I-6a] and [I-6b]).

In principle weak transition matrix elements are required between all $E^<$ and $E^>$ discrete states. Experimentally determined transition matrix elements are employed where known, whether or not they correspond to allowed transitions. Unmeasured Gamow-Teller allowed transitions are assigned log ft = 5.0 (F^2N I and Gleit, Tang, and Coryell 1968), unless experiment gives an indication of log ft $\gg$ 5 despite satisfaction of the allowed selection rules. Such cases of hindered allowed transitions were assigned log ft = 99.9 where they might otherwise be important in the determination of low temperature, low density rates. More discussion of the low temperature, low density rates and the adjustment of experimental log ft values follows in the next section. Fermi transitions are assigned appropriate matrix elements according to equation (I-11). Unmeasured forbidden transitions are neglected due to the dominant effect of the large number of allowed transitions which contribute in most stellar environments. Some log ft values between the parent ground state and low-lying daughter states have been adjusted to reproduce measured laboratory decay rates using accurately computed f-values; this procedure is discussed further in § III.

In order to simulate transitions into and from the continuum, appropriately placed Gamow-Teller resonances are included in each stellar weak rate calculation with the procedure discussed in F^2N II. The excitation energies of the Gamow-Teller resonances are calculated on the basis of a simple shell model employing the tabulated single particle

energies of Seeger and Howard (1975). The procedure for computing the resonance excitation energy differs for $T^{<} \rightarrow T^{>}$ and $T^{>} \rightarrow T^{<}$ transitions; the reader is referred to §§ III and IV of F^2N II for an exhaustive discussion. The sum rules for $T^{<} \rightleftarrows T^{>}$ transitions are estimated by constructing a zero-order shell model configuration for the parent nucleus ground state and applying equation (II-16). The observed discrete state strength for transitions from the parent ground state is summed and subtracted from the equation (II-16) sum rule strength. The remaining strength is lumped into the ground-state $\rightleftarrows$ resonance-state transition.

Resonances corresponding to excited states are taken into account here with a special treatment of the population index for ground state $\rightleftarrows$ resonance transitions. This procedure is based on the assumptions of constant Q-value and sum rule for each discrete-state $\rightleftarrows$ corresponding-state transition and is discussed in detail in § V of F^2N II. In summary the contribution of the $E^{<} \rightarrow R^{>}$ transitions to the total $T^{<} \rightarrow T^{>}$ transition rate can be calculated by including only the $E_1^{<} \rightarrow R_1^{>}$ transition and setting the occupation index for the $E_1^{<}$ state in this transition equal to unity (cf. eqs. [II-43] and [II-44]). The $R^{<}$ to $E^{>}$ transitions proceed through the thermal population of the $R^{<}$ resonances. In the special procedure used in this calculations, the contribution of the $R^{<} \rightarrow E^{>}$ transitions to the total $T^{<} \rightarrow T^{>}$ transition rate can be calculated by including only the $R_1^{<} \rightarrow E_1^{>}$ transition. In addition, the occupation index for the $R_1^{<}$ state in this transition must be set equal to $P = (G^{>}/G^{<}) \exp(-R_1^{<}/kT)$ where $G^{<}$ and $G^{>}$ are the nuclear partition functions at the ambient temperature for the $T^{<}$ and $T^{>}$ nuclei respectively (cf. eqs. [II-52] and [II-53]). The generalization for the contribution of the $E^{>} \rightarrow R^{<}$ and $R^{>} \rightarrow E^{<}$ transitions to the total $T^{>} \rightarrow T^{<}$ transition

rate is obvious.

Fermi transitions involving excited states in the $T^{>}$ nucleus explicitely obey the constant Q-value and sum rule assumptions discussed above. Thus the contributions of these excited states plus that of the ground state to the $T^{>} \rightarrow T^{<}$ rate can be taken into account by calculating $E_1^{>} \rightarrow A_1^{<}$ where $A_1^{<}$ designates the analog state in the $T^{<}$ nucleus corresponding to the ground state of the $T^{>}$ nucleus. In addition the occupation index for the $E_1^{>}$ state in this transition must be set equal to unity. In the $T^{<} \rightarrow T^{>}$ transition the contribution of the analog states can be calculated for $A_1^{<} \rightarrow E_1^{>}$ and setting the population index for the $A_1^{<}$ state equal to $P = (G^{>}/G^{<}) \exp(-A_1^{<}/kT)$.

The total weak transition rate λ is given by

$$\lambda = \sum_i \sum_j P_i \lambda_{ij} \qquad (2)$$

where the sum on i is over parent states, the sum on j is over daughter states, and P_i is the occupation index defined by equation (I-9a), and modified in the manner discussed above for transitions involving resonances and analog states.

The phase space factors in equation (1) were computed numerically, and checked for electron and positron emission, at low temperature and density against the tables of log ft by Gove and Martin (1971). A number of low temperature, high density and high temperature, low density results were checked against easily performed analytic calculations. The definite integrals for the electron and positron emission phase space factors were done by 64-point Gaussian quadrature. The integrands of the electron and positron capture phase-space integrals are modulated strongly by the electron or positron distribution function, so that the

integrand has a characteristically slowly varying part and an exponentially decaying part, corresponding to the shape of the Fermi-Dirac distribution function. The portion of the improper integrals containing the slowly varying part of the integrand was done with 64-point Gaussian quadrature, and the exponential tail was treated with 32-point Gauss-Laguerre quadrature. For each nuclear transition a table of appropriate phase space factors as a function of q_n (eq. [I-3c]) was prepared at each temperature and density grid point and the f_{ij} and f_{ij}^{ν} (eqs. [I-3a], [I-3b], [I-6a], [I-6b]) were obtained by cubic spline interpolation in q_n. This procedure was checked for electron and positron capture in non-degenerate conditions against the analytic phase factors in Fowler and Hoyle (1964).

The free nucleons are unique "nuclei" in that they have no excited states. As a result the interpolation procedure described above for calculating weak phase factors was not used; free nucleon phase space factors were performed by direct numerical integration at each temperature and density point. The matrix elements for the free nucleon transitions are $|M_F|^2 = 1$ (log ft = 3.791 from I-2b) and $|M_{GT}|^2 = 3$ (log ft = 3.596 - log 3 = 3.118 from I-2a) to give an overall log ft = 3.035. (In F^2N I the value $[G_A/G_V]^2 = 1.567$ was used and the half-life of the neutron was taken to be 936 seconds). Nucleon recoil effects (forbidden transitions) are small at the temperatures and densities considered here and are therefore neglected. For a discussion of forbidden transitions see Fuller (1981).

III. RESULTS AND DISCUSSION

In this section the results of the stellar weak interaction

calculations are discussed. The terrestrial decay rates of the nuclear species considered in this survey are tabulated in Table 1 based on experimental measurements when available. These rates can be compared with the lowest temperature and density rates calculated in this work. The stellar rates are tabulated on the very abbreviated temperature and density grid shown in Table 2. As noted previously, the rates can be obtained by request on a detailed grid of temperature and density on magnetic tape.

The stellar rate magnetic tape has electron and positron emission rates, continuum electron and positron capture rates (in sec^{-1}), and the associated ν and $\bar{\nu}$ energy loss rates (in MeV s^{-1}) for the free nucleons and 226 nuclei with masses between A = 21 and A = 60 on a temperature-density grid which includes $0.01 \leq T_9 \leq 100$ and $10 \leq \rho/\mu_e$ (g cm^{-3}) $\leq 10^{11}$. In particular the rates are calculated at T_9 = 0.01, 0.1, 0.2, 0.4, 0.7, 1.0, 1.5, 2.0, 3.0, 5.0, 10.0, 30, and 100 for each density point at log (ρ/μ_e) = 1 to 11 by unit increment; thus there are 143 temperature-density points at which are computed the rates in sec^{-1} of the four weak processes and the sum of continuum electron capture plus positron emission, and continuum positron capture plus electron emission. In addition the total ν-energy loss rate and the total $\bar{\nu}$-energy loss rate in MeV sec^{-1} are given.

At higher temperatures or at higher densities nuclei are completely ionized in astrophysical environments and continuum electron capture predominates over bound state electron capture. At low density intermediate mass nuclei are thermally ionized in the range T_9 = 0.01 to 0.5, at low temperature nuclei are completely pressure ionized due to the combined effects of nuclear charge screening and continuum lowering. At zero temperature, for example, ^{56}Fe will become completely pressure

ionized for $\rho/\mu_e \gtrsim 10^4$ g cm^{-3}. In general, whenever the density of continuum electrons is larger than the K-shell electron density at the nucleus, then continuum electron capture dominates over bound state capture. In the low temperature-low density corner of the temperature-density grid used here bound state capture is important; we do not calculate bound state electron capture, only continuum capture.

An estimate of the bound state electron capture rate, for nuclear transitions where it is important, can be obtained from the terrestrial electron capture decay rate. Terrestrial electron capture decays generally proceed through the capture of electrons in low-lying atomic levels, usually K-shell electrons. Table 1 lists all of the nuclei considered in this survey together with their terrestrial decay modes and rates, where these quantities are known. The logarithms of the electron capture rates for a full K-shell can be read from this table. We designate these rates by λ_K.

As the temperature rises at a given density in a stellar environment the occupation of the K-shell is reduced from two electrons to one at a critical value of the temperature. Similarly at a given temperature the occupation of the K-shell increases from zero to one as the density rises to a critical value. Following Iben, Kalata, and Schwartz (1967) this critical density neglecting screening is given by

$$\left(\frac{\rho}{\mu_e}\right)_c = 2.536 \times 10^5 \, T_9^{3/2} \exp[-1.58 \times 10^{-4} \, (Z - 0.31)^2/T_9] \text{ g cm}^{-3} \quad (3)$$

where $Z - 0.31$ is the effective charge of the capturing nucleus. For example, for $^{49}_{23}V + e^- \rightarrow {}^{49}_{22}Ti + \nu_e$ one finds $(\rho/\mu_e)_c = 0.07$ g cm^{-3} for $T_9 = 0.01$, 3.55×10^3 g cm^{-3} for $T_9 = 0.1$, and 2.34×10^5 g cm^{-3} for

$T_9 = 1$. Below these critical densities the total capture rate is given by the continuum capture rate, λ_C, alone while above these critical densities the total rate is $\lambda_C + \lambda_K$. The transition is not an abrupt one since $\lambda_C \sim \lambda_K$ near the critical transition density and $\lambda_C > \lambda_K$ above this density. For somewhat more accurate calculations a monotonically increasing function of $y = \log (\rho/\mu_e)/(\rho/\mu_e)_c$ can be used passing through $\lambda_C + \lambda_K/3$ at $y \approx -0.3$, $\lambda_C + \lambda_K/2$ at $y = 0$, and $\lambda_C + 2\lambda_K/3$ at $y \approx +0.3$.

The first column in Table 1 gives the parent nucleus while the second column gives the daughter. In the stellar rate computations both forward and reverse rates are calculated and the labels "parent" and "daughter" can alternately apply to both nuclei linked by weak transitions. For example, in the laboratory ^{56}Mn decays by electron emission to ^{56}Fe and this terrestrial decay rate is listed in Table 1; but at high density and temperature $^{56}\text{Fe} \rightarrow {}^{56}\text{Mn}$ proceeds via continuum electron capture at high electron Fermi energy and/or via positron emission through thermally populated ^{56}Fe excited states. The stellar rates for both $^{56}\text{Fe} \rightarrow {}^{56}\text{Mn}$ and $^{56}\text{Mn} \rightarrow {}^{56}\text{Fe}$ are computed. The third column in Table 1 gives the terrestrial decay mode, either β^- for electron emission, β^+ for positron emission, ϵ^- for electron capture, IT for γ-ray transition from a nuclear isomeric state (listed separately with an "m" e.g., $^{24}\text{Na}^m$) to the ground state. In addition, the sum of the rates for the various laboratory decay processes is denoted as "SUM." Where it is known that proton, neutron, or alpha-particle emission from the daughter follows a weak decay process, then that process is designated as, for example, β^+p, β^-n, $\beta^+\alpha$ respectively. In these cases the final nucleus resulting after particle emission from the daughter is listed after the daughter nucleus in column 2. For example, ^{21}Mg decays by positron emission to ^{21}Na which subsequently de-

cays by proton emission to ^{20}Ne.

As indicated in equations (I-3a) and (I-3b), we have found it far simpler to use total particle energies, rest-mass plus kinetic rather than kinetic, and to use nuclear Q-values rather than atomic. Thus, column 4 in Table 1 lists the nuclear Q-value, Q_n, for each nuclear transition where

$$Q_n = M_p c^2 - M_d c^2 \tag{4}$$

with M_p the nuclear mass of the parent ground state and M_d that of the daughter ground state. The dominant allowed transitions may involve excited states in the daughter nucleus. Differential atomic binding energies are negligible and have not been included. In the emission of both positrons and electrons the maximum kinetic energy is given by $Q_n - m_e c^2 = Q_n - 0.511$ MeV and in the capture of positrons and electrons the minimum energy of the antineutrinos or neutrinos is $Q_n + m_e c^2 = Q_n + 0.511$ MeV. On the other hand, the tabulated Fermi energies, U_F, are kinetic energies but can easily be converted to total energies, $W_F = U_F + m_e c^2 = U_F + 0.511$ MeV. Finally, column 5 lists the logarithms of the indicated rates. Those entries in parentheses are cases where no terrestrial decay rate is known and the lowest temperature and density stellar rate from our calculations or an estimate (EST) is provided instead. Exoergic transitions, which are highly forbidden so that the "parent" nucleus is essentially stable, e.g., ^{50}V, are indicated by (HI FRB). At the lowest temperature, $T_9 = 0.01$, excited parent states are almost never appreciably populated, while at the lowest density, $\rho/\mu_e = 10$ g cm^{-3}, the continuum electron density is quite low and, except for electron capture, the stellar rates should be quite close to the

terrestrial values. The exception noted arises because only continuum electron capture and not bound state capture is calculated.

It transpires that the rates calculated for the lowest temperature-density points and the terrestrial rates often disagree. This is because what experimentalists actually measure are branching intensities, not matrix elements. To convert branching intensities for various transitions into log ft-values, equivalent to matrix elements, requires two input quantities: the overall lifetime of the decaying nucleus, and the f-factors (phase space factors) for each of the individual transitions. There is no difficulty with the lifetimes, which are commonly very accurately known, but the appropriate f-factors are usually complicated integrals involving electron and neutrino energies and the Coulomb correction factors (cf. eqs. [I-3a], [I-3b], [I-5b] and Gove and Martin 1971, page 208) which require approximations in actual calculations. Some authors use the tables of log f by Gove and Martin (1971), others use approximate f-factor formulae; some authors use f-factors appropriate for first forbidden transitions (denoted with subscript 1 in Lederer et al. 1978) while others use only allowed phase space factors. In short, the log ft-values tabulated in Endt and van der Leun (1978) and Lederer et al. (1978) are in some cases calculated by methods unknown to us. The f-factors in our stellar rate program are calculated as accurately is possible, using detailed numerical integrations, but these are not applicable if the published log ft-values have been calculated using an unknown approximation to f.

In order to resolve this problem insofar as possible, log ft values were recalculated for cases where the appropriate lowest temperature-

density point stellar rate differed from the terrestrial rate by more than 30% ($\Delta \log \gtrsim 0.1$). The lowest temperature-density point stellar rates presented on the magnetic tape and in this paper differ from the terrestrial decay rates, where known, by no more than 30%, except, as noted, in the case of electron capture.

An example of a reaction where the log ft values were adjusted in this manner is the $^{51}Sc \rightarrow {}^{51}Ti$ electron emission transition. Several log ft values were measured for this and presented in Lederer et al. (1980): from the ^{51}Sc ground state ($J^{\pi} = 7/2^-$) to state 3 ($7/2^-$) of ^{51}Ti, log ft = 5.5; to state 5 ($5/2^-$), log ft = 5.0. In addition, the ground state to state 4 ($5/2^-$) transition is clearly allowed, yet no branch was observed, so that this transition was assigned log ft = 99.9. When the lowest temperature-density point stellar rate calculation was performed the electron emission result was log β^- = 1.059, roughly 50% faster than the known terrestrial decay rate (from the lifetime) namely log β^- = 1.2536. The rate for the ground state to state 3 transition was adjusted to log ft = 5.9, while the rate for the ground state to state 5 was adjusted to log ft = 5.3. When the stellar rates were recalculated the lowest temperature-density point result became log β^- = -1.261, in agreement with the terrestrial rate to better than 2%. This type of procedure was repeated whenever the calculated rate differed from the terrestrial value by 30% or more. This procedure guaranteed that the input data used in the calculations described in this paper are consistent with measurements of terrestrial decay rates.

Table 3 presents the results of the stellar weak rate calculations for free nucleons and the nuclei in Table 1 on an abbreviated tempera-

ture and density grid (Table 2) for log (ρ/μ_e) = 3, 7, 11 and for T_9 = 1, 3, 10, 100. The notation and format of these rate tables are similar to those in F^{2}N I, but the entries presenting the temperature and density are replaced with a single entry (1 to 12) describing a temperature-density combination listed in Table 2.

The remaining columns in Table 3 are the logarithm of the positron emission rate, log β^+, the logarithm of the continuum electron capture rate, log ϵ^-, the logarithm of the total ν-energy loss rate (in MeV s^{-1}), log ν, the logarithm of the electron emission rate, log β^-, the logarithm of the continuum positron capture rate, log ϵ^+, and finally the logarithm of the total $\bar{\nu}$ energy loss rate (in MeV s^{-1}), log $\bar{\nu}$. It is again emphasized that this rate table is reproduced on a wide mesh temperature and density grid designed only to provide active investigators with a readily accessible means for estimating stellar nuclear weak rates. For accurate calculations involving stellar evolution or nucleosynthesis problems readers are urged to write MJN and request the stellar weak rate magnetic tape.

REFERENCES

Arnett, W. D., and Thielemann, F. K. 1981, in preparation.

Baym, G., Bethe, H. A., and Brown, G. E. 1981, preprint.

Cosner, K., and Truran, J. W. 1981, University of Illinois preprint.

Endt, P. M., and van der Leun, C. 1973, Nucl. Phys., A214, 1.

Fowler, W. A., and Hoyle F. 1964, Ap. J. Suppl., 9, 201.

Fuller, G. M. 1981, preprint.

Fuller, G. M., Fowler, W. A., and Newman, M. J. 1980, Ap. J. Suppl., 42, 447.

_____. 1981, preprint.

Gleit, C. E., Tang, C. W., and Coryell, C. D. 1968, Nucl. Data Sheets, 13, 5.

Gove, N. B., and Martin, M. J. 1971, Nuclear Data Tables, 10, 205.

Iben, I., Jr., Kalata, K., and Schwarz, J. 1967, Ap. J., 150, 1001.

Lederer, D. M. et al. 1978, Tables of Isotopes, eds. Lederer, C. M., and Shirley, V. S. (New York: Wiley and Sons).

Seeger, P. A., and Howard, W. M. 1975, Nucl. Phys., A238, 491.

Van Riper, K. A., and Lattimer, J. M. 1981, preprint.

Weaver, T. A., and Woosley, S. E. 1981, in preparation.

TABLE 1a

TERRESTRIAL WEAK INTERACTION RATES (s^{-1})

PARENT	DAUGHTER	DECAY	Q_n(MeV)	LOG RATE
n	p	β^-	1.293	-2.972
^{21}O	^{21}F	β^-	8.678	(+0 EST)
^{21}F	^{21}Ne	β^-	6.197	-0.795
^{21}Na	^{21}Ne	β^+	3.036	-1.511
^{21}Mg	$^{21}Na\,^{20}Ne$	β^+p	12.587	+0.751
^{22}F	^{22}Ne	β^-	11.364	-0.786
^{22}Na	^{22}Ne	β^+	2.331	-8.117
		ϵ^-	2.331	-9.096
		SUM		-8.074
^{22}Mg	^{22}Na	β^+	4.279	-0.746
^{23}F	^{23}Ne	β^-	9.021	-0.502
^{23}Ne	^{23}Na	β^-	4.886	-1.734
^{23}Mg	^{23}Na	β^+	3.548	-1.212
^{23}Al	$^{23}Mg\,^{22}Na$	β^+p	11.727	+0.169
^{24}Ne	^{24}Na	β^-	2.979	-2.466
^{24}Na	^{24}Mg	β^-	6.024	-4.892
$^{24}Na^m$	^{24}Na	IT	0.472	+1.535
	^{24}Mg	β^-	6.494	(-2 EST)
^{24}Al	$^{24}Mg\,^{20}Ne$	$\beta^+\alpha$	13.367	-0.475
$^{24}Al^m$	^{24}Al	IT	0.439	+0.695
	$^{24}Mg\,^{20}Ne$	$\beta^+\alpha$	13.806	-0.428
		SUM		+0.727
^{24}Si	^{24}Al	β^+	10.281	(+0.560)
^{25}Ne	^{25}Na	β^-	7.711	+0.0627
^{25}Na	^{25}Mg	β^-	4.344	-1.937
^{25}Al	^{25}Mg	β^+	3.767	-1.015
^{25}Si	$^{25}Al\,^{24}Mg$	β^+p	12.226	+0.498
^{26}Na	^{26}Mg	β^-	9.836	-0.189
^{26}Al	^{26}Mg	β^+	3.494	-13.602
		ϵ^-	3.494	-14.260
		SUM		-13.516
$^{26}Al^m$	^{26}Mg	β^+	3.722	-0.963
^{26}Si	^{26}Al	β^+	4.553	-0.504
^{27}Na	$^{27}Mg\,^{26}Mg$	β^-n	9.466	+0.364
^{27}Mg	^{27}Al	β^-	3.120	-2.913
^{27}Si	^{27}Al	β^+	4.298	-0.775
^{27}P	^{27}Si	β^+	11.284	(+0.454)
^{28}Na	$^{28}Mg\,^{27}Mg$	β^-n	14.397	+1.349
^{28}Mg	^{28}Al	β^-	2.343	-5.038
^{28}Al	^{28}Si	β^-	5.154	-2.288
^{28}P	^{28}Si	β^+	13.821	+0.409
^{28}S	^{28}P	β^+	10.839	(+0.491)

TABLE 1b

TERRESTRIAL WEAK INTERACTION RATES (s^{-1})

PARENT	DAUGHTER	DECAY	Q_n(MeV)	LOG RATE
^{29}Na	$^{29}Mg\,^{28}Mg$	β^-n	13.921	+1.207
^{29}Mg	^{29}Al	β^-	7.973	-0.305
^{29}Al	^{29}Si	β^-	4.192	-2.757
^{29}P	^{29}Si	β^+	4.433	-0.772
^{29}S	$^{29}P\ ^{29}Si$	β^+p	13.278	+0.562
^{30}Na	$^{30}Mg\,^{29}Mg$	β^-n	18.681	+1.108
^{30}Mg	^{30}Al	β^-	6.611	-0.238
^{30}Al	^{30}Si	β^-	9.050	-0.726
^{30}P	^{30}Si	β^+	3.716	-2.335
		ϵ^-	3.716	-5.241
		SUM		-2.335
^{30}S	^{30}P	β^+	5.631	-0.238
^{31}Na	$^{31}Mg\,^{30}Mg$	β^-n	15.021	+1.610
^{31}Mg	^{31}Al	β^-	11.711	(+1 EST)
^{31}Al	^{31}Si	β^-	8.360	+0.0346
^{31}Si	^{31}P	β^-	2.002	-4.134
^{31}S	^{31}P	β^+	4.884	-0.574
^{31}Cl	^{31}S	β^+	11.463	(+0.405)
^{32}Na	^{32}Mg	β^-	19.811	+1.679
^{32}Mg	^{32}Al	β^-	8.911	(+0 EST)
^{32}Al	^{32}Si	β^-	13.311	(+1 EST)
^{32}Si	^{32}P	β^-	0.724	-9.694
^{32}P	^{32}S	β^-	2.221	-6.250
^{32}Cl	$^{32}S\,^{31}P\,^{28}Si$	$\beta^+p\alpha$	12.176	+0.367
^{32}Ar	^{32}Cl	β^+	10.608	(+0.308)
^{33}Na	^{37}Mg	β^-	18.711	+1.540
^{33}Mg	^{33}Al	β^-	14.011	(+1 EST)
^{33}Al	^{33}Si	β^-	11.711	(+1 EST)
^{33}Si	^{33}P	β^-	6.278	-0.952
^{33}P	^{33}S	β^-	0.760	-6.499
^{33}Cl	^{33}S	β^+	5.072	-0.559
^{33}Ar	$^{33}Al\,^{32}S$	β^+p	11.107	+0.586
^{34}Si	^{34}P	β^-	4.811	-0.606
^{34}P	^{34}S	β^-	5.892	-1.253
^{34}Cl	^{34}S	β^+	4.982	-0.343
$^{34}Cl^m$	^{34}S	IT	0.146	-3.770
		β^+	5.128	-3.718
		SUM		-3.442

TABLE 1c

TERRESTRIAL WEAK INTERACTION RATES (s^{-1})

PARENT	DAUGHTER	DECAY	Q_n(MeV)	LOG RATE
^{34}Ar	^{34}Cl	β^+	5.548	-0.0855
^{35}P	^{35}S	β^-	4.417	-1.831
^{35}S	^{35}Cl	β^-	0.678	-7.037
^{35}Ar	^{35}Cl	β^+	5.454	-0.410
^{35}K	^{35}Ar	β^+	11.369	(+0.592)
^{36}Cl	^{36}Ar	β^-	1.221	-13.144
		ϵ^-	0.633	-14.857
		β^+	0.633	-17.905
		SUM		-13.135
^{36}K	^{36}Ar	β^+	12.294	+0.309
^{36}Ca	^{36}K	β^+	10.265	(+0.538)
^{37}S	^{37}Cl	β^-	5.365	-2.636
^{37}Ar	^{37}Cl	ϵ^-	0.303	-6.640
^{37}K	^{37}Ar	β^+	5.638	-0.249
^{37}Ca	$^{37}K\ ^{36}Ar$	β^+	11.125	+0.603
^{38}S	^{38}Cl	β^-	3.447	-4.168
^{38}Cl	^{38}Ar	β^-	5.428	-3.509
$^{38}Cl^m$	^{38}Cl	IT	0.671	-0.0135
^{38}K	^{38}Ar	β^+	5.402	-2.819
$^{38}K^m$	^{38}Ar	β^+	5.532	-0.128
^{38}Ca	^{38}K	β^+	6.231	+0.197
^{39}Cl	^{39}Ar	β^-	3.949	-3.686
^{39}Ar	^{39}K	β^-	1.076	-10.088
^{39}Ca	^{39}Ca	β^+	6.013	-0.0937
^{40}Cl	^{40}Ar	β^-	8.011	-2.068
^{40}K	^{40}Ca	β^-	1.823	-16.815
	^{40}Ar	ϵ^-	0.994	-17.736
		β^+	0.994	-21.765
		SUM		-16.765
^{40}Sc	$^{40}Ca\ ^{39}K$	β^+p	13.809	+0.581
^{40}Ti	^{40}Sc	β^+	10.976	(+0.645)
^{41}Cl	^{41}Ar	β^-	6.179	-1.691
^{41}Ar	^{41}K	β^-	3.003	-3.978
^{41}Ca	^{41}K	ϵ^-	-0.0897	-12.658
^{41}Sc	^{41}Ca	β^+	5.984	+0.0656
^{41}Ti	^{41}Sc	β^+p	12.351	+0.938
^{42}Ar	^{42}K	β^-	1.114	-9.177
^{42}K	^{42}Ca	β^-	4.032	-4.807
^{42}Sc	^{42}Ca	β^+	5.912	+0.0070
$^{42}Sc^m$	^{42}Ca	β^+	6.529	-1.952

TABLE 1d

TERRESTRIAL WEAK INTERACTION RATES (s^{-1})

PARENT	DAUGHTER	DECAY	Q_n(MeV)	LOG RATE
^{42}Ti	^{42}Sc	β^+	6.488	+0.540
^{43}Cl	^{43}Ar	β^-	9.351	(-2.341)
^{43}Ar	^{43}K	β^-	5.119	-2.670
^{43}K	^{43}Ca	β^-	2.328	-5.064
^{43}Sc	^{43}Ca	$\beta^+\epsilon^-$	1.709	-4.305
^{43}Ti	^{43}Sc	β^+	6.350	+0.151
^{44}Ar	^{44}K	β^-	4.047	-3.013
^{44}K	^{44}Ca	β^-	6.170	-3.282
^{44}Sc	^{44}Ca	β^+	3.144	-4.332
		ϵ^-	3.144	-5.611
		SUM		-4.310
$^{44}Sc^m$	^{44}Sc	IT	0.271	-5.489
	^{44}Ca	ϵ^-	3.415	-7.340
		SUM		-5.483
^{44}Ti	^{44}V	ϵ^-	-0.246	-9.330
^{44}V	$^{44}Ti\,^{40}Ca$	$\beta^+\alpha$	13.185	+0.887
^{45}K	^{45}Ca	β^-	4.709	-3.238
^{45}Ca	^{45}Sc	β^-	0.768	-7.313
$^{45}Sc^m$	^{45}Sc	IT	0.0124	+0.349
^{45}Ti	^{45}Sc	$\beta^+\epsilon^-$	1.552	-4.205
^{45}V	^{45}Ti	β^+	6.614	(-0.034)
^{45}Cr	$^{45}V\,^{44}Ti$	β^+p	11.908	+1.142
^{46}K	^{46}Ca	β^-	8.229	-2.220
^{46}Sc	^{46}Ca	$\beta^-\epsilon^-$	0.872	(HI FRB)
^{46}Sc	^{46}Ti	β^-	2.878	-7.019
$^{46}Sc^m$	^{46}Sc	IT	0.143	-1.431
^{46}V	^{46}Ti	β^+	6.541	0.214
^{46}Cr	^{46}V	β^+	7.099	0.426
^{47}K	^{47}Ca	β^-	7.156	-1.402
^{47}Ca	^{47}Sc	β^-	2.499	-5.752
^{47}Sc	^{47}Ti	β^-	1.112	-5.630
^{47}V	^{47}Ti	$\beta^+\epsilon^-$	2.419	-3.451
^{47}Cr	^{47}V	β^+	6.872	(+0.052)
^{48}K	^{48}Ca	β^-	12.507	-0.922
^{48}Ca	^{48}Sc	β^-	0.792	(HI FRB)
^{48}Sc	^{48}Ti	β^-	4.501	-5.356
^{48}V	^{48}Ti	ϵ^-	3.504	-6.597
		β^+	3.504	-6.604
		SUM		-6.299
^{48}Cr	^{48}V	ϵ^-	1.144	(-5.049)

TABLE 1e

TERRESTRIAL WEAK INTERACTION RATES (s^{-1})

PARENT	DAUGHTER	DECAY	Q_n(MeV)	LOG RATE
^{49}K	^{49}Ca	β^-	14.038	≤ -0.460
^{49}Ca	^{49}Sc	β^-	5.779	-2.878
^{49}Sc	^{49}Ti	β^-	2.515	-3.693
^{49}V	^{49}Ti	ϵ^-	0.0908	-7.614
^{49}Cr	^{49}V	$\beta^+\epsilon^-$	2.117	-3.560
^{49}Mn	^{49}Cr	β^+	7.205	(+0.168)
^{49}Fe	$^{49}Mn\,^{48}Cr$	β^+p	12.632	+0.996
^{50}K	^{50}Ca	β^-	16.511	≈+0.364
^{50}Ca	^{50}Sc	β^-	5.478	-1.305
^{50}Sc	^{50}Ti	β^-	7.404	-2.170
$^{50}Sc^m$	^{50}Sc	IT	0.257	+0.297
^{50}V	^{50}Ti	$\beta^+\epsilon^-$	1.702	(HI FRB)
^{50}V	^{50}Cr	β^-	1.550	(HI FRB)
^{50}Mn	^{50}Cr	β^+	7.121	+0.389
$^{50}Mn^m$	^{50}Cr	β^+	7.351	-2.178
^{51}Sc	^{51}Ti	β^-	7.024	-1.253
^{51}Ti	^{51}V	β^-	2.977	-2.701
^{51}Cr	^{51}V	ϵ^-	0.240	-6.538
^{51}Mn	^{51}Cr	$\beta^+\epsilon^-$	2.697	-3.602
^{52}Ti	^{52}V	β^-	2.481	-2.168
^{52}V	^{52}Cr	β^-	4.488	-2.513
^{52}Mn	^{52}Cr	ϵ^-	4.200	-5.986
		β^+	4.200	-6.396
		SUM		-5.843
$^{52}Mn^m$	^{52}Cr	$\beta^+\epsilon$	4.578	-3.269
	^{52}Mn	IT	0.378	-5.019
		SUM		-3.262
^{52}Fe	^{52}Mn	β^+	1.861	-4.877
		ϵ	1.861	-5.000
		SUM		-4.633
^{53}Ti	^{53}V	β^-	5.484	-1.678
^{53}V	^{53}Cr	β^-	3.932	-2.141
^{53}Mn	^{53}Cr	ϵ^-	0.0853	-14.226
^{53}Fe	^{53}Mn	$\beta^+\epsilon^-$	3.232	-2.867
$^{53}Fe^m$	^{53}Fe	IT	3.041	-2.340
^{53}Co	^{53}Fe	β^+	7.793	+0.426
$^{53}Co^m$	^{53}Fe	β^+	10.983	+0.436
	^{52}Fe	p	1.597	-1.381
		SUM		+0.443
^{53}Ni	^{53}Co	β^+p	12.719	+1.142

TABLE 1f

TERRESTRIAL WEAK INTERACTION RATES (s^{-1})

PARENT	DAUGHTER	DECAY	Q_n(MeV)	LOG RATE
^{54}V	^{54}Cr	β^-	7.512	-1.793
^{54}Mn	^{54}Cr	ϵ^-	0.866	-7.590
^{54}Mn	^{54}Fe	β^-	1.208	(HI FRB)
^{54}Co	^{54}Fe	β^+	7.731	+0.555
$^{54}Co^m$	^{54}Fe	β^+	7.930	-2.102
^{55}Ti	^{55}V	β^-	9.151	(+0.130)
^{55}V	^{55}Cr	β^-	6.607	(-0.486)
^{55}Cr	^{55}Mn	β^-	3.115	-2.488
^{55}Fe	^{55}Mn	ϵ^-	-0.280	-8.090
^{55}Co	^{55}Fe	β^+	2.944	-5.072
		ϵ^-	2.944	-5.597
		SUM		-4.959
^{56}Sc	^{56}Ti	β^-	16.251	(+0.957)
^{56}Ti	^{56}V	β^-	6.801	(+0 EST)
^{56}V	^{56}Cr	β^-	9.566	(+0.505)
^{56}Cr	^{56}Mn	β^-	2.154	-2.708
^{56}Mn	^{56}Fe	β^-	4.206	-4.127
^{56}Co	^{56}Fe	ϵ^-	4.057	-7.084
		β^+	4.057	-7.713
		SUM		-6.992
^{56}Ni	^{56}Co	ϵ^-	1.625	-5.881
^{57}Ti	^{57}V	β^-	11.232	(+0.704)
^{57}V	^{57}Cr	β^-	8.440	(-0.528)
^{57}Cr	^{57}Mn	β^-	5.208	(-0.439)
^{57}Mn	^{57}Fe	β^-	3.203	-2.141
^{57}Co	^{57}Fe	ϵ^-	0.316	-7.529
^{57}Ni	^{57}Co	ϵ^-	2.755	-5.494
		β^+	2.755	-5.670
		SUM		-5.272
^{57}Cu	^{57}Ni	$\beta^+\epsilon^-$	7.968	+0.586
^{57}Zn	^{57}Cu	β^+p	14.479	+1.239
^{58}Ti	^{58}V	β^-	8.611	(+0.239)
^{58}V	^{58}Cr	β^-	12.911	(+0.176)
^{58}Cr	^{58}Mn	β^-	4.671	(-0.904)
^{58}Mn	^{58}Fe	β^-	6.831	-0.636
$^{58}Mn^m$	^{58}Fe	β^-	6.861	-1.972
^{58}Co	^{58}Fe	ϵ^-	1.797	-7.016
		β^+	1.797	-7.770
		SUM		-6.946
^{58}Co	^{58}Ni	β^-	0.891	(HI FRB)
$^{58}Co^m$	^{58}Co	IT	0.0249	-4.679
^{58}Cu	^{58}Ni	β^+	8.052	(-0.664)

TABLE 1g

TERRESTRIAL WEAK INTERACTION RATES (s^{-1})

PARENT	DAUGHTER	DECAY	Q_n(MeV)	LOG RATE
^{59}V	^{59}Cr	β^-	10.161	(+0.005)
^{59}Cr	^{59}Mn	β^-	9.011	(-0.002)
^{59}Mn	^{59}Fe	β^-	5.692	(-1.012)
^{59}Fe	^{59}Co	β^-	2.076	-6.745
^{59}Ni	^{59}Co	ϵ^-	0.562	-12.533
		β^+	0.562	-19.357
		SUM		-12.533
^{59}Cu	^{59}Ni	β^+	4.290	-2.073
^{60}Ti	^{60}V	β^-	10.721	(+0.601)
^{60}V	^{60}Cr	β^-	14.911	(+1 EST)
^{60}Cr	^{60}Mn	β^-	5.771	(-0.802)
^{60}Mn	^{60}Fe	β^-	10.228	(+0 EST)
^{60}Fe	^{60}Co	β^-	0.720	-13.135
^{60}Co	^{60}Ni	β^-	3.335	-8.380
$^{60}Co^m$	^{60}Co	IT	0.0586	-2.960
		β^-	3.394	-5.561
		SUM		-2.959
^{60}Cu	^{60}Ni	β^+	5.616	-3.338
		ϵ^-	5.616	-4.461
		SUM		-3.307
^{60}Zn	^{60}Cu	β^+	3.648	-2.331
		ϵ^-	3.648	-3.840
		SUM		-2.318

TABLE 2

THE TEMPERATURE AND DENSITY POINTS (pt) AT WHICH THE RATES IN TABLE 3 ARE EVALUATED. THE TEMPERATURE IS IN BILLIONS OF DEGREES AND ρ/μ_e IS IN g cm^{-3}.

pt	T_9	log (ρ/μ_e)
1	1	3
2	3	3
3	10	3
4	100	3
5	1	7
6	3	7
7	10	7
8	100	7
9	1	11
10	3	11
11	10	11
12	100	11

TABLE 3

THE STELLAR WEAK RATES EVALUATED AT THE TEMPERATURE AND DENSITY POINTS, pt, GIVEN IN TABLE 2. THE RATES β^+, ε^-, β^-, ε^+ ARE IN s^{-1}. THE NEUTRINO ENERGY LOSS RATES ν AND $\overline{\nu}$ ARE IN MeV s^{-1}. BASE TEN LOGARITHMS ARE PRESENTED.

	$^{1}p \rightarrow {}^{1}n$			$^{1}n \rightarrow {}^{1}p$		
pt	log β^+	log ε^-	log ν	log β^-	log ε^+	log $\bar{\nu}$
1	-99.999	-10.546	-11.083	-2.968	-6.767	-3.281
2	-99.999	-4.722	-4.726	-2.987	-2.744	-2.299
3	-99.999	-1.042	-0.457	-3.109	-0.422	0.297
4	-99.999	4.286	5.920	-3.247	4.340	5.987
5	-99.999	-4.741	-5.271	-4.303	-11.586	-4.922
6	-99.999	-3.017	-3.015	-3.457	-4.448	-3.632
7	-99.999	-0.944	-0.359	-3.139	-0.517	0.201
8	-99.999	4.286	5.920	-3.247	4.340	5.987
9	-99.999	4.409	5.682	-99.999	-99.999	-99.999
10	-99.999	4.410	5.684	-41.704	-42.926	-41.985
11	-99.999	4.419	5.701	-14.560	-12.416	-11.703
12	-99.999	4.982	6.632	-3.737	3.618	5.261

	$^{21}Ne \rightarrow {}^{21}F$			$^{21}F \rightarrow {}^{21}Ne$		
pt	log β^+	log ε^-	log ν	log β^-	log ε^+	log $\bar{\nu}$
1	-45.998	-35.139	-35.705	-0.759	-6.202	-0.295
2	-16.335	-13.090	-13.142	-0.759	-3.211	-0.289
3	-6.138	-3.968	-3.390	-0.790	-1.098	0.033
4	1.299	4.241	5.879	2.861	4.669	6.347
5	-45.998	-29.322	-29.890	-0.783	-12.021	-0.332
6	-16.330	-11.379	-11.430	-0.779	-4.915	-0.322
7	-6.125	-3.870	-3.293	-0.795	-1.193	-0.016
8	1.299	4.241	5.879	2.861	4.669	6.347
9	-45.998	3.170	4.074	-91.464	-99.999	-92.055
10	-16.330	3.179	4.088	-30.380	-43.393	-30.503
11	-6.067	3.240	4.168	-7.960	-13.090	-7.594
12	1.429	4.943	6.589	2.544	3.948	5.625

	$^{21}Mg \rightarrow {}^{21}Na$			$^{21}Na \rightarrow {}^{21}Mg$		
pt	log β^+	log ε^-	log ν	log β^-	log ε^+	log $\bar{\nu}$
1	0.741	-4.186	1.462	-99.999	-66.837	-67.411
2	0.721	-1.835	1.446	-33.550	-22.913	-22.985
3	0.708	0.095	1.593	-8.811	-6.496	-5.986
4	3.793	5.388	7.139	-0.181	3.713	5.290
5	0.741	-0.406	1.502	-99.999	-72.657	-73.230
6	0.721	-0.398	1.488	-33.557	-24.629	-24.701
7	0.710	0.188	1.624	-8.813	-6.595	-6.084
8	3.793	5.389	7.139	-0.181	3.713	5.290
9	0.741	4.929	6.243	-99.999	-99.999	-99.999
10	0.721	4.918	6.230	-62.197	-63.107	-62.278
11	0.716	4.877	6.185	-17.987	-18.507	-17.517
12	3.877	6.063	7.827	-0.602	2.985	4.561

	$^{21}F \rightarrow {}^{21}O$			$^{21}O \rightarrow {}^{21}F$		
pt	log β^+	log ε^-	log ν	log β^-	log ε^+	log $\bar{\nu}$
1	-66.641	-49.924	-50.503	-2.181	-8.261	-1.546
2	-20.040	-18.064	-18.139	-0.877	-3.954	-0.243
3	-7.110	-5.449	-4.792	-0.461	-1.295	0.285
4	0.333	3.929	5.557	2.963	4.790	6.477
5	-66.641	-44.105	-44.684	-2.190	-14.081	-1.560
6	-20.032	-16.350	-16.431	-0.885	-5.658	-0.256
7	-7.100	-5.352	-4.697	-0.464	-1.391	0.264
8	0.333	3.929	5.557	2.963	4.790	6.477
9	-66.641	2.710	3.493	-79.048	-99.999	-79.640
10	-20.032	2.725	3.521	-26.483	-44.135	-26.606
11	-7.055	2.779	3.598	-6.972	-13.289	-6.607
12	0.482	4.632	6.269	2.645	4.071	5.755

	$^{21}Na \rightarrow {}^{21}Ne$			$^{21}Ne \rightarrow {}^{21}Na$		
pt	log β^+	log ε^-	log ν	log β^-	log ε^+	log $\bar{\nu}$
1	-1.479	-5.060	-1.321	-25.810	-19.741	-20.308
2	-1.522	-2.691	-1.287	-11.492	-7.788	-7.842
3	-1.342	-0.624	0.231	-3.510	-2.326	-1.751
4	1.621	4.889	6.549	0.580	4.505	6.136
5	-1.479	-1.245	-0.552	-27.896	-25.561	-26.125
6	-1.518	-1.239	-0.526	-11.769	-9.504	-9.555
7	-1.335	-0.530	0.319	-3.515	-2.425	-1.844
8	1.621	4.889	6.549	0.580	4.505	6.136
9	-1.479	4.693	5.920	-99.999	-99.999	-99.999
10	-1.518	4.682	5.906	-46.529	-47.981	-46.658
11	-1.303	4.679	5.906	-13.472	-14.337	-13.109
12	1.765	5.579	7.255	0.138	3.782	5.409

	$^{22}Mg \rightarrow {}^{22}Na$			$^{22}Na \rightarrow {}^{22}Mg$		
pt	log β^+	log ε^-	log ν	log β^-	log ε^+	log $\bar{\nu}$
1	-0.708	-4.470	-0.472	-50.789	-26.281	-26.848
2	-0.717	-2.078	-0.435	-16.812	-10.156	-10.213
3	-0.673	-0.137	0.756	-4.907	-3.332	-2.787
4	2.623	5.181	6.874	-0.199	4.230	5.834
5	-0.708	-0.665	0.108	-50.812	-32.101	-32.668
6	-0.715	-0.629	0.155	-16.832	-11.872	-11.929
7	-0.666	-0.044	0.842	-4.913	-3.430	-2.884
8	2.623	5.181	6.875	-0.199	4.229	5.834
9	-0.708	4.970	6.256	-99.999	-99.999	-99.999
10	-0.714	4.966	6.252	-49.587	-60.350	-49.656
11	-0.636	4.893	6.170	-15.065	-15.343	-14.529
12	2.745	5.864	7.574	-0.648	3.503	5.105

	$^{22}Na \rightarrow {}^{22}Ne$			$^{22}Ne \rightarrow {}^{22}Na$		
pt	log β^+	log ε^-	log ν	log β^-	log ε^+	log $\bar{\nu}$
1	-6.159	-8.653	-6.011	-21.452	-18.973	-19.532
2	-3.108	-4.254	-2.874	-9.738	-7.316	-7.362
3	-2.218	-1.410	-0.582	-3.000	-1.924	-1.317
4	1.311	4.700	6.343	1.578	4.632	6.284
5	-6.159	-4.751	-4.179	-23.730	-24.792	-24.370
6	-3.104	-2.797	-2.103	-10.008	-9.031	-9.032
7	-2.210	-1.316	-0.491	-3.004	-2.022	-1.406
8	1.311	4.700	6.343	1.578	4.632	6.283
9	-6.159	4.330	5.415	-99.999	-99.999	-99.999
10	-3.104	4.338	5.430	-44.134	-47.509	-44.269
11	-2.171	4.373	5.499	-11.845	-13.933	-11.524
12	1.455	5.396	7.053	1.169	3.910	5.558

	$^{22}Ne \rightarrow {}^{22}F$			$^{22}F \rightarrow {}^{22}Ne$		
pt	log β^+	log ε^-	log ν	log β^-	log ε^+	log $\bar{\nu}$
1	-99.999	-60.472	-61.046	-0.780	-6.320	-0.321
2	-37.209	-20.960	-21.034	-0.616	-3.305	-0.076
3	-8.707	-5.871	-5.372	-0.228	-1.127	0.507
4	0.999	4.051	5.670	3.399	4.847	6.563
5	-99.999	-54.653	-55.226	-0.805	-12.140	-0.359
6	-37.209	-19.244	-19.318	-0.632	-5.009	-0.099
7	-8.707	-5.772	-5.274	-0.231	-1.220	0.484
8	0.999	4.051	5.670	3.399	4.847	6.563
9	-99.999	2.188	2.549	-66.138	-99.999	-66.729
10	-37.209	2.203	2.633	-22.500	-43.486	-22.622
11	-8.703	2.524	3.248	-5.981	-13.111	-5.608
12	1.131	4.758	6.384	3.107	4.129	5.846

	$^{23}Al \rightarrow {}^{23}Mg$			$^{23}Mg \rightarrow {}^{23}Al$		
pt	log β^+	log ε^-	log ν	log β^-	log ε^+	log $\bar{\nu}$
1	0.204	-4.444	0.880	-85.080	-62.805	-63.377
2	0.209	-2.075	0.889	-27.595	-21.743	-21.811
3	0.476	-0.138	1.385	-7.585	-6.300	-6.765
4	3.311	5.343	7.055	-0.458	4.039	5.637
5	0.204	-0.666	0.950	-85.109	-68.625	-69.197
6	0.209	-0.638	0.963	-27.619	-23.458	-23.527
7	0.477	-0.045	1.413	-7.591	-6.399	-6.859
8	3.311	5.343	7.055	-0.458	4.038	5.637
9	0.204	5.027	6.283	-99.999	-99.999	-99.999
10	0.209	5.027	6.284	-61.004	-61.936	-61.104
11	0.483	5.004	6.259	-17.910	-18.311	-17.440
12	3.411	6.023	7.751	-0.912	3.312	4.908

	$^{23}Mg \rightarrow {}^{23}Na$			$^{23}Na \rightarrow {}^{23}Mg$		
pt	log β^+	log ε^-	log ν	log β^-	log ε^+	log $\bar{\nu}$
1	-1.181	-4.963	-0.953	-28.208	-22.255	-22.822
2	-1.204	-2.592	-0.930	-12.443	-8.583	-8.640
3	-1.212	-0.561	0.310	-4.094	-2.542	-1.993
4	2.070	4.913	6.576	1.100	4.568	6.202
5	-1.181	-1.162	-0.374	-30.753	-28.074	-28.641
6	-1.201	-1.144	-0.345	-12.725	-10.298	-10.355
7	-1.203	-0.467	0.400	-4.097	-2.641	-2.088
8	2.070	4.913	6.576	1.100	4.568	6.202
9	-1.181	4.677	5.886	-99.999	-99.999	-99.999
10	-1.201	4.670	5.877	-47.096	-48.776	-47.225
11	-1.164	4.666	5.876	-13.381	-14.563	-13.039
12	2.197	5.605	7.282	0.676	3.845	5.475

	$^{23}Na \rightarrow {}^{23}Ne$			$^{23}Ne \rightarrow {}^{23}Na$		
pt	log β^+	log ε^-	log ν	log β^-	log ε^+	log $\bar{\nu}$
1	-34.966	-29.299	-29.866	-1.729	-6.981	-1.364
2	-14.413	-11.629	-11.675	-1.708	-3.953	-1.331
3	-5.071	-3.611	-2.976	-1.014	-1.442	-0.207
4	1.398	4.706	6.360	2.269	4.687	6.333
5	-34.966	-23.490	-24.056	-1.771	-12.801	-1.432
6	-14.408	-8.922	-8.970	-1.742	-5.658	-1.388
7	-5.062	-3.514	-2.881	-1.018	-1.537	-0.246
8	1.398	4.706	6.361	2.269	4.687	6.333
9	-34.966	3.823	4.762	-98.160	-99.999	-98.753
10	-14.408	3.827	4.769	-32.665	-44.135	-32.791
11	-5.024	3.858	4.826	-8.717	-13.434	-8.367
12	1.544	5.399	7.068	1.909	3.964	5.607

	$^{23}Ne \rightarrow {}^{23}F$			$^{23}F \rightarrow {}^{23}Ne$		
pt	log β^+	log ε^-	log ν	log β^-	log ε^+	log $\bar{\nu}$
1	-59.715	-49.286	-49.860	-0.468	-6.002	-0.013
2	-20.778	-17.673	-17.747	-0.407	-3.035	0.080
3	-7.253	-5.263	-4.691	-0.205	-0.936	0.525
4	1.024	4.109	5.741	3.359	4.910	6.603
5	-59.715	-43.466	-44.040	-0.493	-11.822	-0.053
6	-20.773	-15.958	-16.032	-0.426	-4.739	0.049
7	-7.240	-5.165	-4.594	-0.209	-1.030	0.496
8	1.024	4.109	5.741	3.359	4.910	6.603
9	-59.715	2.320	3.068	-77.064	-99.999	-77.655
10	-20.773	2.340	3.090	-25.572	-43.216	-25.694
11	-7.180	2.550	3.378	-8.432	-12.924	-8.059
12	1.157	4.812	6.453	3.067	4.190	5.883

	$^{24}Si \rightarrow {}^{24}Al$			$^{24}Al \rightarrow {}^{24}Si$		
pt	log β^+	log ε^-	log ν	log β^-	log ε^+	log $\bar{\nu}$
1	0.560	-4.166	1.200	-76.477	-56.565	-57.139
2	0.560	-1.811	1.203	-25.546	-20.220	-20.293
3	0.706	0.049	1.583	-7.801	-6.465	-6.940
4	3.348	5.347	7.056	-0.632	3.978	5.581
5	0.560	-0.403	1.270	-76.515	-62.384	-62.958
6	0.560	-0.377	1.277	-25.579	-21.935	-22.008
7	0.707	0.141	1.613	-7.809	-6.564	-6.035
8	3.348	5.347	7.056	-0.632	3.978	5.581
9	0.560	5.164	6.441	-99.999	-99.999	-99.999
10	0.560	5.165	6.443	-59.753	-60.413	-59.814
11	0.714	5.122	6.392	-18.309	-18.476	-17.734
12	3.443	6.029	7.752	-1.090	3.252	4.853

	$^{24}Na \rightarrow {}^{24}Ne$			$^{24}Ne \rightarrow {}^{24}Na$		
pt	log β^+	log ε^-	log ν	log β^-	log ε^+	log $\bar{\nu}$
1	-27.134	-20.568	-21.123	-2.467	-6.689	-2.416
2	-12.181	-9.210	-9.236	-2.460	-3.634	-2.323
3	-5.117	-3.482	-2.870	-1.087	-1.143	-0.126
4	1.123	4.532	6.174	2.604	4.659	6.524
5	-27.133	-14.748	-15.304	-2.707	-12.509	-2.756
6	-12.177	-7.501	-7.528	-2.618	-5.339	-2.601
7	-5.109	-3.384	-2.774	-1.093	-1.238	-0.185
8	1.123	4.532	6.174	2.604	4.659	6.523
9	-27.133	3.688	4.573	-99.999	-99.999	-99.999
10	-12.177	3.699	4.594	-34.802	-43.817	-34.929
11	-5.070	3.759	4.706	-8.573	-13.135	-8.222
12	1.269	5.230	6.884	2.248	4.138	5.799

	$^{24}Al \rightarrow {}^{24}Mg$			$^{24}Mg \rightarrow {}^{24}Al$		
pt	log β^+	log ε^-	log ν	log β^-	log ε^+	log $\bar{\nu}$
1	-0.433	-4.558	-0.040	-99.999	-70.399	-70.970
2	-0.242	-2.186	0.345	-32.751	-23.680	-23.748
3	0.247	-0.246	1.179	-7.857	-6.227	-5.705
4	3.020	5.043	6.732	0.713	4.244	5.866
5	-0.433	-0.775	0.257	-99.999	-76.218	-76.789
6	-0.241	-0.747	0.507	-32.760	-25.396	-25.462
7	0.249	-0.153	1.214	-7.860	-6.326	-5.801
8	3.020	5.044	6.733	0.713	4.244	5.866
9	-0.433	4.864	6.104	-99.999	-99.999	-99.999
10	-0.241	4.861	6.100	-62.522	-63.873	-62.641
11	0.256	4.828	6.060	-17.312	-18.239	-16.948
12	3.112	5.731	7.433	0.284	3.519	5.139

	$^{25}Si \rightarrow {}^{25}Al$			$^{25}Al \rightarrow {}^{25}Si$		
pt	log β^+	log ε^-	log ν	log β^-	log ε^+	log $\bar{\nu}$
1	0.606	-4.075	1.284	-96.216	-64.995	-65.568
2	0.628	-1.720	1.315	-30.849	-22.156	-22.228
3	0.738	0.231	1.654	-8.141	-6.147	-5.636
4	3.350	5.187	6.904	0.178	4.030	5.632
5	0.606	-0.307	1.352	-96.230	-70.814	-71.388
6	0.629	-0.286	1.383	-30.861	-23.871	-23.944
7	0.740	0.323	1.690	-8.145	-6.246	-5.734
8	3.350	5.187	6.904	0.178	4.030	5.632
9	0.606	5.054	6.362	-99.999	-99.999	-99.999
10	0.629	5.050	6.357	-61.560	-62.349	-61.628
11	0.748	5.028	6.336	-17.826	-18.159	-17.300
12	3.438	5.869	7.598	-0.257	3.304	4.903

	$^{24}Mg \rightarrow {}^{24}Na$			$^{24}Na \rightarrow {}^{24}Mg$		
pt	log β^+	log ε^-	log ν	log β^-	log ε^+	log $\bar{\nu}$
1	-42.297	-36.014	-36.567	-4.232	-8.731	-3.869
2	-15.408	-13.466	-13.511	-2.474	-4.848	-2.030
3	-4.977	-3.472	-2.844	-1.392	-1.689	-0.563
4	1.876	4.719	6.375	2.381	4.591	6.243
5	-42.297	-30.193	-30.753	-4.336	-14.550	-3.954
6	-15.402	-11.754	-11.807	-2.499	-6.553	-2.070
7	-4.967	-3.375	-2.748	-1.396	-1.785	-0.809
8	1.876	4.719	6.375	2.381	4.591	6.243
9	-42.297	3.795	4.652	-92.991	-99.999	-93.583
10	-15.402	3.802	4.656	-31.458	-45.030	-31.584
11	-4.924	3.897	4.839	-8.902	-13.683	-8.547
12	2.004	5.415	7.082	2.032	3.868	5.518

	$^{25}Al \rightarrow {}^{25}Mg$			$^{25}Mg \rightarrow {}^{25}Al$		
pt	log β^+	log ε^-	log ν	log β^-	log ε^+	log $\bar{\nu}$
1	-0.972	-4.822	-0.709	-30.102	-23.240	-23.809
2	-0.987	-2.446	-0.688	-14.179	-8.812	-8.871
3	-0.877	-0.434	0.475	-3.634	-2.526	-1.957
4	1.682	5.033	6.690	0.402	4.686	6.319
5	-0.972	-1.029	-0.199	-33.453	-29.060	-29.628
6	-0.985	-1.001	-0.165	-14.231	-10.528	-10.587
7	-0.871	-0.341	0.559	-3.641	-2.625	-2.051
8	1.682	5.033	6.690	0.402	4.686	6.319
9	-0.972	4.872	6.110	-99.999	-99.999	-99.999
10	-0.985	4.870	6.108	-47.824	-49.006	-47.949
11	-0.843	4.862	6.102	-13.971	-14.537	-13.558
12	1.824	5.724	7.396	-0.051	3.963	5.592

	$^{25}Mg \rightarrow {}^{25}Na$			$^{25}Na \rightarrow {}^{25}Mg$		
pt	log β^+	log ε^-	log ν	log β^-	log ε^+	log $\bar{\nu}$
1	-40.077	-26.377	-26.940	-1.785	-6.738	-1.498
2	-13.864	-10.336	-10.382	-1.723	-3.672	-1.420
3	-4.924	-3.300	-2.696	-1.414	-1.389	-0.432
4	1.699	4.588	6.238	2.807	4.704	6.363
5	-40.077	-20.561	-21.126	-1.856	-12.558	-1.602
6	-13.861	-8.625	-8.670	-1.777	-5.376	-1.507
7	-4.914	-3.203	-2.600	-1.421	-1.484	-0.499
8	1.699	4.588	6.238	2.807	4.704	6.363
9	-40.077	3.686	4.577	-99.999	-99.999	-99.999
10	-13.861	3.692	4.587	-33.464	-43.854	-33.589
11	-4.871	3.737	4.668	-8.805	-13.382	-8.448
12	1.828	5.285	6.946	2.264	3.982	5.639

	$^{25}Na \rightarrow {}^{25}Ne$			$^{25}Ne \rightarrow {}^{25}Na$		
pt	log β^+	log ε^-	log ν	log β^-	log ε^+	log $\bar{\nu}$
1	-55.291	-43.072	-43.648	0.074	-5.801	0.632
2	-19.621	-15.945	-16.023	0.075	-2.833	0.635
3	-6.881	-4.603	-4.105	1.056	-0.444	1.821
4	0.880	4.461	6.093	2.348	5.009	6.678
5	-55.291	-37.252	-37.828	0.061	-11.621	0.610
6	-19.617	-14.229	-14.307	0.063	-4.536	0.615
7	-6.872	-4.504	-4.007	1.054	-0.537	1.813
8	0.880	4.462	6.093	2.348	5.009	6.678
9	-55.291	3.982	4.983	-83.429	-99.999	-84.023
10	-19.616	3.986	4.989	-27.482	-43.014	-27.613
11	-6.831	4.008	5.032	-7.063	-12.426	-6.733
12	1.027	5.161	6.805	1.957	4.288	5.953

	$^{26}Si \rightarrow {}^{26}Al$			$^{26}Al \rightarrow {}^{26}Si$		
pt	log β^+	log ε^-	log ν	log β^-	log ε^+	log $\bar{\nu}$
1	-0.444	-4.379	-0.137	-35.380	-27.835	-28.404
2	-0.445	-2.000	-0.111	-15.228	-10.826	-10.887
3	-0.293	-0.049	0.923	-4.959	-3.575	-3.030
4	2.579	5.255	6.942	-0.347	4.380	5.990
5	-0.444	-0.595	0.293	-36.483	-33.654	-34.222
6	-0.444	-0.558	0.332	-15.504	-12.542	-12.602
7	-0.287	0.045	1.001	-4.967	-3.673	-3.126
8	2.579	5.255	6.942	-0.347	4.380	5.989
9	-0.444	5.073	6.353	-99.999	-99.999	-99.999
10	-0.443	5.074	6.354	-50.346	-51.020	-50.408
11	-0.285	5.029	6.306	-15.509	-15.586	-14.867
12	2.703	5.940	7.643	-0.807	3.655	5.261

	$^{26}Al \rightarrow {}^{26}Mg$			$^{26}Mg \rightarrow {}^{26}Al$		
pt	log β^+	log ε^-	log ν	log β^-	log ε^+	log $\bar{\nu}$
1	-3.073	-8.964	-2.808	-25.975	-22.998	-23.562
2	-2.324	-3.744	-2.018	-10.600	-8.597	-8.625
3	-1.676	-0.959	-0.144	-2.879	-1.928	-1.295
4	1.482	4.872	6.519	1.447	4.833	6.478
5	-3.073	-3.119	-2.325	-28.039	-28.815	-28.528
6	-2.323	-2.275	-1.501	-11.009	-10.312	-10.296
7	-1.669	-0.864	-0.055	-2.882	-2.026	-1.382
8	1.482	4.872	6.519	1.447	4.833	6.478
9	-3.073	4.600	5.745	-99.999	-99.999	-99.999
10	-2.322	4.613	5.765	-45.902	-48.790	-46.042
11	-1.639	4.653	5.832	-12.336	-13.935	-12.023
12	1.624	5.567	7.228	1.019	4.111	5.752

	$^{26}Mg \rightarrow {}^{26}Na$			$^{26}Na \rightarrow {}^{26}Mg$		
pt	log β^+	log ε^-	log ν	log β^-	log ε^+	log $\bar{\nu}$
1	-66.311	-52.346	-52.921	-0.099	-5.948	0.462
2	-21.908	-17.893	-17.969	-0.083	-2.959	0.482
3	-6.638	-4.679	-4.150	0.273	-0.921	1.065
4	2.079	4.484	6.116	2.520	4.754	6.438
5	-66.311	-46.526	-47.101	-0.118	-11.767	0.436
6	-21.906	-16.178	-16.254	-0.096	-4.662	0.461
7	-6.627	-4.580	-4.052	0.271	-1.015	1.054
8	2.079	4.484	6.116	2.520	4.754	6.438
9	-66.311	3.901	4.825	-74.011	-99.999	-74.604
10	-21.906	3.904	4.831	-25.367	-43.140	-25.495
11	-6.580	3.946	4.905	-7.133	-12.906	-6.788
12	2.172	5.187	6.828	2.151	4.035	5.715

	$^{27}P \rightarrow {}^{27}Si$			$^{27}Si \rightarrow {}^{27}P$		
pt	log β^+	log ε^-	log ν	log β^-	log ε^+	log $\bar{\nu}$
1	0.454	-4.262	1.109	-99.999	-60.252	-60.827
2	0.468	-1.920	1.132	-34.434	-21.138	-21.213
3	0.658	-0.109	1.516	-8.613	-6.007	-5.508
4	3.575	5.330	7.062	0.988	4.151	5.747
5	0.454	-0.504	1.179	-99.999	-66.071	-66.646
6	0.468	-0.489	1.201	-34.438	-22.854	-22.929
7	0.660	-0.017	1.543	-8.615	-6.106	-5.606
8	3.575	5.330	7.062	0.988	4.151	5.747
9	0.454	4.862	6.127	-99.999	-99.999	-99.999
10	0.468	4.855	6.119	-69.828	-61.331	-69.946
11	0.666	4.755	5.987	-16.965	-16.019	-16.587
12	3.662	6.009	7.754	0.589	3.424	5.019

	$^{27}Si \rightarrow {}^{27}Al$			$^{27}Al \rightarrow {}^{27}Si$		
pt	log β^+	log ε^-	log ν	log β^-	log ε^+	log $\bar{\nu}$
1	-0.738	-4.744	-0.415	-31.897	-25.882	-26.452
2	-0.744	-2.374	-0.397	-14.006	-9.676	-9.738
3	-0.752	-0.370	0.561	-4.033	-2.767	-2.214
4	2.217	5.078	6.745	0.859	4.561	6.189
5	-0.738	-0.964	-0.022	-34.040	-31.702	-32.270
6	-0.742	-0.933	0.009	-14.556	-11.391	-11.453
7	-0.745	-0.276	0.646	-4.037	-2.866	-2.307
8	2.217	5.078	6.745	0.859	4.561	6.189
9	-0.738	4.837	6.063	-99.999	-99.999	-99.999
10	-0.742	4.837	6.063	-48.403	-49.869	-48.530
11	-0.716	4.831	6.059	-13.831	-14.778	-13.477
12	2.342	5.768	7.450	0.421	3.837	5.462

	$^{28}S \rightarrow {}^{28}P$			$^{28}P \rightarrow {}^{28}S$		
pt	log β^+	log ε^-	log ν	log β^-	log ε^+	log $\bar{\nu}$
1	0.491	-4.098	1.083	-99.999	-69.173	-69.749
2	0.498	-1.757	1.100	-33.342	-21.075	-21.153
3	1.881	0.527	2.767	-8.717	-5.984	-5.510
4	2.797	5.451	7.141	1.038	4.275	5.888
5	0.491	-0.346	1.183	-99.999	-64.993	-65.568
6	0.499	-0.328	1.202	-33.347	-22.791	-22.868
7	1.881	0.619	2.777	-8.719	-6.083	-5.608
8	2.797	5.451	7.141	1.038	4.275	5.888
9	0.491	5.025	6.285	-99.999	-99.999	-99.999
10	0.499	5.023	6.283	-59.834	-61.269	-59.951
11	1.884	5.076	6.412	-17.350	-17.996	-16.911
12	2.921	6.136	7.841	0.632	3.549	5.160

	$^{27}Al \rightarrow {}^{27}Mg$			$^{27}Mg \rightarrow {}^{27}Al$		
pt	log β^+	log ε^-	log ν	log β^-	log ε^+	log $\bar{\nu}$
1	-26.749	-21.087	-21.642	-2.781	-7.045	-2.761
2	-12.636	-9.166	-9.192	-2.568	-3.948	-2.355
3	-4.743	-2.444	-1.917	-0.119	-0.851	0.552
4	2.370	4.773	6.433	1.089	4.699	6.339
5	-26.748	-15.270	-15.827	-3.047	-12.864	-3.155
6	-12.628	-7.458	-7.485	-2.688	-5.654	-2.520
7	-4.734	-2.345	-1.819	-0.123	-1.045	0.524
8	2.370	4.773	6.433	1.089	4.698	6.339
9	-26.748	4.576	5.724	-99.999	-99.999	-99.999
10	-12.628	4.577	5.727	-35.612	-44.131	-35.756
11	-4.691	4.591	5.753	-10.032	-12.938	-9.757
12	2.472	5.467	7.139	0.649	3.976	5.612

	$^{28}P \rightarrow {}^{28}Si$			$^{28}Si \rightarrow {}^{28}P$		
pt	log β^+	log ε^-	log ν	log β^-	log ε^+	log $\bar{\nu}$
1	0.443	-4.285	1.143	-99.999	-72.501	-73.075
2	0.538	-1.936	1.291	-44.074	-24.235	-24.308
3	1.455	0.205	2.365	-10.185	-6.041	-5.558
4	2.853	5.314	7.013	1.729	4.274	5.884
5	0.443	-0.526	1.204	-99.999	-78.320	-78.894
6	0.539	-0.505	1.338	-44.075	-25.950	-26.024
7	1.455	0.297	2.375	-10.185	-6.140	-5.657
8	2.853	5.314	7.013	1.729	4.274	5.884
9	0.443	4.693	6.013	-99.999	-99.999	-99.999
10	0.539	4.686	6.006	-62.566	-64.428	-62.685
11	1.458	4.733	6.092	-16.721	-18.053	-16.340
12	2.971	5.997	7.711	1.377	3.548	5.156

	$^{27}Mg \rightarrow {}^{27}Na$			$^{27}Na \rightarrow {}^{27}Mg$		
pt	log β^+	log ε^-	log ν	log β^-	log ε^+	log $\bar{\nu}$
1	-64.586	-60.586	-51.163	0.469	-6.577	1.067
2	-21.790	-17.529	-17.611	0.469	-2.610	1.069
3	-7.173	-4.936	-4.426	0.593	-0.601	1.341
4	1.656	4.334	5.938	3.330	5.240	6.949
5	-64.586	-44.766	-45.344	0.458	-11.396	1.049
6	-21.786	-15.814	-15.896	0.460	-4.314	1.053
7	-7.162	-4.837	-4.328	0.591	-0.695	1.328
8	1.656	4.334	5.938	3.330	5.240	6.949
9	-64.586	3.664	4.504	-75.274	-99.999	-75.866
10	-21.786	3.673	4.520	-25.254	-42.791	-25.380
11	-7.118	3.734	4.634	-6.430	-12.585	-6.076
12	1.750	5.045	6.656	2.981	4.522	6.228

	$^{28}Si \rightarrow {}^{28}Al$			$^{28}Al \rightarrow {}^{28}Si$		
pt	log β^+	log ε^-	log ν	log β^-	log ε^+	log $\bar{\nu}$
1	-35.899	-29.983	-30.550	-2.341	-7.264	-2.130
2	-14.153	-11.298	-11.351	-2.324	-4.238	-2.081
3	-4.389	-2.850	-2.253	-0.775	-1.613	-0.055
4	2.579	4.819	6.473	1.508	4.648	6.299
5	-35.899	-24.165	-24.732	-2.441	-13.083	-2.288
6	-14.143	-9.584	-9.638	-2.398	-5.942	-2.200
7	-4.380	-2.753	-2.156	-0.778	-1.708	-0.077
8	2.579	4.819	6.473	1.508	4.648	6.299
9	-35.899	4.524	5.613	-97.858	-99.999	-98.454
10	-14.143	4.526	5.617	-33.426	-44.420	-33.565
11	-4.343	4.556	5.665	-9.933	-13.605	-9.633
12	2.670	5.514	7.180	1.089	3.927	5.573

	$^{28}Al \rightarrow {}^{28}Mg$			$^{28}Mg \rightarrow {}^{28}Al$		
pt	log β^+	log ε^-	log ν	log β^-	log ε^+	log $\bar{\nu}$
1	-31.851	-18.186	-18.695	-4.967	-7.310	-5.462
2	-11.756	-8.692	-8.663	-3.478	-4.101	-3.131
3	-4.657	-2.895	-2.335	-0.082	-1.052	0.621
4	2.032	4.774	6.423	1.713	4.915	6.565
5	-31.851	-12.697	-13.100	-7.371	-13.129	-7.919
6	-11.754	-7.026	-6.977	-3.560	-6.806	-3.347
7	-4.647	-2.797	-2.238	-0.123	-1.147	0.563
8	2.032	4.774	6.423	1.713	4.914	6.565
9	-31.851	4.473	5.577	-99.999	-99.999	-99.999
10	-11.754	4.474	5.580	-36.143	-44.285	-36.282
11	-4.808	4.491	5.611	-9.449	-13.040	-9.149
12	2.145	5.470	7.132	1.288	4.193	5.839

	$^{28}Mg \rightarrow {}^{28}Na$			$^{28}Na \rightarrow {}^{28}Mg$		
pt	log β^+	log ε^-	log ν	log β^-	log ε^+	log $\bar{\nu}$
1	-89.238	-75.102	-75.683	1.235	-6.459	2.048
2	-29.708	-25.492	-25.584	1.173	-2.572	1.987
3	-9.236	-6.631	-6.165	2.012	-0.119	2.919
4	1.424	4.420	6.003	3.937	5.668	7.397
5	-89.238	-69.282	-69.864	1.233	-11.279	2.043
6	-29.706	-23.776	-23.869	1.171	-4.275	1.983
7	-9.225	-6.532	-6.067	2.011	-0.212	2.917
8	1.424	4.421	6.003	3.937	5.668	7.397
9	-89.238	3.690	4.469	-50.373	-99.999	-50.965
10	-29.706	3.696	4.478	-16.992	-42.753	-17.117
11	-9.177	3.737	4.565	-3.994	-12.098	-3.634
12	1.513	5.136	6.725	3.600	4.952	6.677

	$^{29}S \rightarrow {}^{29}P$			$^{29}P \rightarrow {}^{29}S$		
pt	log β^+	log ε^-	log ν	log β^-	log ε^+	log $\bar{\nu}$
1	0.674	-3.976	1.319	-99.999	-69.884	-70.460
2	0.675	-1.631	1.323	-39.297	-23.545	-23.623
3	1.276	0.309	2.212	-9.542	-6.362	-6.871
4	3.311	5.595	7.311	1.108	4.188	5.781
5	0.674	-0.224	1.400	-99.999	-75.704	-76.280
6	0.675	-0.201	1.407	-39.300	-25.261	-25.339
7	1.276	0.401	2.226	-9.543	-6.461	-5.970
8	3.311	5.595	7.311	1.108	4.188	5.781
9	0.674	4.995	6.310	-99.999	-99.999	-99.999
10	0.675	4.996	6.311	-62.319	-63.738	-62.431
11	1.280	4.954	6.272	-17.279	-18.375	-16.894
12	3.422	6.274	8.006	0.725	3.461	5.052

	$^{29}P \rightarrow {}^{29}Si$			$^{29}Si \rightarrow {}^{29}P$		
pt	log β^+	log ε^-	log ν	log β^-	log ε^+	log $\bar{\nu}$
1	-0.706	-4.791	-0.360	-34.243	-26.817	-27.188
2	-0.707	-2.429	-0.341	-14.276	-9.969	-10.036
3	-0.676	-0.421	0.550	-4.112	-2.918	-2.367
4	2.220	5.159	6.828	1.019	4.606	6.235
5	-0.706	-1.023	-0.019	-35.160	-32.436	-33.007
6	-0.706	-0.992	0.010	-14.654	-11.684	-11.752
7	-0.670	-0.328	0.630	-4.115	-3.017	-2.458
8	2.220	5.159	6.828	1.019	4.606	6.234
9	-0.706	4.838	6.035	-99.999	-99.999	-99.999
10	-0.706	4.840	6.037	-48.487	-60.162	-48.618
11	-0.645	4.850	6.055	-13.752	-14.929	-13.422
12	2.350	5.848	7.532	0.586	3.883	5.507

	$^{29}Si \rightarrow {}^{29}Al$			$^{29}Al \rightarrow {}^{29}Si$		
pt	log β^+	log ε^-	log ν	log β^-	log ε^+	log $\bar{\nu}$
1	-30.847	-25.705	-25.263	-2.719	-7.250	-2.590
2	-13.236	-10.217	-10.232	-2.691	-4.148	-2.503
3	-4.536	-2.950	-2.346	-0.798	-1.455	-0.016
4	2.437	4.800	6.460	1.853	4.724	6.372
5	-30.847	-19.888	-20.448	-2.883	-13.070	-2.825
6	-13.222	-8.513	-8.532	-2.801	-5.854	-2.678
7	-4.528	-2.852	-2.249	-0.801	-1.551	-0.040
8	2.437	4.800	6.460	1.853	4.723	6.372
9	-30.847	4.410	5.460	-99.999	-99.999	-99.999
10	-13.221	4.413	5.465	-34.324	-44.331	-34.458
11	-4.495	4.444	5.519	-9.525	-13.448	-9.205
12	2.539	5.495	7.166	1.447	4.001	5.646

	$^{29}Al \rightarrow {}^{29}Mg$			$^{29}Mg \rightarrow {}^{29}Al$		
pt	log β^+	log ε^-	log ν	log β^-	log ε^+	log $\bar{\nu}$
1	-59.256	-44.083	-44.657	-0.172	-5.975	0.374
2	-20.282	-15.998	-16.073	-0.099	-2.970	0.476
3	-6.714	-3.918	-3.439	1.471	-0.015	2.199
4	1.916	4.609	6.231	2.470	5.214	6.893
5	-59.256	-38.268	-38.842	-0.190	-11.794	0.349
6	-20.280	-14.283	-14.358	-0.112	-4.674	0.457
7	-6.704	-3.819	-3.341	1.469	-0.108	2.190
8	1.916	4.609	6.231	2.470	5.214	6.893
9	-59.256	4.333	5.382	-82.412	-99.999	-83.007
10	-20.280	4.336	5.385	-27.402	-43.151	-27.537
11	-6.660	4.355	5.422	-7.177	-11.998	-6.859
12	2.013	5.312	6.945	2.064	4.495	6.169

	$^{29}Mg \rightarrow {}^{29}Na$			$^{29}Na \rightarrow {}^{29}Mg$		
pt	log β^+	log ε^-	log ν	log β^-	log ε^+	log $\bar{\nu}$
1	-86.944	-73.559	-74.140	1.127	-5.855	1.950
2	-29.490	-25.542	-25.636	1.140	-2.700	1.965
3	-9.472	-6.791	-6.327	2.096	-0.044	2.996
4	1.733	4.272	5.896	3.142	5.048	6.743
5	-86.944	-67.739	-68.321	1.125	-11.475	1.945
6	-29.487	-23.826	-23.920	1.138	-4.403	1.961
7	-9.460	-6.693	-6.229	2.096	-0.137	2.994
8	1.733	4.272	5.896	3.142	5.048	6.743
9	-86.944	3.447	4.248	-52.436	-99.999	-53.029
10	-29.487	3.452	4.257	-17.396	-42.881	-17.522
11	-9.408	3.499	4.348	-4.093	-12.024	-3.735
12	1.832	4.978	6.610	2.799	4.329	6.021

	$^{30}Si \rightarrow {}^{30}Al$			$^{30}Al \rightarrow {}^{30}Si$		
pt	log β^+	log ε^-	log ν	log β^-	log ε^+	log $\bar{\nu}$
1	-65.168	-48.698	-49.268	-0.689	-6.171	-0.258
2	-21.353	-16.945	-17.011	-0.783	-3.289	-0.307
3	-6.142	-4.164	-3.652	0.596	-0.903	1.358
4	1.849	4.622	6.229	2.832	5.331	7.024
5	-65.168	-42.879	-43.450	-0.722	-11.991	-0.306
6	-21.351	-15.228	-15.295	-0.808	-4.993	-0.343
7	-6.133	-4.065	-3.555	0.694	-0.996	1.350
8	1.849	4.622	6.229	2.832	5.331	7.024
9	-65.168	4.332	5.345	-77.806	-99.999	-78.401
10	-21.351	4.334	5.349	-26.583	-43.470	-26.715
11	-6.096	4.357	5.392	-7.610	-12.886	-7.282
12	1.937	5.330	6.946	2.438	4.613	6.301

	$^{30}S \rightarrow {}^{30}P$			$^{30}P \rightarrow {}^{30}S$		
pt	log β^+	log ε^-	log ν	log β^-	log ε^+	log $\bar{\nu}$
1	-0.202	-4.343	0.195	-51.088	-32.712	-33.283
2	-0.203	-1.982	0.209	-16.830	-12.070	-12.138
3	-0.134	0.027	1.023	-5.063	-3.805	-3.258
4	3.277	5.629	7.340	-0.688	4.286	5.876
5	-0.202	-0.577	0.480	-51.133	-38.531	-39.102
6	-0.202	-0.545	0.508	-16.868	-13.785	-13.851
7	-0.129	0.120	1.100	-5.072	-3.903	-3.353
8	3.277	5.629	7.340	-0.688	4.286	5.876
9	-0.202	5.157	6.422	-99.999	-99.999	-99.999
10	-0.202	5.158	6.423	-51.442	-52.263	-51.535
11	-0.107	5.152	6.422	-15.663	-15.816	-15.073
12	3.390	6.308	8.036	-1.149	3.558	5.147

	$^{31}Cl \rightarrow {}^{31}S$			$^{31}S \rightarrow {}^{31}Cl$		
pt	log β^+	log ε^-	log ν	log β^-	log ε^+	log $\bar{\nu}$
1	0.405	-4.118	0.977	-84.741	-60.861	-61.436
2	0.408	-1.789	0.991	-27.106	-20.778	-20.854
3	0.507	0.062	1.418	-7.073	-5.662	-5.144
4	3.449	5.451	7.165	-0.096	4.181	5.781
5	0.405	-0.374	1.096	-84.766	-66.681	-67.256
6	0.409	-0.361	1.110	-27.127	-22.493	-22.569
7	0.510	0.155	1.462	-7.079	-5.761	-5.240
8	3.449	5.451	7.165	-0.096	4.181	5.781
9	0.405	5.162	6.424	-99.999	-99.999	-99.999
10	0.409	5.160	6.422	-60.032	-60.971	-60.131
11	0.519	5.131	6.386	-17.287	-17.674	-16.810
12	3.543	6.131	7.860	-0.546	3.455	5.052

	$^{30}P \rightarrow {}^{30}Si$			$^{30}Si \rightarrow {}^{30}P$		
pt	log β^+	log ε^-	log ν	log β^-	log ε^+	log $\bar{\nu}$
1	-2.317	-6.000	-2.067	-29.240	-23.865	-24.423
2	-1.984	-3.405	-1.650	-11.883	-9.278	-9.308
3	-1.236	-0.856	0.048	-3.899	-2.308	-1.733
4	1.782	5.040	6.704	1.587	4.680	6.311
5	-2.317	-2.163	-1.463	-30.684	-29.684	-30.189
6	-1.982	-1.939	-1.146	-12.188	-10.993	-10.999
7	-1.231	-0.762	0.129	-3.903	-2.406	-1.828
8	1.782	5.040	6.704	1.587	4.680	6.310
9	-2.317	4.520	5.645	-99.999	-99.999	-99.999
10	-1.982	4.525	5.656	-46.537	-49.471	-46.770
11	-1.210	4.563	5.726	-12.501	-14.316	-12.171
12	1.906	5.731	7.410	1.183	3.956	5.584

	$^{31}S \rightarrow {}^{31}P$			$^{31}P \rightarrow {}^{31}S$		
pt	log β^+	log ε^-	log ν	log β^-	log ε^+	log $\bar{\nu}$
1	-0.498	-4.674	-0.107	-34.907	-29.054	-29.625
2	-0.500	-2.309	-0.094	-15.069	-10.714	-10.777
3	-0.442	-0.272	0.716	-4.312	-3.037	-2.485
4	2.288	5.231	6.904	0.629	4.544	6.164
5	-0.498	-0.905	0.168	-37.761	-34.874	-35.444
6	-0.499	-0.870	0.193	-15.379	-12.430	-12.492
7	-0.437	-0.179	0.794	-4.317	-3.136	-2.579
8	2.288	5.231	6.904	0.629	4.544	6.164
9	-0.498	4.936	6.168	-99.999	-99.999	-99.999
10	-0.499	4.936	6.169	-49.491	-50.907	-49.619
11	-0.416	4.919	6.155	-14.203	-15.047	-13.841
12	2.417	5.918	7.607	0.189	3.820	5.436

$^{31}P \rightarrow {}^{31}Si$ and $^{31}Si \rightarrow {}^{31}P$

pt	log β^+	log ε^-	log ν	log β^-	log ε^+	log $\bar{\nu}$
1	-20.936	-15.731	-16.277	-4.064	-8.091	-4.097
2	-9.517	-7.427	-7.396	-3.902	-4.846	-3.777
3	-3.373	-2.293	-1.578	-2.359	-1.823	-1.036
4	1.884	4.810	6.458	2.349	4.800	6.458
5	-20.936	-9.959	-10.501	-4.414	-13.910	-4.605
6	-9.506	-6.746	-6.720	-4.090	-6.553	-4.114
7	-3.365	-2.197	-1.484	-2.363	-1.920	-1.108
8	1.884	4.810	6.458	2.349	4.800	6.458
9	-20.936	4.257	5.249	-99.999	-99.999	-99.999
10	-9.505	4.260	5.254	-37.640	-45.031	-37.769
11	-3.333	4.298	5.321	-10.284	-13.823	-9.944
12	2.008	5.508	7.167	1.966	4.078	5.733

$^{32}Cl \rightarrow {}^{32}S$ and $^{32}S \rightarrow {}^{32}Cl$

pt	log β^+	log ε^-	log ν	log β^-	log ε^+	log $\bar{\nu}$
1	0.322	-4.273	0.932	-97.594	-64.458	-65.033
2	0.287	-1.947	0.894	-30.626	-21.691	-21.767
3	0.291	-0.070	1.233	-7.251	-5.664	-5.152
4	3.431	5.499	7.221	0.301	4.131	5.722
5	0.322	-0.529	1.028	-97.605	-70.277	-70.853
6	0.287	-0.519	1.000	-30.635	-23.406	-23.483
7	0.293	0.023	1.281	-7.254	-5.763	-5.247
8	3.431	5.499	7.221	0.301	4.131	5.722
9	0.322	4.955	6.203	-99.999	-99.999	-99.999
10	0.287	4.953	6.200	-60.592	-61.884	-60.710
11	0.304	4.934	6.175	-16.755	-17.676	-16.394
12	3.531	6.178	7.915	-0.129	3.404	4.993

$^{31}Si \rightarrow {}^{31}Al$ and $^{31}Al \rightarrow {}^{31}Si$

pt	log β^+	log ε^-	log ν	log β^-	log ε^+	log $\bar{\nu}$
1	-62.311	-45.794	-46.371	-0.112	-6.137	0.471
2	-20.960	-16.444	-16.525	-0.083	-3.148	0.511
3	-6.628	-4.111	-3.633	1.235	-0.305	1.971
4	1.815	4.556	6.176	2.501	5.171	6.851
5	-62.311	-39.975	-40.552	-0.124	-11.957	0.451
6	-20.958	-14.728	-14.810	-0.094	-4.849	0.494
7	-6.619	-4.012	-3.535	1.233	-0.398	1.963
8	1.815	4.556	6.176	2.501	5.171	6.851
9	-62.311	4.271	5.310	-80.827	-99.999	-81.422
10	-20.958	4.273	5.313	-27.107	-43.327	-27.240
11	-6.580	4.292	5.348	-7.256	-12.287	-6.935
12	1.912	5.260	6.890	2.099	4.452	6.127

$^{32}S \rightarrow {}^{32}P$ and $^{32}P \rightarrow {}^{32}S$

pt	log β^+	log ε^-	log ν	log β^-	log ε^+	log $\bar{\nu}$
1	-23.666	-18.087	-18.267	-6.435	-8.653	-6.411
2	-10.054	-7.787	-7.684	-4.061	-5.296	-3.802
3	-3.141	-1.974	-1.301	-2.201	-2.138	-1.220
4	2.636	5.014	6.708	1.303	4.411	6.025
5	-23.666	-13.137	-13.559	-6.730	-14.472	-6.838
6	-10.047	-6.183	-6.058	-4.127	-7.005	-3.928
7	-3.135	-1.881	-1.209	-2.206	-2.234	-1.281
8	2.636	5.014	6.708	1.303	4.411	6.025
9	-23.666	4.528	5.629	-99.999	-99.999	-99.999
10	-10.047	4.530	5.632	-38.037	-45.482	-38.172
11	-3.107	4.510	5.624	-11.203	-14.136	-10.885
12	2.747	5.699	7.407	0.897	3.685	5.297

$^{32}Ar \rightarrow {}^{32}Cl$ and $^{32}Cl \rightarrow {}^{32}Ar$

pt	log β^+	log ε^-	log ν	log β^-	log ε^+	log $\bar{\nu}$
1	0.308	-4.058	0.801	-69.276	-57.766	-58.341
2	0.309	-1.725	0.812	-23.703	-20.533	-20.609
3	0.549	0.150	1.515	-7.765	-6.202	-5.666
4	3.190	5.397	7.093	-1.196	4.319	5.927
5	0.308	-0.319	0.982	-69.416	-63.586	-64.161
6	0.310	-0.298	0.998	-23.807	-22.249	-22.307
7	0.551	0.243	1.555	-7.781	-6.300	-5.763
8	3.190	5.397	7.093	-1.196	4.319	5.927
9	0.308	5.305	6.593	-99.999	-99.999	-99.999
10	0.310	5.306	6.595	-60.478	-60.727	-60.439
11	0.559	5.276	6.561	-18.833	-18.212	-17.647
12	3.287	6.083	7.793	-1.672	3.594	5.199

$^{32}P \rightarrow {}^{32}Si$ and $^{32}Si \rightarrow {}^{32}P$

pt	log β^+	log ε^-	log ν	log β^-	log ε^+	log $\bar{\nu}$
1	-16.140	-13.387	-13.402	-10.191	-9.182	-9.564
2	-8.494	-7.098	-6.862	-5.275	-5.308	-4.891
3	-3.794	-2.670	-1.967	-1.653	-1.684	-0.675
4	1.045	4.587	6.208	2.574	5.184	6.863
5	-16.140	-8.831	-8.975	-12.029	-15.002	-12.063
6	-8.483	-5.572	-5.315	-5.444	-7.020	-5.394
7	-3.787	-2.574	-1.874	-1.656	-1.781	-0.721
8	1.045	4.587	6.207	2.574	5.184	6.863
9	-16.140	4.259	5.292	-99.999	-99.999	-99.999
10	-8.482	4.260	5.295	-38.891	-45.497	-39.023
11	-3.756	4.281	5.335	-10.043	-13.684	-9.718
12	1.182	5.290	6.921	2.176	4.465	6.139

	$^{33}Ar \rightarrow {}^{33}Cl$			$^{33}Cl \rightarrow {}^{33}Ar$		
pt	log β^+	log ε^-	log ν	log β^-	log ε^+	log $\bar{\nu}$
1	0.652	-3.973	1.297	-80.962	-59.808	-60.383
2	0.653	-1.642	1.302	-26.498	-20.761	-20.836
3	0.761	0.135	1.666	-7.379	-6.004	-6.487
4	3.083	5.352	7.059	-0.375	4.088	5.687
5	0.652	-0.233	1.381	-80.986	-65.628	-66.203
6	0.653	-0.215	1.388	-26.519	-22.476	-22.552
7	0.762	0.227	1.697	-7.386	-6.103	-6.583
8	3.083	5.352	7.059	-0.375	4.088	5.687
9	0.652	5.173	6.478	-99.999	-99.999	-99.999
10	0.653	5.172	6.477	-60.378	-60.954	-60.415
11	0.789	5.087	6.377	-17.819	-18.015	-17.258
12	3.188	6.032	7.755	-0.832	3.362	4.959

	$^{33}P \rightarrow {}^{33}Si$			$^{33}Si \rightarrow {}^{33}P$		
pt	log β^+	log ε^-	log ν	log β^-	log ε^+	log $\bar{\nu}$
1	-53.305	-35.211	-35.779	-0.911	-6.151	-0.586
2	-17.694	-12.804	-12.863	-0.912	-3.125	-0.580
3	-5.438	-3.756	-3.201	-0.811	-1.040	0.045
4	1.163	4.302	5.922	3.181	5.064	6.746
5	-53.305	-29.391	-29.960	-0.976	-11.970	-0.683
6	-17.692	-11.089	-11.148	-0.956	-4.830	-0.652
7	-5.431	-3.658	-3.103	-0.818	-1.135	-0.012
8	1.163	4.302	5.922	3.180	5.064	6.746
9	-53.305	3.451	4.261	-91.217	-99.999	-91.809
10	-17.692	3.457	4.272	-30.491	-43.307	-30.616
11	-5.400	3.560	4.464	-8.045	-13.030	-7.887
12	1.288	5.007	6.636	2.841	4.344	6.024

	$^{33}Cl \rightarrow {}^{33}S$			$^{33}S \rightarrow {}^{33}Cl$		
pt	log β^+	log ε^-	log ν	log β^-	log ε^+	log $\bar{\nu}$
1	-0.538	-4.659	-0.144	-35.045	-29.772	-30.343
2	-0.539	-2.305	-0.129	-14.945	-10.967	-11.033
3	-0.521	-0.272	0.694	-4.229	-3.141	-2.572
4	2.317	5.050	6.718	-0.226	4.570	6.193
5	-0.538	-0.900	0.154	-38.155	-35.591	-36.162
6	-0.538	-0.869	0.179	-15.014	-12.683	-12.744
7	-0.516	-0.179	0.775	-4.239	-3.240	-2.666
8	2.317	5.050	6.718	-0.226	4.569	6.193
9	-0.538	4.967	6.223	-99.999	-99.999	-99.999
10	-0.538	4.967	6.224	-50.257	-51.161	-50.369
11	-0.492	4.964	6.226	-14.980	-15.151	-14.401
12	2.433	5.739	7.423	-0.692	3.846	5.466

	$^{34}Ar \rightarrow {}^{34}Cl$			$^{34}Cl \rightarrow {}^{34}Ar$		
pt	log β^+	log ε^-	log ν	log β^-	log ε^+	log $\bar{\nu}$
1	-0.080	-4.233	0.348	-37.737	-32.128	-32.700
2	-0.080	-1.883	0.362	-14.530	-12.127	-12.192
3	-0.005	0.162	1.142	-6.552	-3.898	-3.336
4	2.684	5.265	6.959	-2.971	4.248	5.850
5	-0.080	-0.481	0.617	-38.663	-37.948	-38.431
6	-0.079	-0.448	0.640	-14.934	-13.843	-13.888
7	-0.001	0.256	1.217	-6.581	-3.996	-3.434
8	2.684	5.265	6.959	-2.971	4.248	5.850
9	-0.080	5.168	6.480	-99.999	-99.999	-99.999
10	-0.079	5.169	6.481	-53.094	-52.321	-52.351
11	0.018	5.144	6.460	-17.975	-15.906	-15.344
12	2.800	5.947	7.658	-3.460	3.522	5.121

	$^{33}S \rightarrow {}^{33}P$			$^{33}P \rightarrow {}^{33}S$		
pt	log β^+	log ε^-	log ν	log β^-	log ε^+	log $\bar{\nu}$
1	-16.890	-10.328	-10.818	-6.500	-8.055	-7.189
2	-8.947	-5.890	-5.804	-5.104	-4.745	-4.401
3	-3.255	-2.075	-1.409	-1.721	-1.850	-0.822
4	2.343	5.075	6.759	1.093	4.497	6.112
5	-16.890	-5.118	-5.428	-9.459	-13.874	-10.177
6	-8.937	-4.277	-4.160	-5.277	-6.453	-5.218
7	-3.249	-1.978	-1.315	-1.725	-1.946	-0.871
8	2.343	5.075	6.760	1.093	4.497	6.112
9	-16.890	4.469	5.587	-99.999	-99.999	-99.999
10	-8.937	4.470	5.588	-39.578	-44.931	-39.717
11	-3.221	4.465	5.595	-11.029	-13.846	-10.726
12	2.466	5.760	7.461	0.672	3.772	5.384

	$^{34}Cl \rightarrow {}^{34}S$			$^{34}S \rightarrow {}^{34}Cl$		
pt	log β^+	log ε^-	log ν	log β^-	log ε^+	log $\bar{\nu}$
1	-0.702	-4.834	-0.319	-35.266	-29.114	-29.687
2	-1.094	-2.848	-0.694	-14.083	-10.596	-10.662
3	-1.174	-0.813	0.089	-3.317	-2.719	-2.055
4	1.912	4.958	6.622	-0.155	4.547	6.174
5	-0.702	-1.081	-0.011	-37.998	-34.933	-35.506
6	-1.093	-1.413	-0.371	-14.157	-12.312	-12.364
7	-1.169	-0.719	0.171	-3.327	-2.817	-2.142
8	1.912	4.959	6.622	-0.156	4.547	6.174
9	-0.702	4.838	6.084	-99.999	-99.999	-99.999
10	-1.093	4.802	6.033	-49.418	-60.790	-49.568
11	-1.147	4.807	6.043	-14.076	-14.725	-13.704
12	2.042	5.648	7.327	-0.622	3.823	5.446

	$^{34}S \rightarrow {}^{34}P$			$^{34}P \rightarrow {}^{34}S$		
pt	log β^+	log ε^-	log ν	log β^-	log ε^+	log $\bar{\nu}$
1	-52.827	-33.574	-34.139	-1.221	-6.620	-0.791
2	-17.299	-12.340	-12.386	-1.302	-3.597	-0.877
3	-4.936	-3.383	-2.799	-1.144	-1.368	-0.260
4	1.645	4.437	6.076	2.592	4.775	6.447
5	-52.827	-27.764	-28.328	-1.257	-12.440	-0.841
6	-17.298	-10.617	-10.666	-1.333	-5.302	-0.923
7	-4.929	-3.285	-2.702	-1.149	-1.463	-0.310
8	1.645	4.437	6.076	2.592	4.775	6.447
9	-52.827	3.807	4.745	-93.470	-99.999	-94.063
10	-17.298	3.810	4.751	-31.582	-43.780	-31.710
11	-4.899	3.856	4.835	-8.890	-13.358	-8.544
12	1.758	5.137	6.786	2.225	4.054	5.724

	$^{35}Ar \rightarrow {}^{35}Cl$			$^{35}Cl \rightarrow {}^{35}Ar$		
pt	log β^+	log ε^-	log ν	log β^-	log ε^+	log $\bar{\nu}$
1	-0.367	-4.635	0.067	-37.059	-31.703	-32.276
2	-0.368	-2.291	0.078	-13.611	-11.594	-11.661
3	-0.337	-0.116	0.821	-5.544	-3.253	-2.661
4	2.298	5.237	6.918	-2.696	4.347	5.958
5	-0.367	-0.889	0.294	-37.967	-37.523	-37.933
6	-0.367	-0.858	0.313	-13.976	-13.309	-13.323
7	-0.333	-0.021	0.899	-5.572	-3.351	-2.758
8	2.298	5.237	6.918	-2.696	4.347	5.958
9	-0.367	4.999	6.293	-99.999	-99.999	-99.999
10	-0.367	5.000	6.295	-52.134	-51.787	-51.762
11	-0.314	5.006	6.307	-16.955	-15.259	-14.666
12	2.425	5.922	7.620	-3.185	3.622	5.227

	$^{34}P \rightarrow {}^{34}Si$			$^{34}Si \rightarrow {}^{34}P$		
pt	log β^+	log ε^-	log ν	log β^-	log ε^+	log $\bar{\nu}$
1	-48.202	-30.113	-30.681	-0.583	-5.664	-0.335
2	-16.648	-11.415	-11.475	-0.585	-2.634	-0.328
3	-5.786	-3.601	-3.067	-0.518	-0.655	0.397
4	1.297	4.360	6.026	2.353	4.694	6.331
5	-48.202	-24.294	-24.862	-0.661	-11.483	-0.462
6	-16.646	-9.699	-9.759	-0.648	-4.338	-0.432
7	-5.779	-3.502	-2.969	-0.526	-0.749	0.335
8	1.297	4.360	6.026	2.353	4.694	6.331
9	-48.202	3.364	4.256	-98.190	-99.999	-98.782
10	-16.646	3.370	4.267	-31.760	-42.816	-31.887
11	-5.749	3.456	4.428	-8.188	-12.643	-7.835
12	1.434	5.051	6.731	2.001	3.970	5.605

	$^{35}Cl \rightarrow {}^{35}S$			$^{35}S \rightarrow {}^{35}Cl$		
pt	log β^+	log ε^-	log ν	log β^-	log ε^+	log $\bar{\nu}$
1	-14.327	-9.676	-10.183	-7.000	-8.334	-7.729
2	-7.802	-5.755	-5.701	-5.925	-5.110	-4.787
3	-3.112	-2.126	-1.396	-2.457	-2.111	-1.301
4	2.079	4.752	6.426	1.386	4.452	6.079
5	-14.327	-4.618	-4.882	-10.184	-14.154	-11.085
6	-7.791	-4.109	-4.031	-6.108	-6.818	-5.934
7	-3.106	-2.030	-1.304	-2.460	-2.208	-1.367
8	2.079	4.752	6.426	1.386	4.452	6.079
9	-14.327	4.228	5.310	-99.999	-99.999	-99.999
10	-7.791	4.230	5.313	-40.044	-45.296	-40.179
11	-3.078	4.244	5.343	-11.268	-14.113	-10.953
12	2.198	5.441	7.129	0.976	3.728	5.352

	$^{35}K \rightarrow {}^{35}Ar$			$^{35}Ar \rightarrow {}^{35}K$		
pt	log β^+	log ε^-	log ν	log β^-	log ε^+	log $\bar{\nu}$
1	0.592	-4.029	1.217	-99.999	-60.912	-61.488
2	0.591	-1.702	1.221	-99.999	-20.980	-21.057
3	0.500	0.239	1.455	-99.999	-5.768	-5.219
4	3.124	5.238	6.934	-99.999	4.037	5.843
5	0.592	-0.299	1.308	-99.999	-66.732	-67.308
6	0.592	-0.275	1.315	-99.999	-22.696	-22.773
7	0.503	0.333	1.506	-99.999	-5.866	-5.317
8	3.124	5.238	6.934	-99.999	4.037	5.843
9	0.592	5.248	6.569	-99.999	-99.999	-99.999
10	0.592	5.249	6.571	-99.999	-61.174	-61.250
11	0.513	5.220	6.538	-99.999	-17.776	-17.227
12	3.214	5.921	7.633	-99.999	3.311	4.915

	$^{35}S \rightarrow {}^{35}P$			$^{35}P \rightarrow {}^{35}S$		
pt	log β^+	log ε^-	log ν	log β^-	log ε^+	log $\bar{\nu}$
1	-45.792	-26.859	-27.419	-1.809	-6.554	-1.667
2	-15.550	-10.652	-10.698	-1.795	-3.500	-1.611
3	-4.952	-3.470	-2.886	-1.070	-1.349	-0.186
4	1.209	4.228	5.872	2.337	4.794	6.456
5	-45.792	-21.039	-21.600	-2.029	-12.373	-1.983
6	-15.549	-8.937	-8.982	-1.933	-5.205	-1.812
7	-4.945	-3.372	-2.790	-1.075	-1.444	-0.230
8	1.209	4.228	5.872	2.337	4.794	6.456
9	-45.792	3.704	4.704	-99.999	-99.999	-99.999
10	-15.549	3.707	4.709	-33.572	-43.683	-33.703
11	-4.915	3.729	4.756	-9.202	-13.339	-8.865
12	1.333	4.925	6.581	1.953	4.073	5.732

	$^{36}Co \rightarrow {}^{36}K$			$^{36}K \rightarrow {}^{36}Ca$		
pt	log β^+	log ε^-	log ν	log β^-	log ε^+	log $\bar{\nu}$
1	0.538	-3.910	1.085	-99.999	-57.024	-57.600
2	0.537	-1.581	1.072	-99.999	-20.128	-20.201
3	0.618	0.431	1.609	-99.999	-6.157	-6.608
4	2.832	5.234	6.909	-99.999	3.945	5.562
5	0.538	-0.181	1.218	-99.999	-62.843	-63.420
6	0.538	-0.152	1.229	-99.999	-21.843	-21.916
7	0.620	0.525	1.663	-99.999	-6.255	-6.706
8	2.832	5.234	6.909	-99.999	3.945	5.562
9	0.538	5.356	6.681	-99.999	-99.999	-99.999
10	0.538	5.357	6.682	-99.999	-60.321	-60.394
11	0.631	5.344	6.672	-99.999	-18.185	-17.817
12	2.925	5.921	7.612	-99.999	3.221	4.834

	$^{36}Cl \rightarrow {}^{36}S$			$^{36}S \rightarrow {}^{36}Cl$		
pt	log β^+	log ε^-	log ν	log β^-	log ε^+	log $\bar{\nu}$
1	-10.261	-12.820	-10.366	-18.656	-14.910	-15.464
2	-6.155	-6.407	-5.742	-7.545	-6.911	-6.812
3	-2.789	-2.336	-1.509	-2.065	-1.995	-1.095
4	0.615	4.666	6.326	1.084	4.624	6.252
5	-10.261	-9.001	-8.541	-18.932	-20.730	-18.949
6	-6.147	-4.934	-4.431	-7.729	-8.627	-7.626
7	-2.785	-2.240	-1.427	-2.070	-2.091	-1.153
8	0.615	4.667	6.328	1.084	4.624	6.252
9	-10.261	4.043	5.166	-99.999	-99.999	-99.999
10	-6.146	4.045	5.170	-41.983	-47.105	-42.124
11	-2.787	4.052	5.193	-11.428	-13.996	-11.132
12	0.782	5.353	7.029	0.660	3.900	5.525

	$^{36}K \rightarrow {}^{36}Ar$			$^{36}Ar \rightarrow {}^{36}K$		
pt	log β^+	log ε^-	log ν	log β^-	log ε^+	log $\bar{\nu}$
1	0.357	-4.182	0.949	-77.783	-65.016	-65.591
2	0.368	-1.851	0.969	-25.509	-21.943	-22.021
3	0.432	0.085	1.370	-7.188	-5.626	-5.102
4	3.055	5.179	6.884	-1.397	3.951	5.553
5	0.357	-0.450	1.059	-77.893	-70.835	-71.411
6	0.368	-0.426	1.080	-25.503	-23.658	-23.728
7	0.434	0.177	1.419	-7.203	-5.724	-5.199
8	3.055	5.179	6.884	-1.397	3.951	5.553
9	0.357	5.034	6.335	-99.999	-99.999	-99.999
10	0.368	5.035	6.337	-61.953	-62.136	-61.880
11	0.445	5.025	6.330	-18.189	-17.636	-17.075
12	3.150	5.860	7.581	-1.871	3.226	4.825

	$^{37}Ca \rightarrow {}^{37}K$			$^{37}K \rightarrow {}^{37}Ca$		
pt	log β^+	log ε^-	log ν	log β^-	log ε^+	log $\bar{\nu}$
1	0.648	-3.878	1.219	-99.999	-69.563	-60.139
2	0.648	-1.555	1.224	-99.999	-20.454	-20.531
3	0.649	0.408	1.613	-99.999	-5.781	-5.249
4	2.810	5.132	6.823	-99.999	3.758	5.364
5	0.648	-0.153	1.340	-99.999	-65.383	-65.959
6	0.648	-0.130	1.348	-99.999	-22.170	-22.247
7	0.651	0.501	1.668	-99.999	-5.879	-5.347
8	2.810	5.132	6.823	-99.999	3.758	5.364
9	0.648	5.212	6.554	-99.999	-99.999	-99.999
10	0.648	5.213	6.556	-99.999	-60.648	-60.724
11	0.663	5.198	6.542	-99.999	-17.790	-17.259
12	2.908	5.815	7.523	-99.999	3.033	4.636

	$^{36}Ar \rightarrow {}^{36}Cl$			$^{36}Cl \rightarrow {}^{36}Ar$		
pt	log β^+	log ε^-	log ν	log β^-	log ε^+	log $\bar{\nu}$
1	-16.473	-16.274	-16.169	-9.664	-10.778	-9.599
2	-8.929	-7.008	-6.795	-5.631	-6.037	-5.386
3	-2.660	-1.837	-1.070	-2.648	-2.422	-1.601
4	1.949	4.712	6.373	1.159	4.441	6.078
5	-16.473	-11.456	-11.811	-9.955	-16.598	-10.030
6	-8.921	-6.446	-6.220	-6.777	-7.749	-5.739
7	-2.654	-1.742	-0.979	-2.651	-2.520	-1.863
8	1.949	4.712	6.373	1.159	4.441	6.078
9	-16.473	4.357	5.467	-99.999	-99.999	-99.999
10	-8.921	4.359	5.470	-39.976	-46.227	-40.116
11	-2.629	4.395	5.531	-12.004	-14.426	-11.709
12	2.066	5.404	7.079	0.733	3.718	5.352

	$^{37}K \rightarrow {}^{37}Ar$			$^{37}Ar \rightarrow {}^{37}K$		
pt	log β^+	log ε^-	log ν	log β^-	log ε^+	log $\bar{\nu}$
1	-0.219	-4.435	0.223	-38.848	-32.449	-33.022
2	-0.221	-2.098	0.233	-15.224	-11.756	-11.825
3	-0.269	-0.174	0.850	-4.884	-3.361	-2.819
4	2.121	4.864	6.540	-1.092	4.184	5.802
5	-0.219	-0.692	0.463	-41.085	-38.269	-38.841
6	-0.220	-0.664	0.484	-15.329	-13.470	-13.530
7	-0.264	-0.081	0.926	-4.899	-3.459	-2.917
8	2.121	4.865	6.540	-1.092	4.184	5.802
9	-0.219	4.870	6.171	-99.999	-99.999	-99.999
10	-0.220	4.870	6.171	-61.725	-61.948	-61.667
11	-0.245	4.832	6.132	-15.891	-15.371	-14.792
12	2.237	5.551	7.243	-1.567	3.460	5.074

	$^{37}Ar \rightarrow {}^{37}Cl$			$^{37}Cl \rightarrow {}^{37}Ar$		
pt	log β^+	log ε^-	log ν	log β^-	log ε^+	log $\bar{\nu}$
1	-11.795	-7.829	-7.640	-13.095	-9.500	-9.818
2	-6.820	-4.992	-4.779	-7.175	-5.841	-5.729
3	-2.767	-1.950	-1.201	-2.298	-2.281	-1.382
4	1.750	4.625	6.304	0.484	4.325	5.941
5	-11.795	-3.648	-3.507	-14.131	-15.319	-14.618
6	-6.812	-3.467	-3.211	-7.485	-7.552	-7.198
7	-2.761	-1.854	-1.110	-2.302	-2.377	-1.440
8	1.750	4.625	6.304	0.484	4.325	5.941
9	-11.795	4.206	5.371	-99.999	-99.999	-99.999
10	-6.812	4.207	5.373	-42.280	-46.030	-42.427
11	-2.738	4.213	5.392	-12.263	-14.281	-11.987
12	1.879	5.311	7.006	0.042	3.601	5.213

	$^{38}K \rightarrow {}^{38}Ar$			$^{38}Ar \rightarrow {}^{38}K$		
pt	log β^+	log ε^-	log ν	log β^-	log ε^+	log $\bar{\nu}$
1	-1.551	-5.695	-1.118	-43.981	-31.864	-32.234
2	-1.016	-2.931	-0.557	-14.384	-11.279	-11.345
3	-0.807	-0.694	0.310	-4.164	-2.917	-2.351
4	1.610	4.592	6.264	-1.105	4.070	5.689
5	-1.551	-1.930	-0.856	-44.072	-37.484	-38.054
6	-1.015	-1.498	-0.325	-14.462	-12.994	-13.036
7	-0.803	-0.600	0.386	-4.177	-3.016	-2.447
8	1.610	4.592	6.264	-1.105	4.070	5.689
9	-1.551	4.415	5.660	-99.999	-99.999	-99.999
10	-1.015	4.447	5.706	-50.643	-61.472	-50.758
11	-0.784	4.479	5.758	-15.128	-14.928	-14.285
12	1.738	5.279	6.967	-1.578	3.345	4.961

	$^{37}Cl \rightarrow {}^{37}S$			$^{37}S \rightarrow {}^{37}Cl$		
pt	log β^+	log ε^-	log ν	log β^-	log ε^+	log $\bar{\nu}$
1	-51.224	-31.546	-32.101	-2.577	-6.974	-2.523
2	-16.837	-12.087	-12.102	-2.621	-3.935	-2.509
3	-4.735	-3.752	-3.081	-2.942	-1.881	-1.125
4	1.990	4.237	5.955	-3.603	4.226	5.796
5	-51.224	-25.704	-26.261	-2.845	-12.794	-2.874
6	-16.836	-10.360	-10.393	-2.818	-5.640	-2.805
7	-4.729	-3.655	-2.988	-2.962	-1.977	-1.220
8	1.990	4.237	5.955	-3.603	4.226	5.796
9	-51.224	0.168	1.348	-99.999	-99.999	-99.999
10	-16.836	0.175	1.356	-37.356	-44.118	-37.515
11	-4.702	1.871	3.134	-14.044	-13.875	-13.074
12	2.093	4.914	6.649	-4.084	3.497	5.066

	$^{38}Ar \rightarrow {}^{38}Cl$			$^{38}Cl \rightarrow {}^{38}Ar$		
pt	log β^+	log ε^-	log ν	log β^-	log ε^+	log $\bar{\nu}$
1	-50.729	-32.083	-32.607	-3.500	-7.583	-3.205
2	-16.447	-12.127	-12.112	-3.361	-4.360	-3.043
3	-4.261	-3.030	-2.389	-2.193	-1.768	-0.942
4	2.163	4.470	6.184	-1.938	4.183	5.754
5	-50.729	-26.368	-26.902	-3.670	-13.403	-3.304
6	-16.446	-10.449	-10.424	-3.481	-6.067	-3.182
7	-4.254	-2.933	-2.294	-2.202	-1.863	-1.024
8	2.163	4.470	6.184	-1.938	4.183	5.754
9	-50.729	2.548	3.664	-98.288	-99.999	-98.886
10	-16.445	2.550	3.667	-34.840	-44.544	-34.982
11	-4.225	2.857	4.073	-12.130	-13.761	-11.827
12	2.269	5.147	6.879	-2.389	3.454	5.024

	$^{38}Ca \rightarrow {}^{38}K$			$^{38}K \rightarrow {}^{38}Ca$		
pt	log β^+	log ε^-	log ν	log β^-	log ε^+	log $\bar{\nu}$
1	0.211	-3.973	0.656	-40.480	-35.851	-36.424
2	0.210	-1.640	0.669	-17.123	-13.220	-13.291
3	0.130	0.234	1.258	-8.998	-4.126	-3.598
4	2.206	4.835	6.523	-5.418	3.804	5.410
5	0.211	-0.237	0.911	-43.531	-41.670	-42.241
6	0.211	-0.210	0.931	-17.886	-14.936	-15.006
7	0.135	0.327	1.333	-9.034	-4.224	-3.696
8	2.206	4.835	6.523	-5.418	3.804	5.410
9	0.211	5.069	6.423	-99.999	-99.999	-99.999
10	0.211	5.070	6.425	-56.289	-53.413	-53.484
11	0.153	4.976	6.329	-20.538	-16.136	-15.606
12	2.320	5.518	7.223	-5.913	3.079	4.681

	$^{38}Cl \rightarrow {}^{38}S$			$^{38}S \rightarrow {}^{38}Cl$		
pt	log β^+	log ε^-	log ν	log β^-	log ε^+	log $\bar{\nu}$
1	-42.052	-23.094	-23.607	-4.132	-7.128	-4.265
2	-14.539	-10.019	-9.994	-3.978	-3.952	-3.467
3	-5.070	-3.996	-3.321	-2.655	-1.694	-0.967
4	1.176	3.841	5.547	-2.491	4.465	6.043
5	-42.052	-17.685	-18.110	-4.840	-12.949	-4.919
6	-14.538	-8.355	-8.305	-4.225	-5.659	-4.188
7	-5.064	-3.899	-3.227	-2.668	-1.789	-1.060
8	1.176	3.841	5.547	-2.491	4.465	6.043
9	-42.052	-1.001	0.225	-99.999	-99.999	-99.999
10	-14.538	-0.398	0.837	-40.661	-44.137	-40.850
11	-5.037	1.552	2.817	-13.573	-13.689	-12.858
12	1.299	4.519	6.244	-2.962	3.737	5.313

	$^{39}Ca \rightarrow {}^{39}K$			$^{39}K \rightarrow {}^{39}Ca$		
pt	log β^+	log ε^-	log ν	log β^-	log ε^+	log $\bar{\nu}$
1	-0.069	-4.386	0.400	-38.915	-34.287	-34.862
2	-0.070	-2.057	0.409	-16.087	-12.351	-12.427
3	-0.108	-0.045	0.990	-8.222	-3.486	-2.966
4	1.852	4.794	6.475	-5.377	4.076	5.667
5	-0.069	-0.656	0.606	-41.845	-40.106	-40.678
6	-0.069	-0.629	0.621	-16.828	-14.066	-14.142
7	-0.103	0.048	1.064	-8.258	-3.584	-3.064
8	1.852	4.794	6.476	-5.377	4.076	5.667
9	-0.069	4.770	6.106	-99.999	-99.999	-99.999
10	-0.069	4.771	6.107	-55.224	-52.544	-52.620
11	-0.085	4.766	6.108	-19.756	-15.496	-14.976
12	1.977	5.478	7.177	-5.871	3.349	4.838

	$^{39}K \rightarrow {}^{39}Ar$			$^{39}Ar \rightarrow {}^{39}K$		
pt	log β^+	log ε^-	log ν	log β^-	log ε^+	log $\bar{\nu}$
1	-18.174	-15.946	-16.471	-9.964	-13.057	-10.252
2	-8.497	-8.018	-7.775	-5.588	-6.992	-5.414
3	-2.794	-2.133	-1.343	-3.341	-2.432	-1.764
4	2.331	4.594	6.312	-1.126	4.035	5.605
5	-18.174	-10.238	-10.718	-10.946	-18.876	-10.952
6	-8.489	-8.363	-8.250	-5.694	-8.702	-5.588
7	-2.789	-2.038	-1.255	-3.353	-2.529	-1.857
8	2.331	4.594	6.312	-1.126	4.035	5.605
9	-18.174	3.286	4.484	-99.999	-99.999	-99.999
10	-8.489	3.287	4.486	-41.090	-47.180	-41.227
11	-2.768	3.337	4.580	-13.013	-14.434	-12.660
12	2.434	5.271	7.006	-1.525	3.306	4.874

	$^{39}Ar \rightarrow {}^{39}Cl$			$^{39}Cl \rightarrow {}^{39}Ar$		
pt	log β^+	log ε^-	log ν	log β^-	log ε^+	log $\bar{\nu}$
1	-45.928	-25.645	-26.188	-3.618	-7.697	-3.556
2	-15.385	-10.761	-10.781	-3.203	-4.462	-3.040
3	-4.869	-3.901	-3.233	-2.591	-2.068	-1.281
4	1.867	4.101	5.834	-2.142	4.590	6.161
5	-45.928	-19.909	-20.420	-3.865	-13.516	-3.878
6	-15.384	-9.056	-9.070	-3.337	-6.168	-3.263
7	-4.863	-3.804	-3.140	-2.602	-2.164	-1.369
8	1.867	4.101	5.834	-2.142	4.590	6.161
9	-45.928	-0.622	0.598	-99.999	-99.999	-99.999
10	-15.384	0.228	1.449	-39.441	-44.645	-39.609
11	-4.839	1.915	3.155	-13.125	-14.063	-12.779
12	1.977	4.774	6.526	-2.595	3.861	5.430

	$^{40}Ti \rightarrow {}^{40}Sc$			$^{40}Sc \rightarrow {}^{40}Ti$		
pt	log β^+	log ε^-	log ν	log β^-	log ε^+	log $\bar{\nu}$
1	0.645	-3.853	1.181	-73.276	-69.386	-69.964
2	0.638	-1.551	1.180	-25.296	-21.210	-21.293
3	0.228	-0.060	1.170	-7.928	-6.362	-5.845
4	-0.547	4.941	6.557	-0.151	3.960	5.607
5	0.645	-0.140	1.318	-73.375	-65.206	-65.784
6	0.639	-0.133	1.320	-25.372	-22.925	-23.005
7	0.230	0.033	1.228	-7.937	-6.451	-5.943
8	-0.547	4.941	6.557	-0.151	3.960	5.607
9	0.645	5.200	6.503	-99.999	-99.999	-99.999
10	0.639	5.198	6.501	-60.875	-61.403	-60.906
11	0.242	5.079	6.340	-18.387	-18.363	-17.693
12	-0.398	5.641	7.272	-0.604	3.239	4.881

	$^{40}Sc \rightarrow {}^{40}Ca$			$^{40}Ca \rightarrow {}^{40}Sc$		
pt	log β^+	log ε^-	log ν	log β^-	log ε^+	log $\bar{\nu}$
1	0.536	-3.979	1.114	-97.772	-72.067	-72.644
2	0.517	-1.682	1.099	-31.170	-23.903	-23.983
3	0.459	0.186	1.419	-7.750	-5.910	-5.411
4	1.030	4.695	6.332	-0.356	3.356	5.007
5	0.536	-0.261	1.237	-97.795	-77.887	-78.464
6	0.517	-0.261	1.226	-31.189	-25.618	-25.699
7	0.462	0.278	1.477	-7.756	-6.009	-5.508
8	1.030	4.695	6.332	-0.356	3.356	5.007
9	0.536	4.907	6.243	-99.999	-99.999	-99.999
10	0.517	4.898	6.232	-63.571	-64.096	-63.592
11	0.474	4.872	6.205	-17.829	-17.922	-17.200
12	1.149	5.390	7.042	-0.802	2.635	4.281

	$^{40}Ca \rightarrow {}^{40}K$			$^{40}K \rightarrow {}^{40}Ca$		
pt	log β^+	log ε^-	log ν	log β^-	log ε^+	log $\bar{\nu}$
1	-21.597	-24.046	-21.684	-14.542	-15.743	-14.227
2	-8.907	-8.984	-8.404	-6.906	-7.382	-6.527
3	-2.481	-1.919	-1.065	-4.506	-2.705	-2.134
4	2.039	4.307	6.032	-4.245	3.860	5.438
5	-21.597	-19.621	-19.680	-14.648	-21.562	-14.383
6	-8.899	-7.493	-7.047	-6.952	-9.097	-6.664
7	-2.477	-1.825	-0.979	-4.516	-2.803	-2.232
8	2.039	4.307	6.032	-4.245	3.860	5.438
9	-21.597	2.495	3.705	-99.999	-99.999	-99.999
10	-8.899	2.496	3.708	-42.197	-47.575	-42.370
11	-2.455	3.054	4.368	-15.264	-14.713	-14.102
12	2.145	4.982	6.725	-4.711	3.132	4.708

	$^{40}K \rightarrow {}^{40}Ar$			$^{40}Ar \rightarrow {}^{40}K$		
pt	log β^+	log ε^-	log ν	log β^-	log ε^+	log $\bar{\nu}$
1	-14.718	-16.884	-14.688	-20.201	-20.591	-20.067
2	-7.280	-7.461	-6.818	-7.680	-8.271	-7.455
3	-3.008	-2.343	-1.564	-3.477	-2.413	-1.722
4	2.054	4.534	6.245	-3.000	4.130	5.702
5	-14.718	-12.508	-12.555	-20.404	-26.411	-20.408
6	-7.276	-6.910	-6.579	-7.804	-9.984	-7.716
7	-3.003	-2.248	-1.476	-3.492	-2.509	-1.817
8	2.054	4.534	6.245	-3.000	4.130	5.702
9	-14.718	3.014	4.247	-99.999	-99.999	-99.999
10	-7.275	3.009	4.244	-44.373	-48.462	-44.570
11	-2.980	3.065	4.337	-14.487	-14.412	-13.652
12	2.167	5.211	6.941	-3.474	3.401	4.972

	$^{41}Sc \rightarrow {}^{41}Ca$			$^{41}Ca \rightarrow {}^{41}Sc$		
pt	log β^+	log ε^-	log ν	log β^-	log ε^+	log $\bar{\nu}$
1	0.074	-4.233	0.545	-48.868	-34.024	-34.599
2	0.073	-1.913	0.555	-16.085	-12.185	-12.262
3	0.006	-0.019	1.070	-5.390	-3.428	-2.920
4	1.489	4.609	6.280	-1.361	3.939	5.557
5	0.074	-0.509	0.752	-46.990	-39.843	-40.419
6	0.074	-0.490	0.766	-16.188	-13.901	-13.974
7	0.010	0.073	1.142	-5.405	-3.527	-3.018
8	1.489	4.609	6.280	-1.361	3.939	5.557
9	0.074	4.729	6.074	-99.999	-99.999	-99.999
10	0.074	4.730	6.076	-62.633	-62.378	-62.303
11	0.027	4.699	6.044	-16.414	-15.439	-14.918
12	1.618	5.296	6.984	-1.836	3.214	4.829

	$^{40}Ar \rightarrow {}^{40}Cl$			$^{40}Cl \rightarrow {}^{40}Ar$		
pt	log β^+	log ε^-	log ν	log β^-	log ε^+	log $\bar{\nu}$
1	-67.467	-44.544	-45.112	-2.008	-7.225	-1.700
2	-21.683	-16.202	-16.265	-1.898	-4.165	-1.559
3	-5.871	-4.913	-4.285	-1.584	-1.933	-0.819
4	1.797	4.052	5.773	-1.637	4.351	5.921
5	-67.467	-38.725	-39.293	-2.080	-13.044	-1.802
6	-21.682	-14.487	-14.550	-1.946	-5.870	-1.630
7	-5.866	-4.815	-4.194	-1.592	-2.027	-0.877
8	1.797	4.052	5.773	-1.637	4.351	5.921
9	-67.467	0.322	1.430	-87.457	-99.999	-88.055
10	-21.682	0.317	1.426	-32.685	-44.347	-32.827
11	-5.845	1.517	2.719	-12.001	-13.920	-11.765
12	1.901	4.728	6.467	-2.094	3.622	5.191

	$^{41}Ca \rightarrow {}^{41}K$			$^{41}K \rightarrow {}^{41}Ca$		
pt	log β^+	log ε^-	log ν	log β^-	log ε^+	log $\bar{\nu}$
1	-14.341	-12.627	-13.104	-10.668	-13.937	-10.923
2	-7.348	-6.490	-6.358	-6.178	-6.596	-5.977
3	-2.727	-1.964	-1.180	-4.054	-2.419	-1.796
4	2.108	4.512	6.223	-1.412	3.954	5.526
5	-14.341	-6.865	-7.404	-11.832	-19.756	-12.395
6	-7.338	-4.817	-4.749	-6.502	-8.305	-6.611
7	-2.722	-1.869	-1.090	-4.064	-2.516	-1.892
8	2.108	4.512	6.223	-1.412	3.954	5.526
9	-14.341	3.055	4.274	-99.999	-99.999	-99.999
10	-7.338	3.057	4.277	-42.600	-46.782	-42.741
11	-2.701	3.224	4.502	-13.642	-14.422	-13.218
12	2.215	5.189	6.919	-1.844	3.225	4.795

	$^{41}Ti \rightarrow {}^{41}Sc$			$^{41}Sc \rightarrow {}^{41}Ti$		
pt	log β^+	log ε^-	log ν	log β^-	log ε^+	log $\bar{\nu}$
1	0.932	-3.663	1.527	-81.646	-66.270	-66.848
2	0.923	-1.370	1.526	-27.571	-22.771	-22.855
3	0.758	0.222	1.652	-8.056	-6.233	-6.738
4	0.503	4.779	6.404	-0.552	3.479	5.121
5	0.932	0.047	1.634	-81.731	-72.090	-72.668
6	0.923	0.047	1.632	-27.637	-24.487	-24.570
7	0.759	0.314	1.894	-8.064	-6.332	-6.838
8	0.503	4.779	6.405	-0.552	3.478	5.121
9	0.932	5.161	6.513	-99.999	-99.999	-99.999
10	0.923	5.153	6.504	-62.745	-62.965	-62.670
11	0.768	4.981	6.298	-18.413	-18.244	-17.619
12	0.651	5.476	7.117	-1.002	2.757	4.395

	$^{41}K \rightarrow {}^{41}Ar$			$^{41}Ar \rightarrow {}^{41}K$		
pt	log β^+	log ε^-	log ν	log β^-	log ε^+	log $\bar{\nu}$
1	-41.538	-20.267	-20.809	-3.881	-7.749	-3.996
2	-13.378	-8.461	-8.475	-3.518	-4.479	-3.332
3	-3.973	-2.846	-2.209	-2.397	-1.902	-1.107
4	2.030	4.386	6.112	-2.017	4.341	5.917
5	-41.538	-14.508	-15.044	-4.463	-13.568	-4.774
6	-13.378	-6.769	-6.774	-3.702	-6.186	-3.593
7	-3.968	-2.748	-2.115	-2.408	-1.998	-1.194
8	2.030	4.386	6.112	-2.017	4.341	5.917
9	-41.538	2.917	4.110	-99.999	-99.999	-99.999
10	-13.377	2.920	4.116	-38.808	-44.663	-38.967
11	-3.945	2.952	4.194	-13.011	-13.896	-12.652
12	2.143	5.061	6.805	-2.480	3.612	5.186

	$^{41}Ar \rightarrow {}^{41}Cl$			$^{41}Cl \rightarrow {}^{41}Ar$		
pt	log β^+	log ε^-	log ν	log β^-	log ε^+	log $\bar{\nu}$
1	-56.936	-36.193	-36.765	-1.687	-7.095	-1.361
2	-19.160	-14.261	-14.330	-1.683	-4.062	-1.351
3	-6.082	-6.068	-4.446	-0.832	-1.721	-0.131
4	1.785	4.064	5.781	-0.204	4.437	6.010
5	-56.936	-30.373	-30.945	-1.740	-12.914	-1.449
6	-19.159	-12.546	-12.614	-1.726	-5.766	-1.422
7	-6.076	-4.970	-4.353	-0.836	-1.816	-0.153
8	1.785	4.064	5.782	-0.204	4.437	6.010
9	-56.936	2.169	3.239	-93.575	-99.999	-94.171
10	-19.159	2.236	3.307	-32.352	-44.244	-32.488
11	-6.052	2.291	3.398	-9.933	-13.710	-9.627
12	1.890	4.740	6.476	-0.623	3.708	5.279

	$^{42}Ca \rightarrow {}^{42}K$			$^{42}K \rightarrow {}^{42}Ca$		
pt	log β^+	log ε^-	log ν	log β^-	log ε^+	log $\bar{\nu}$
1	-47.945	-25.559	-26.032	-4.963	-8.117	-4.704
2	-14.863	-9.768	-9.724	-4.230	-4.756	-3.944
3	-3.490	-2.588	-1.902	-3.332	-2.143	-1.416
4	2.409	4.683	6.402	-3.292	4.126	5.692
5	-47.945	-20.537	-20.827	-5.058	-13.937	-4.833
6	-14.862	-8.128	-8.056	-4.374	-6.464	-4.263
7	-3.486	-2.491	-1.812	-3.349	-2.238	-1.511
8	2.409	4.683	6.402	-3.292	4.126	5.692
9	-47.945	0.257	1.468	-99.999	-99.999	-99.999
10	-14.862	0.829	2.047	-40.248	-44.941	-40.428
11	-3.468	2.892	4.164	-14.358	-14.137	-13.367
12	2.512	5.359	7.096	-3.768	3.396	4.961

	$^{42}Ti \rightarrow {}^{42}Sc$			$^{42}Sc \rightarrow {}^{42}Ti$		
pt	log β^+	log ε^-	log ν	log β^-	log ε^+	log $\bar{\nu}$
1	0.556	-3.757	1.041	-46.845	-36.126	-36.702
2	0.552	-1.444	1.047	-16.681	-13.028	-13.104
3	0.173	0.055	1.194	-6.254	-4.256	-3.743
4	1.972	4.735	6.414	-1.776	3.880	5.493
5	0.556	-0.037	1.244	-47.067	-41.946	-42.521
6	0.553	-0.022	1.253	-16.820	-14.741	-14.814
7	0.176	0.148	1.260	-6.272	-4.355	-3.841
8	1.972	4.735	6.414	-1.776	3.880	5.493
9	0.556	5.098	6.469	-99.999	-99.999	-99.999
10	0.553	5.096	6.467	-53.957	-53.219	-53.243
11	0.191	4.816	6.155	-17.427	-16.267	-15.746
12	2.088	5.420	7.116	-2.256	3.155	4.765

	$^{42}K \rightarrow {}^{42}Ar$			$^{42}Ar \rightarrow {}^{42}K$		
pt	log β^+	log ε^-	log ν	log β^-	log ε^+	log $\bar{\nu}$
1	-33.089	-16.470	-16.999	-9.144	-12.200	-9.543
2	-11.727	-8.671	-8.662	-5.558	-6.190	-5.319
3	-4.050	-3.363	-2.626	-2.809	-2.236	-1.434
4	2.162	4.626	6.341	-2.530	4.366	5.937
5	-33.089	-10.709	-11.201	-11.071	-18.019	-11.756
6	-11.726	-6.987	-6.963	-5.716	-7.896	-5.675
7	-4.045	-3.266	-2.537	-2.824	-2.331	-1.524
8	2.162	4.626	6.341	-2.531	4.366	5.937
9	-33.089	-2.033	-0.772	-99.999	-99.999	-99.999
10	-11.726	1.372	2.615	-42.550	-46.374	-42.749
11	-4.023	2.360	3.613	-13.749	-14.228	-13.240
12	2.275	5.303	7.036	-2.997	3.637	5.206

	$^{42}Sc \rightarrow {}^{42}Ca$			$^{42}Ca \rightarrow {}^{42}Sc$		
pt	log β^+	log ε^-	log ν	log β^-	log ε^+	log $\bar{\nu}$
1	0.045	-4.281	0.518	-54.795	-33.714	-34.290
2	-0.270	-2.259	0.218	-17.556	-11.988	-12.063
3	-0.668	-0.631	0.427	-4.449	-3.305	-2.766
4	2.098	4.546	6.220	-0.292	3.924	5.548
5	0.045	-0.559	0.718	-54.830	-39.534	-40.109
6	-0.269	-0.835	0.424	-17.586	-13.703	-13.779
7	-0.663	-0.538	0.501	-4.456	-3.404	-2.860
8	2.098	4.546	6.220	-0.292	3.924	5.548
9	0.045	4.695	6.024	-99.999	-99.999	-99.999
10	-0.269	4.563	5.857	-51.502	-52.181	-51.565
11	-0.646	4.465	5.729	-14.900	-15.317	-14.446
12	2.198	5.234	6.923	-0.749	3.200	4.821

	$^{43}Ti \rightarrow {}^{43}Sc$			$^{43}Sc \rightarrow {}^{43}Ti$		
pt	log β^+	log ε^-	log ν	log β^-	log ε^+	log $\bar{\nu}$
1	0.199	-4.186	0.701	-46.360	-35.906	-36.482
2	0.163	-1.908	0.674	-15.990	-12.894	-12.972
3	0.032	-0.062	1.054	-5.514	-3.828	-3.299
4	2.175	4.937	6.619	-1.543	4.092	5.703
5	0.199	-0.470	0.874	-46.558	-41.725	-42.301
6	0.164	-0.487	0.851	-16.123	-14.610	-14.671
7	0.035	0.031	1.123	-5.532	-3.928	-3.396
8	2.175	4.937	6.619	-1.543	4.092	5.703
9	0.199	4.916	6.236	-99.999	-99.999	-99.999
10	0.164	4.903	6.221	-63.165	-63.088	-62.961
11	0.051	4.866	6.179	-16.666	-15.838	-15.292
12	2.292	5.622	7.320	-2.023	3.367	4.975

	$^{43}Sc \rightarrow {}^{43}Ca$			$^{43}Ca \rightarrow {}^{43}Sc$		
pt	log β^+	log ε^-	log ν	log β^-	log ε^+	log $\bar{\nu}$
1	-4.374	-6.459	-4.551	-20.658	-14.845	-15.385
2	-4.208	-3.975	-3.499	-13.169	-7.099	-7.083
3	-1.995	-1.373	-0.538	-3.306	-2.621	-1.954
4	1.861	4.853	6.537	0.513	4.274	5.883
5	-4.374	-2.605	-2.231	-24.093	-20.664	-21.205
6	-4.198	-2.487	-2.068	-13.727	-8.814	-8.798
7	-1.990	-1.279	-0.451	-3.310	-2.719	-2.036
8	1.861	4.853	6.537	0.513	4.274	5.883
9	-4.374	4.205	5.375	-99.999	-99.999	-99.999
10	-4.198	4.202	5.371	-44.497	-47.291	-44.640
11	-1.970	4.218	5.404	-12.951	-14.627	-12.658
12	1.991	5.537	7.238	0.079	3.549	5.155

	$^{43}Ar \rightarrow {}^{43}Cl$			$^{43}Cl \rightarrow {}^{43}Ar$		
pt	log β^+	log ε^-	log ν	log β^-	log ε^+	log $\bar{\nu}$
1	-72.022	-53.344	-53.923	-2.341	-8.626	-1.722
2	-23.756	-19.788	-19.873	-1.547	-4.802	-0.943
3	-6.753	-5.862	-5.207	-0.641	-1.812	0.023
4	1.862	4.358	6.070	-0.648	4.605	6.181
5	-72.022	-47.525	-48.103	-2.351	-14.445	-1.739
6	-23.755	-18.073	-18.158	-1.556	-6.506	-0.959
7	-6.747	-5.764	-5.116	-0.644	-1.906	0.007
8	1.862	4.358	6.070	-0.648	4.605	6.181
9	-72.022	-0.379	0.688	-80.466	-99.999	-81.062
10	-23.755	-0.149	0.930	-29.963	-44.984	-30.100
11	-6.721	1.637	2.758	-9.957	-13.798	-9.862
12	1.978	5.035	6.766	-1.075	3.876	5.451

	$^{43}Ca \rightarrow {}^{43}K$			$^{43}K \rightarrow {}^{43}Ca$		
pt	log β^+	log ε^-	log ν	log β^-	log ε^+	log $\bar{\nu}$
1	-40.223	-18.152	-18.649	-4.961	-8.196	-5.115
2	-13.377	-8.164	-8.165	-3.144	-4.551	-2.953
3	-3.902	-2.730	-2.104	-2.308	-1.796	-0.990
4	1.965	4.329	6.040	-2.191	4.071	5.641
5	-40.223	-12.465	-12.981	-6.680	-14.016	-6.722
6	-13.377	-6.470	-6.464	-3.250	-6.257	-3.125
7	-3.897	-2.632	-2.010	-2.321	-1.891	-1.079
8	1.965	4.329	6.040	-2.191	4.071	5.641
9	-40.223	2.997	4.218	-99.999	-99.999	-99.999
10	-13.377	3.032	4.257	-39.454	-44.735	-39.635
11	-3.878	3.052	4.300	-13.168	-13.788	-12.729
12	2.069	5.007	6.735	-2.660	3.342	4.911

	$^{44}V \rightarrow {}^{44}Ti$			$^{44}Ti \rightarrow {}^{44}V$		
pt	log β^+	log ε^-	log ν	log β^-	log ε^+	log $\bar{\nu}$
1	0.695	-4.069	1.386	-86.328	-69.306	-69.885
2	0.391	-2.070	1.082	-27.479	-23.234	-23.318
3	0.228	-0.331	1.130	-7.405	-6.504	-5.949
4	3.026	5.187	6.894	-0.814	3.884	5.485
5	0.695	-0.355	1.451	-86.387	-75.126	-75.704
6	0.391	-0.654	1.149	-27.527	-24.949	-25.031
7	0.230	-0.238	1.168	-7.415	-6.602	-6.041
8	3.026	5.187	6.894	-0.814	3.884	5.485
9	0.695	5.018	6.313	-99.999	-99.999	-99.999
10	0.391	4.939	6.201	-62.600	-63.427	-62.701
11	0.237	4.917	6.172	-18.120	-18.514	-17.676
12	3.120	5.868	7.590	-1.279	3.158	4.757

	$^{43}K \rightarrow {}^{43}Ar$			$^{43}Ar \rightarrow {}^{43}K$		
pt	log β^+	log ε^-	log ν	log β^-	log ε^+	log $\bar{\nu}$
1	-52.618	-31.143	-31.708	-2.745	-7.721	-2.525
2	-17.396	-12.684	-12.738	-2.538	-4.646	-2.339
3	-6.443	-4.499	-3.860	-1.160	-1.874	-0.492
4	1.961	4.327	6.044	-0.983	4.719	6.287
5	-52.618	-25.324	-25.889	-2.855	-13.541	-2.681
6	-17.395	-10.968	-11.022	-2.706	-6.351	-2.430
7	-6.436	-4.401	-3.788	-1.165	-1.968	-0.528
8	1.962	4.327	6.044	-0.983	4.719	6.287
9	-52.618	-0.625	0.516	-99.999	-99.999	-99.999
10	-17.396	1.831	2.977	-36.361	-44.829	-36.506
11	-6.415	2.342	3.508	-11.068	-13.863	-10.798
12	2.070	5.003	6.739	-1.420	3.990	5.556

	$^{44}Ti \rightarrow {}^{44}Sc$			$^{44}Sc \rightarrow {}^{44}Ti$		
pt	log β^+	log ε^-	log ν	log β^-	log ε^+	log $\bar{\nu}$
1	-11.534	-9.839	-10.265	-9.869	-11.154	-10.377
2	-6.514	-5.297	-5.069	-8.118	-6.631	-6.504
3	-2.768	-1.618	-0.846	-3.682	-3.071	-2.380
4	2.188	4.870	6.551	1.139	4.227	5.848
5	-11.534	-4.929	-5.230	-12.467	-16.973	-13.210
6	-6.506	-3.736	-3.499	-8.801	-8.343	-8.192
7	-2.762	-1.523	-0.754	-3.685	-3.169	-2.454
8	2.188	4.870	6.551	1.139	4.227	5.848
9	-11.534	4.316	5.393	-99.999	-99.999	-99.999
10	-6.506	4.321	5.401	-42.021	-46.821	-42.158
11	-2.734	4.364	5.478	-12.606	-15.078	-12.295
12	2.306	5.557	7.253	0.724	3.502	5.120

	$^{44}Sc \rightarrow {}^{44}Ca$			$^{44}Ca \rightarrow {}^{44}Sc$		
pt	log β^+	log ε^-	log ν	log β^-	log ε^+	log $\bar{\nu}$
1	-4.490	-6.946	-4.544	-26.137	-21.701	-22.239
2	-4.117	-4.476	-3.683	-10.617	-8.763	-8.742
3	-2.190	-1.696	-0.845	-3.109	-2.689	-1.937
4	1.969	4.923	6.612	0.574	4.364	5.965
5	-4.490	-3.104	-2.681	-27.974	-27.521	-27.905
6	-4.113	-2.990	-2.538	-10.984	-10.477	-10.385
7	-2.186	-1.601	-0.762	-3.112	-2.786	-2.009
8	1.969	4.923	6.612	0.574	4.363	5.965
9	-4.490	4.090	5.229	-99.999	-99.999	-99.999
10	-4.113	4.099	5.243	-45.661	-48.955	-45.803
11	-2.188	4.128	5.293	-12.637	-14.892	-12.347
12	2.099	5.605	7.312	0.143	3.637	5.237

	$^{44}Ca \rightarrow {}^{44}K$			$^{44}K \rightarrow {}^{44}Ca$		
pt	log β^+	log ε^-	log ν	log β^-	log ε^+	log $\bar{\nu}$
1	-58.832	-35.315	-35.857	-2.917	-7.286	-2.721
2	-18.510	-12.716	-12.739	-2.554	-4.066	-2.341
3	-4.772	-3.698	-3.061	-1.762	-1.885	-0.862
4	1.991	4.431	6.147	-1.307	4.363	5.933
5	-58.832	-29.634	-30.160	-3.078	-13.106	-2.892
6	-18.509	-11.012	-11.031	-2.661	-5.772	-2.494
7	-4.767	-3.600	-2.969	-1.768	-1.980	-0.919
8	1.991	4.432	6.148	-1.307	4.363	5.933
9	-58.832	2.697	3.794	-94.352	-99.999	-94.948
10	-18.509	2.703	3.804	-33.604	-44.250	-33.743
11	-4.747	2.626	3.796	-11.441	-13.876	-11.150
12	2.103	5.108	6.842	-1.745	3.634	5.203

	$^{44}K \rightarrow {}^{44}Ar$			$^{44}Ar \rightarrow {}^{44}K$		
pt	log β^+	log ε^-	log ν	log β^-	log ε^+	log $\bar{\nu}$
1	-47.675	-26.183	-26.740	-2.986	-7.353	-2.990
2	-16.429	-11.527	-11.564	-2.985	-4.284	-2.901
3	-5.493	-4.752	-4.042	-2.105	-2.013	-1.102
4	1.650	4.130	5.844	-1.498	4.504	6.077
5	-47.675	-20.363	-20.920	-3.293	-13.173	-3.442
6	-16.428	-9.811	-9.848	-3.181	-6.989	-3.212
7	-5.488	-4.655	-3.953	-2.114	-2.108	-1.178
8	1.650	4.130	5.844	-1.498	4.504	6.077
9	-47.675	-6.765	-5.559	-99.999	-99.999	-99.999
10	-16.428	-0.682	0.524	-39.153	-44.467	-39.311
11	-5.486	1.301	2.516	-12.437	-14.005	-12.170
12	1.765	4.807	6.539	-1.946	3.775	5.346

	$^{45}Cr \rightarrow {}^{45}V$			$^{45}V \rightarrow {}^{45}Cr$		
pt	log β^+	log ε^-	log ν	log β^-	log ε^+	log $\bar{\nu}$
1	0.945	-3.875	1.656	-77.339	-63.580	-64.158
2	0.879	-1.662	1.596	-25.708	-21.877	-21.962
3	0.703	0.035	1.597	-7.615	-6.049	-5.549
4	2.839	5.178	6.656	-0.901	4.081	5.698
5	0.945	-0.178	1.714	-77.438	-69.399	-69.978
6	0.879	-0.249	1.653	-25.785	-23.592	-23.672
7	0.705	0.127	1.629	-7.629	-6.148	-5.646
8	2.839	5.178	6.857	-0.901	4.081	5.698
9	0.945	5.185	6.488	-99.999	-99.999	-99.999
10	0.879	5.163	6.458	-61.876	-62.070	-61.808
11	0.711	5.123	6.404	-18.558	-18.060	-17.514
12	2.932	5.863	7.558	-1.373	3.357	4.970

	$^{45}V \rightarrow {}^{45}Ti$			$^{45}Ti \rightarrow {}^{45}V$		
pt	log β^+	log ε^-	log ν	log β^-	log ε^+	log $\bar{\nu}$
1	-0.029	-4.406	0.484	-45.890	-37.427	-38.004
2	-0.029	-2.099	0.492	-15.847	-13.480	-13.558
3	0.000	-0.087	1.029	-5.518	-3.960	-3.398
4	2.431	5.388	7.075	-1.842	4.264	5.866
5	-0.029	-0.697	0.660	-46.150	-43.247	-43.822
6	-0.028	-0.681	0.671	-16.023	-15.196	-15.208
7	0.003	0.006	1.094	-5.538	-4.058	-3.495
8	2.431	5.388	7.075	-1.842	4.264	5.866
9	-0.029	5.006	6.291	-99.999	-99.999	-99.999
10	-0.028	5.007	6.292	-53.482	-53.673	-53.436
11	0.017	5.014	6.306	-16.763	-15.968	-15.391
12	2.558	6.070	7.775	-2.324	3.538	5.138

	$^{45}Ti \rightarrow {}^{45}Sc$			$^{45}Sc \rightarrow {}^{45}Ti$		
pt	log β^+	log ε^-	log ν	log β^-	log ε^+	log $\bar{\nu}$
1	-4.383	-6.336	-4.579	-19.831	-13.893	-14.429
2	-4.327	-3.874	-3.442	-12.950	-6.703	-6.696
3	-2.029	-1.472	-0.626	-3.463	-2.759	-2.082
4	2.158	4.918	6.599	1.255	4.368	5.988
5	-4.383	-2.499	-2.130	-23.265	-19.712	-20.249
6	-4.315	-2.395	-1.972	-13.796	-8.418	-8.411
7	-2.025	-1.378	-0.541	-3.465	-2.857	-2.160
8	2.158	4.918	6.599	1.254	4.368	5.988
9	-4.383	4.325	5.436	-99.999	-99.999	-99.999
10	-4.315	4.328	5.441	-43.682	-46.896	-43.818
11	-2.008	4.340	5.466	-12.411	-14.766	-12.100
12	2.276	5.604	7.300	0.840	3.643	5.260

	$^{45}Sc \rightarrow {}^{45}Ca$			$^{45}Ca \rightarrow {}^{45}Sc$		
pt	log β^+	log ε^-	log ν	log β^-	log ε^+	log $\bar{\nu}$
1	-14.782	-10.587	-11.064	-8.397	-8.609	-8.935
2	-8.772	-5.869	-5.787	-5.449	-5.012	-4.688
3	-3.253	-2.358	-1.653	-2.413	-2.146	-1.277
4	1.848	4.799	6.485	1.277	4.485	6.094
5	-14.782	-6.207	-5.588	-8.954	-14.429	-9.688
6	-8.750	-4.243	-4.139	-5.714	-6.721	-5.657
7	-3.249	-2.261	-1.562	-2.417	-2.243	-1.340
8	1.848	4.799	6.485	1.277	4.485	6.093
9	-14.782	3.953	5.036	-99.999	-99.999	-99.999
10	-8.750	3.960	5.047	-40.039	-45.198	-40.173
11	-3.232	3.978	5.081	-11.202	-14.144	-10.885
12	1.978	5.483	7.186	0.868	3.759	5.365

	$^{45}Ca \rightarrow {}^{45}K$			$^{45}K \rightarrow {}^{45}Ca$		
pt	log β^+	log ε^-	log ν	log β^-	log ε^+	log $\bar{\nu}$
1	-52.282	-29.694	-30.255	-3.200	-7.993	-3.055
2	-17.395	-12.234	-12.290	-2.328	-4.600	-1.941
3	-5.116	-4.189	-3.549	-1.487	-1.962	-0.770
4	1.820	4.230	5.947	-1.439	4.427	5.999
5	-52.282	-23.875	-24.436	-3.364	-13.812	-3.287
6	-17.394	-10.518	-10.574	-2.372	-6.305	-1.999
7	-5.111	-4.092	-3.458	-1.494	-2.057	-0.819
8	1.820	4.230	5.947	-1.439	4.427	5.999
9	-52.282	2.397	3.566	-99.999	-99.999	-99.999
10	-17.394	2.398	3.570	-35.441	-44.782	-35.596
11	-5.090	2.341	3.531	-11.743	-13.951	-11.505
12	1.930	4.906	6.642	-1.888	3.698	5.268

	$^{46}Cr \rightarrow {}^{46}V$			$^{46}V \rightarrow {}^{46}Cr$		
pt	log β^+	log ε^-	log ν	log β^-	log ε^+	log $\bar{\nu}$
1	0.488	-3.988	1.038	-46.123	-39.466	-40.044
2	0.475	-1.699	1.030	-16.463	-14.124	-14.204
3	0.327	0.166	1.318	-6.590	-4.554	-3.998
4	2.736	5.381	7.075	-2.419	4.166	5.767
5	0.488	-0.287	1.179	-46.685	-45.265	-45.833
6	0.476	-0.284	1.173	-16.767	-15.839	-15.882
7	0.330	0.259	1.379	-6.615	-4.652	-4.095
8	2.736	5.381	7.075	-2.419	4.166	5.767
9	0.486	5.223	6.533	-99.999	-99.999	-99.999
10	0.476	5.222	6.532	-54.708	-54.317	-54.303
11	0.342	5.197	6.502	-17.953	-16.561	-16.003
12	2.850	6.063	7.773	-2.906	3.440	5.039

	$^{46}V \rightarrow {}^{46}Ti$			$^{46}Ti \rightarrow {}^{46}V$		
pt	log β^+	log ε^-	log ν	log β^-	log ε^+	log $\bar{\nu}$
1	0.206	-4.171	0.716	-53.282	-36.814	-37.391
2	-0.013	-2.076	0.505	-17.257	-13.115	-13.195
3	-0.557	-0.623	0.484	-4.336	-3.687	-3.080
4	2.055	5.064	6.735	-0.164	4.470	6.090
5	0.206	-0.462	0.893	-53.364	-42.634	-43.211
6	-0.013	-0.657	0.686	-17.306	-14.830	-14.907
7	-0.554	-0.529	0.551	-4.347	-3.785	-3.168
8	2.055	5.064	6.735	-0.164	4.470	6.090
9	0.206	4.980	6.270	-99.999	-99.999	-99.999
10	-0.013	4.925	6.193	-52.530	-53.308	-52.623
11	-0.540	4.857	6.097	-15.088	-15.696	-14.725
12	2.182	5.751	7.438	-0.630	3.746	5.363

	$^{46}Ti \rightarrow {}^{46}Sc$			$^{46}Sc \rightarrow {}^{46}Ti$		
pt	log β^+	log ε^-	log ν	log β^-	log ε^+	log $\bar{\nu}$
1	-26.042	-19.925	-20.460	-4.864	-8.940	-4.855
2	-13.113	-7.868	-7.840	-4.078	-5.120	-3.939
3	-3.004	-2.234	-1.512	-3.052	-2.442	-1.649
4	2.347	5.038	6.730	1.601	4.381	5.989
5	-26.041	-14.172	-14.689	-5.189	-14.759	-5.308
6	-13.085	-6.195	-6.159	-4.248	-6.828	-4.223
7	-3.000	-2.138	-1.424	-3.056	-2.538	-1.725
8	2.347	5.038	6.730	1.601	4.381	5.989
9	-26.041	4.040	5.033	-99.999	-99.999	-99.999
10	-13.085	4.048	5.047	-37.585	-45.305	-37.715
11	-2.985	4.104	5.150	-11.056	-14.438	-10.720
12	2.465	5.721	7.429	1.214	3.655	5.261

	$^{46}Sc \rightarrow {}^{46}Ca$			$^{46}Ca \rightarrow {}^{46}Sc$		
pt	log β^+	log ε^-	log ν	log β^-	log ε^+	log $\bar{\nu}$
1	-8.920	-8.707	-8.715	-15.638	-14.418	-14.481
2	-6.879	-6.006	-5.812	-6.606	-6.437	-6.101
3	-3.374	-2.425	-1.752	-2.244	-2.017	-1.118
4	1.959	4.896	6.587	1.158	4.520	6.120
5	-8.920	-5.461	-5.493	-16.391	-20.238	-16.781
6	-6.870	-4.423	-4.240	-6.869	-8.147	-6.907
7	-3.370	-2.328	-1.661	-2.249	-2.113	-1.185
8	1.959	4.896	6.587	1.158	4.519	6.120
9	-8.920	3.894	4.978	-99.999	-99.999	-99.999
10	-6.870	3.909	5.001	-41.450	-46.624	-41.585
11	-3.352	3.935	5.046	-11.066	-14.011	-10.750
12	2.089	5.578	7.286	0.750	3.793	5.391

	$^{46}Ca \rightarrow {}^{46}K$			$^{46}K \rightarrow {}^{46}Ca$		
pt	log β^+	log ε^-	log ν	log β^-	log ε^+	log $\bar{\nu}$
1	-68.652	-45.902	-46.469	-2.109	-7.522	-1.704
2	-21.933	-16.326	-16.394	-1.480	-4.009	-1.089
3	-6.758	-4.573	-3.995	-0.885	-1.589	-0.186
4	2.160	4.459	6.179	-0.386	4.437	6.005
5	-68.652	-40.082	-40.649	-2.183	-13.341	-1.778
6	-21.932	-14.610	-14.678	-1.525	-5.714	-1.153
7	-6.753	-4.474	-3.901	-0.890	-1.683	-0.220
8	2.160	4.459	6.179	-0.386	4.437	6.005
9	-68.652	2.074	3.114	-84.220	-99.999	-84.815
10	-21.932	2.102	3.145	-30.166	-44.191	-30.300
11	-6.734	2.453	3.568	-10.015	-13.575	-9.700
12	2.265	5.135	6.873	-0.796	3.708	5.274

	$^{47}Ti \rightarrow {}^{47}Sc$			$^{47}Sc \rightarrow {}^{47}Ti$		
pt	log β^+	log ε^-	log ν	log β^-	log ε^+	log $\bar{\nu}$
1	-16.880	-11.743	-12.260	-5.592	-8.375	-8.057
2	-8.889	-6.401	-6.341	-4.725	-5.038	-4.444
3	-3.098	-2.326	-1.598	-2.960	-2.338	-1.555
4	2.251	4.956	6.647	1.662	4.464	6.072
5	-16.889	-6.129	-6.565	-7.655	-14.194	-8.190
6	-8.872	-4.752	-4.679	-4.967	-6.746	-5.017
7	-3.095	-2.230	-1.510	-2.963	-2.434	-1.631
8	2.251	4.956	6.647	1.662	4.464	6.072
9	-16.889	4.000	5.020	-99.999	-99.999	-99.999
10	-8.872	4.004	5.027	-39.100	-45.224	-39.231
11	-3.079	4.030	5.078	-10.966	-14.336	-10.631
12	2.370	5.639	7.346	1.274	3.738	5.344

	$^{47}Cr \rightarrow {}^{47}V$			$^{47}V \rightarrow {}^{47}Cr$		
pt	log β^+	log ε^-	log ν	log β^-	log ε^+	log $\bar{\nu}$
1	0.063	-4.301	0.587	-53.072	-38.674	-39.250
2	0.062	-2.005	0.595	-17.476	-13.845	-13.925
3	0.042	-0.083	1.063	-5.118	-4.047	-3.499
4	2.671	5.336	7.028	-0.721	4.271	5.875
5	0.063	-0.596	0.762	-53.154	-44.494	-45.070
6	0.063	-0.587	0.771	-17.541	-15.561	-15.632
7	0.045	0.010	1.129	-5.130	-4.145	-3.594
8	2.671	5.336	7.028	-0.721	4.271	5.875
9	0.063	5.053	6.321	-99.999	-99.999	-99.999
10	0.063	5.052	6.320	-53.284	-54.039	-53.380
11	0.059	5.054	6.325	-15.977	-16.057	-15.360
12	2.787	6.019	7.727	-1.191	3.545	5.146

	$^{47}Sc \rightarrow {}^{47}Ca$			$^{47}Ca \rightarrow {}^{47}Sc$		
pt	log β^+	log ε^-	log ν	log β^-	log ε^+	log $\bar{\nu}$
1	-42.111	-19.379	-19.912	-5.721	-9.069	-5.951
2	-13.692	-9.505	-9.506	-5.110	-5.895	-4.788
3	-4.133	-3.516	-2.786	-1.644	-2.275	-0.890
4	1.827	4.780	6.470	1.608	4.606	6.209
5	-42.111	-13.602	-14.117	-6.601	-14.888	-6.673
6	-13.692	-7.796	-7.790	-5.226	-7.602	-4.973
7	-4.128	-3.418	-2.701	-1.648	-2.370	-0.918
8	1.827	4.780	6.470	1.608	4.605	6.209
9	-42.111	3.744	4.777	-99.999	-99.999	-99.999
10	-13.691	3.745	4.781	-37.142	-46.080	-37.273
11	-4.111	3.743	4.792	-10.079	-14.267	-9.745
12	1.957	5.463	7.170	1.216	3.879	5.481

	$^{47}V \rightarrow {}^{47}Ti$			$^{47}Ti \rightarrow {}^{47}V$		
pt	log β^+	log ε^-	log ν	log β^-	log ε^+	log $\bar{\nu}$
1	-3.302	-6.107	-3.254	-43.131	-18.068	-18.620
2	-3.290	-3.682	-2.913	-13.325	-7.909	-7.922
3	-1.833	-1.289	-0.431	-2.928	-2.825	-2.006
4	2.080	5.077	6.750	0.759	4.507	6.129
5	-3.302	-2.303	-1.816	-43.182	-23.888	-24.440
6	-3.284	-2.215	-1.698	-13.340	-9.624	-9.637
7	-1.829	-1.195	-0.347	-2.932	-2.923	-2.067
8	2.080	5.077	6.750	0.759	4.507	6.129
9	-3.302	4.665	5.832	-99.999	-99.999	-99.999
10	-3.284	4.687	5.835	-45.250	-48.102	-45.398
11	-1.811	4.677	5.857	-12.911	-14.832	-12.646
12	2.206	5.764	7.453	0.315	3.783	5.401

	$^{47}Ca \rightarrow {}^{47}K$			$^{47}K \rightarrow {}^{47}Ca$		
pt	log β^+	log ε^-	log ν	log β^-	log ε^+	log $\bar{\nu}$
1	-64.186	-41.140	-41.712	-1.347	-6.910	-0.987
2	-21.219	-15.587	-15.656	-1.300	-3.825	-0.930
3	-6.159	-5.164	-4.549	-1.310	-1.687	-0.568
4	1.802	4.112	5.832	-2.009	4.494	6.062
5	-64.186	-35.320	-35.892	-1.391	-12.729	-1.060
6	-21.218	-13.871	-13.940	-1.335	-5.530	-0.988
7	-6.155	-5.066	-4.457	-1.318	-1.781	-0.626
8	1.802	4.112	5.832	-2.009	4.494	6.062
9	-64.186	-9.269	-8.104	-99.999	-99.999	-99.999
10	-21.218	-1.732	-0.536	-35.636	-44.007	-35.798
11	-6.136	1.226	2.437	-11.868	-13.674	-11.643
12	1.908	4.788	6.526	-2.470	3.765	5.331

	$^{48}Cr \rightarrow {}^{48}V$			$^{48}V \rightarrow {}^{48}Cr$		
pt	log β^+	log ε^-	log ν	log β^-	log ε^+	log $\bar{\nu}$
1	-6.780	-6.389	-6.219	-43.419	-13.128	-13.632
2	-4.714	-3.869	-3.515	-14.033	-7.306	-7.284
3	-1.440	-1.199	-0.235	-3.644	-3.448	-2.654
4	2.517	5.226	6.912	0.935	4.369	5.983
5	-6.779	-2.518	-2.264	-43.431	-18.947	-19.451
6	-4.706	-2.385	-2.015	-14.043	-9.020	-8.999
7	-1.437	-1.105	-0.158	-3.648	-3.546	-2.714
8	2.517	5.226	6.912	0.935	4.369	5.983
9	-6.779	4.706	5.839	-99.999	-99.999	-99.999
10	-4.705	4.707	5.840	-44.104	-47.498	-44.246
11	-1.422	4.725	5.875	-13.177	-15.456	-12.890
12	2.633	5.911	7.612	0.504	3.644	5.255

	$^{48}Sc \rightarrow {}^{48}Ca$			$^{48}Ca \rightarrow {}^{48}Sc$		
pt	log β^+	log ε^-	log ν	log β^-	log ε^+	log $\bar{\nu}$
1	-17.810	-20.088	-17.960	-20.188	-14.818	-15.166
2	-9.584	-9.437	-8.912	-7.001	-6.944	-6.489
3	-4.374	-3.658	-2.940	-1.492	-2.103	-0.707
4	1.818	4.781	6.470	1.645	4.658	6.261
5	-17.810	-16.284	-15.839	-20.266	-20.436	-19.982
6	-9.573	-7.973	-7.487	-7.048	-8.560	-6.727
7	-4.370	-3.561	-2.852	-1.496	-2.198	-0.733
8	1.818	4.781	6.470	1.645	4.658	6.261
9	-17.810	3.663	4.665	-99.999	-99.999	-99.999
10	-9.573	3.675	4.685	-38.644	-47.138	-38.775
11	-4.352	3.712	4.749	-9.787	-14.096	-9.455
12	1.947	5.463	7.170	1.253	3.932	5.532

	$^{48}V \rightarrow {}^{48}Ti$			$^{48}Ti \rightarrow {}^{48}V$		
pt	log β^+	log ε^-	log ν	log β^-	log ε^+	log $\bar{\nu}$
1	-4.657	-7.478	-4.472	-50.546	-24.019	-24.562
2	-3.584	-4.105	-3.192	-14.937	-9.134	-9.137
3	-2.062	-1.516	-0.675	-2.692	-2.726	-1.821
4	2.202	5.037	6.713	1.015	4.558	6.179
5	-4.657	-3.644	-3.214	-50.585	-29.839	-30.381
6	-3.581	-2.634	-2.127	-14.950	-10.849	-10.852
7	-2.059	-1.421	-0.591	-2.696	-2.823	-1.873
8	2.202	5.037	6.713	1.015	4.558	6.179
9	-4.657	4.570	5.708	-99.999	-99.999	-99.999
10	-3.581	4.585	5.730	-45.967	-49.327	-46.112
11	-2.043	4.606	5.767	-12.463	-14.730	-12.187
12	2.321	5.724	7.415	0.577	3.834	5.452

	$^{48}Ca \rightarrow {}^{48}K$			$^{48}K \rightarrow {}^{48}Ca$		
pt	log β^+	log ε^-	log ν	log β^-	log ε^+	log $\bar{\nu}$
1	-89.496	-66.421	-65.997	-0.628	-5.653	-0.097
2	-28.639	-22.756	-22.836	-0.386	-3.489	0.170
3	-7.413	-6.184	-5.626	-0.341	-1.412	0.304
4	1.839	3.804	5.534	-0.524	4.466	6.032
5	-89.496	-60.601	-61.177	-0.646	-12.472	-0.126
6	-28.639	-21.040	-21.121	-0.399	-5.193	0.149
7	-7.409	-6.085	-5.532	-0.344	-1.505	0.284
8	1.839	3.804	5.534	-0.524	4.466	6.032
9	-89.496	-18.203	-17.114	-83.322	-99.999	-83.918
10	-28.639	-4.372	-3.264	-30.050	-43.671	-30.191
11	-7.389	1.109	2.247	-9.902	-13.396	-9.617
12	1.927	4.479	6.226	-0.958	3.737	5.301

	$^{48}Ti \rightarrow {}^{48}Sc$			$^{48}Sc \rightarrow {}^{48}Ti$		
pt	log β^+	log ε^-	log ν	log β^-	log ε^+	log $\bar{\nu}$
1	-52.753	-27.105	-27.652	-3.796	-8.010	-3.760
2	-16.261	-10.056	-10.082	-3.077	-4.554	-2.855
3	-3.929	-2.799	-2.179	-2.115	-2.020	-1.078
4	2.305	4.993	6.688	1.885	4.517	6.122
5	-52.753	-21.315	-21.851	-4.070	-13.829	-4.112
6	-16.260	-8.344	-8.368	-3.186	-6.260	-3.001
7	-3.925	-2.701	-2.088	-2.123	-2.115	-1.148
8	2.306	4.993	6.688	1.885	4.517	6.122
9	-52.753	3.816	4.748	-99.999	-99.999	-99.999
10	-16.260	3.828	4.768	-34.728	-44.738	-34.856
11	-3.908	3.916	4.928	-10.029	-14.011	-9.684
12	2.425	5.675	7.386	1.514	3.790	5.394

	$^{49}Fe \rightarrow {}^{49}Mn$			$^{49}Mn \rightarrow {}^{49}Fe$		
pt	log β^+	log ε^-	log ν	log β^-	log ε^+	log $\bar{\nu}$
1	0.986	-3.698	1.651	-77.061	-66.850	-67.430
2	0.992	-1.419	1.667	-25.682	-22.745	-22.830
3	0.855	0.328	1.769	-7.827	-6.340	-5.813
4	3.191	5.418	7.115	-1.400	4.127	5.733
5	0.986	-0.011	1.731	-77.258	-72.670	-73.250
6	0.993	-0.008	1.745	-25.822	-24.460	-24.521
7	0.857	0.421	1.809	-7.845	-6.439	-5.911
8	3.191	5.418	7.116	-1.400	4.127	5.733
9	0.986	5.364	6.674	-99.999	-99.999	-99.999
10	0.993	5.363	6.673	-62.898	-62.938	-62.768
11	0.864	5.325	6.625	-18.987	-18.350	-17.798
12	3.281	6.101	7.813	-1.879	3.401	5.005

	$^{49}Mn \rightarrow {}^{49}Cr$			$^{49}Cr \rightarrow {}^{49}Mn$		
pt	log β^+	log ε^-	log ν	log β^-	log ε^+	log $\bar{\nu}$
1	0.169	-4.259	0.719	-45.704	-40.314	-40.891
2	0.171	-1.964	0.730	-16.323	-14.386	-14.461
3	0.219	0.122	1.236	-6.147	-3.995	-3.411
4	2.353	5.329	7.005	-2.304	4.502	8.114
5	0.169	-0.559	0.870	-46.536	-46.134	-46.530
6	0.172	-0.546	0.881	-16.707	-16.102	-16.115
7	0.222	0.216	1.296	-6.176	-4.093	-3.509
8	2.353	5.329	7.005	-2.304	4.502	8.114
9	0.169	5.216	6.509	-99.999	-99.999	-99.999
10	0.172	5.216	6.509	-54.835	-54.579	-54.543
11	0.233	5.221	6.521	-17.562	-16.001	-15.416
12	2.476	6.014	7.707	-2.793	3.777	5.386

	$^{49}Cr \rightarrow {}^{49}V$			$^{49}V \rightarrow {}^{49}Cr$		
pt	log β^+	log ε^-	log ν	log β^-	log ε^+	log $\bar{\nu}$
1	-3.484	-6.040	-3.526	-50.925	-16.755	-17.307
2	-3.410	-3.622	-2.950	-15.765	-7.749	-7.773
3	-2.089	-1.341	-0.505	-3.499	-3.117	-2.385
4	2.405	5.104	6.785	1.171	4.398	6.017
5	-3.484	-2.256	-1.776	-50.934	-22.574	-23.127
6	-3.403	-2.165	-1.642	-15.773	-9.465	-9.489
7	-2.084	-1.247	-0.417	-3.502	-3.215	-2.451
8	2.406	5.104	6.785	1.171	4.398	6.017
9	-3.484	4.632	5.749	-99.999	-99.999	-99.999
10	-3.403	4.636	5.754	-44.776	-47.942	-44.915
11	-2.064	4.651	5.783	-12.771	-15.125	-12.472
12	2.522	5.791	7.486	0.748	3.673	5.290

	$^{49}V \rightarrow {}^{49}Ti$			$^{49}Ti \rightarrow {}^{49}V$		
pt	log β^+	log ε^-	log ν	log β^-	log ε^+	log $\bar{\nu}$
1	-11.128	-8.177	-8.249	-11.519	-9.326	-9.547
2	-7.045	-5.326	-5.143	-6.069	-5.693	-5.453
3	-3.043	-2.138	-1.433	-2.080	-2.270	-1.205
4	2.079	5.030	6.709	1.498	4.739	6.357
5	-11.128	-4.180	-4.081	-12.826	-15.145	-13.331
6	-7.031	-3.763	-3.543	-6.362	-7.404	-6.418
7	-3.040	-2.041	-1.343	-2.083	-2.366	-1.247
8	2.079	5.030	6.709	1.498	4.739	6.357
9	-11.128	4.439	5.543	-99.999	-99.999	-99.999
10	-7.031	4.443	5.550	-41.013	-45.881	-41.152
11	-3.025	4.447	5.564	-11.238	-14.267	-10.937
12	2.206	5.717	7.411	1.077	4.015	5.630

	$^{49}Ti \rightarrow {}^{49}Sc$			$^{49}Sc \rightarrow {}^{49}Ti$		
pt	log β^+	log ε^-	log ν	log β^-	log ε^+	log $\bar{\nu}$
1	-43.547	-18.478	-18.999	-3.630	-8.030	-3.548
2	-14.050	-8.405	-8.361	-3.635	-4.792	-3.501
3	-3.967	-3.097	-2.412	-1.772	-2.057	-0.950
4	2.135	4.874	6.563	1.999	4.610	6.222
5	-43.547	-12.756	-13.301	-3.835	-13.849	-3.858
6	-14.050	-6.763	-6.701	-3.780	-6.500	-3.753
7	-3.964	-3.000	-2.323	-1.777	-2.153	-0.994
8	2.135	4.874	6.563	1.999	4.610	6.221
9	-43.547	3.870	4.855	-99.999	-99.999	-99.999
10	-14.050	3.873	4.860	-36.765	-44.978	-36.893
11	-3.948	3.905	4.921	-9.876	-14.052	-9.534
12	2.255	5.558	7.263	1.625	3.885	5.494

	$^{49}Sc \rightarrow {}^{49}Ca$			$^{49}Ca \rightarrow {}^{49}Sc$		
pt	log β^+	log ε^-	log ν	log β^-	log ε^+	log $\bar{\nu}$
1	-58.408	-34.450	-35.001	-2.862	-7.369	-2.767
2	-19.231	-13.588	-13.595	-2.853	-4.216	-2.689
3	-5.498	-4.080	-3.522	-0.048	-1.367	0.664
4	2.450	4.844	6.550	1.172	4.556	6.145
5	-58.408	-28.679	-29.223	-3.066	-13.188	-3.055
6	-19.231	-11.893	-11.896	-2.969	-5.922	-2.895
7	-5.494	-3.981	-3.427	-0.050	-1.462	0.654
8	2.450	4.844	6.550	1.172	4.556	6.145
9	-58.408	3.787	4.847	-93.950	-99.999	-94.545
10	-19.231	3.789	4.851	-31.572	-44.400	-31.707
11	-5.475	3.810	4.889	-8.841	-13.355	-8.527
12	2.556	5.524	7.247	0.762	3.828	5.415

	$^{49}Ca \rightarrow {}^{49}K$			$^{49}K \rightarrow {}^{49}Ca$		
pt	log β^+	log ε^-	log ν	log β^-	log ε^+	log $\bar{\nu}$
1	-97.039	-75.388	-75.968	-0.527	-7.123	0.159
2	-31.549	-26.658	-26.749	-0.170	-3.846	0.549
3	-8.300	-7.610	-6.999	0.549	-1.306	1.340
4	0.522	4.138	5.823	0.637	4.861	6.458
5	-97.039	-69.569	-70.149	-0.533	-12.942	0.148
6	-31.548	-24.943	-25.033	-0.175	-5.550	0.541
7	-8.297	-7.512	-6.917	0.548	-1.399	1.335
8	0.522	4.138	5.823	0.637	4.860	6.458
9	-97.039	1.460	2.268	-53.867	-99.999	-54.459
10	-31.548	1.465	2.277	-19.275	-44.028	-19.400
11	-8.284	1.613	2.528	-6.440	-13.288	-6.085
12	0.680	4.820	6.524	0.259	4.134	5.729

	$^{50}Mn \rightarrow {}^{50}Cr$			$^{50}Cr \rightarrow {}^{50}Mn$		
pt	log β^+	log ε^-	log ν	log β^-	log ε^+	log $\bar{\nu}$
1	0.131	-4.280	0.876	-52.019	-39.660	-40.238
2	-0.306	-2.355	0.240	-16.610	-13.923	-14.001
3	-0.349	-0.368	0.712	-4.492	-3.788	-3.157
4	2.356	5.303	6.982	-0.568	4.520	6.133
5	0.131	-0.578	0.836	-52.174	-45.480	-46.057
6	-0.306	-0.938	0.417	-16.739	-15.639	-15.662
7	-0.346	-0.275	0.779	-4.506	-3.886	-3.249
8	2.356	5.304	6.982	-0.566	4.520	6.133
9	0.131	5.115	6.383	-99.999	-99.999	-99.999
10	-0.306	5.077	6.327	-53.045	-54.116	-53.192
11	-0.333	5.080	6.335	-15.498	-15.795	-14.987
12	2.481	5.989	7.683	-1.040	3.795	5.405

	$^{50}Cr \rightarrow {}^{50}V$			$^{50}V \rightarrow {}^{50}Cr$		
pt	log β^+	log ε^-	log ν	log β^-	log ε^+	log $\bar{\nu}$
1	-19.060	-14.444	-14.948	-6.932	-9.917	-7.314
2	-8.119	-6.323	-6.239	-5.244	-5.624	-4.985
3	-2.632	-1.691	-0.959	-2.904	-2.403	-1.630
4	2.372	5.110	6.792	1.683	4.526	6.147
5	-19.060	-8.720	-9.220	-8.784	-15.737	-9.400
6	-8.108	-4.685	-4.594	-5.465	-7.333	-5.462
7	-2.629	-1.596	-0.868	-2.907	-2.500	-1.702
8	2.372	5.111	6.792	1.683	4.526	6.147
9	-19.060	4.439	5.487	-99.999	-99.999	-99.999
10	-8.108	4.451	5.507	-39.521	-45.810	-39.655
11	-2.614	4.493	5.583	-11.466	-14.404	-11.144
12	2.488	5.797	7.493	1.279	3.801	5.420

	$^{50}V \rightarrow {}^{50}Ti$			$^{50}Ti \rightarrow {}^{50}V$		
pt	log β^+	log ε^-	log ν	log β^-	log ε^+	log $\bar{\nu}$
1	-10.217	-9.165	-9.055	-18.588	-16.758	-17.197
2	-5.780	-5.402	-5.034	-8.141	-7.335	-7.184
3	-3.034	-2.151	-1.425	-2.038	-2.208	-1.160
4	2.085	5.037	6.717	1.415	4.657	6.274
5	-10.217	-5.118	-5.011	-20.093	-22.578	-20.596
6	-6.777	-3.853	-3.595	-6.483	-9.047	-6.474
7	-3.030	-2.055	-1.335	-2.041	-2.304	-1.202
8	2.085	5.037	6.717	1.415	4.657	6.274
9	-10.217	4.402	5.500	-99.999	-99.999	-99.999
10	-6.776	4.410	5.512	-42.634	-47.524	-42.773
11	-3.014	4.430	5.548	-11.175	-14.214	-10.874
12	2.192	5.723	7.418	0.995	3.832	5.546

	$^{50}Ti \rightarrow {}^{50}Sc$			$^{50}Sc \rightarrow {}^{50}Ti$		
pt	log β^+	log ε^-	log ν	log β^-	log ε^+	log $\bar{\nu}$
1	-66.792	-41.051	-41.621	-1.835	-7.271	-1.487
2	-20.975	-14.514	-14.580	-1.357	-3.981	-0.925
3	-5.252	-3.970	-3.409	-0.478	-1.662	0.260
4	2.078	4.743	6.425	1.826	4.542	6.163
5	-66.792	-35.232	-35.801	-1.895	-13.091	-1.570
6	-20.975	-12.798	-12.864	-1.387	-5.686	-0.969
7	-5.248	-3.872	-3.314	-0.480	-1.746	0.248
8	2.078	4.743	6.425	1.826	4.542	6.163
9	-66.792	3.941	4.945	-86.689	-99.999	-87.284
10	-20.975	3.944	4.950	-29.884	-44.164	-30.016
11	-5.230	3.981	5.015	-8.747	-13.638	-8.417
12	2.191	5.429	7.126	1.433	3.817	5.436

	$^{50}Sc \rightarrow {}^{50}Ca$			$^{50}Ca \rightarrow {}^{50}Sc$		
pt	log β^+	log ε^-	log ν	log β^-	log ε^+	log $\bar{\nu}$
1	-67.331	-32.710	-33.279	-1.206	-6.503	-0.947
2	-19.452	-13.077	-13.139	-1.088	-3.435	-0.748
3	-5.998	-4.358	-3.835	0.148	-1.173	0.892
4	1.863	4.451	6.135	1.938	4.699	6.320
5	-67.331	-26.890	-27.459	-1.281	-12.322	-1.068
6	-19.451	-11.362	-11.424	-1.135	-5.140	-0.817
7	-5.993	-4.259	-3.738	0.146	-1.267	0.882
8	1.863	4.462	6.135	1.938	4.699	6.320
9	-67.331	3.694	4.722	-94.610	-99.999	-95.204
10	-19.451	3.704	4.736	-31.120	-43.618	-31.252
11	-5.974	3.730	4.783	-8.151	-13.158	-7.822
12	1.973	5.138	6.836	1.543	3.974	5.593

	$^{51}Mn \rightarrow {}^{51}Cr$			$^{51}Cr \rightarrow {}^{51}Mn$		
pt	log β^+	log ε^-	log ν	log β^-	log ε^+	log $\bar{\nu}$
1	-3.535	-6.366	-3.439	-42.338	-19.938	-20.486
2	-3.300	-3.689	-2.896	-13.108	-8.559	-8.569
3	-1.573	-1.119	-0.236	-3.030	-3.062	-2.190
4	2.393	5.335	7.017	0.599	4.531	6.144
5	-3.535	-2.559	-2.078	-42.361	-25.758	-26.305
6	-3.296	-2.224	-1.710	-13.128	-10.273	-10.282
7	-1.570	-1.025	-0.155	-3.036	-3.160	-2.247
8	2.393	5.335	7.017	0.599	4.531	6.144
9	-3.535	4.858	6.027	-99.999	-99.999	-99.999
10	-3.296	4.868	6.039	-45.719	-48.751	-45.871
11	-1.554	4.884	6.071	-13.176	-15.068	-12.923
12	2.518	6.020	7.718	0.151	3.806	5.416

	$^{51}Cr \rightarrow {}^{51}V$			$^{51}V \rightarrow {}^{51}Cr$		
pt	log β^+	log ε^-	log ν	log β^-	log ε^+	log $\bar{\nu}$
1	-10.842	-7.821	-7.880	-13.151	-9.742	-10.001
2	-6.166	-5.042	-4.796	-7.059	-5.973	-5.854
3	-2.676	-1.832	-1.064	-2.732	-2.360	-1.563
4	2.192	5.010	6.682	1.848	4.645	6.274
5	-10.642	-3.831	-3.725	-13.872	-15.561	-14.281
6	-6.156	-3.522	-3.249	-7.373	-7.684	-7.249
7	-2.673	-1.737	-0.975	-2.734	-2.457	-1.627
8	2.192	5.010	6.682	1.848	4.644	6.274
9	-10.642	4.422	5.478	-99.999	-99.999	-99.999
10	-6.156	4.425	5.483	-41.344	-46.162	-41.478
11	-2.657	4.453	5.534	-11.328	-14.364	-11.008
12	2.310	5.699	7.385	1.441	3.921	5.548

	$^{52}Fe \rightarrow {}^{52}Mn$			$^{52}Mn \rightarrow {}^{52}Fe$		
pt	log β^+	log ε^-	log ν	log β^-	log ε^+	log $\bar{\nu}$
1	-4.815	-6.444	-5.086	-42.794	-18.886	-17.420
2	-4.062	-3.922	-3.386	-13.867	-8.589	-8.604
3	-1.227	-1.107	-0.081	-3.683	-3.763	-2.863
4	2.744	5.416	7.107	0.731	4.411	6.019
5	-4.814	-2.639	-2.266	-42.810	-22.706	-23.240
6	-4.054	-2.462	-1.986	-13.881	-10.304	-10.319
7	-1.224	-1.014	-0.008	-3.687	-3.861	-2.913
8	2.744	5.416	7.107	0.731	4.411	6.019
9	-4.814	4.891	6.037	-99.999	-99.999	-99.999
10	-4.054	4.893	6.041	-45.293	-48.782	-45.440
11	-1.210	4.919	6.068	-13.548	-15.771	-13.278
12	2.858	6.099	7.806	0.291	3.685	5.291

	$^{51}V \rightarrow {}^{51}Ti$			$^{51}Ti \rightarrow {}^{51}V$		
pt	log β^+	log ε^-	log ν	log β^-	log ε^+	log $\bar{\nu}$
1	-46.911	-20.318	-20.877	-2.671	-7.446	-2.573
2	-15.440	-8.986	-9.013	-2.578	-4.300	-2.399
3	-4.254	-2.843	-2.283	-0.612	-1.617	0.074
4	2.596	5.037	6.732	1.332	4.574	6.182
5	-46.911	-14.502	-15.062	-2.868	-13.265	-2.867
6	-15.440	-7.280	-7.309	-2.695	-6.006	-2.564
7	-4.251	-2.744	-2.187	-0.615	-1.711	0.055
8	2.596	5.037	6.732	1.332	4.574	6.182
9	-46.911	4.393	5.495	-99.999	-99.999	-99.999
10	-15.440	4.396	5.500	-35.799	-44.483	-35.937
11	-4.234	4.407	5.525	-9.914	-13.604	-9.611
12	2.700	5.721	7.431	0.909	3.849	5.454

	$^{52}Mn \rightarrow {}^{52}Cr$			$^{52}Cr \rightarrow {}^{52}Mn$		
pt	log β^+	log ε^-	log ν	log β^-	log ε^+	log $\bar{\nu}$
1	-5.069	-7.362	-4.803	-30.520	-27.352	-27.885
2	-3.406	-4.213	-3.014	-12.493	-10.424	-10.437
3	-1.792	-1.145	-0.368	-2.586	-2.781	-1.817
4	2.262	5.254	6.931	0.211	4.641	6.256
5	-5.069	-3.478	-3.169	-33.850	-33.171	-33.681
6	-3.404	-2.752	-2.158	-12.535	-12.139	-11.881
7	-1.789	-1.049	-0.283	-2.595	-2.877	-1.880
8	2.262	5.254	6.931	0.211	4.641	6.256
9	-5.069	4.901	6.104	-99.999	-99.999	-99.999
10	-3.404	4.904	6.109	-47.382	-50.617	-47.548
11	-1.774	4.921	6.138	-13.261	-14.778	-13.033
12	2.387	5.940	7.633	-0.253	3.916	5.528

	$^{51}Ti \rightarrow {}^{51}Sc$			$^{51}Sc \rightarrow {}^{51}Ti$		
pt	log β^+	log ε^-	log ν	log β^-	log ε^+	log $\bar{\nu}$
1	-64.928	-39.329	-39.888	-1.261	-6.706	-0.931
2	-20.949	-14.399	-14.463	-1.173	-3.634	-0.790
3	-6.761	-4.374	-3.826	-0.254	-1.449	0.510
4	2.102	4.565	6.240	2.352	4.744	6.380
5	-64.928	-33.509	-34.079	-1.321	-12.525	-1.020
6	-20.948	-12.683	-12.748	-1.213	-6.339	-0.848
7	-6.757	-4.278	-3.731	-0.256	-1.543	0.499
8	2.102	4.565	6.240	2.352	4.744	6.380
9	-64.928	3.837	4.805	-87.763	-99.999	-88.356
10	-20.948	3.839	4.809	-29.567	-43.817	-29.696
11	-6.740	3.858	4.851	-8.034	-13.434	-7.694
12	2.204	5.254	6.943	1.973	4.020	5.654

	$^{52}Cr \rightarrow {}^{52}V$			$^{52}V \rightarrow {}^{52}Cr$		
pt	log β^+	log ε^-	log ν	log β^-	log ε^+	log $\bar{\nu}$
1	-54.330	-26.180	-26.731	-2.592	-7.350	-2.419
2	-16.541	-9.487	-9.507	-2.505	-4.146	-2.286
3	-3.786	-2.385	-1.796	-1.059	-1.699	-0.319
4	2.515	4.972	6.651	1.506	4.639	6.266
5	-54.330	-20.395	-20.942	-2.739	-13.169	-2.615
6	-16.540	-7.795	-7.809	-2.604	-5.852	-2.427
7	-3.783	-2.288	-1.701	-1.062	-1.794	-0.347
8	2.515	4.973	6.651	1.506	4.639	6.266
9	-54.330	4.505	5.605	-99.999	-99.999	-99.999
10	-16.540	4.507	5.609	-35.035	-44.330	-35.175
11	-3.769	4.538	5.659	-10.364	-13.690	-10.069
12	2.615	5.660	7.353	1.082	3.915	5.539

	$^{52}V \rightarrow {}^{52}Ti$			$^{52}Ti \rightarrow {}^{52}V$		
pt	log β^+	log ε^-	log ν	log β^-	log ε^+	log $\bar{\nu}$
1	-45.186	-18.162	-18.721	-2.110	-6.779	-2.060
2	-15.557	-8.560	-8.601	-2.029	-3.666	-1.896
3	-4.795	-2.439	-1.935	0.318	-0.611	0.934
4	2.184	4.855	6.527	1.106	4.808	6.436
5	-45.186	-12.342	-12.901	-2.417	-12.599	-2.505
6	-15.556	-6.845	-6.886	-2.171	-5.371	-2.102
7	-4.792	-2.340	-1.837	0.312	-0.705	0.906
8	2.184	4.855	6.527	1.106	4.808	6.435
9	-45.186	4.525	5.685	-99.999	-99.999	-99.999
10	-15.556	4.526	5.687	-35.886	-43.849	-35.036
11	-4.775	4.538	5.710	-9.708	-12.596	-9.459
12	2.293	5.544	7.230	0.661	4.084	5.709

	$^{53}Co \rightarrow {}^{53}Fe$			$^{53}Fe \rightarrow {}^{53}Co$		
pt	log β^+	log ε^-	log ν	log β^-	log ε^+	log $\bar{\nu}$
1	0.484	-4.035	1.077	-46.710	-43.104	-43.683
2	0.479	-1.738	1.077	-17.936	-15.203	-15.278
3	0.453	0.331	1.460	-7.987	-4.124	-3.543
4	2.504	5.454	7.135	-4.228	4.516	6.124
5	0.484	-0.342	1.200	-49.702	-48.924	-49.461
6	0.479	-0.315	1.202	-18.687	-18.919	-18.992
7	0.455	0.425	1.519	-8.023	-4.222	-3.641
8	2.504	5.454	7.136	-4.228	4.516	6.124
9	0.484	5.349	6.658	-99.999	-99.999	-99.999
10	0.479	5.349	6.659	-57.089	-55.396	-55.469
11	0.464	5.349	6.662	-19.524	-16.129	-15.550
12	2.626	6.138	7.836	-4.722	3.791	5.396

	$^{53}Fe \rightarrow {}^{53}Mn$			$^{53}Mn \rightarrow {}^{53}Fe$		
pt	log β^+	log ε^-	log ν	log β^-	log ε^+	log $\bar{\nu}$
1	-2.878	-6.842	-2.722	-49.725	-22.039	-22.589
2	-2.818	-3.416	-2.454	-15.426	-9.309	-9.315
3	-1.340	-0.978	-0.054	-3.423	-3.219	-2.442
4	2.457	5.238	6.913	1.104	4.558	6.180
5	-2.878	-2.040	-1.533	-49.767	-27.859	-28.409
6	-2.815	-1.950	-1.410	-15.436	-11.023	-11.030
7	-1.336	-0.884	0.026	-3.427	-3.317	-2.504
8	2.457	5.238	6.913	1.104	4.558	6.180
9	-2.878	4.862	6.019	-99.999	-99.999	-99.999
10	-2.815	4.863	6.021	-46.512	-49.501	-46.656
11	-1.321	4.873	6.042	-13.209	-15.226	-12.930
12	2.572	5.925	7.615	0.666	3.834	5.453

	$^{53}Mn \rightarrow {}^{53}Cr$			$^{53}Cr \rightarrow {}^{53}Mn$		
pt	log β^+	log ε^-	log ν	log β^-	log ε^+	log $\bar{\nu}$
1	-11.864	-9.255	-9.222	-10.170	-9.681	-9.991
2	-7.101	-5.221	-5.058	-5.500	-5.599	-5.087
3	-2.919	-1.130	-0.562	-1.487	-1.528	-0.593
4	2.595	5.111	6.789	-0.025	4.670	6.290
5	-11.864	-4.830	-4.960	-12.200	-15.501	-12.795
6	-7.091	-3.631	-3.460	-5.657	-7.310	-5.490
7	-2.916	-1.032	-0.465	-1.499	-1.623	-0.668
8	2.595	5.111	6.789	-0.025	4.670	6.290
9	-11.864	4.913	6.135	-99.999	-99.999	-99.999
10	-7.091	4.915	6.138	-41.587	-45.788	-41.768
11	-2.901	4.923	6.156	-12.387	-13.518	-12.110
12	2.684	5.797	7.490	-0.495	3.946	5.563

	$^{53}Cr \rightarrow {}^{53}V$			$^{53}V \rightarrow {}^{53}Cr$		
pt	log β^+	log ε^-	log ν	log β^-	log ε^+	log $\bar{\nu}$
1	-52.268	-23.853	-24.411	-2.018	-6.900	-1.845
2	-16.521	-9.129	-9.169	-1.890	-3.749	-1.664
3	-4.267	-2.675	-2.114	-0.713	-1.484	0.034
4	2.564	5.001	6.684	1.773	4.651	6.276
5	-52.268	-18.046	-18.601	-2.166	-12.720	-2.047
6	-16.521	-7.412	-7.452	-1.981	-5.455	-1.794
7	-4.264	-2.577	-2.018	-0.716	-1.578	0.012
8	2.564	5.002	6.684	1.773	4.651	6.276
9	-52.268	4.458	5.534	-99.999	-99.999	-99.999
10	-16.521	4.461	5.538	-34.834	-43.933	-34.969
11	-4.249	4.479	5.575	-9.682	-13.473	-9.366
12	2.664	5.688	7.385	1.360	3.927	5.549

	$^{53}V \rightarrow {}^{53}Ti$			$^{53}Ti \rightarrow {}^{53}V$		
pt	log β^+	log ε^-	log ν	log β^-	log ε^+	log $\bar{\nu}$
1	-44.651	-32.557	-33.123	-1.544	-6.794	-1.257
2	-15.555	-12.377	-12.440	-0.936	-3.486	-0.523
3	-5.388	-3.451	-2.893	0.444	-0.906	1.136
4	1.599	4.731	6.381	2.157	5.011	6.659
5	-44.651	-26.738	-27.304	-1.640	-12.613	-1.382
6	-15.552	-10.662	-10.725	-0.970	-5.191	-0.572
7	-5.377	-3.353	-2.795	0.441	-1.000	1.125
8	1.599	4.731	6.381	2.157	5.011	6.658
9	-44.651	4.306	5.378	-94.664	-99.999	-95.260
10	-15.552	4.309	5.383	-31.491	-43.668	-31.628
11	-5.330	4.326	5.414	-8.472	-12.892	-8.163
12	1.725	5.425	7.088	1.743	4.289	5.933

	$^{54}Co \rightarrow {}^{54}Fe$			$^{54}Fe \rightarrow {}^{54}Co$		
pt	log β^+	log ε^-	log ν	log β^-	log ε^+	log $\bar{\nu}$
1	0.173	-4.341	0.763	-51.249	-42.707	-43.285
2	-0.319	-2.531	0.274	-16.590	-14.998	-15.066
3	-0.042	-0.320	0.927	-4.958	-4.175	-3.457
4	2.680	5.602	7.286	-1.315	4.475	6.077
5	0.173	-0.655	0.888	-51.535	-48.526	-49.103
6	-0.319	-1.120	0.403	-16.746	-16.714	-16.465
7	-0.040	-0.227	0.983	-4.978	-4.271	-3.551
8	2.680	5.602	7.286	-1.315	4.475	6.077
9	0.173	4.887	6.180	-99.999	-99.999	-99.999
10	-0.319	4.395	5.692	-54.111	-55.192	-54.293
11	-0.030	4.848	5.952	-16.184	-16.173	-15.398
12	2.802	6.286	7.986	-1.796	3.749	5.349

	$^{54}Cr \rightarrow {}^{54}V$			$^{54}V \rightarrow {}^{54}Cr$		
pt	log β^+	log ε^-	log ν	log β^-	log ε^+	log $\bar{\nu}$
1	-69.513	-41.036	-41.600	-1.047	-6.628	-0.593
2	-21.734	-14.106	-14.168	-0.747	-3.435	-0.287
3	-5.452	-3.690	-3.160	-0.077	-1.272	0.671
4	2.324	4.848	8.513	2.312	4.784	8.428
5	-69.513	-35.216	-35.781	-1.086	-12.445	-0.641
6	-21.734	-12.391	-12.452	-0.774	-5.140	-0.326
7	-5.449	-3.591	-3.063	-0.080	-1.366	0.659
8	2.324	4.848	8.513	2.312	4.784	8.428
9	-69.513	4.270	5.276	-85.697	-99.999	-86.292
10	-21.734	4.275	5.283	-29.380	-43.618	-29.511
11	-5.433	4.308	5.337	-8.277	-13.258	-7.947
12	2.424	5.538	7.217	1.920	4.061	5.702

	$^{54}Fe \rightarrow {}^{54}Mn$			$^{54}Mn \rightarrow {}^{54}Fe$		
pt	log β^+	log ε^-	log ν	log β^-	log ε^+	log $\bar{\nu}$
1	-16.769	-13.539	-13.635	-10.578	-9.445	-9.614
2	-7.419	-6.022	-5.823	-6.039	-5.861	-5.490
3	-2.451	-1.247	-0.570	-2.008	-2.262	-1.256
4	2.841	5.228	6.912	0.411	4.543	6.161
5	-16.769	-9.508	-9.439	-10.889	-15.264	-10.893
6	-7.409	-4.476	-4.252	-6.173	-7.572	-5.995
7	-2.448	-1.151	-0.477	-2.015	-2.358	-1.313
8	2.841	5.228	6.913	0.411	4.543	6.161
9	-16.769	4.931	6.122	-99.999	-99.999	-99.999
10	-7.409	4.933	6.125	-40.673	-46.050	-40.835
11	-2.433	4.957	6.163	-12.474	-14.259	-12.249
12	2.936	5.914	7.613	-0.047	3.819	5.433

	$^{55}Co \rightarrow {}^{55}Fe$			$^{55}Fe \rightarrow {}^{55}Co$		
pt	log β^+	log ε^-	log ν	log β^-	log ε^+	log $\bar{\nu}$
1	-5.078	-6.985	-6.187	-22.069	-21.584	-22.014
2	-4.842	-3.275	-3.229	-9.445	-8.751	-8.431
3	-1.722	-0.061	0.560	-5.513	-2.265	-1.580
4	2.854	5.329	7.018	-3.856	4.558	6.165
5	-5.078	-2.273	-2.466	-24.763	-27.404	-25.541
6	-4.836	-1.616	-1.563	-10.069	-10.460	-10.041
7	-1.718	0.035	0.656	-5.548	-2.361	-1.677
8	2.854	5.329	7.019	-3.856	4.558	6.165
9	-5.078	5.216	6.498	-99.999	-99.999	-99.999
10	-4.836	5.217	6.500	-48.480	-48.937	-48.504
11	-1.703	5.228	6.518	-17.041	-14.262	-13.582
12	2.953	6.012	7.718	-4.350	3.833	5.437

	$^{54}Mn \rightarrow {}^{54}Cr$			$^{54}Cr \rightarrow {}^{54}Mn$		
pt	log β^+	log ε^-	log ν	log β^-	log ε^+	log $\bar{\nu}$
1	-10.801	-8.165	-8.277	-13.597	-12.468	-12.647
2	-6.507	-5.192	-5.017	-5.278	-5.953	-5.032
3	-3.246	-0.914	-0.368	-1.183	-0.917	-0.057
4	2.517	5.167	6.848	-0.447	4.741	6.356
5	-10.801	-4.110	-4.064	-15.959	-18.288	-16.466
6	-6.500	-3.816	-3.432	-6.380	-7.663	-6.261
7	-3.243	-0.816	-0.270	-1.198	-1.012	-0.144
8	2.517	5.167	6.846	-0.447	4.741	6.356
9	-10.801	4.959	6.197	-99.999	-99.999	-99.999
10	-6.499	4.956	6.198	-42.203	-46.141	-42.403
11	-3.229	4.966	6.214	-12.285	-12.907	-11.858
12	2.623	5.853	7.547	-0.924	4.016	5.629

	$^{55}Fe \rightarrow {}^{55}Mn$			$^{55}Mn \rightarrow {}^{55}Fe$		
pt	log β^+	log ε^-	log ν	log β^-	log ε^+	log $\bar{\nu}$
1	-11.887	-9.185	-9.537	-10.726	-9.887	-9.934
2	-6.714	-5.286	-5.055	-4.869	-5.728	-4.675
3	-2.856	-0.768	-0.203	-1.783	-1.396	-0.563
4	2.807	5.253	6.937	-0.621	4.647	6.261
5	-11.886	-4.917	-4.988	-11.530	-15.707	-11.939
6	-6.703	-3.723	-3.494	-4.987	-7.440	-4.895
7	-2.853	-0.670	-0.108	-1.800	-1.491	-0.652
8	2.807	5.253	6.937	-0.621	4.647	6.261
9	-11.886	5.045	6.283	-99.999	-99.999	-99.999
10	-6.703	5.046	6.285	-41.870	-45.918	-42.077
11	-2.840	5.061	6.309	-12.900	-13.387	-12.406
12	2.903	5.938	7.637	-1.099	3.923	5.534

	$^{55}Mn \rightarrow {}^{55}Cr$			$^{55}Cr \rightarrow {}^{55}Mn$		
pt	log β^+	log ε^-	log ν	log β^-	log ε^+	log $\bar{\nu}$
1	-52.522	-20.911	-21.474	-2.440	-7.460	-2.270
2	-16.973	-8.824	-8.866	-2.188	-4.111	-1.956
3	-4.426	-2.364	-1.847	-0.172	-1.208	0.454
4	2.423	4.997	6.668	1.403	4.799	6.433
5	-52.522	-15.095	-15.657	-2.582	-13.279	-2.481
6	-16.973	-7.107	-7.149	-2.273	-6.816	-2.080
7	-4.423	-2.265	-1.750	-0.177	-1.302	0.432
8	2.423	4.997	6.668	1.403	4.799	6.432
9	-52.522	4.703	5.846	-99.999	-99.999	-99.999
10	-16.973	4.703	5.847	-35.703	-44.294	-35.848
11	-4.411	4.715	5.870	-9.998	-13.193	-9.728
12	2.524	5.686	7.369	0.964	4.076	5.706

	$^{55}Cr \rightarrow {}^{55}V$			$^{55}V \rightarrow {}^{55}Cr$		
pt	log β^+	log ε^-	log ν	log β^-	log ε^+	log $\bar{\nu}$
1	-70.281	-39.505	-40.082	-0.366	-6.498	0.138
2	-22.575	-14.310	-14.390	-0.298	-3.397	0.214
3	-6.238	-4.355	-3.858	0.379	-1.190	1.150
4	1.990	4.686	6.331	2.867	4.979	6.645
5	-70.281	-33.686	-34.262	-0.386	-12.318	0.105
6	-22.574	-12.594	-12.674	-0.314	-5.101	0.187
7	-6.235	-4.256	-3.761	0.377	-1.283	1.144
8	1.990	4.686	6.331	2.867	4.979	6.645
9	-70.281	4.157	5.120	-86.926	-99.999	-87.519
10	-22.574	4.159	5.125	-28.991	-43.579	-29.120
11	-6.222	4.183	5.172	-7.379	-13.173	-7.036
12	2.092	5.384	7.040	2.489	4.258	5.921

	$^{55}V \rightarrow {}^{55}Ti$			$^{55}Ti \rightarrow {}^{55}V$		
pt	log β^+	log ε^-	log ν	log β^-	log ε^+	log $\bar{\nu}$
1	-79.743	-50.613	-51.192	0.130	-6.320	0.745
2	-26.474	-18.615	-18.702	0.317	-3.209	0.983
3	-7.765	-4.565	-4.099	2.161	0.292	2.918
4	2.137	4.583	6.229	2.558	4.956	6.622
5	-79.743	-44.793	-45.372	0.121	-12.139	0.727
6	-26.473	-16.899	-16.987	0.310	-4.914	0.971
7	-7.764	-4.466	-4.000	2.159	0.199	2.913
8	2.137	4.583	6.229	2.558	4.956	6.622
9	-79.743	4.146	5.156	-75.931	-99.999	-76.526
10	-26.473	4.149	5.161	-24.791	-43.391	-24.923
11	-7.749	4.171	5.202	-6.006	-11.689	-5.676
12	2.225	5.281	6.938	2.164	4.236	5.897

	$^{56}Ni \rightarrow {}^{56}Co$			$^{56}Co \rightarrow {}^{56}Ni$		
pt	log β^+	log ε^-	log ν	log β^-	log ε^+	log $\bar{\nu}$
1	-14.981	-7.199	-7.425	-19.208	-18.034	-18.097
2	-5.846	-4.308	-4.203	-8.150	-8.909	-8.020
3	-1.111	-0.309	0.382	-4.049	-3.183	-2.430
4	3.202	5.500	7.203	-1.543	4.378	5.977
5	-14.981	-3.079	-3.074	-21.007	-23.854	-21.185
6	-5.843	-2.711	-2.590	-8.343	-10.618	-8.391
7	-1.109	-0.212	0.469	-4.071	-3.279	-2.524
8	3.202	5.501	7.203	-1.543	4.378	5.977
9	-14.981	5.234	6.492	-99.999	-99.999	-99.999
10	-5.843	5.235	6.494	-46.025	-49.096	-46.270
11	-1.096	5.248	6.517	-15.346	-15.177	-14.394
12	3.295	6.181	7.899	-2.027	3.652	5.249

	$^{56}Co \rightarrow {}^{56}Fe$			$^{56}Fe \rightarrow {}^{56}Co$		
pt	log β^+	log ε^-	log ν	log β^-	log ε^+	log $\bar{\nu}$
1	-3.727	-6.599	-3.543	-28.066	-25.987	-26.525
2	-3.207	-3.504	-2.767	-9.924	-9.744	-9.523
3	-1.691	-0.193	0.432	-3.991	-1.955	-1.246
4	2.693	5.340	7.021	-2.390	4.692	6.303
5	-3.727	-2.782	-2.316	-29.392	-31.807	-29.984
6	-3.204	-1.938	-1.599	-10.405	-11.457	-10.652
7	-1.688	-0.096	0.528	-4.022	-2.050	-1.343
8	2.693	5.340	7.021	-2.390	4.692	6.303
9	-3.727	5.197	6.469	-99.999	-99.999	-99.999
10	-3.204	5.203	6.476	-48.653	-49.935	-48.979
11	-1.673	5.216	6.498	-15.447	-13.948	-13.245
12	2.797	6.025	7.722	-2.881	3.967	5.575

	$^{56}Fe \rightarrow {}^{56}Mn$			$^{56}Mn \rightarrow {}^{56}Fe$		
pt	log β^+	log ε^-	log ν	log β^-	log ε^+	log $\bar{\nu}$
1	-55.626	-24.968	-25.507	-2.482	-7.331	-2.252
2	-16.931	-8.973	-8.986	-2.300	-4.038	-2.049
3	-3.845	-2.086	-1.510	-0.860	-1.527	-0.140
4	2.633	5.101	6.771	1.628	4.728	6.364
5	-55.626	-19.237	-19.773	-2.589	-13.150	-2.404
6	-16.930	-7.281	-7.285	-2.381	-5.745	-2.167
7	-3.842	-1.988	-1.413	-0.864	-1.622	-0.168
8	2.633	5.101	6.771	1.628	4.728	6.364
9	-55.626	4.727	5.836	-99.999	-99.999	-99.999
10	-16.930	4.733	5.845	-35.240	-44.222	-35.381
11	-3.829	4.766	5.897	-10.299	-13.519	-10.009
12	2.728	5.791	7.474	1.201	4.006	5.638

	$^{56}Mn \rightarrow {}^{56}Cr$			$^{56}Cr \rightarrow {}^{56}Mn$		
pt	log β^+	log ε^-	log ν	log β^-	log ε^+	log $\bar{\nu}$
1	-45.809	-16.543	-17.094	-2.678	-7.031	-2.709
2	-15.695	-8.098	-8.129	-2.319	-3.815	-2.180
3	-4.782	-2.553	-2.042	0.301	-0.879	0.943
4	2.289	5.000	6.662	1.753	4.914	6.552
5	-45.809	-10.747	-11.289	-3.076	-12.851	-3.277
6	-15.695	-6.383	-6.411	-2.470	-5.521	-2.393
7	-4.779	-2.454	-1.944	0.298	-0.973	0.927
8	2.289	5.000	6.662	1.753	4.914	6.552
9	-45.809	4.683	5.807	-99.999	-99.999	-99.999
10	-15.695	4.682	5.807	-36.022	-43.998	-36.163
11	-4.765	4.697	5.835	-9.313	-12.865	-9.025
12	2.376	5.691	7.367	1.320	4.191	5.826

	$^{56}Ti \rightarrow {}^{56}Sc$			$^{56}Sc \rightarrow {}^{56}Ti$		
pt	log β^+	log ε^-	log ν	log β^-	log ε^+	log $\bar{\nu}$
1	-99.999	-84.917	-85.500	0.523	-8.728	1.403
2	-35.037	-28.983	-29.080	0.485	-3.763	1.367
3	-9.353	-7.984	-7.475	1.202	-1.303	2.152
4	2.727	4.878	6.593	2.377	4.594	6.182
5	-99.999	-79.098	-79.681	0.522	-12.546	1.400
6	-35.036	-27.267	-27.365	0.483	-6.467	1.364
7	-9.348	-7.885	-7.380	1.201	-1.396	2.150
8	2.727	4.878	6.593	2.377	4.594	6.182
9	-99.999	2.801	3.449	-41.959	-99.999	-42.550
10	-35.036	2.812	3.470	-14.887	-43.944	-15.010
11	-9.329	2.915	3.654	-4.028	-13.282	-3.862
12	2.820	5.557	7.288	2.058	3.866	5.454

	$^{56}Cr \rightarrow {}^{56}V$			$^{56}V \rightarrow {}^{56}Cr$		
pt	log β^+	log ε^-	log ν	log β^-	log ε^+	log $\bar{\nu}$
1	-87.412	-58.878	-59.457	0.505	-6.140	1.179
2	-28.119	-20.349	-20.436	0.515	-3.103	1.194
3	-7.964	-5.253	-4.789	1.879	-0.234	2.701
4	1.591	4.516	6.122	3.509	5.448	7.146
5	-87.412	-53.058	-53.637	0.498	-11.959	1.167
6	-28.118	-18.609	-18.697	0.510	-4.807	1.184
7	-7.960	-5.154	-4.691	1.878	-0.327	2.698
8	1.591	4.516	6.122	3.509	5.448	7.146
9	-87.412	4.072	5.002	-67.204	-99.999	-67.798
10	-28.118	4.075	5.008	-22.667	-43.284	-22.795
11	-7.946	4.108	5.068	-5.507	-12.214	-5.162
12	1.681	5.224	6.839	3.136	4.730	6.424

	$^{57}Zn \rightarrow {}^{57}Cu$			$^{57}Cu \rightarrow {}^{57}Zn$		
pt	log β^+	log ε^-	log ν	log β^-	log ε^+	log $\bar{\nu}$
1	1.166	-3.522	1.869	-80.403	-76.056	-76.636
2	1.162	-1.253	1.870	-28.943	-25.732	-25.819
3	1.691	0.604	2.655	-8.626	-6.803	-6.307
4	2.954	5.606	7.294	0.789	4.374	5.982
5	1.166	0.153	1.947	-83.189	-81.876	-82.442
6	1.162	0.154	1.947	-29.657	-27.447	-27.534
7	1.692	0.696	2.669	-8.630	-6.901	-6.404
8	2.954	5.606	7.295	0.789	4.374	5.982
9	1.166	5.430	6.731	-99.999	-99.999	-99.999
10	1.162	5.429	6.729	-64.867	-65.925	-64.970
11	1.694	5.402	6.705	-18.293	-18.813	-17.844
12	3.064	6.289	7.994	0.354	3.649	5.254

	$^{56}V \rightarrow {}^{56}Ti$			$^{56}Ti \rightarrow {}^{56}V$		
pt	log β^+	log ε^-	log ν	log β^-	log ε^+	log $\bar{\nu}$
1	-65.366	-44.464	-45.042	-5.579	-12.011	-4.973
2	-21.629	-15.620	-15.707	-0.787	-4.290	-0.148
3	-6.937	-3.605	-3.126	1.089	-0.425	1.763
4	2.667	5.116	6.817	1.327	4.696	6.291
5	-65.366	-38.644	-39.223	-5.589	-17.830	-4.990
6	-21.629	-13.904	-13.992	-0.795	-6.994	-0.161
7	-6.934	-3.506	-3.027	1.087	-0.518	1.753
8	2.667	5.117	6.817	1.327	4.696	6.291
9	-65.366	4.268	5.356	-88.075	-99.999	-88.672
10	-21.629	4.270	5.359	-29.158	-44.472	-29.296
11	-6.917	4.286	5.390	-8.014	-12.407	-7.712
12	2.773	5.798	7.515	0.908	3.963	5.559

	$^{57}Cu \rightarrow {}^{57}Ni$			$^{57}Ni \rightarrow {}^{57}Cu$		
pt	log β^+	log ε^-	log ν	log β^-	log ε^+	log $\bar{\nu}$
1	0.439	-3.867	1.044	-56.186	-43.888	-44.462
2	0.441	-1.568	1.053	-18.549	-15.376	-15.447
3	0.658	0.460	1.676	-5.437	-4.126	-3.586
4	2.416	5.617	7.295	-0.581	4.608	6.217
5	0.439	-0.171	1.194	-56.341	-49.708	-50.281
6	0.441	-0.150	1.206	-18.634	-17.092	-17.142
7	0.660	0.543	1.729	-5.451	-4.224	-3.682
8	2.416	5.617	7.295	-0.582	4.608	6.217
9	0.439	5.379	6.672	-99.999	-99.999	-99.999
10	0.441	5.381	6.674	-65.041	-65.570	-65.091
11	0.667	5.396	6.699	-16.454	-16.136	-15.536
12	2.547	6.300	7.996	-1.056	3.883	5.489

	$^{57}Ni \rightarrow {}^{57}Co$			$^{57}Co \rightarrow {}^{57}Ni$		
pt	log β^+	log ε^-	log ν	log β^-	log ε^+	log $\bar{\nu}$
1	-5.524	-6.990	-5.668	-27.557	-21.199	-21.729
2	-3.764	-4.137	-3.312	-9.541	-9.487	-9.169
3	-1.420	-0.479	0.200	-3.387	-2.790	-2.013
4	2.964	5.402	7.090	-0.932	4.548	6.158
5	-5.524	-3.185	-2.830	-27.766	-27.018	-27.347
6	-3.761	-2.669	-2.165	-9.688	-11.203	-9.641
7	-1.417	-0.381	0.289	-3.406	-2.886	-2.106
8	2.964	5.402	7.090	-0.932	4.548	6.158
9	-5.524	5.206	6.453	-99.999	-99.999	-99.999
10	-3.761	5.208	6.456	-46.841	-49.680	-47.064
11	-1.403	5.225	6.483	-14.585	-14.785	-13.921
12	3.060	6.086	7.789	-1.412	3.823	5.430

	$^{57}Co \rightarrow {}^{57}Fe$			$^{57}Fe \rightarrow {}^{57}Co$		
pt	log β^+	log ε^-	log ν	log β^-	log ε^+	log $\bar{\nu}$
1	-11.176	-8.769	-8.898	-11.236	-11.311	-11.360
2	-6.008	-5.092	-4.893	-6.027	-6.384	-5.676
3	-2.943	-0.846	-0.283	-1.772	-1.756	-0.853
4	2.773	5.243	6.921	-0.043	4.718	6.340
5	-11.176	-4.197	-4.385	-13.725	-17.131	-14.289
6	-6.000	-3.484	-3.318	-6.138	-8.095	-5.958
7	-2.940	-0.748	-0.186	-1.784	-1.851	-0.932
8	2.773	5.244	6.921	-0.043	4.718	6.339
9	-11.176	5.087	6.313	-99.999	-99.999	-99.999
10	-6.000	5.088	6.315	-42.348	-46.572	-42.534
11	-2.928	5.100	6.336	-12.738	-13.749	-12.458
12	2.867	5.930	7.623	-0.516	3.995	5.612

	$^{57}Fe \rightarrow {}^{57}Mn$			$^{57}Mn \rightarrow {}^{57}Fe$		
pt	log β^+	log ε^-	log ν	log β^-	log ε^+	log $\bar{\nu}$
1	-51.326	-20.585	-21.146	-2.131	-7.121	-1.968
2	-16.482	-8.474	-8.517	-1.879	-3.925	-1.585
3	-4.381	-1.689	-1.181	0.160	-0.565	0.776
4	2.482	5.103	6.767	0.964	4.885	6.518
5	-51.326	-14.774	-15.332	-2.281	-12.941	-2.186
6	-16.481	-6.760	-6.802	-1.953	-6.631	-1.679
7	-4.378	-1.590	-1.082	0.153	-0.659	0.736
8	2.482	5.104	6.767	0.964	4.885	6.518
9	-51.326	4.923	6.110	-99.999	-99.999	-99.999
10	-16.481	4.924	6.112	-36.007	-44.106	-36.166
11	-4.365	4.935	6.133	-10.251	-12.551	-10.028
12	2.581	5.794	7.472	0.509	4.162	5.791

	$^{57}Mn \rightarrow {}^{57}Cr$			$^{57}Cr \rightarrow {}^{57}Mn$		
pt	log β^+	log ε^-	log ν	log β^-	log ε^+	log $\bar{\nu}$
1	-66.982	-37.398	-37.974	-0.439	-8.584	0.063
2	-21.887	-13.991	-14.072	-0.284	-3.469	0.260
3	-6.141	-3.189	-2.709	1.425	-0.102	2.089
4	2.190	4.843	6.485	2.236	5.069	6.729
5	-66.982	-31.578	-32.154	-0.459	-12.403	0.030
6	-21.887	-12.277	-12.358	-0.298	-5.174	0.237
7	-6.138	-3.090	-2.610	1.422	-0.195	2.079
8	2.190	4.843	6.485	2.236	5.069	6.729
9	-66.982	4.595	5.686	-89.315	-99.999	-89.911
10	-21.887	4.596	5.689	-29.626	-43.661	-29.764
11	-6.123	4.612	5.718	-7.781	-12.085	-7.479
12	2.283	5.541	7.194	1.814	4.348	6.004

	$^{57}Cr \rightarrow {}^{57}V$			$^{57}V \rightarrow {}^{57}Cr$		
pt	log β^+	log ε^-	log ν	log β^-	log ε^+	log $\bar{\nu}$
1	-74.153	-46.644	-47.222	-0.528	-6.958	0.073
2	-24.074	-17.134	-17.220	-0.430	-3.871	0.193
3	-6.653	-4.193	-3.719	1.186	-0.590	1.916
4	2.569	4.900	6.585	1.835	4.685	6.298
5	-74.153	-40.824	-41.403	-0.539	-12.777	0.053
6	-24.074	-15.419	-15.505	-0.438	-5.576	0.179
7	-6.649	-4.094	-3.621	1.184	-0.684	1.909
8	2.569	4.900	6.585	1.835	4.685	6.298
9	-74.153	4.256	5.287	-80.696	-99.999	-81.291
10	-24.074	4.259	5.293	-27.087	-44.053	-27.221
11	-6.633	4.281	5.333	-7.281	-12.572	-6.958
12	2.663	5.587	7.285	1.433	3.960	5.570

	$^{57}V \rightarrow {}^{57}Ti$			$^{57}Ti \rightarrow {}^{57}V$		
pt	log β^+	log ε^-	log ν	log β^-	log ε^+	log $\bar{\nu}$
1	-84.611	-60.265	-60.846	0.704	-6.091	1.431
2	-26.118	-21.279	-21.370	0.724	-3.057	1.456
3	-5.727	-5.613	-4.615	1.845	-0.250	2.667
4	2.346	4.521	6.191	2.638	4.873	6.517
5	-84.611	-54.445	-55.026	0.699	-11.910	1.422
6	-26.118	-19.563	-19.654	0.720	-4.761	1.448
7	-5.727	-5.515	-4.584	1.844	-0.343	2.664
8	2.346	4.521	6.191	2.638	4.873	6.517
9	-84.611	3.769	4.701	-66.057	-99.999	-66.650
10	-26.118	3.772	4.707	-21.981	-43.239	-22.109
11	-5.725	3.801	4.762	-5.486	-12.230	-5.141
12	2.445	5.213	6.895	2.266	4.150	5.791

	$^{58}Cu \rightarrow {}^{58}Ni$			$^{58}Ni \rightarrow {}^{58}Cu$		
pt	log β^+	log ε^-	log ν	log β^-	log ε^+	log $\bar{\nu}$
1	-0.452	-4.414	0.122	-55.539	-44.413	-44.977
2	-0.192	-1.994	0.405	-17.917	-15.285	-15.339
3	0.084	0.133	1.198	-4.953	-3.885	-3.293
4	2.458	5.594	7.275	-0.699	4.617	6.224
5	-0.452	-0.686	0.367	-55.675	-50.233	-50.797
6	-0.191	-0.564	0.609	-18.018	-17.001	-16.996
7	0.086	0.226	1.260	-4.969	-3.983	-3.388
8	2.458	5.594	7.275	-0.699	4.617	6.224
9	-0.452	5.321	6.587	-99.999	-99.999	-99.999
10	-0.191	5.328	6.599	-54.581	-55.478	-54.712
11	0.094	5.338	6.617	-16.002	-15.892	-15.222
12	2.589	6.277	7.976	-1.175	3.891	5.495

	$^{58}Fe \rightarrow {}^{58}Mn$			$^{58}Mn \rightarrow {}^{58}Fe$		
pt	log β^+	log ε^-	log ν	log β^-	log ε^+	log $\bar{\nu}$
1	-68.327	-37.413	-37.983	-0.908	-6.727	-0.456
2	-21.184	-12.916	-12.983	-0.836	-3.560	-0.397
3	-5.258	-3.054	-2.561	0.430	-1.001	1.101
4	2.628	4.998	6.659	1.983	4.813	6.462
5	-68.327	-31.595	-32.165	-0.943	-12.547	-0.505
6	-21.184	-11.201	-11.267	-0.866	-5.265	-0.440
7	-5.255	-2.955	-2.462	0.427	-1.095	1.090
8	2.628	4.998	6.659	1.983	4.813	6.461
9	-68.327	4.673	5.760	-89.367	-99.999	-89.963
10	-21.184	4.675	5.763	-30.695	-43.743	-30.833
11	-5.242	4.691	5.794	-8.675	-12.985	-8.372
12	2.714	5.691	7.364	1.564	4.091	5.736

	$^{58}Ni \rightarrow {}^{58}Co$			$^{58}Co \rightarrow {}^{58}Ni$		
pt	log β^+	log ε^-	log ν	log β^-	log ε^+	log $\bar{\nu}$
1	-19.421	-15.053	-15.518	-8.404	-9.092	-8.754
2	-8.398	-6.526	-6.389	-6.069	-5.519	-5.207
3	-2.778	-1.356	-0.713	-1.707	-2.230	-1.044
4	2.912	5.355	7.039	0.773	4.586	6.204
5	-19.421	-10.425	-10.608	-10.675	-14.911	-11.179
6	-8.383	-4.940	-4.779	-6.234	-7.229	-5.882
7	-2.775	-1.259	-0.619	-1.713	-2.326	-1.085
8	2.912	5.355	7.039	0.773	4.586	6.204
9	-19.421	5.028	6.200	-99.999	-99.999	-99.999
10	-8.383	5.030	6.203	-39.452	-45.707	-39.607
11	-2.763	5.053	6.241	-11.968	-14.226	-11.729
12	3.009	6.041	7.739	0.321	3.862	5.477

	$^{58}Mn \rightarrow {}^{58}Cr$			$^{58}Cr \rightarrow {}^{58}Mn$		
pt	log β^+	log ε^-	log ν	log β^-	log ε^+	log $\bar{\nu}$
1	-69.963	-30.776	-31.349	-0.904	-6.729	-0.505
2	-20.340	-12.432	-12.511	-0.227	-3.328	0.296
3	-6.532	-2.639	-2.153	2.141	0.929	2.757
4	1.333	4.697	6.312	2.565	5.708	7.379
5	-69.963	-24.956	-25.530	-0.941	-12.549	-0.567
6	-20.340	-10.717	-10.795	-0.243	-5.032	0.270
7	-6.529	-2.540	-2.055	2.138	0.835	2.739
8	1.333	4.697	6.312	2.565	5.708	7.379
9	-69.963	4.622	5.757	-96.382	-99.999	-96.981
10	-20.340	4.623	5.758	-31.323	-43.510	-31.468
11	-6.515	4.637	5.785	-7.618	-11.054	-7.346
12	1.433	5.399	7.027	2.118	4.984	6.651

	$^{58}Co \rightarrow {}^{58}Fe$			$^{58}Fe \rightarrow {}^{58}Co$		
pt	log β^+	log ε^-	log ν	log β^-	log ε^+	log $\bar{\nu}$
1	-4.909	-6.683	-4.947	-22.767	-19.585	-20.092
2	-4.450	-3.997	-3.593	-7.910	-7.738	-7.454
3	-2.381	-0.594	-0.019	-2.162	-1.568	-0.770
4	2.594	5.285	6.960	-0.661	4.814	6.432
5	-4.909	-2.784	-2.511	-24.999	-25.405	-25.397
6	-4.443	-2.500	-2.134	-8.062	-9.452	-8.019
7	-2.378	-0.495	0.079	-2.181	-1.663	-0.862
8	2.594	5.285	6.961	-0.661	4.814	6.432
9	-4.909	5.129	6.377	-99.999	-99.999	-99.999
10	-4.443	5.130	6.379	-45.305	-47.930	-45.529
11	-2.366	5.139	6.395	-13.360	-13.559	-12.885
12	2.699	5.971	7.662	-1.139	4.090	5.704

	$^{58}Cr \rightarrow {}^{58}V$			$^{58}V \rightarrow {}^{58}Cr$		
pt	log β^+	log ε^-	log ν	log β^-	log ε^+	log $\bar{\nu}$
1	-95.758	-68.968	-69.550	-0.409	-7.503	0.406
2	-30.497	-24.322	-24.416	-0.443	-4.532	0.378
3	-7.733	-6.281	-5.781	0.939	-1.404	1.820
4	3.118	5.199	6.918	2.069	4.511	6.098
5	-95.758	-63.149	-63.730	-0.411	-13.323	0.401
6	-30.496	-22.607	-22.700	-0.445	-6.236	0.374
7	-7.730	-6.182	-5.685	0.938	-1.497	1.818
8	3.118	5.199	6.918	2.069	4.511	6.098
9	-95.758	3.676	4.526	-58.532	-99.999	-59.124
10	-30.496	3.681	4.533	-20.175	-44.713	-20.301
11	-7.714	3.720	4.608	-5.680	-13.384	-5.327
12	3.207	5.877	7.612	1.716	3.783	5.370

	$^{58}V \rightarrow {}^{58}Ti$			$^{58}Ti \rightarrow {}^{58}V$		
pt	log β^+	log ε^-	log ν	log β^-	log ε^+	log $\bar{\nu}$
1	-74.447	-48.195	-48.774	0.239	-6.290	0.875
2	-24.966	-18.017	-18.105	0.370	-3.186	1.032
3	-7.606	-4.626	-4.158	2.107	0.313	2.846
4	1.649	4.340	5.991	2.486	5.035	6.691
5	-74.447	-42.375	-42.955	0.231	-12.109	0.860
6	-24.965	-16.301	-16.389	0.364	-4.890	1.020
7	-7.604	-4.527	-4.060	2.106	0.220	2.840
8	1.649	4.340	5.991	2.486	5.035	6.691
9	-74.447	3.886	4.914	-78.656	-99.999	-79.251
10	-24.965	3.888	4.918	-25.710	-43.368	-25.843
11	-7.587	3.908	4.956	-6.278	-11.668	-6.954
12	1.752	5.036	6.698	2.086	4.314	5.966

	$^{59}Co \rightarrow {}^{59}Fe$			$^{59}Fe \rightarrow {}^{59}Co$		
pt	log β^+	log ε^-	log ν	log β^-	log ε^+	log $\bar{\nu}$
1	-47.247	-17.107	-17.803	-4.829	-8.547	-4.784
2	-15.021	-7.244	-7.260	-2.578	-4.482	-2.298
3	-3.648	-1.178	-0.663	-0.547	-0.833	0.217
4	2.835	5.254	6.932	0.272	4.754	6.375
5	-47.247	-11.496	-11.977	-5.106	-14.367	-5.124
6	-15.021	-5.547	-5.557	-2.647	-6.189	-2.399
7	-3.643	-1.080	-0.555	-0.557	-0.927	0.151
8	2.835	5.254	6.932	0.272	4.753	6.375
9	-47.247	5.054	6.265	-99.999	-99.999	-99.999
10	-15.021	5.055	6.267	-37.984	-44.666	-38.160
11	-3.631	5.066	6.287	-11.310	-12.820	-11.098
12	2.926	5.941	7.634	-0.195	4.030	5.648

	$^{59}Cu \rightarrow {}^{59}Ni$			$^{59}Ni \rightarrow {}^{59}Cu$		
pt	log β^+	log ε^-	log ν	log β^-	log ε^+	log $\bar{\nu}$
1	-2.001	-6.364	-1.718	-54.008	-26.912	-27.478
2	-1.904	-2.921	-1.528	-16.877	-10.742	-10.755
3	-0.972	-0.453	0.408	-3.914	-3.388	-2.683
4	2.451	5.487	7.164	1.056	4.653	6.268
5	-2.001	-1.581	-0.923	-54.024	-32.731	-33.297
6	-1.902	-1.452	-0.789	-16.890	-12.457	-12.469
7	-0.969	-0.358	0.488	-3.918	-3.485	-2.761
8	2.451	5.487	7.164	1.055	4.653	6.267
9	-2.001	5.102	6.293	-99.999	-99.999	-99.999
10	-1.902	5.105	6.297	-48.258	-50.934	-48.403
11	-0.955	5.121	6.326	-13.774	-15.392	-13.484
12	2.578	6.172	7.866	0.615	3.929	5.540

	$^{59}Fe \rightarrow {}^{59}Mn$			$^{59}Mn \rightarrow {}^{59}Fe$		
pt	log β^+	log ε^-	log ν	log β^-	log ε^+	log $\bar{\nu}$
1	-63.209	-32.536	-33.108	-1.012	-6.727	-0.645
2	-20.455	-12.345	-12.414	-0.884	-3.626	-0.447
3	-5.978	-2.814	-2.329	1.425	0.033	2.059
4	1.812	4.797	6.419	2.478	5.404	7.072
5	-63.209	-26.716	-27.288	-1.058	-12.546	-0.720
6	-20.454	-10.629	-10.698	-0.915	-5.331	-0.491
7	-5.975	-2.715	-2.231	1.422	-0.060	2.046
8	1.812	4.797	6.419	2.478	5.404	7.072
9	-63.209	4.665	5.781	-94.405	-99.999	-95.002
10	-20.454	4.667	5.785	-31.493	-43.808	-31.633
11	-5.962	4.683	5.813	-8.095	-11.950	-7.804
12	1.905	5.498	7.132	2.060	4.685	6.348

	$^{59}Ni \rightarrow {}^{59}Co$			$^{59}Co \rightarrow {}^{59}Ni$		
pt	log β^+	log ε^-	log ν	log β^-	log ε^+	log $\bar{\nu}$
1	-8.044	-8.261	-8.079	-12.713	-11.645	-12.126
2	-5.710	-4.591	-4.348	-7.348	-6.218	-6.076
3	-2.696	-1.150	-0.548	-1.544	-2.019	-0.884
4	2.827	5.292	6.967	0.686	4.715	6.339
5	-8.044	-3.845	-3.935	-15.308	-17.464	-15.947
6	-6.701	-3.037	-2.796	-7.664	-7.930	-7.315
7	-2.693	-1.052	-0.453	-1.552	-2.114	-0.933
8	2.827	5.292	6.968	0.686	4.715	6.339
9	-8.044	5.088	6.286	-99.999	-99.999	-99.999
10	-6.701	5.090	6.290	-42.317	-46.408	-42.478
11	-2.680	5.102	6.311	-12.126	-14.012	-11.900
12	2.920	5.979	7.669	0.225	3.991	5.612

	$^{59}Mn \rightarrow {}^{59}Cr$			$^{59}Cr \rightarrow {}^{59}Mn$		
pt	log β^+	log ε^-	log ν	log β^-	log ε^+	log $\bar{\nu}$
1	-78.742	-49.573	-50.153	-0.088	-6.723	0.566
2	-25.655	-18.012	-18.100	-0.136	-3.761	0.532
3	-7.112	-4.442	-3.971	1.309	-0.574	2.060
4	2.695	4.899	6.598	1.977	4.670	6.286
5	-78.742	-43.754	-44.333	-0.096	-12.542	0.552
6	-25.654	-16.296	-16.385	-0.143	-5.465	0.521
7	-7.109	-4.343	-3.873	1.308	-0.667	2.055
8	2.695	4.899	6.598	1.977	4.670	6.286
9	-78.742	4.222	5.236	-77.257	-99.999	-77.852
10	-25.654	4.225	5.240	-25.847	-43.943	-25.979
11	-7.094	4.236	5.268	-6.922	-12.555	-6.594
12	2.788	5.583	7.295	1.581	3.950	5.562

	$^{59}Cr \rightarrow {}^{59}V$			$^{59}V \rightarrow {}^{59}Cr$		
pt	log β^+	log ε^-	log ν	log β^-	log ε^+	log $\bar{\nu}$
1	-82.654	-55.369	-55.950	0.005	-6.774	0.713
2	-26.995	-20.066	-20.156	0.063	-3.709	0.781
3	-7.557	-5.165	-4.698	1.583	-0.429	2.374
4	2.281	4.629	6.309	2.355	4.820	6.450
5	-82.654	-49.550	-50.130	0.000	-12.594	0.704
6	-26.994	-18.350	-18.441	0.058	-6.414	0.773
7	-7.553	-5.066	-4.600	1.582	-0.522	2.370
8	2.281	4.629	6.310	2.355	4.820	6.450
9	-82.654	3.885	4.859	-71.685	-99.999	-72.279
10	-26.994	3.886	4.862	-23.903	-43.891	-24.033
11	-7.537	3.910	4.908	-6.177	-12.410	-5.839
12	2.356	5.317	7.011	1.972	4.096	5.723

	$^{60}Ni \rightarrow {}^{60}Co$			$^{60}Co \rightarrow {}^{60}Ni$		
pt	log β^+	log ε^-	log ν	log β^-	log ε^+	log $\bar{\nu}$
1	-26.954	-21.762	-22.231	-4.766	-8.365	-4.753
2	-12.307	-8.013	-7.985	-3.151	-4.561	-2.793
3	-3.429	-1.428	-0.888	-0.759	-1.484	-0.146
4	2.916	5.253	6.926	0.954	4.717	6.347
5	-26.954	-16.314	-16.769	-5.092	-14.184	-5.165
6	-12.280	-6.348	-6.307	-3.221	-6.268	-2.875
7	-3.426	-1.330	-0.790	-0.765	-1.578	-0.182
8	2.916	5.253	6.926	0.954	4.717	6.347
9	-26.954	5.052	6.234	-99.999	-99.999	-99.999
10	-12.280	5.054	6.237	-36.937	-44.745	-37.092
11	-3.415	5.074	6.269	-11.148	-13.473	-10.909
12	3.001	5.944	7.631	0.499	3.994	5.620

	$^{60}Zn \rightarrow {}^{60}Cu$			$^{60}Cu \rightarrow {}^{60}Zn$		
pt	log β^+	log ε^-	log ν	log β^-	log ε^+	log $\bar{\nu}$
1	-2.290	-5.313	-2.132	-27.583	-24.510	-25.074
2	-2.086	-2.919	-1.718	-12.084	-10.692	-10.713
3	-0.552	-0.302	0.634	-4.290	-3.841	-3.095
4	2.846	5.650	7.340	0.510	4.564	6.168
5	-2.290	-1.585	-0.956	-29.727	-30.329	-30.292
6	-2.084	-1.455	-0.813	-12.696	-12.407	-12.362
7	-0.550	-0.207	0.705	-4.296	-3.938	-3.175
8	2.846	5.651	7.341	0.510	4.564	6.168
9	-2.290	5.250	6.466	-99.999	-99.999	-99.999
10	-2.084	5.251	6.469	-48.349	-50.885	-48.502
11	-0.540	5.265	6.495	-14.480	-15.842	-14.199
12	2.964	6.333	8.040	0.060	3.838	5.440

	$^{60}Co \rightarrow {}^{60}Fe$			$^{60}Fe \rightarrow {}^{60}Co$		
pt	log β^+	log ε^-	log ν	log β^-	log ε^+	log $\bar{\nu}$
1	-41.074	-12.026	-12.194	-7.364	-8.542	-7.586
2	-13.943	-5.838	-5.863	-2.269	-4.067	-2.126
3	-4.237	-0.777	-0.235	-0.151	0.206	1.049
4	2.115	5.022	6.665	0.154	5.269	6.912
5	-41.074	-7.390	-7.682	-8.458	-14.362	-8.840
6	-13.943	-4.136	-4.160	-2.388	-5.773	-2.311
7	-4.234	-0.679	-0.137	-0.169	0.112	0.960
8	2.115	5.022	6.665	0.154	5.269	6.912
9	-41.074	5.048	6.289	-99.999	-99.999	-99.999
10	-13.943	5.049	6.292	-39.448	-44.251	-39.659
11	-4.222	5.059	6.310	-11.311	-11.783	-10.805
12	2.207	5.715	7.374	-0.326	4.547	6.185

	$^{60}Cu \rightarrow {}^{60}Ni$			$^{60}Ni \rightarrow {}^{60}Cu$		
pt	log β^+	log ε^-	log ν	log β^-	log ε^+	log $\bar{\nu}$
1	-2.107	-5.501	-1.733	-36.142	-32.856	-33.418
2	-1.942	-2.968	-1.512	-14.848	-11.678	-11.700
3	-1.029	-0.553	0.308	-3.536	-3.099	-2.359
4	2.536	5.651	7.336	0.966	4.660	6.267
5	-2.107	-1.725	-1.059	-39.416	-38.676	-39.213
6	-1.940	-1.504	-0.831	-15.658	-13.393	-13.415
7	-1.027	-0.458	0.386	-3.540	-3.198	-2.434
8	2.536	5.651	7.336	0.966	4.660	6.267
9	-2.107	5.085	6.270	-99.999	-99.999	-99.999
10	-1.940	5.091	6.279	-49.144	-51.871	-49.289
11	-1.016	5.104	6.303	-13.329	-15.102	-13.044
12	2.668	6.334	8.036	0.528	3.935	5.539

	$^{60}Fe \rightarrow {}^{60}Mn$			$^{60}Mn \rightarrow {}^{60}Fe$		
pt	log β^+	log ε^-	log ν	log β^-	log ε^+	log $\bar{\nu}$
1	-84.932	-54.800	-55.380	-0.447	-7.089	0.211
2	-26.735	-19.005	-19.093	-0.316	-3.935	0.353
3	-6.831	-4.815	-4.339	0.970	-1.074	1.762
4	2.745	4.952	6.641	2.291	4.645	6.273
5	-84.932	-48.981	-49.560	-0.455	-12.908	0.197
6	-26.735	-17.290	-17.377	-0.322	-5.639	0.342
7	-6.828	-4.716	-4.242	0.969	-1.167	1.758
8	2.745	4.952	6.641	2.291	4.645	6.272
9	-84.932	4.189	5.156	-72.177	-99.999	-72.770
10	-26.735	4.194	5.163	-24.804	-44.117	-24.934
11	-6.815	4.222	5.215	-6.792	-13.055	-6.452
12	2.832	5.639	7.340	1.909	3.921	5.546

	$^{60}Mn \rightarrow {}^{60}Cr$			$^{60}Cr \rightarrow {}^{60}Mn$		
pt	log β^+	log ε^-	log ν	log β^-	log ε^+	log $\bar{\nu}$
1	-63.191	-34.452	-35.025	-0.802	-6.897	-0.383
2	-21.293	-13.660	-13.738	-0.236	-3.412	0.320
3	-6.234	-3.138	-2.660	1.593	0.193	2.230
4	2.189	4.758	6.429	1.688	4.848	6.480
5	-63.191	-28.632	-29.206	-0.834	-12.516	-0.437
6	-21.292	-11.944	-12.023	-0.250	-6.116	0.298
7	-6.230	-3.039	-2.561	1.590	0.100	2.217
8	2.189	4.758	6.429	1.688	4.848	6.480
9	-63.191	4.363	5.481	-92.827	-99.999	-93.424
10	-21.292	4.365	5.484	-30.295	-43.594	-30.436
11	-6.217	4.380	5.512	-7.913	-11.789	-7.823
12	2.290	5.447	7.132	1.258	4.125	5.754

	$^{60}Cr \rightarrow {}^{60}V$			$^{60}V \rightarrow {}^{60}Cr$		
pt	log β^+	log ε^-	log ν	log β^-	log ε^+	log $\bar{\nu}$
1	-99.999	-78.364	-78.946	0.187	-6.968	1.022
2	-33.477	-26.792	-26.886	0.308	-3.843	1.147
3	-8.792	-7.349	-6.848	1.130	-1.324	2.053
4	2.670	4.798	6.511	2.420	4.589	6.185
5	-99.999	-72.544	-73.126	0.185	-12.787	1.017
6	-33.476	-25.076	-25.171	0.304	-6.547	1.143
7	-8.788	-7.250	-6.753	1.129	-1.417	2.051
8	2.670	4.798	6.512	2.420	4.588	6.184
9	-99.999	3.086	3.826	-48.787	-99.999	-49.379
10	-33.476	3.093	3.840	-17.203	-44.024	-17.327
11	-8.771	3.164	3.970	-4.724	-13.304	-4.362
12	2.759	5.477	7.206	2.089	3.862	5.457

	$^{60}V \rightarrow {}^{60}Ti$			$^{60}Ti \rightarrow {}^{60}V$		
pt	log β^+	log ε^-	log ν	log β^-	log ε^+	log $\bar{\nu}$
1	-84.885	-58.806	-59.387	0.601	-6.150	1.310
2	-28.583	-21.649	-21.741	0.681	-3.084	1.409
3	-8.654	-6.030	-6.567	2.082	0.021	2.892
4	1.770	4.228	5.920	2.221	4.746	6.359
5	-84.885	-52.987	-53.568	0.595	-11.969	1.300
6	-28.583	-19.934	-20.026	0.677	-4.788	1.401
7	-8.650	-5.931	-5.469	2.081	-0.072	2.889
8	1.770	4.228	5.921	2.221	4.746	6.359
9	-84.885	3.213	4.164	-68.193	-99.999	-68.786
10	-28.583	3.217	4.170	-22.261	-43.266	-22.390
11	-8.633	3.245	4.222	-5.443	-11.959	-5.101
12	1.874	4.912	6.619	1.843	4.021	5.632

Figure 1

A schematic representation of a typical excited state problem is shown. $E_1^<$, $E_2^<$, ... $E_i^<$ are the discrete states of the $T^<$-nucleus. $E_1^>$, $E_2^>$, ... $E_j^>$ are the discrete states in the $T^>$-nucleus. $A_1^<$, $A_2^<$, ... $A_j^<$ are the analogs of $E_1^>$, $E_2^>$, ... $E_j^>$. Transitions from the discrete states of the $T^<$-nucleus to Gamow-Teller collective resonances ($R_1^>$, $R_2^>$, ... $R_i^>$) in the $T^>$-nucleus, and the reverse transitions, are shown with rates $\lambda_{ii} = \lambda_{er}$. Similarly, transitions from the discrete states of the $T^>$-nucleus to collective Gamow-Teller resonances in the $T^<$-nucleus ($R_1^<$, $R_2^<$, ... $R_j^<$), and the reverse transitions are shown with rates $\lambda_{jj} = \lambda_{re}$. For clarity the Fermi transitions λ^F_{jj} between $E_j^> \rightleftarrows A_j^<$ are not illustrated.

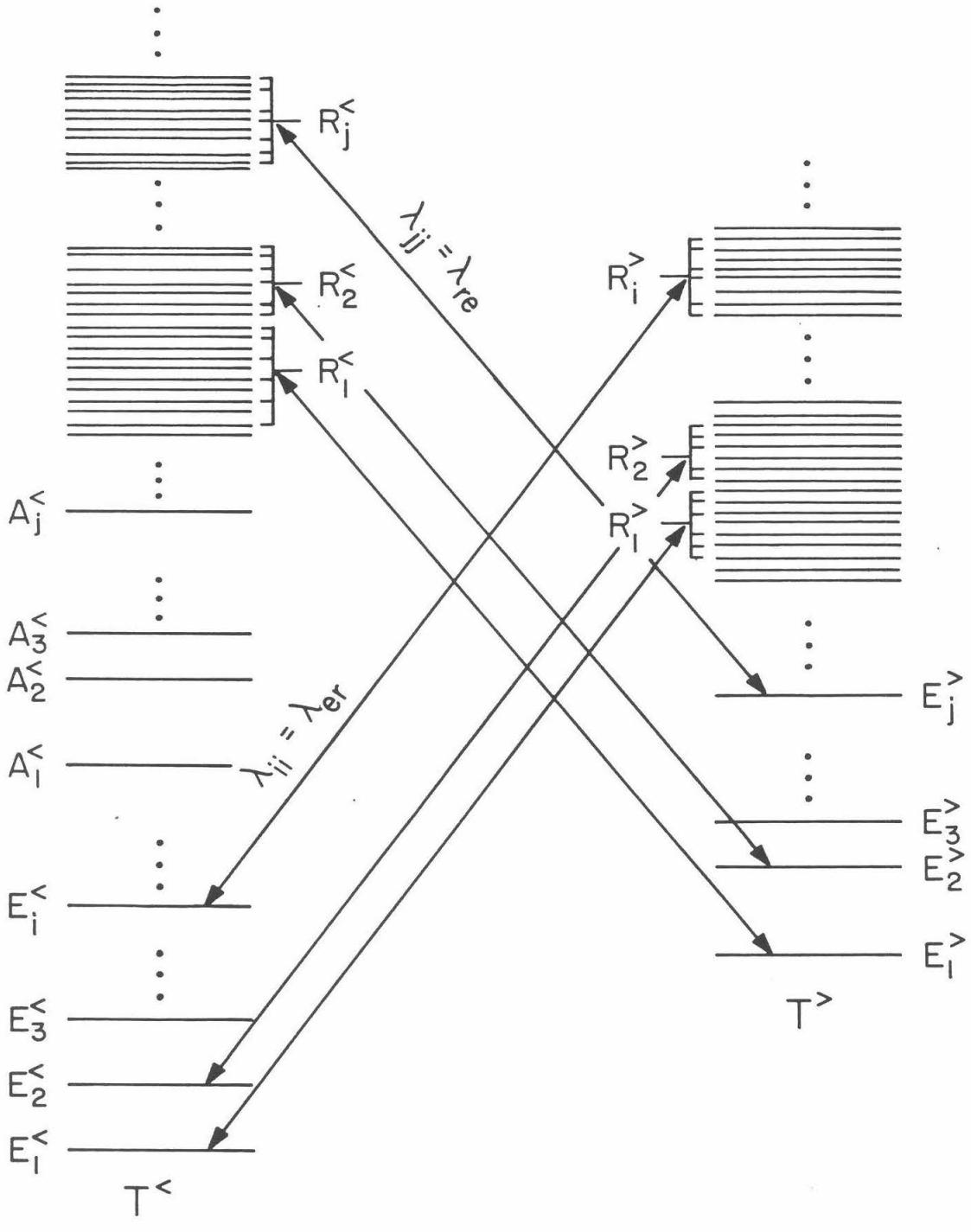
$R_j^<$
$R_2^<$
$R_1^<$
$A_j^<$
$A_3^<$
$A_2^<$
$A_1^<$
$E_i^<$
$E_3^<$
$E_2^<$
$E_1^<$
$T^<$
$\lambda_{ij} = \lambda_{re}$
$\lambda_{ii} = \lambda_{er}$
$R_i^>$
$R_2^>$
$R_1^>$
$E_j^>$
$E_3^>$
$E_2^>$
$E_1^>$
$T^>$

Fig. 1

V. NEUTRON SHELL BLOCKING OF ELECTRON CAPTURE DURING GRAVITATIONAL COLLAPSE

NEUTRON SHELL BLOCKING OF ELECTRON CAPTURE DURING GRAVITATIONAL COLLAPSE[1]

GEORGE M. FULLER[2]

W. K. Kellogg Radiation Laboratory

California Institute of Technology, Pasadena, California 91125

[1]Supported in part by the National Science Foundation [PHY79-23638].

[2]Fannie and John Hertz Foundation Fellow.

ABSTRACT

Current ideas on the nuclear equation of state predict that early on in the collapse of the iron core of a massive star the nuclei present will become so neutron rich that allowed electron capture is blocked. This neutron shell blocking phenomenon and several unblocking mechanisms operative at high temperature and density, including forbidden electron capture, are discussed in terms of the simple shell model. Though the unblocking mechanisms are sensitive to details of the equation of state, typical conditions result in a considerable reduction of the electron capture rates on heavy nuclei leading to dominance of electron capture on free protons and a large decrease in the overall neutronization rate. The results of one-zone collapse calculations are presented which suggest that the effect of neutron shell blocking is to produce a larger core lepton fraction at neutrino trapping which may lead to a larger inner-core mass and hence a stronger post-bounce shock.

Subject headings:

I. INTRODUCTION

The pioneering work by Bethe et al. (1979; hereafter referred to as BBAL) on the nuclear equation of state during gravitational collapse has laid the basis for current models of the core bounce supernova. In particular, great simplification in the equation of state has resulted from the recognition by BBAL that the entropy per nucleon remains of order k (Boltzmann's constant) throughout the collapse and that, as a result, nucleons reside primarily in nuclei right up to nuclear matter density. The general features of this equation of state are confirmed by the work of Lamb et al. (1978; hereafter referred to as L^2PR), Bonche and Vautherin (1981), and El Eid and Hillebrandt (1980).

Since most nucleons reside in nuclei, the question of electron capture rates on heavy nuclei becomes of central importance for determining the overall neutronization rate of the material in the collapsing core. In turn, the neutronization rate helps determine the lepton-to-baryon ratio at neutrino trapping, which is important in determining the inner-core mass and possibly the strength of the shock formed at core bounce (Baym, Bethe, and Brown 1981; Van Riper and Lattimer 1981).

The problem of electron capture on nuclei at high temperature and density has been treated by many authors. Notably, Cameron (1959) pointed out the high temperature, high density enhancement of nuclear electron capture rates due to thermal population of nuclear parent states and the opening of many otherwise unattainable electron capture channels to nuclear daughter excited states at high electron Fermi energy. Fowler and Hoyle (1964) and Hansen (1966) took these effects into account and made use of available experimental information to compile nuclear weak rates for some key nuclear species. Mazurek et al. (1974) extended these

rate tabulations making use of more recent experimental data and taking account of the limitations of the Gamow-Teller sum rule. BBAL pointed out the importance of the low-lying Gamow-Teller resonance in computing $T^{<} \rightarrow T^{>}$ weak transition rates and estimated electron capture rates on heavy nuclei which were approximately 200 times faster than previous estimates. Guided by the BBAL and Klapdor (1976) methods for handling the Gamow-Teller resonance, Fuller, Fowler, and Newman (1981a,b; hereafter referred to as F^2N II and F^2N III) computed and tabulated the weak interaction rates for nuclei with masses between 20 and 60.

F^2N II and F^2N III provide most of the nuclear weak interaction rates, including electron capture, required in calculations of the hydrostatic phases of presupernova evolution through core silicon burning and the onset of core collapse. These rates, together with the beta-equilibrium systematics of Arnett (1977, 1980), should suffice to provide an accurate picture of the nuclear composition and electron to baryon ratio (Y_e) in the core just prior to collapse (Weaver and Woosley 1981, and Arnett and Thielemann 1981). Meanwhile there is already considerable convergence in the calculations of the collapse starting conditions (Arnett 1977, and Weaver, Zimmerman, and Woosley 1978). A 15 $M_\odot$ star will have a core of about 1.5 $M_\odot$ at the onset of collapse with central lepton fraction $Y_e = 0.42$, temperature $T = 0.69$ MeV, density $\rho \approx 3.7 \times 10^9$ g cm^{-3}, and entropy per nucleon $S/k \approx 0.905$.

At the onset of collapse the core consists primarily of iron group nuclei. BBAL took $^{56}Fe \rightarrow {}^{56}Mn$ as being representative of the electron capture characteristics of these nuclei and predicted that the Gamow-Teller resonance in ^{56}Mn corresponding to the ground state of ^{56}Fe is primarily due to one of six $1f_{7/2}$ protons transforming into one of six

$1f_{5/2}$ neutron holes, and should then lie at an excitation energy of 3 MeV in ^{56}Mn based on the $f_{5/2} - f_{7/2}$ spin-orbit splitting and a characteristic particle-hole repulsion energy. Subsequent detailed moment method shell model calculations by Bloom and Fuller (1981) calculate this resonance energy as 2.7 MeV, confirming the BBAL procedure. However, as the collapse proceeds and the material is neutronized the mean nucleus becomes more massive and more neutron rich. Eventually the mean nucleus will have all the neutron fp-shell orbits filled, with valence neutrons filling the gd-orbits, while the valence protons will be filling the fp-shell. In this situation all allowed neutron hole orbits available via the Gamow-Teller operator to protons capturing electrons are filled or, in other words, blocked. When neutron shell blocking sets in for the mean nucleus the electron capture rate for ^{56}Fe $\rightarrow$ ^{56}Mn is no longer representative of typical nuclear electron capture rates. Configuration mixing is discussed later.

The blocking can only be relieved by thermal population of unblocked nuclear configurations, or through first forbidden transitions which are able to change principal nuclear quantum number. Though the effectiveness of these unblocking mechanisms is sensitive to details of the nuclear equation of state, typical conditions discussed in the literature result in a significant reduction of the mean heavy nucleus electron capture rate with a concomitant reduction in the overall neutronization rate. With electron capture on most nuclei blocked, captures on free protons dominate the neutronization rate, with interesting consequences for the electron capture neutrino production spectrum and neutrino mean free path (see Van Riper and Lattimer 1981).

The remainder of this paper focuses on a discussion of electron capture on heavy nuclei and the blocking phenomenon in terms of the simple

shell model, as well as on the unblocking mechanisms; these include spreading of the ensemble of nuclei in nuclear statistical equilibrium to include unblocked nuclei, thermal population of unblocked nuclear configurations, and first forbidden electron capture. Finally, a modified BBAL equation of state, including dripped protons and neutrons, is used to calculate one-zone collapse models with representative values of the blocked electron capture rate. The equation of state and one-zone calculations are compared with the more detailed calculations of Van Riper and Lattimer (1981). The results of these one-zone calculations suggest that the effect of neutron shell blocking is to produce a larger lepton-to-baryon ratio at neutrino trapping, with $Y_e \approx 0.27$ in the core without blocking and $Y_e \approx 0.34$ with the blocking effect. The large lepton fraction after neutrino trapping in turn suggests a larger inner core mass (up to 60% larger) and this may lead to a stronger post-bounce shock.

II. THE SHELL BLOCKING EFFECT

a) Nuclear Electron Capture Rates at High Temperature and Density

The nuclear physics of weak interaction processes involving heavy nuclei at high temperature and density is discussed in some detail in F^2N II and results of that work will be drawn upon here. However, specializing to the problem of electron capture on neutron-rich nuclei during the collapse of the core up to neutrino trapping density, $4 \times 10^9 \leq \rho\ (g/cm^3) \leq 10^{12}$ (Arnett 1977), allows some simplification of the very general F^2N II discussion.

In particular, since electron capture proceeds on neutron-rich nuclei during collapse only $T^< \rightarrow T^>$ transitions need be considered. Where

allowed electron capture is not blocked it dominates over forbidden capture. Of the allowed operators, Gamow-Teller and Fermi, the Gammow-Teller operator mediates almost all allowed electron capture reactions. This is because the Fermi operator is unable to change the total nuclear isospin quantum number, so that a Fermi transition must take place through the thermal population of a $T^>$ isobaric analog state in the $T^<$ parent nucleus. Typically these isobaric analog states in neutron-rich iron group nuclei lie at high excitation energy, 11.44 MeV for ^{56}Fe and $\sim$ 30 MeV for a typical blocked mass 80 nucleus. The probability of thermal population of the isobaric analog state is thus considerably cut down by the Boltzmann factor at the usually assumed collapse temperatures ($\sim$ 1 MeV), though Fermi transitions can be quite important for higher temperatures as discussed in F^2N II.

In general the allowed electron capture rate from the i^{th} state of the parent to the j^{th} state of the daughter is given by equation (1) of F^2N I (hereafter F^2N I equations will be referred to by I-1, etc.),

$$\lambda_{ij} = \ell n\ 2\ \frac{f_{ij}\ (T,\rho,U_F)}{(ft)_{ij}} \qquad (1)$$

where $(ft)_{ij}$ is the comparative half-life, which is related to the allowed weak-interaction matrix elements by equations (I-2a) and (I-2b), and where f_{ij} is the allowed electron capture phase space integral which depends on the temperature T, density ρ, and electron Fermi kinetic energy U_F through the lepton distribution functions.

For the purposes of discussing $T^< \rightarrow T^>$ transitions, only the $T^<$-ground-state $\rightarrow$ $T^>$-resonance transition need be considered for sufficiently high temperature and density, as discussed in F^2N II. In this case the i and j state indices can be dropped to give the phase space factor

$$f = (m_e c^2)^{-5} \int_Q^\infty W^2 (W - Q)^2 \; G \; S_e (1 - S_\nu) \, dW \tag{2}$$

where W is the total electron energy, where S_e and S_ν are the electron and neutrino Fermi-Dirac distribution functions respectively, and where G is the relativistic Coulomb barrier penetration factor given by equations (I-5a) through (I-5f). Since the temperatures and densities of interest here are those of typical collapse conditions <u>before</u> the onset of neutrino trapping, the neutrino phase space blocking factor $(1 - S_\nu)$ can be set to unity. Q is the $T^<$-ground-state $\rightarrow$ $T^>$-resonance nuclear Q-value defined here as

$$Q = M^> c^2 - M^< c^2 + E_R \; , \tag{3}$$

where $M^>$ and $M^<$ are the <u>nuclear</u> masses of the $T^>$ and $T^<$ nuclei respectively, and where E_R is the excitation energy of the Gamow-Teller resonance in the $T^>$-daughter nucleus. Note that equation (2) agrees with the general expression in equation (I-3b) if one makes the identification $\omega_\ell = Q/m_e c^2$ and $q_n = -Q/m_e c^2$.

The electron distribution function S_e in equation (2) is given by equation (I-4a) and is repeated here for clarity as

$$S_e = \left(\exp\left(\frac{W - W_F}{kT} \right) + 1 \right)^{-1} \tag{4}$$

where $W_F = U_F + m_e c^2$ is the total electron Fermi energy (rest plus kinetic) and is hereafter denoted by $\mu_e = W_F$. Throughout the collapse phase considered here the electrons remain relativistically degenerate and so equation (I-4c) becomes

$$\mu_e = \left[1.02 \times 10^{-4} \, (\rho Y_e)^{2/3} + 1\right]^{\frac{1}{2}} \times 0.511 \text{ MeV}$$

$$\approx 5.16 \times 10^{-3} \, (\rho Y_e)^{1/3} = 11.1 \, (\rho_{10} Y_e)^{1/3} \text{ MeV} \tag{5}$$

in the degenerate limit where, following BBAL, $\rho_{10} \equiv \rho \text{ (in g/cm}^3)/10^{10}$.

Taking the degenerate limit in equation (2) and factoring out an average value of the relativistic Coulomb barrier penetration factor G allows the integral to be evaluated explicitly. With $S_e = 1$ for $W \leq \mu_e$ and $S_e = 0$ for $W > \mu_e$, and with the other approximations discussed above, equation (2) becomes

$$f = \langle G \rangle (m_e c^2)^{-5} \int_Q^{\mu_e} W^2 \, (W - Q)^2 \, dW \; ; \tag{6}$$

evaluating the integral yields

$$f = \langle G \rangle \, (u^5/5 - qu^4/2 + q^2 u^3/3 - q^5/30), \tag{7}$$

where $u = \mu_e / m_e c^2$ and $q = Q/m_e c^2$ with $m_e c^2 = 0.511$ MeV.

A similar expression can be derived for the neutrino energy loss phase space factor (which will be required in the equation of state discussed below) by including another factor of the neutrino energy $(W - Q)$ in the integrand of equation (6) to yield

$$f^{\nu} = \langle G \rangle \, (u^6/6 - 3q^5/5 + 3q^2 u^4/4 - q^3 u^3/3) \times (0.511) \text{ MeV} \tag{8}$$

where the notation is as before.

The relativistic Coulomb barrier penetration factor can be expressed in the extreme relativistic limit as (from eq. [I-5e]),

$$G \approx \left(\frac{A^{1/3}}{80.2}\right)^{-\alpha^2 Z^2} \exp(\pi \alpha Z)(W/m_e c^2)^{-\alpha^2 Z^2} \qquad (9)$$

where A is the nuclear mass number, Z the nuclear charge, $\alpha \approx 1/137$ the fine structure constant, and W the electron energy. For $\alpha Z < 1$

$$\langle G \rangle \approx \exp(\pi \alpha Z) \ , \qquad (10)$$

so that for a free proton $\langle G \rangle \approx 1$ and for a typical heavy nucleus with Z = 30, $\langle G \rangle \approx 2$. The nuclear radius used in (9) is $R = 1.23\ A^{1/3}$ fermi.

For free protons the electron capture reaction $e^- + p \rightarrow n + \nu_e$ has Q = 1.297 MeV, the neutron-proton mass difference [note: more accurately $m_n - m_p = 1.293$ MeV but the 1.297 value is adopted here to facilitate comparison with BBAL and Van Riper and Lattimer (1981) both of which use this value] so that q = 2.538 in equations (7) and (8). Both Fermi and Gamow-Teller matrix elements contribute in this reaction with $|M_F|^2 = 1$ and $|M_{GT}|^2 = 3$, so that using

$$(\log ft)_{GT} = 3.596 - \log |M_{GT}|^2 \ ; \ (\log ft)_F = 3.791 - \log |M_F|^2 \ , \qquad (11)$$

from F^2N I and combining the ft-values in the manner discussed in F^2N II yields for the total ft-value

$$\log (ft)_{f.p.} = 3.035. \qquad (12)$$

Calculation of the electron capture Q-value for heavy nuclei involves an estimate of the $T^< \rightarrow T^>$ Gamow-Teller resonance excitation energy, while an estimate of the overall resonance ft-value requires an explicit Gamow-Teller sum rule. Both of these quantities can be estimated using a simple shell model for the capturing nucleus, as was discussed in F^2N II,

and such simple shell models lead to the prediction of neutron shell blocking.

b) The Gamow-Teller Sum Rule and Neutron Shell Blocking

The zero-order shell model together with the tabulated single particle energies of Seeger and Perisho (1967) and Seeger and Howard (1975) were used in F^2N II to estimate the Gamow-Teller sum rules and resonance excitation energies for $T^< \rightleftarrows T^>$ transitions. For the case of $T^< \rightarrow T^>$ transitions of interest in the collapse problem a zero-order shell model diagram for the $T^<$-parent nucleus is constructed using the single particle neutron and proton orbit energy orderings of Seeger and Perisho (1967). The allowed spin-flip transitions, if any, are made and the resulting excited $T^>$-daughter configuration is compared with that of the zero-order $T^>$-ground state configuration; particle excitations and nucleon-pair breakings are noted. The resonance excitation energy is then estimated as the sum of the appropriate single-particle orbit energy differences and pairing energies, $\Delta E_{pair} = 12/\sqrt{A}$ MeV (A = nuclear mass number), and a particle-hole repulsion energy argued in F^2N II to be approximately 2.0 MeV. In the $^{56}_{26}Fe_{30} \rightarrow {}^{56}_{25}Mn_{31}$ transition, for instance, one of six $1f_{7/2}$ protons transforms into one of six $1f_{5/2}$ neutron holes, so that the resulting excited ^{56}Mn resonance configuration differs from the zero-order ^{56}Mn ground state by

$$E_R(^{56}Mn) = \left[\varepsilon(1f_{5/2}) - \varepsilon(2p_{3/2})\right]_{neutron} + 2.0 \qquad (13)$$

$$= 3.777 \text{ MeV}.$$

The relevant Gamow-Teller operator for $T^< \rightarrow T^>$ transitions is

$$GT = \sum_n \vec{\sigma}_n \, \tau_n^- \tag{14}$$

where $\vec{\sigma}$ is the Pauli spin operator, τ^- is the isospin lowering operator (here $\tau_z^p = 1/2$, $\tau_z^n = -1/2$) and the sum is over all nucleons in the nucleus. This operator is clearly an isovector and spatial vector and hence has selection rules $\Delta T = 0, \pm 1$; $\Delta J = 0, \pm 1$; no $0 \to 0$; since $\vec{\sigma}\tau^-$ has no dependence on the radial coordinate Gamow-Teller cannot change orbital angular momentum, principal quantum number or parity ($\Delta\pi = 0$).

In F^2N II it was shown that the sum rule for this operator and an initial configuration with $(n_p)_i$ proton particles in single-particle orbit i and $(n_h)_f$ neutron-holes in single-particle orbit f is

$$|M_{GT}|^2 = \sum_{if} \frac{(n_p)_i \, (n_h)_f}{2j_f + 1} \cdot |M_{GT}^{sp}|^2_{if} \tag{15}$$

where j_f is the spin of the final neutron orbit and where $|M_{GT}^{sp}|^2_{if}$ is the appropriate single-particle Gamow-Teller matrix element between single-particle orbits i and f (see Table 1 in F^2N II). Note that $(n_h)_f/2j_f + 1$ is the fractional number of neutron-holes available in single-particle orbit f. In the example of $^{56}_{26}Fe_{30} \to {}^{56}_{25}Mn_{31}$, $n_p = 6$ protons ($1f_{7/2}$) can transform into $n_h = 6$ neutron holes ($1f_{5/2}$) with $|M_{GT}^{sp}|^2 = 12/7$. In principle Gamow-Teller allows $1f_{7/2} \to 1f_{7/2}$ transitions, but the neutron $1f_{7/2}$ orbit is completely filled, or blocked, and has $n_h = 0$ and thus makes no contribution to the equation (15) sum. For the $^{56}Fe \to {}^{56}Mn$ case equation (15) reduces to $|M_{GT}|^2 = (6 \cdot 6/6) \cdot 12/7 = 72/7$, which by equation (11) implies log ft = 2.58, very close to the effective matrix element used for all heavy nuclei in BBAL and worth remembering for comparison with the effective matrix elements for blocked nuclei discussed below (the actual Fermi gas electron capture formula used by BBAL uses an effective $|M_{GT}|^2$ somewhat smaller than 72/7, more like $|M_{GT}|^2 \sim 3\text{-}4$).

As the collapse proceeds from its starting point, where the average $T^{<} \rightarrow T^{>}$ transition is like $^{56}Fe \rightarrow {}^{56}Mn$, the density increases (Y_e decreases) to a point where the average capturing nucleus is so neutron rich that while the valence protons are still filling proton fp-shell orbits ($1f_{7/2}$, $1f_{5/2}$, $2p_{3/2}$, $2p_{1/2}$) all the corresponding neutron orbits are filled and the valence neutrons are filling orbits in the neutron gd-shell. In such a situation, for each proton orbit i all $(n_h)_f = 0$ for which there exists a nonzero $|M_{GT}^{sp}|^2_{if}$ and thus equation (15) gives $|M_{GT}|^2 = 0$. The only available neutron holes are in gd-orbits, but since fp-orbit $\rightarrow$ gd-orbit transitions involve a change of parity they cannot be mediated by the Gamow-Teller operator. This is an example of neutron shell blocking for $T^{<} \rightarrow T^{>}$ transitions; blocking occurs whenever nuclear neutron number $N \geq 40$ and nuclear proton number $Z \leq 40$. If the zero-order shell model picture of the nucleus is absolutely correct then the blocked $T^{<} \rightarrow T^{>}$ transition is at best a first forbidden transition, since forbidden operators explicitly involve the radial coordinate and can change principle quantum number, orbital angular momentum, and thus parity. The first forbidden transition will be discussed in detail below as a possible unblocking mechanism.

The density and electron-to-baryon ratio at which blocking sets in for the mean nucleus is defined as the blocking point. As discussed below this blocking point depends on the parameters of the equation of state. However, in order to illustrate the blocking phenomenon it is convenient to jump ahead of the forthcoming discussion and to select for study the calculated mean nucleus in one of the one-zone collapse calculations performed with the modified BBAL equation of state. In one of those calculations at $\rho_{10} = 9.867$, $Y_e = 0.409$, $kT = 1.15$ MeV, shortly after the

blocking point is reached, the mean nucleus is $^{74}_{32}Ge_{42}$. The characteristic heavy nucleus electron capture reaction is then $e^- + {}^{74}_{32}Ge_{42} \rightarrow {}^{74}_{31}Ga_{43} + \nu_e$, which has allowed electron capture blocked in the zero-order shell model. The zero-order shell model diagram for ^{74}Ge is shown in Figure 1, where the ordering of neutron and proton orbits follows the tabulation of Seeger and Howard (1975) and Seeger and Perisho (1967). The figure indicates the allowed (blocked) and first forbidden transitions for each occupied proton fp-shell orbit. Note that both the no-spin-flip $1f_{7/2} \rightarrow 1f_{7/2}$ and $1f_{5/2} \rightarrow 1f_{5/2}$ transitions are blocked, as is the spin-flip transition $1f_{7/2} \rightarrow 1f_{5/2}$. Though not explicitly shown, the back-spin-flip $1f_{5/2} \rightarrow 1f_{7/2}$ transition is also clearly blocked. The approximate scales of electron Fermi energy, μ_e, temperature, and single-particle energies are illustrated in the figure for the conditions where ^{74}Ge is the mean nucleus.

The ground state configuration for ^{74}Ge is in reality more complicated than that given by the zero-order shell model. The residual nucleon-nucleon interaction serves to mix many such simple shell model configurations into the ^{74}Ge ground state, including unblocked configurations. However, it is clear from Figure 1 that a substantial excitation energy penalty is paid in producing unblocked configurations, and thus it is argued that the ground state of ^{74}Ge is predominantly given by the zero-order shell model configuration. The simplest unblocked ^{74}Ge configuration can be built from the Figure 1 ground state by the excitation of a $1f_{5/2}$ neutron to the $1g_{9/2}$ shell. The excitation energy of this excited configuration can be estimated with the method discussed above to give

$$E(^{74}\text{Ge UNBLOCKED}) = \left(\varepsilon(1g_{9/2}) - \varepsilon(1f_{5/2})\right) + \frac{12}{\sqrt{74}} + 2.0 = 5.13 \text{ MeV} \quad (16)$$

The effect of thermal population of such unblocked configurations is discussed below.

Note, however, that the excitation energy of the first unblocked configuration can depend sensitively on the energy ordering of the single-particle orbits. Though the Seeger and Howard (1975) orderings are adopted here (on the basis of completeness and most recent data) the Nilsson (1955) orderings would place the proton $2p_{3/2}$ shell below the proton $1f_{5/2}$ shell. Were this the case for ^{74}Ge, an unblocked configuration could be constructed by promoting a $2p_{1/2}$ neutron to the $1g_{9/2}$ neutron shell, allowing a $2p_{3/2} \rightarrow 2p_{1/2}$ spin-flip transition. This unblocked configuration would have a lower excitation energy than the equation (16) result. These considerations are important for just-blocked nuclei and become less important as the blocking becomes more severe.

The Bloom and Fuller (1981) shell model calculations of the beta strength functions for the iron isotopes give an idea of the extent of configuration mixing unblocking for ^{64}Fe which, with 38 neutrons, is just barely blocked in the zero-order Seeger shell model. Though the equation (15) sum rule would predict $|M_{GT}|^2 = 0$ in the zero-order model, Bloom and Fuller found $|M_{GT}|^2 = 1.06$, which is still a small matrix element by typical iron-group nucleus standards.

III. THE ONSET AND EFFECTIVENESS OF BLOCKING

a) Nuclear Statistical Equilibrium and the Mean Nucleus

The equation of state adopted here for the calculation of the mean nucleus and for the one-zone collapse calculations discussed below is similar to that of BBAL. When the temperature climbs above a few $\times 10^9$ K strong and electromagnetic reactions come into equilibrium and the ensemble of nuclear species present, the pressure and adiabatic index can all be calculated via statistical techniques. The BBAL equation of state makes use of this equilibrium and the large values of the nuclear partition function at high temperatures to approximate the ensemble of nuclear species present as a mean heavy nucleus and a sea of dripped neutrons. The equilibrium conditions are those appropriate for a compressible liquid drop model of the nucleus: neutron and proton chemical potentials inside nuclei are equal to their respective outside values, while the pressure is similarly continuous, and charge is conserved. A complete discussion of the equilibrium problem for neutron star matter is given by Baym, Bethe, and Pethick (1971) (hereafter referred to as BBP), but unlike that work beta equilibrium does not obtain in the initial phase of stellar core collapse, and there is thus no simple relation between the electron chemical potential (μ_e) and the neutron and proton chemical potentials (μ_n and μ_p respectively). The BBAL results are, however, based on the simple model of the energy of bulk nuclear matter, the nuclear surface energy, and the nuclear Coulomb and lattice energies derived in BBP.

The neutron chemical potential is defined here as

$$\mu_n \equiv \left(\frac{\partial E}{\partial N_n}\right)\Bigg|_{S,V} - m_n c^2 \qquad (17)$$

where E is the total energy of the system, N_n is the total number of neutrons, and the derivative is taken while holding the total volume and entropy of the system constant. An analogous expression holds for the proton chemical potential. Note that the BBP convention of not including the nucleon rest mass in the appropriate nucleon chemical potential is adopted here, while the electron chemical potential in equation (5) does include the electron rest mass. Simple thermodynamics indicates that the chemical potential in a nondegenerate system is usually negative, since an increase in the number of particles at fixed volume would increase the entropy unless energy were removed from the system, $dE < 0$. This is the situation for the nondegenerate sea of dripped nucleons during collapse. However, nuclei are clearly degenerate systems where the nucleon Fermi energies inside nuclei are large and positive, on the order of 40 MeV. The nucleon chemical potentials inside nuclei are negative, however, since the nucleons move in a deep collective potential well ($\sim$ 50 MeV), and the value of this potential energy must be subtracted from the otherwise positive chemical potentials characteristic of degenerate bulk nuclear matter.

Following BBP equation (2.4) the total energy per unit volume of the system can be written as

$$E_{tot}(Y_e,\rho_N,V_N,u,n_N,n_n) = n_N(W_N + W_L) + (1 - u)\, E_n(n_n) + E_e(n_e) \qquad (18)$$

where Y_e is the electron/baryon ratio, ρ_N is the density inside nuclei, and V_N is the nuclear volume ($A = \rho_N V_N$), $u = \rho/\rho_N$ is the fraction of the total volume occupied by nuclei, n_N and n_n are the number densities of nuclei and neutrons respectively, E_n and E_e are the energy densities of the dripped neutron gas and the degenerate electron gas respectively, W_N is the total energy of a single nucleus and W_L is the coulomb lattice energy. Dripped protons are not important for the overall energetics of

the system. The energy of a nucleus can be expanded in the usual liquid drop model method to yield, following BBAL equation (4.1),

$$W_N(Y_e,\rho_N,V_N,u) = W_{bulk} + W_{surf}\, A^{2/3} + W_{coul}\, A^{5/3} \tag{19}$$

where again $A = \rho_N V_N$ is the nuclear atomic number, W_{surf} and W_{coul} are the coefficients of the surface and Coulomb energies, respectively, and each coefficient depends on Y_e, ρ_N, V_N, u, and n_n. The energy of bulk nuclear matter is dependent on the proton-to-neutron ratio (i.e., the symmetry energy) and the overall density and is discussed at length in BBP.

The BBAL values of W_{coul} and W_{surf} are adopted here,

$$W_{surf} = 290\ Y_e^{\,2}(1 - Y_e)^2 \tag{20}$$

$$W_{coul} = 0.75\ Y_e^{\,2}(1 - 0.236\ \rho_{12}^{1/2} + 0.00194\ \rho_{12}) \tag{21}$$

where $\rho_{12} \equiv \rho\ (\text{in g cm}^{-3})/10^{12}$. The value of the mean nuclear mass A is then derived from the condition that the nuclear surface energy is twice the Coulomb energy, which yields

$$A = 194\ (1 - Y_e)^2\ (1 - 0.236\ \rho_{12}^{1/2})^{-1}\ . \tag{22}$$

Taking the derivative of the energy of a nucleus in equation (17) gives

$$\mu_n = \left.\frac{\partial(W_N + W_L)}{\partial A}\right|_{Z,V_N,u,S,V}\ , \tag{23}$$

while noting that $dA = -(A/Y_e)dY_e + V_N d\rho_N$ (for constant Z) gives

$$\mu_n = \frac{1}{V_N}\left.\frac{\partial(W_N + W_L)}{\partial \rho_N}\right|_{Y_e,V_N,u} - \frac{Y_e}{A}\left(\left.\frac{\partial(W_N + W_L)}{\partial Y_e}\right)\right|_{\rho_N,V_N,u}\ . \tag{24}$$

Similarly noting that for constant A-Z, $dZ = (A/(1 - Y_e))dY_e$ gives

$$\mu_p = \frac{1}{V_N} \left.\frac{\partial(W_N + W_L)}{\partial \rho_N}\right|_{Y_e, V_N, u} + \frac{1 - Y_e}{A} \left.\frac{\partial(W_N + W_L)}{\partial Y_e}\right|_{\rho_N, V_N, u} , \qquad (25)$$

so that the important neutron-proton chemical potential difference $\hat{\mu}$ is given by

$$\hat{\mu} \equiv \mu_n - \mu_p = - \frac{1}{A} \frac{\partial(W_N + W_L)}{\partial Y_e} . \qquad (26)$$

The neutron-proton chemical potential difference can be thought of as roughly the difference in the neutron and proton Fermi levels in a nucleus. In the one-zone calculations which follow $\hat{\mu}$ is taken to be the value given by BBAL,

$$\hat{\mu} = 250(0.5 - Y_e) - W_{surf} A^{-1/3} \left(\frac{1}{Y_e} + \frac{2}{Y_e} \frac{1 - 2Y_e}{1 - Y_e} \right) . \qquad (27)$$

The neutron chemical potential is here taken from Lattimer (1980),

$$\mu_n = -16 + 125 \left(\frac{1}{2} - Y_e\right) - 125 \left(\frac{1}{2} - Y_e\right)^2 - \frac{W_{surf}}{A^{1/3}} \frac{3 - 7Y_e}{2(1 - Y_e)} - \frac{1}{4} \frac{W_{surf}}{A^{1/2}} u^{1/3} \frac{(1 - u^{2/3})}{(1 - 3/2\, u^{1/3} + 1/2\, u)} . \qquad (28)$$

In the one-zone calculations which follow, the last term in the equation (28) expression for μ_n is neglected since the fraction of the total volume occupied by nuclei, u, is small. The one-zone collapse calculations thus use

$$\mu_n = -16 + 125(0.5 - Y_e) - 125(0.5 - Y_e)^2 - \frac{W_{surf}}{A^{1/3}} \frac{3 - 7Y_e}{2(1 - Y_e)} . \qquad (29)$$

This expression for μ_n yields a numerical value roughly 2 MeV larger than the BBAL calculations over most of the density and Y_e range encountered in the one-zone collapse models. As shown below, the free nucleon number densities are sensitive functions of μ_n and thus the larger value of μ_n used here results in a considerably larger free nucleon number density than that found by BBAL, in fact redressing the disparity in free nucleon abundance found by BBAL and El Eid and Hillebrandt (1980). Neglect of the last term in equation (28) makes a negligible difference in free nucleon abundance in the one-zone collapse calculations for $\rho < 10^{11}$ g cm^{-3}, and at larger densities μ_n becomes between 0.1 and 0.2 MeV smaller, making roughly a 10% decrease in free nucleon abundance which is well within other errors in the problem.

The mass fraction of free neutrons X_n (neutron-to-baryon ratio) is derived from the condition of equal abundances for very heavy neutron-rich nuclei differing by one unit in neutron number, and is here taken as

$$X_n = 79 \frac{T^{3/2}}{\rho_{10}} \exp(\mu_n/T) \ , \tag{30}$$

where the temperature, T, is expressed in MeV. Using the Saha equation gives the free proton mass fraction X_p (free proton-to-baryon ratio),

$$X_p = X_n \cdot \exp(-\hat{\mu}/T) \ , \tag{31}$$

with the notation as before. It is thus clear that for the typical values of $\hat{\mu}$ encountered for neutron-rich nuclei during collapse the free proton concentration will be a small fraction of the free neutron concentration. Over the range of density and lepton fraction encountered in the one-zone collapse calculations presented below $X_n \lesssim$ 10-20% while $X_p \sim 10^{-3}$-10^{-4}, and this is similar to the results of Van Riper and Lattimer (1981).

The modified BBAL equation of state is thus complete and its application to the one-zone collapse calculations with blocking and electron capture on free protons will be discussed. However, it is first necessary to evaluate at length the approximations inherent in this equation of state, as they bear on the onset and effectiveness of the blocking mechanism.

As outlined above, the modified BBAL equation of state approximates the ensemble of nuclear species present during the collapse phase as a mean heavy nucleus, a sea of dripped neutrons, and a smaller sea of dripped protons. In fact, many nuclear species will be in equilibrium with each other and with the dripped nucleons at high temperature and density. The equilibrium conditions for a large ensemble of nuclei is as above: at constant temperature and pressure the Gibbs potential must be a minimum and thus the chemical potentials of all species are related by their appropriate reaction weights. Approximating the nuclear chemical potentials by their perfect gas values yields the Saha equation for the mass fraction of nucleus A(Z,N) with Z protons and N neutrons,

$$X(N,Z) = \frac{G(N,Z)}{\rho N_A} A^{\frac{5}{2}} \left[\frac{2\pi\hbar^2 N_A}{kT}\right]^{\frac{3}{2}(A-1)} \left(\frac{\rho N_A X_n}{A_n}\right)^N \left(\frac{\rho N_A X_p}{A_p}\right)^Z 2^{-A} \exp(Q(N,Z)/kT) \quad (32)$$

with $A_n = 1.00866$ and $A_p = 1.007825$ the neutron and proton atomic masses respectively, N_A Avogadro's number, $G(N,Z)$ the high temperature nuclear partition function, and $Q(N,Z)$ the nuclear Q-value for the reaction $N(\text{neutrons}) + Z(\text{protons}) \rightarrow A(Z,N)$ (see Burbidge et al. 1957). Equation (32) can be simplified as

$$X(N,Z) \approx G(N,Z) \frac{A^{\frac{5}{2}}}{2^A} \left[\frac{1.013 \times 10^{-10} \rho}{T_9^{\frac{3}{2}}}\right]^{A-1} \left(\frac{X_n}{A_n}\right)^N \left(\frac{X_p}{A_p}\right)^Z \exp\left(\frac{11.605\ Q(N,Z)}{T_9}\right) \quad (33)$$

where the temperature is $T_9 \equiv T(K)/10^9$ and Q is in MeV. The nuclear Q-value is, neglecting atomic binding energies,

$$Q(N,Z) = 8.0714\ N + 7.2890\ Z - \Delta(N,Z), \qquad (34)$$

where $\Delta(N,Z)$ is the atomic mass excess.

The modified BBAL equation of state predicts a mean nucleus which should be thought of as representative of the large ensemble of nuclear species obtained by the global solution of equation (33). As the temperature increases for a given ρ and Y_e this nuclear distribution will become more spread out, eventually encompassing nuclei whose electron capture properties may be significantly different from the mean nucleus. The relevant question becomes whether or not, when the mean nucleus is blocked, a significant fraction of the protons bound in nuclei are in unblocked nuclear species.

Equation (33) can be used to study the sharpness of the ensemble peak near the mean nucleus for various temperatures, densities, and electron-to-baryon ratios. First consider moving along an isobaric (constant nuclear mass number, A) path in the (N,Z) plane, studying the gradient in mass fractions as the path heads away from the mean nucleus and toward the terrestrial valley of β-stability. It is clear that the mean-nucleus-peak is quite steep along such a path since protons must be added and neutrons subtracted; though the nuclear Q-values in equation (33) usually favor a motion toward decreasing neutron richness (through the symmetry energy), the addition of each extra proton means an extra factor of X_p, a very small number, which usually swamps any increase in abundance due to the exponential involving the Q-value. If, for example, $^{66}_{28}Ni_{38}$ is the blocked mean nucleus at kT = 0.70 MeV, $Y_e = 0.42$, and $\rho = 3 \times 10^9$ g cm^{-3} then the

nearest even-even unblocked nucleus along the isobaric path is $^{66}_{30}Zn_{36}$ and equation (33) gives

$$\frac{X(^{66}Zn)}{X(^{66}Ni)} = \left(\frac{X_p}{X_n}\right)^2 \frac{G(^{66}Zn)}{G(^{66}Ni)} \exp\left(\frac{\Delta Q}{kT}\right) \approx \exp\left(\frac{-2\hat{\mu} + 1.312}{kT}\right) \sim 10^{-8} \qquad (35)$$

where equation (31) has been used to re-express the ratio (X_p/X_n) in terms of $\hat{\mu}$, the partition functions of ^{66}Zn and ^{66}Ni are taken to be equal (Woosley et al. 1978, hereafter WFHZ), and where the expression is estimated using a standard table of nuclear binding energies (Wapstra and Bos 1977) and the value $\hat{\mu} \approx 4.3$ MeV from the modified BBAL equation of state. For the large values of $\hat{\mu}$ in the collapsing core the nuclear mass fractions along the isobaric path fall off very steeply from the mean nucleus.

In contrast, for a neutron-rich mean nucleus at high temperature and density, it is relatively easy to add or remove a neutron and not change the resultant nuclear mass fraction by a large factor. This is because the neutron mass fraction X_n is relatively much larger than X_p and hence does not as easily overcome the Q-value enhancement factor gained by moving toward less neutron-rich, unblocked nuclei. For the conditions $\rho_{10} = 9.868$, $Y_e = 0.4089$, $T_9 = 13.34$, $\hat{\mu} = 5.012$, $X_n = 0.02389$, $X_p = 3.055 \times 10^{-4}$, from one of the one-zone collapse calculations discussed below, the mean nucleus is predicted to be $^{74}_{32}Ge_{42}$ so that the nearest unblocked isotope is, using the single particle orbit orderings discussed above, $^{69}_{32}Ge_{37}$. Equation (33) can be used to estimate the mass fraction ratios of the unblocked and blocked nuclei for the above conditions

$$\frac{X(^{69}Ge)}{X(^{74}Ge)} \approx (4 \times 10^{-5}) \frac{G(^{69}Ge)}{G(^{74}Ge)} \sim 10^{-4} \qquad (36)$$

where the ratio of partition functions is of order unity (WFHZ). If now,

for the same conditions, the mass fraction ratio is calculated for ^{74}Ge and an even more neutron-rich isotope, $^{78}_{32}Ge_{46}$, then equation (33) yields

$$\frac{X(^{78}Ge)}{X(^{74}Ge)} \approx (16.18)\ \frac{G(^{78}Ge)}{G(^{74}Ge)} \sim 10 \qquad (37)$$

where the WFHZ partition functions are used. ^{74}Ge is the mean nucleus calculated from (22). It is not necessarily the most abundant nucleus when actual Q-values are used in (33). But from (37) it is clear that it is easier to add neutrons to the mean blocked nucleus than it is to remove enough to unblock, at least for the conditions near $\rho \approx 10^{11}$, $Y_e \approx 0.41$. For these conditions it would seem relatively difficult for the spread in the ensemble of nuclear species to affect significant unblocking.

In principle a global solution to equation (33) could give the abundances of all nuclear species in nuclear statistical equilibrium and thus answer any question involving the fraction of unblocked protons in nuclei. This is, however, very difficult and beyond the scope of this paper, both because a very large network of nuclei would have to be employed and because such a global solution would require a very accurate expression for nuclear partition functions in just the range of temperatures where the standard partition function works are not accurate: T too high for WFHZ and too low for the statistical treatment of Tubbs and Koonin (1979) to be effective.

Nuclear statistical equilibrium network calculations performed in the past and using the best partition function prescriptions then available clearly show a two humped distribution with one peak centered on ^{48}Ca and one centered on a nucleus nearer the BBAL mean, ^{74}Ge, for $\rho \approx 10^{11}$ g cm^{-3}, $Y_e \approx 0.409$, kT $\sim$ 1 MeV (see e.g., Tsuruta and Cameron 1965). Such a two-peaked distribution of nuclear species will be adopted here for the purposes of estimating thermal unblocking. For the

$\rho_{10} = 9.868$, $Y_e = 0.4089$, kT = 1.15 MeV conditions cited above it is useful to estimate the mass fractions of n, p, α, ^{48}Ca, and the nuclei in the ^{74}Ge peak, but to do this requires a brief discussion of the nuclear partition function which will be done below in connection with the discussion of thermal unblocking.

The one-zone collapse calculations presented below predict that the mean nucleus is blocked very early in the collapse $\rho \approx 4 \times 10^9$ g cm^{-3} and $Y_e \approx 0.42$ (note for the mean nucleus $Z/A \approx Y_e/(1 - X_n)$. This is contradicted by more detailed nuclear statistical equilibrium calculations (e.g., Weaver and Woosley 1980) and by hydrodynamic collapse calculations performed with the full L^2PR equation of state by Van Riper and Lattimer (1981). Both Van Riper and Lattimer (1981) with the L^2PR equation of state and Bowers and Wilson (1980) with another equation of state predict that for the same initial adiabat employed in the one-zone collapse calculations in this paper the mean nucleus will not be blocked until $\rho \approx 10^{11}$ g cm^{-3}. This is not greatly at odds with the results presented here since roughly 90% of the neutronization (Y_e drop) occurs during the collapse between $\rho \approx 10^{11}$ g cm^{-3} and neutrino trapping density $\rho \gtrsim 6 \times 10^{11}$ g cm^{-3}. Van Riper and Lattimer (1981) blocked electron capture on heavy nuclei when the L^2PR mean nucleus reached a neutron number of 40 (as discussed above for $Z \leq 34$ blocking technically occurs for the even smaller $N \geq 38$) which for a typical adiabat and neutrino optical depth parameter occurred for $\rho \approx 7.5 \times 10^{10}$ g cm^{-3}. For extremely high temperatures those authors found that the L^2PR mean nucleus became considerably smaller and for collapse from initial conditions with high enough entropy the mean nucleus never became blocked. The reader is referred to Van Riper and Lattimer for an in depth discussion of this point.

Given that the mean nucleus does become blocked, the above discussion indicates that there will be some unblocking from the spreading of the ensemble of nuclei in nuclear statistical equilibrium to include unblocked nuclei. Potentially more important to the overall neutronization rate is the thermal population of unblocked configurations in blocked nuclei. Both of these effects will be combined in the following section to estimate an effective Gamow-Teller electron capture matrix element for heavy nuclei.

b) Thermal Unblocking

An examination of the Gamow-Teller sum rule, equation (15), shows that the smallest overall electron capture Gamow-Teller strength that a nucleus can have occurs for its zero-order shell model ground state; excited configurations built from both neutron and proton particle-hole excitations always have larger Gamow-Teller strengths. As the temperature rises in the collapsing stellar core these excited nuclear configurations become more easily populated and thus the average effective nuclear Gamow-Teller strength grows. In the limit of extremely high temperature, where the occupation probabilities of all single particle orbits in the nucleus become small, the fraction of neutron holes available to protons capturing electrons goes to unity, and equation (15) indicates

$$|M_{GT}|^2 \xrightarrow[T \to \infty]{} 3Z \ , \quad |M_F|^2 \xrightarrow[T \to \infty]{} Z \tag{38}$$

for a nucleus of charge Z. Thus, each proton in the nucleus will behave as a free proton, with the free proton allowed matrix elements $|M_F|^2 = 1$,

$|M_{GT}|^2 = 3$ as the temperature becomes extremely large. The discussion in F^{2}N II suggests that this free-proton-limit temperature occurs for $T \sim 10\text{-}30$ MeV. This is the β-strength catastrophe. Practically, for temperatures this high, nuclei would dissolve into free nucleons in the relatively low densities encountered before neutrino trapping during the collapse.

Fortunately, it is unlikely that such high temperatures will be reached during this initial collapse phase; the capture of electrons on free protons at high electron Fermi energy produces very energetic neutrinos which serve to cool the matter before neutrino trapping. Van Riper and Lattimer (1981) even discuss a sort of feedback process: were the temperature high the mean nuclear size would be smaller, and thus the neutrino-nucleus coherent scattering cross section is smaller, implying lower overall neutrino opacities and a higher neutrino trapping density, thus allowing more neutrinos to escape at later collapse epochs, significantly adding to the cooling of the core material. The effect of added neutrino cooling due to electron capture on free protons will be pointed out in the one-zone collapse calculations below. Still, the average Gamow-Teller strength available for electron capture on heavy nuclei depends sensitively on the temperature. Some typical collapse conditions and simple shell model arguments can be used to estimate the value of this effective Gamow-Teller matrix element for use in the one-zone collapse models.

In the last section the ensemble of nuclei in nuclear statistical equilibrium was taken to be a two-peaked distribution; for $Y_e \approx 0.41$, $\rho \approx 10^{11}$ g cm^{-3}, and kT $\sim$ 1.2 MeV there was a small peak at ^{48}Ca and a much larger peak at ^{74}Ge. In addition, the ensemble of nuclear species

was taken to include free neutrons and protons and alpha particles. A simplified form of the nuclear partition function can be used to estimate the mass fractions of each of these species in equilibrium at high temperature with equation (33).

The nuclear partition function is defined as

$$G(N,Z) = \sum_{i} (2J_i + 1)\, e^{-E_i/kT} \tag{39}$$

where the sum is over all nuclear states, J_i and E_i are the spin and excitation energy of the i^{th} state respectively. Following WFHZ this partition function can be approximated as

$$G(N,Z) = \sum_{i=1}^{d} (2J_i + 1)\, e^{-E_i/kT} + \int_{E_d}^{\infty} \rho(E)\, \exp(-E/kT)\, dE \tag{40}$$

where the sum is over the first d discrete nuclear levels and the energy integral is over the level density $\rho(E)$, from the energy of the last discrete level E_d, into the continuum. The level density is usually taken to be of the form

$$\rho(E) = \frac{\pi^{1/2}}{12} \frac{\exp\left(2(aU)^{1/2}\right)}{a^{1/4}\, U^{5/4}} \tag{41}$$

where U is related to the excitation energy E by a backshifting parameter δ,

$$U = E - \delta\ . \tag{42}$$

With such a form for the level density the integral in equation (40) can be performed to yield

$$G(N,Z) \approx \sum_{i=1}^{d} (2J_i + 1)\, e^{-E_i/kT} + \frac{\pi}{6akT} \exp\left(akT - \frac{\delta}{kT} - \frac{E_d}{kT}\right) \quad . \tag{43}$$

This expression can be further approximated by taking $E_d = 0$, thereby eliminating the sum over discrete levels in equation (40) to give the continuum covering case

$$G(N,Z) \approx \frac{\pi}{6akT} \exp(akT - \delta/kT). \tag{44}$$

The parameters a and δ can be obtained in WHFZ to give an estimate of the partition function using equation (44) or, if a few discrete states are employed, equation (43). Tubbs and Koonin (1979) show that continuum subtraction effects are not yet very important for $kT \lesssim 2$ MeV.

The above expressions can now be used to estimate the mass fractions of the principal nuclear species at the one-zone collapse point ρ_{10} = 9.868, kT = 1.150 MeV, Y_e = 0.4089, $\hat{\mu}$ = 5.012 MeV, X_n = 0.02390, X_p = 3.055×10^{-4}. This point in the collapse will be hereafter referred to as the blocking point, since it is on the order of the blocking density used by Van Riper and Lattimer (1981). The ^{48}Ca partition function is difficult to calculate accurately at this temperature, but summing over all discrete states up to an excitation energy of 7.659 MeV (Lederer et al. 1978) and making cogent estimates of the contribution of higher lying states gives,

$$G(^{48}\text{Ca}) \approx 2.70. \tag{45}$$

Using the ^{48}Ca atomic Q-value of 416.0134 MeV, and correcting for atomic binding energies, together with this value of $G(^{48}\text{Ca})$ in equation (33)

yields

$$X(^{48}Ca) \approx 0.115. \tag{46}$$

The mass fraction for alpha particles is easily estimated as

$$X_{\alpha} \approx 0.05. \tag{47}$$

Finally, it is interesting to estimate the mass fraction of some nuclear species in the "^{74}Ge peak." From WFHZ a = 10.44, δ = 1.66 MeV for ^{74}Ge so that, using the continuum covering partition function formula, equation (44) gives

$$G(^{74}Ge) \approx 1680.5 \ , \tag{48}$$

and this value together with the appropriate ^{74}Ge Q-value implies, through equation (33),

$$X(^{74}Ge) \approx 0.033. \tag{49}$$

Though this seems like a very small mass fraction for the mean nucleus, recall that it is very easy to add or remove a single neutron near this blocking point. It is then expected that in the "mean nucleus peak," though the mean nucleus itself has a small mass fraction, very many nearby nuclei will have roughly similar abundances, with the result that nearly all of the nuclear material is in this peak. For example, as shown in the last section, the abundance of ^{78}Ge is expected to be about 10 times that of ^{74}Ge at the blocking point. For the purposes of this paper roughly 80% by mass of the nuclear material in nuclear statistical equilibrium will be taken to lie in the blocked mean-nucleus-peak at the blocking point, and all of the nuclei in this peak will be taken to have electron capture characteristics similar to ^{74}Ge.

In § IIb it was estimated that the first unblocked configuration in ^{74}Ge lies at an excitation energy of 5.13 MeV (eq. [16]). This means that, on the average, nuclear levels below this excitation energy are blocked, while those above it are primarily unblocked, capturing electrons according to their thermal population and an average Gamow-Teller matrix element characteristic of this first unblocked configuration. If, indeed, all levels of ^{74}Ge above 5.13 MeV are unblocked, then a "partition function" for unblocked levels, ΔG, can be estimated using equation (43). Taking E_d = 5.13 MeV gives

$$\Delta G(^{74}\text{Ge}) = \frac{\pi}{6akT} \exp\left(akT - \frac{\delta}{kT} - \frac{5.13}{kT}\right)$$
$$= G(^{74}\text{Ge}) \cdot \exp(-5.13/kT). \tag{50}$$

The "mass fraction" or abundance of unblocked ^{74}Ge can now be calculated from equation (33) or from the ratio $\Delta G/G$ and equation (49). At the blocking point

$$\frac{\Delta G}{G} \approx 1.15 \times 10^{-2} , \tag{51}$$

and this will be taken as the characteristic $\Delta G/G$ ratio for nuclei in the mean-nucleus-peak.

The equation (15) sum rule can be applied to the first unblocked configuration in ^{74}Ge to yield an average Gamow-Teller matrix element for the unblocked configurations. In § IIb it was argued that the first unblocked configuration should correspond to the excitation of a $1f_{5/2}$ neutron to the $1g_{9/2}$ neutron shell. This leaves a neutron hole in the $1f_{5/2}$ neutron shell, allowing $1f_{5/2} \rightarrow 1f_{5/2}$ and $1f_{7/2} \rightarrow 1f_{5/2}$ proton $\rightarrow$ neutron transformations induced by electron capture. Noting that $1f_{5/2} \rightarrow 1f_{5/2}$ has $|M_{GT}|^2 = 5/7$ and $1f_{7/2} \rightarrow 1f_{5/2}$ has $|M_{GT}|^2 = 12/7$ and using

equation (15) and the occupation numbers in Figure 1 gives

$$|M_{GT}|^2_{\text{unblocked}} = 8 \times \frac{1}{6} \times \frac{12}{7} + 4 \times \frac{5}{7} \times \frac{1}{6} = \frac{58}{21} = 2.76 \qquad (52)$$

for unblocked ^{74}Ge. This will be taken as the average Gamow-Teller matrix element for unblocked configurations in the blocked mean-nucleus-peak. An estimate of the overall average Gamow-Teller matrix element for a heavy nucleus requires an estimate of $\Delta G/G$ and $|M_{GT}|^2_{\text{unblocked}}$ for the ^{48}Ca-peak. ^{48}Ca itself is not very representative of the electron capture properties of nuclei in the ^{48}Ca-peak. This is because the ground-state to ground-state electron capture Q-value for the reaction $e^- + {}^{48}Ca \rightarrow {}^{48}K + \nu_e$ is $Q_n = -12.502$ MeV (Q_n is defined in eq. [3c] of F^{2}N I; in terms of Q in eq. [3] of this paper for $E_R = 0$, $Q = 12.502$ MeV); whereas, as will be seen in the discussion of the one-zone collapse calculations below, the average electron capture Q-value is, in terms of equation (3),

$$Q = \hat{\mu} + 1.297 + E_R \ , \qquad (53)$$

where E_R, $\hat{\mu}$, and Q are in MeV. Following BBAL, the average $T^< \rightarrow T^>$ unblocked electron capture is given $E_R = 3.0$. The average ground-state to ground-state Q_n will be

$$Q_n \approx - \hat{\mu} - 1.297 \qquad (54)$$

which is roughly -6.3 MeV for the blocking point, agreeing well with $Q_n = -5.911$ MeV for $e^- + {}^{74}Ge \rightarrow {}^{74}Ga + \nu_e$. The much larger negative Q_n for $e^- + {}^{48}Ca \rightarrow {}^{48}K + \nu_e$ means that the rate will be considerably Q-value inhibited, relative to the average capture reaction, due to the strong final neutrino energy dependence of the phase space factor, equation (7). In fact, the F^{2}N II calculations show that the electron capture rate on

^{48}Ca at $T_9 = 10$ and $\rho Y_e = 10^{11}$ g cm^{-3} is almost a factor of 10^3 slower than that on ^{49}Sc ($Q_n = -5.780$) at the same temperature and density.

Though blocked ^{48}Ca can be unblocked through thermal population of the first negative parity level ($J^\pi = 3^-$) at an excitation energy of 4.5073 MeV (Lederer et al. 1978) the above discussion shows that ^{48}Ca cannot practically contribute to the ^{48}Ca-peak neutronization rate. In contrast, ^{49}Sc has not only a smaller electron capture Q-value barrier close to the equation (54) average, but also an appreciable abundance at the blocking point. The abundance of ^{49}Sc is the largest in the ^{48}Ca-peak, next to ^{48}Ca itself. At the blocking point equation (33) can be used to find

$$\frac{X(^{49}\mathrm{Sc})}{X(^{48}\mathrm{Ca})} \approx (0.141)\,\frac{G(^{49}\mathrm{Sc})}{G(^{48}\mathrm{Ca})} \approx 0.22 \qquad (55)$$

where, from WFHZ, $\Delta Q = 9.6274$ MeV, $G(^{49}\mathrm{Sc}) \approx 16.56$, and $G(^{48}\mathrm{Ca}) \approx 10.76$. The more accurate, smaller value of $G(^{48}\mathrm{Ca})$ in equation (45) above is not used here because for a ratio of partition functions it is more accurate to use the same partition function formula for each nucleus. The ratio in equation (55) implies a mass fraction for ^{49}Sc

$$X(^{49}\mathrm{Sc}) \approx 0.0253\ , \qquad (56)$$

where equation (46) for the mass fraction of ^{48}Ca has been used.

Allowed electron capture on ^{49}Sc is not blocked since, in the zero-order shell model, it has one proton in the $1f_{7/2}$ proton orbit and though the $1f_{7/2} \rightarrow 1f_{7/2}$ no-spin-flip transition is blocked due to a filled $1f_{7/2}$ neutron orbit, the $1f_{7/2} \rightarrow 1f_{5/2}$ transition is possible with an equation (15) sum rule of $|M_{GT}|^2 = 12/7$. In order to estimate the overall Gamow-Teller matrix element appropriate for electron capture on heavy nuclei in

the ^{48}Ca-peak ^{49}Sc is adopted as the average unblocked nucleus. In the language of the above thermal unblocking discussion for ^{74}Ge, the $\Delta G/G$ for the ^{48}Ca-peak is taken as the ratio of the ^{49}Sc and ^{48}Ca mass fractions, equation (55).

It is now possible to estimate an effective Gamow-Teller matrix element for electron capture on heavy nuclei with an average Q-value given by equation (53) with E_R = 3.0 MeV. The procedure is to weight the average unblocked matrix element for the mean-nucleus-peak and ^{48}Ca-peak by the appropriate unblocked partition function ratio $\Delta G/G$ for each peak and the overall number density of nuclei in each peak. The effective Gamow-Teller matrix element for capture on heavy nuclei due to thermal unblocking is defined as

$$|M_{GT}|^2_{eff} = \frac{n_{48}\ (\Delta G/G)_{48}\ |M_{GT}|^2_{48} + n_M\ (\Delta G/G)_M\ |M_{GT}|^2_M}{n_\alpha + n_{48} + n_M} \tag{57}$$

where, for instance, n_M is the overall number density of nuclei in the mean-nucleus-peak which, in terms of the overall mean-nucleus-peak mass fraction, is

$$n_M = \rho \frac{X_M\ N_A}{A} \tag{58}$$

with A the mean nuclear mass from equation (22). Similar expressions hold for n_α and n_{48}. In equation (57) $|M_{GT}|^2_M$ is the Gamow-Teller matrix element for the unblocked configurations in the mean nucleus.

Equation (57) for the effective Gamow-Teller matrix can be evaluated at the blocking point conditions by taking, as previously discussed, X_α = 0.05, X_{48} = 0.115, $X(^{49}Sc)$ = 0.0253, X_M = 0.786, and the mean nucleus as ^{74}Ge. Then $(\Delta G/G)_{48}$ can be identified with $X(^{49}Sc)$ and $|M_{GT}|^2_{48}$ with the

^{49}Sc sum rule of 12/7, while $(\Delta G/G)_M$ is taken to be $(\Delta G/G) = 1.15 \times 10^{-2}$ for ^{74}Ge in equation (51) and $|M_{GT}|^2_M = |M_{GT}|^2_{unblocked}$ from equation (52). Equation (57) then becomes

$$|M_{GT}|^2_{eff} = \frac{[X(^{49}Sc)\cdot(12/7)/49] + [(X_M/74)(1.15\times10^{-2})(2.76)]}{X(^{49}Sc)/49 + X_{48}/48 + X_\alpha/4 + X_M/74} \approx 0.0469 \qquad (59)$$

which, from equation (11), implies an effective ft-value of

$$\log(ft)_{eff} = 4.925. \qquad (60)$$

This value of the effective Gamow-Teller matrix element at the blocking point, $|M_{GT}|^2 = 0.0469$, should be compared with the much larger ^{56}Fe sum rule discussed in § IIb, $|M_{GT}|^2 = 10.29$, which is roughly characteristic of the electron capture sum rule used throughout the collapse calculations of BBAL. At least for the conditions at the blocking point the average Gamow-Teller matrix element for heavy nuclei is still characteristic of blocked electron capture, being some 50-100 times smaller than the BBAL Fermi gas matrix element. It should be kept in mind, however, that the thermal unblocking mechanism is very sensitive to the ambient temperature through the expressions for the unblocked partition function ratio $\Delta G/G$ in equations (51) and (56). Were the temperature of order 10 MeV then $\Delta G/G \sim 0.6$, so that $|M_{GT}|^2_{eff} \sim 1$, indicating that the assumption of neutron shell blocking of allowed electron capture would be in jeopardy.

As the collapse progresses from the blocking point the temperature will increase somewhat, but the mean nucleus will become even more neutron rich making it harder in general to thermally populate unblocked configurations. In the one-zone collapse calculations presented below the effective Gamow-Teller matrix element at the blocking point will be

taken as representative of the effective weak matrix element throughout the collapse. Before proceeding to an investigation of the effect of blocking in the collapse, it is first necessary to discuss yet another possible unblocking mechanism: forbidden electron capture.

c) Forbidden Electron Capture

As the collapse proceeds to higher densities, equation (5) shows that the electron Fermi energy increases considerably. By the time the blocking point is reached $\mu_e \sim 18$ MeV. As the density increases past $\rho = 4 \times 10^{11}$ g cm^{-3} a typical, blocked, one-zone collapse shows $\mu_e \sim 25$ MeV. With such high electron energies the allowed approximation for the expansion of the weak current-current Hamiltonian becomes questionable.

The weak current-current Hamiltonian can be written as

$$H_{weak}(x) = \frac{G_V}{\sqrt{2}}\left(\bar{\Psi}_f \frac{\tau_+}{\sqrt{2}} \gamma_\mu \Psi_i\right) L^\mu(x) - \frac{G_A}{\sqrt{2}}\left(\bar{\Psi}_f \frac{\tau_+}{\sqrt{2}} \gamma_\mu\gamma_5 \Psi_i\right) L^\mu(x) + \text{c.c.} \qquad (61)$$

where a V-A interaction is assumed, G_V and G_A are the usual vector and axial vector weak coupling constants, Ψ_i and Ψ_f are the initial and final nuclear wave functions respectively, and the γ's are the Dirac matrices. The leptonic weak current, $L^\mu(x)$, can be expressed for electron capture as

$$L^\mu(x) = \bar{\nu}_e(x)\gamma^\mu (1 - \gamma_5)\, e(x) \ , \qquad (62)$$

where $\nu_e(x)$ and $e(x)$ represent the final neutrino and initial electron wave functions respectively. The Bjorken and Drell (1964) normalization convention can be used for the Dirac spinors and, for example, the initial electron spinor is

$$e(x) = \left(\frac{m_e c^2}{W}\right)^{\frac{1}{2}} u\, e^{ip_e \cdot x} \qquad (63)$$

where p_e is the electron four-momentum, W the total electron energy, u the Dirac spinor, and m_e the electron rest mass.

The electron capture rate is given by an integral of $|H_{weak}|^2$ over the final nuclear and neutrino momenta. The allowed approximation to $|H_{weak}|^2$ consists of two parts: 1) an assumption of nonrelativistic nucleons, so that only the large components of the nucleon spinors in the nucleon currents are connected, and 2) an assumption of small leptonic momentum transfer in the capture reaction. The first approximation depends on the proton velocities being small compared to the velocity of light and is valid for the nuclei encountered in the collapsing stellar core.

The second approximation has its origin in the exponentials in the lepton spinors (e.g., eq. [63]). The Hamiltonian $H_{weak}(x)$ will contain a factor

$$H_{weak}(x) \propto e^{i(q_\nu - p_e)\cdot x} \tag{64}$$

where q_ν is the neutrino four-momentum. The integral over the time components of equation (64) and the similar term for the nucleons gives the familiar energy conserving δ-function of Fermi's Golden Rule. The spatial components of equation (64) can be expanded as

$$e^{i(\vec{q}_\nu - \vec{p}_e)\cdot\vec{x}} \approx 1 + i\,(\vec{q}_\nu - \vec{p}_e)\cdot\vec{x} - \ldots \tag{65}$$

where $\vec{q}_\nu - \vec{p}_e$ is now the momentum transfer in the electron capture, and the expansion is in powers of this momentum transfer. For small momentum transfer the allowed approximation 2) is made and the exponential is taken equal to unity. However, as the electron energy increases, the momentum transfer increases and the second term in the equation (65) expansion must be retained. This is the first-forbidden term. It is

potentially important whenever the electron wavelength is not large compared to the nuclear radius.

Retention of $(\vec{q}_\nu - \vec{p}_e)\cdot\vec{x}$ in $H_{weak}(x)$ leads to a term of order $R^2(q_\nu^2 - 2\vec{q}_\nu\cdot\vec{p}_e + p_e^2)$, where R is the nuclear radius, in the first-forbidden electron capture phase space integral and a factor of the radial coordinate in the first-forbidden weak matrix element. This factor of the radial coordinate gives part of the first-forbidden operator a rank-2 tensor component and leads to the selection rules $\Delta J = 0, \pm 1$, no $0 \rightarrow 0$, $\Delta\pi$ = yes; and for the first-forbidden unique operator, $\Delta J = \pm 2$, $\Delta\pi$ = yes. Furthermore, the extra factor of the radial coordinate allows the first-forbidden transitions to change orbital angular momentum and principal quantum number. As a result, the first-forbidden operator can induce fp-shell $\rightarrow$ gd-shell transitions in otherwise blocked nuclei.

An expression for the unique first-forbidden phase space factor can be found by including the extra factor $R^2(q_\nu^2 - 2\vec{q}_\nu\cdot\vec{p}_e + p_e^2)$ in the usual weak transition phase space prescription. The average over initial and sum over final lepton spins causes the cross term to average to zero, $\langle\vec{q}_\nu\cdot\vec{p}_e\rangle = 0$. Finally, noting that $q_\nu^2 = (W - Q)^2$, approximating $p_e^2 \approx W_e^2$, and using the correct prescription for the Coulomb wave function factors from Zyryanova (1963) yields an expression for the electron capture first-forbidden unique phase space factor

$$f_{for}(\text{unique}) = \frac{1}{12}\left(\frac{m_e cR}{\hbar}\right)\left(\frac{1}{m_e c^2}\right)^7 \int_Q^\infty W^2(W - Q)^2\left[W^2 + (W - Q)^2\right] GS_e(1 - S_\nu)\, dW \quad (66)$$

where the notation is as in equations (2) and (3). Switching to Fuller, Fowler, and Newman (1980) (hereafter F^2N I) dimensionless-integrand notation $\omega = W/m_e c^2$ and $q_n = -Q/m_e c^2$, and making the degenerate electron,

free-streaming neutrino approximation yields

$$f_{for}(\text{unique}) = \frac{1}{12}\left(\frac{m_e cR}{\hbar}\right)^2 \int_{|q_n|}^{u} G\omega^2 (\omega - |q_n|)^2 \left[\omega^2 + (\omega - |q_n|)^2\right] d\omega \qquad (67)$$

where $u \equiv \mu_e / m_e c^2$, as in equation (7).

It is well known that the first-forbidden unique transitions are slower than other first-forbidden transitions at the relatively low electron energies characteristic of terrestrial β-decay. In contrast, at the much higher electron energies encountered in the collapsing stellar core first-forbidden unique transitions become the fastest of the first-forbidden transitions. For a detailed treatment of the first-forbidden phase space factors the reader is referred to Zyryanova (1963). Because of the dominance of the first-forbidden unique phase space factor it will be sufficient for the purposes of this discussion to use equation (67) in any estimates of the effect of first-forbidden electron capture.

Taking $q \equiv |q_n|$ and factoring out an average value of the relativistic Coulomb barrier penetration factor G allows the integral in equation (67) to be evaluated explicitly,

$$f_{for} \approx \langle G \rangle \left(\frac{A^{1/3}}{314}\right)^2 \frac{1}{12}\left(\frac{2}{7}u^7 - qu^6 + \frac{7}{5}q^2u^5 - q^3u^4 + \frac{1}{3}q^4u^3 - \frac{2}{105}q^7\right); \qquad (68)$$

note that the term involving the nuclear radius, $R = 1.23\ A^{1/3}$ fm, has been evaluated explicitly for a nucleus of mass number A. Because of the extra energy dependence in the equation (67) integrand the appropriate average value of G for forbidden electron capture should be calculated at a higher electron energy, yielding $\langle G \rangle \approx 1$ for nuclei of charge $Z \sim 30$.

The factor $(A^{1/3}/314)^2$ is not placed in the first-forbidden phase

space factor in the usual discussion of forbidden transitions, but rather in the ft-value. If equation (1) is used to form a ratio of forbidden-to-allowed electron capture rates and a value of A = 80 is employed (typical of the mean nuclear mass near where $\mu_e \sim 25$ MeV in the collapse) then a standard discussion, such as Zyryanova (1963), would give

$$\frac{(ft)_{\text{forbidden}}}{(ft)_{\text{allowed}}} \sim \left(\frac{314}{A^{1/3}}\right)^2 \sim 5 \times 10^3 \ , \tag{69}$$

a factor which acts to reduce substantially the forbidden-to-allowed capture rate. However, the leading order terms in electron Fermi energy in equation (7) for the allowed phase space factor and in equation (68) for the forbidden phase space factor, without the reducing radius-dependent term, are

$$\begin{aligned} f_{\text{for}} &\sim \frac{1}{42} \left(\mu_e/m_e c^2\right)^7 - \ . \ . \ . \\ f_{\text{allowed}} &\sim \frac{2}{5} \left(\mu_e/m_e c^2\right)^5 - \ . \ . \ . \end{aligned} \tag{70}$$

where $\langle G \rangle_{\text{allowed}} \approx 2$, $\langle G \rangle_{\text{for}} \approx 1$. Though the radius-dependent factor (69) may substantially reduce the forbidden-to-allowed ratio, it is clear that greater energy sensitivity in f_{for} will quickly compensate and eventually cause forbidden capture to dominate as μ_e increases without bound. It is cautioned, however, that inclusion of the subtraction terms due to the electron capture Q-value is necessary for a correct ratio of forbidden-to-allowed rates.

Since the actual non-energy dependent unique first-forbidden nuclear matrix element is of the same order as the Gamow-Teller matrix element ($|M_{\text{for}}|^2 \sim |M_{GT}|^2$) the radius-dependent factor (69) is here, correctly,

left in the first-forbidden phase space factor as written in equation (68). Either formulation for the forbidden transition rate is fully equivalent in an estimate of the forbidden-to-allowed electron capture rate ratio.

The forbidden-to-allowed electron capture rate ratio can now be calculated for some representative collapse conditions in order to estimate an effective log ft for blocked heavy nuclei due to first-forbidden electron capture transitions. There are two cases of concern as possible unblocking mechanisms. The first of these is a first-forbidden transition from the ground state of the $T^{<}$-parent nucleus to a <u>single</u> level at, or near, the ground state of the $T^{>}$-daughter nucleus. Though not possessing the full forbidden-strength of all the parent valence protons, such a transition is potentially dangerous to the neutron shell blocking assumption since it has the smallest possible capture Q-value, maximizing the effect of the extra energy dependence of the first-forbidden phase space factor evident in equation (70). The second first-forbidden-unblocking mechanism involves an electron capture transition from the ground state of the $T^{<}$-parent to the "collective" first-forbidden state in the $T^{>}$-daughter. This first-forbidden resonance transition is taken to include the full forbidden-strength of the parent valence protons, yet has a larger electron capture Q-value to surmount due to the likely large particle-hole shift in the first-forbidden resonance excitation energy.

It is convenient to examine both of these forbidden-unblocking-mechanisms at a representative point in the blocked one-zone collapse models. The maximum neutronization rate will occur for high densities, just before neutrino trapping density is reached (at $\rho_{trapping}$ significant electron capture through both forbidden and allowed channels is blocked by the filling of neutrino phase space), where μ_e is very large and

forbidden capture is most important. Therefore the conditions near $\rho \approx 4 \times 10^{11}$ g cm^{-3}, $Y_e \approx 0.35$, $\mu_e \approx 26.8$ MeV, $\hat{\mu} \approx 10.3$ are adopted in the calculations below.

Consider first the first-forbidden transition to the ground state of the daughter nucleus. Near the representative conditions discussed above the mean nucleus has $A \approx 80$ so that the relative ratio of forbidden to allowed ft-values is as given in equation (69), then taking

$$\begin{aligned} Q_{all} &\approx \hat{\mu} + 3.0 + 1.297 \approx 14.597 \text{ MeV} \Rightarrow q \approx 28 \\ Q_{for} &\approx \hat{\mu} + 1.297 \approx 11.597 \text{ MeV} \Rightarrow q \approx 23 \end{aligned} \tag{71}$$

and using $u \approx 50$ in equations (7) and (68), with $\langle G \rangle_{all} \approx 2$, $\langle G \rangle_{for} \approx 1$, and without the $(A^{1/3}/314)^2$ term in equation (68), gives

$$\frac{f_{for}}{f_{all}} \approx 188, \tag{72}$$

so that the ratio of forbidden-to-allowed capture rates is, from equations (1) and (69),

$$\frac{\lambda_{for}}{\lambda_{all}} = \frac{f_{for}}{f_{all}} \frac{(ft)_{all}}{(ft)_{for}} \approx 0.035 \sim 0.04. \tag{73}$$

The rate for a <u>single</u> first-forbidden transition in these conditions is then a few percent of a single allowed transition and thus, if the effective heavy nucleus ft-value from thermal unblocking is $\log(ft)_{eff} \approx 4.9$, single forbidden captures are negligible.

The electron capture transition from the ground state of the mean nucleus (for the above conditions, $^{80}_{30}Zn_{50}$) to the first-forbidden resonance will involve the transformation of fp-shell protons into neutron-holes in the gd-shell. For $^{80}_{30}Zn_{50}$ the $1g_{9/2}$ neutron shell is filled, blocking the

first-forbidden $1f_{7/2} \rightarrow 1g_{9/2}$ and $1f_{5/2} \rightarrow 1g_{9/2}$ transitions. The most likely transitions will involve $1f_{7/2} \rightarrow 1g_{7/2}$, $1f_{5/2} \rightarrow 1g_{7/2}$, $1f_{7/2} \rightarrow 2d_{5/2}$, and $1f_{5/2} \rightarrow 2d_{5/2}$. All 10 fp-shell protons can make these transitions so the first-forbidden collective matrix is here taken to be (taking $|M_{GT}^{sp}|^2 \sim 2$),

$$|M_{for}|^2 \sim 10 \cdot 2 = 20 \quad . \tag{74}$$

The degeneracy of possible particle-hole pairs in these forbidden-resonance transitions is considerably greater than for the allowed-resonance transitions since the selection rules for first-forbidden transitions allow a broader range of single particle orbits to participate than do the more restrictive allowed selection rules. The larger number of particle-hole pairs may mean a greater particle-hole repulsion energy and hence a forbidden resonance at higher excitation energy than the allowed resonance (see e.g., the discussion in F^2N II and Bertsch 1980).

The $^{80}_{30}Zn_{50}$ first-forbidden resonance excitation energy is here estimated to be at an average of the $1g_{7/2}$(neutron)-$1g_{9/2}$(neutron) and $1f_{5/2}$(proton)-$1f_{7/2}$(proton) single particle energy differences. From the Seeger and Howard (1975) average single particle orbit energies

$$\begin{aligned} \left(\varepsilon(1g_{7/2}) - \varepsilon(1g_{9/2})\right)_{\text{neutron}} + 2.0 &= 8.452 \text{ MeV} \\ \left(\varepsilon(1f_{5/2}) - \varepsilon(1f_{7/2})\right)_{\text{proton}} + 2.0 &= 12.908 \text{ MeV} \end{aligned} \tag{75}$$

to give an average $E_R = 10.68$ MeV. The electron capture Q-value for the forbidden resonance transition is then, for $\hat{\mu} \approx 10$ MeV,

$$Q_{for} = \hat{\mu} + 1.297 + 10.68 \approx 21.980 \text{ MeV} \Rightarrow q \approx 43. \tag{76}$$

An effective "Gamow-Teller" matrix element for first-forbidden

transitions can be defined as

$$|M_{GT}|^2_{eff} = |M_{for}|^2 \frac{f_{for}}{f_{all}} \approx (20)\ (7.4 \times 10^{-4}) \approx 0.015 \tag{77}$$

where the first factor is taken from equation (74), and the phase space factors are evaluated with $\langle G \rangle_{for} \approx 1$, u = 50, A = 80, and q = 43 in equation (68), and $\langle G \rangle_{all} \approx 2$, u = 50, and q = 28 in equation (7).

The effective matrix element in equation (77) represents the effect of unblocking due to first-forbidden electron capture on heavy nuclei. This value of $|M_{GT}|^2_{eff}$ corresponds to an ft-value of

$$\log(ft)_{eff} \approx 5.4\ , \tag{78}$$

and is sensitive to the estimated first-forbidden resonance excitation energy. It would seem reasonable to assume an overall effective capture matrix element due to thermal, configuration mixing, and forbidden electron capture unblocking as twice the thermal unblocking result: $|M_{eff}|^2 \approx 0.094$, which corresponds to

$$\log(ft)_{eff} \approx 4.6, \tag{79}$$

a value which will be used below to test the sensitivity of the one-zone collapse results to the unblocking mechanisms.

IV. ONE-ZONE COLLAPSE CALCULATIONS WITH BLOCKING

The effect of neutron shell blocking of electron capture on heavy nuclei during stellar core collapse can be studied with a one-zone calculation. The calculations presented here are modeled after Table X in BBAL, but include a modified equation of state, electron capture on free protons, and electron capture on heavy nuclei with an ft-value characteristic of blocked nuclei.

The intent in doing these calculations is to obtain a general idea of how the temperature, free nucleon fractions, entropy, and especially the lepton-to-baryon ratio in the stellar core might change relative to some standard calculation (Table X, BBAL) as the details of the electron capture physics are varied. This will serve to point up the salient features of both the electron capture physics and the nuclear equation of state which may deserve further work, as well as suggest trends in equation of state parameters which are important in current models of the supernova explosion. The reader is cautioned, however, that only large scale multi-zone, hydrodynamic calculations with a sophisticated equation of state can ultimately give a complete picture of the collapsing stellar core, and is thus referred to Van Riper and Lattimer (1981) for a detailed discussion of the core infall epoch and the effects of complete blocking of nuclear electron capture for $N \geq 40$. The work of Bowers and Wilson (1981) uses a sophisticated approach to neutrino transport to study the collapse infall epoch, while Epstein and Pethick (1980) have varied the parameters of the collapse input physics over a wide range to obtain limits on the final characteristics of the neutronized core.

In the calculations performed here the evolution of a single zone with initial density ρ, entropy-per-nucleon S, temperature T, and electron

fraction Y_e is examined for a simple uniform collapse rate. In brief, as the collapse proceeds ρ increases, thus increasing the electron Fermi energy μ_e and causing the electron capture rate to rise. Electron capture lowers Y_e and adds entropy S, though the magnitudes of these effects depend on the detailed electron capture physics. The increase in entropy causes a rise in both temperature and the mass fraction of dripped nucleons, but the relative magnitude of each depends on other equation of state parameters.

The electron capture rates on free protons and heavy nuclei for a given ρ, Y_e are calculated with equations (1) and (7) as discussed above, and are hereby designated by λ_{fp} and λ_H respectively. The modified BBAL equation of state is used to calculate all important nuclear parameters, μ_n, $\hat{\mu}$, X_p, X_n as discussed in § IIIa. The mass fraction of heavy nuclei is

$$X_H = 1 - X_n - X_p \tag{80}$$

so that the total neutronization rate is ($\dot{Y}_e \equiv dY_e/dt$)

$$\dot{Y}_e = - \lambda_{fp} X_p - \lambda_H \frac{(1 - X_n - X_p)}{A} \tag{81}$$

where A is the mean nuclear mass in equation (22).

The collapse rate is taken to be the same as that used in Table X of BBAL to facilitate comparison with that work. For a core of mass M interior to a radius R an equation for the free fall velocity $\dot{R}$ can be found from a first integral of the equations of motion (energy conservation):

$$\frac{-\dot{R}}{R} = \left(\frac{2GM}{R^3}\right)^{1/2} \propto \rho^{1/2} . \tag{82}$$

Equation (82) can be simplified by noting that $(d\,\ell n\,R/dt) = -1/3\ (d\,\ell n\,\rho/dt)$, so that

$$\frac{d\,\ell n\,\rho}{dt} = 3\left(\frac{8\pi G}{3}\right)^{1/2} \times 10^5\ (\rho_{10})^{1/2} \approx 224\ \rho_{10}^{1/2}. \tag{83}$$

The dominant contribution to the pressure during the collapse comes from the relativistically degenerate electron gas and, in fact, the collapse rate will be considerably slower than equation (83) due to this pressure. BBAL estimate an average of 20% of the initial lepton support pressure present during the collapse and obtain the collapse rate used here,

$$\frac{d\,\ell n\,\rho}{dt} = 100\ \rho_{10}^{1/2}\ . \tag{84}$$

Though the sensitivity of the final Y_e at neutrino trapping to the collapse rate should be further investigated, this study shows little sensitivity: were the collapse slower than equation (84) there would be a longer time for electron captures to take place but a much slower rise in μ_e and hence slower overall neutronization rates, while for faster collapse the reverse is true. Thus the changes in electron capture rates and the time available for electron captures tend to compensate each other as the collapse rate is varied.

Equations (81) and (84) can be combined to give the density differential of the electron-fraction,

$$\frac{dY_e}{d\rho} = \left(-\lambda_{fp} X_p - \lambda_H\left(\frac{1 - X_n - X_p}{A}\right)\right) \cdot \frac{10^{-12}}{\rho_{10}^{3/2}} \tag{85}$$

which is then used to compute ΔY_e given $\Delta\rho$.

The first-law of thermodynamics,

$$dE + PdV = dQ = TdS + \sum_i \mu_i\ dN_i \tag{86}$$

can be used to calculate the change of entropy-per-nucleon with changes in Y_e. The entropy-per-nucleon will now be denoted S, where it is hoped that no confusion will result from having used the same symbol for the total entropy in equation (86). For the capture reaction $e^- + p \rightarrow n + \nu_e$ <u>in nuclei</u> the term $\sum_i \mu_i \, dN_i$ becomes, dividing by the total number of baryons,

$$\left(\sum_i \mu_i dY_i\right)_H = \mu_e dY_e + \mu_p dY_p - \mu_n dY_n - \mu_\nu dY_\nu - 1.297$$
$$= dY_e \, (\mu_e - \hat{\mu} - 1.297) \quad \text{MeV}, \tag{87}$$

where $\mu_\nu = 0$ since beta equilibrium does not obtain, and $dY_e = dY_p = -dY_n$. This same term for capture on <u>free</u> protons becomes simply

$$\left(\sum_i \mu_i dY_i\right)_{fp} = dY_e \, (\mu_e - 1.297) \quad \text{MeV}. \tag{88}$$

If dQ is taken to represent the added heat per baryon due to electron capture, then clearly

$$dQ = - \bar{\varepsilon}_\nu \, (- dY_e) \tag{89}$$

where $\bar{\varepsilon}_\nu$ is the average neutrino energy per electron capture. If λ^ν_{fp} and λ^ν_H are the neutrino energy loss rates (MeV s^{-1}) for electron capture on free protons and heavy nuclei respectively (from eqs. [1] and [8]), then the average neutrino energies (in MeV) for capture on free protons $\bar{\varepsilon}_\nu(fp)$ and heavy nuclei $\bar{\varepsilon}_\nu(H)$ are

$$\bar{\varepsilon}_\nu(fp) = \lambda^\nu_{fp}/\lambda_{fp} \quad ; \quad \bar{\varepsilon}_\nu(H) = \lambda^\nu_H/\lambda_H \, . \tag{90}$$

Equation (86) for dQ, together with equations (87) and (88) can be used to write an expression for the entropy-per-baryon change dS

$$TdS = dQ - \sum_i \mu_i \, dY_i = (-dY_e)_H \left(\mu_e - \hat{\mu} - 1.297 - \bar{\varepsilon}_\nu(H)\right) + (-dY_e)_{fp} \left(\mu_e - 1.297 - \bar{\varepsilon}_\nu(fp)\right) \tag{91}$$

where $(dY_e)_H$ is the change in Y_e due to electron capture on heavy nuclei, $(dY_e)_{fp}$ the change due to capture on free protons ($dY_e = (dY_e)_H + (dY_e)_{fp}$), and the temperature is expressed in MeV, dS in units of Boltzmann's constant (k). Equation (91) can now be rewritten using $(dY_e)_H = [(1 - X_n - X_p)/A]\lambda_H dt$ and $(dY_e)_{fp} = X_p \lambda_{fp} dt$ to yield an expression for the change in entropy-per-baryon with density in terms of the change in Y_e with density,

$$T\left(\frac{dS}{d\rho}\right) = \left(\frac{-dY_e}{d\rho}\right)\left\{\left(\mu_e - \hat{\mu} - 1.297 - \bar{\varepsilon}_\nu(H)\right) \frac{(1 - X_p - X_n)\lambda_H}{AX_p + (1 - X_p - X_n)\lambda_H} + \left(\mu_e - 1.297 - \bar{\varepsilon}_\nu(fp)\right) \frac{X_p A \lambda_{fp}}{AX_p + (1 - X_p - X_n)\lambda_H}\right\} \tag{92}$$

where A is, again, the mean nuclear mass number.

Equation (92) becomes more transparent if it is noted that $(\mu_e - \hat{\mu} - 1.297 - \bar{\varepsilon}_\nu(H))$ is the average excitation energy per baryon left in the system nucleus-plus-electron-gas per electron captured on heavy nuclei, while $(\mu_e - 1.297 - \bar{\varepsilon}_\nu(fp))$ is the average excitation energy per baryon left in the degenerate electron gas per electron captured on free protons. The excitation of internal degrees of freedom in a system must appear as an increase in entropy. Since the electron capture Q-value (eq. [3]) is taken for the mean nucleus as $Q = \hat{\mu} + 3.0 + 1.297$ (in MeV), electron captures on heavy nuclei add a considerable amount of entropy to the system, whereas, electron captures on free protons, with their smaller Q-value (Q = 1.297 MeV), add very little entropy yet produce

very energetic neutrinos which efficiently cool the system.

The procedure followed in these one-zone collapse calculations is to increment the density and use equation (85) to give ΔY_e and equation (92) to then get $T\Delta S$. With a new ρ, Y_e, S it is necessary to compute a new temperature T and neutron fraction X_n, and subsequently new values of $\hat{\mu}$ and μ_n. This can be accomplished via an explicit expression for S and a two-dimensional root finder using equation (30) and

$$\Delta T = \left(\left.\frac{\partial S}{\partial T}\right|_{\rho,Y_e}\right)^{-1}\left\{\Delta S - \left.\frac{\partial S}{\partial Y_e}\right|_{\rho,T}\Delta Y_e - \left.\frac{\partial S}{\partial \rho}\right|_{Y_e,T}\Delta\rho\right\}. \tag{93}$$

The entropy per nucleon is taken to include terms due to the internal excitation energy of the electron gas, $S \approx \pi^2 kT/\mu_e$ and of nuclei, $S \approx \pi^2 kT/\varepsilon_F$, where the formula is for a nearly degenerate Fermi gas with ε_F the nucleon Fermi energy in nuclei. The other contributions to the entropy come from the nondegenerate gas of neutrons and nuclei and make use of a nondegenerate expression for the Landau potential Ω to give,

$$S = -\left.\frac{\partial\Omega}{\partial T}\right|_{V,\mu} \Rightarrow S \approx \frac{5}{2}N + \frac{3}{2}N\left\{\ell n(kT) + \ell n\left(\frac{mc^2}{2\pi\hbar^2}\right) + \ell n\left(\frac{V}{N}\right)\right\} \tag{94}$$

for a gas of N particles of mass m in volume V and where S is here the <u>total</u> entropy in units of k. Neglecting the small contribution of dripped protons, the entropy per nucleon of the system of electrons, nuclei, and nucleons is (in units of k),

$$\begin{aligned} S \approx &\left\{\frac{\pi^2 Y_e}{\mu_e} + 0.2467(1 - X_n)\right\}kT + \left\{\frac{2.5(1 - X_n)}{A} + \frac{(1 - X_n)}{A}\,\ell n\left(\frac{39.49\,A^{\frac{5}{2}}(kT)^{\frac{3}{2}}}{\rho_{10}(1 - X_n)}\right)\right\} \\ &+ \left\{2.5\,X_n + X_n\,\ell n\left(\frac{79.07(kT)^{\frac{3}{2}}}{\rho_{10}\,X_n}\right)\right\}, \end{aligned} \tag{95}$$

with μ_e and kT expressed in MeV.

Three examples of one-zone collapse models are presented in Tables 1 through 3. Each of these calculations starts from the same initial conditions $\rho_{10} = 0.37$, $Y_e = 0.42$, kT $\approx$ 0.66 MeV, $X_n \approx 0.0024$, S/K = 0.905, and $\mu_n \approx$ -7.1 MeV. These variables differ very slightly in temperature and considerably in neutron-fraction from the initial BBAL Table X conditions because of the differing μ_n, which is here roughly 2 MeV larger throughout the collapse. The effect of the larger free nucleon concentration and the inclusion of electron capture on free protons can be seen in Table 1, which allows electron capture on the mean heavy nucleus with $Q = \hat{\mu} + 4.297$ MeV and $|M_{GT}|^2 \approx 2.5$ (log ft$\approx$3.2) — note the lower temperatures and larger neutron fractions as compared with BBAL Table X which has no capture on free protons and $|M_{GT}|^2_{eff} \approx 3\text{-}4$ in the Fermi gas formulation of heavy nuclei.

The effect of complete blocking ($|M_{GT}|^2 = 0$, log ft = ∞) of electron capture on heavy nuclei is presented in Table 2. This calculation does, however, include captures on free protons which help to cool the material considerably. The lack of electron capture on heavy nuclei, with its large entropy input, and this extra neutrino cooling serve to keep the dripped nucleon fraction smaller than in Table 1.

The effect of a nominal amount of configuration mixing, thermal, and forbidden-electron-capture unblocking can be seen in Table 3. This calculation has electron capture on free protons and allows captures on heavy nuclei with the characteristic "blocked" matrix element of $|M_{GT}|^2 \approx 0.1$ (log ft $\approx$ 4.6), as discussed in the last section. The effect of unblocking of otherwise blocked nuclei makes a small difference in the final Y_e at neutrino trapping density, which is here taken to occur

between $\rho_{10} = 59.16$ and $\rho_{10} = 79.74$. The completely blocked calculation, Table 2, gives $Y_e^f \approx 0.37$, while the addition of what is probably an overestimate of unblocking in Table 3 gives $Y_e^f \approx 0.34$. In contrast the completely unblocked Table 1 calculation and the BBAL Table X calculation each give $Y_e^f \approx 0.27$, pointing up the considerable reduction in the neutronization rate caused by blocking.

Where electron capture on heavy nuclei is allowed in the above calculations, $Q = \hat{\mu} + 3.0 + 1.297$. If most of the unblocking in Table 3 were due to forbidden electron capture then, as discussed in the last section, the mean excitation energy per heavy-nucleus-electron-capture may be somewhat higher than 3.0 MeV. Use of a larger Q would lead to a slight increase in entropy production in Table 3.

As noted in § IIIa the Table 2 calculation takes the mean nucleus as blocked from the beginning of the collapse on. Similarly, electron capture on heavy nuclei is given the small characteristic unblocking matrix element in Table 3 from the beginning of the collapse on. As discussed in § IIIa this approximation of collapse-onset blocking makes little difference in Y_e^f. Were unrestricted electron capture on heavy nuclei allowed up to the actual blocking point ($\rho_{10} \sim 10$) the mean heavy nucleus would be more neutron rich going into the regime of rapid neutronization ($10 \lesssim \rho_{10} \lesssim 40\text{-}60$) and would therefore be harder to unblock thermally, leading to possibly less neutronization than in collapse calculations blocked from the beginning.

V. CONCLUSION

It is found from a study of the simple shell model and using a modified BBAL equation of state that as stellar core collapse proceeds

nuclei become more and more neutron rich, eventually reaching a point where all neutron fp-shell orbits are filled, blocking allowed electron capture on fp-shell protons. This neutron shell blocking effect can be relieved through configuration mixing, spreading of the ensemble of nuclei in nuclear statistical equilibrium to include unblocked nuclei, the thermal population of unblocked configurations in blocked nuclei, and forbidden electron capture at high electron Fermi energy. An estimate of these unblocking mechanisms was made for appropriate collapse conditions to give a characteristic electron capture matrix element for heavy nuclei. Though sensitive to the temperature and other state variables, this "unblocking" matrix element, $|M_{GT}|^2 \approx 0.1$, was found to be quite small in comparison to that of BBAL Table X, $|M_{GT}|^2 \sim 2.5$, for typical collapse conditions. One-zone collapse calculations performed with this small "unblocking" matrix element yield an electron-fraction at neutrino trapping of roughly $Y_e^f \approx 0.34$, versus the value of $Y_e^f \approx 0.27$ for completely unblocked calculations.

This larger lepton-fraction at neutrino trapping may lead to a larger inner-core mass as discussed by Van Riper and Lattimer (1981) and Baym, Bethe, and Brown (1981), and may in turn lead to a stronger post-bounce shock.

At the beginning of collapse the stellar core has a mass which is slightly larger than the Chandrasekhar mass due to the extra thermal pressure from the hot electrons (Fowler 1980),

$$M_{HC} \equiv M_{\text{hot core}} \gtrsim M_{CHAND} = 5.8 \langle Y_e^2 \rangle M_\odot \qquad (96)$$

where $\langle Y_e^2 \rangle$ is the average of Y_e^2 over the core. For an initial $Y_e = 0.43$, Baym, Bethe, and Brown (1981) and hereafter B^3, found an initial

core mass of $M_{HC}^{i} \approx 1.5\ M_{\odot}$, while Van Riper and Lattimer (1981) take $M_{HC}^{i} \approx 1.9\ M_{\odot}$. The inner-core mass is defined as that mass interior to the sonic point in the homologously collapsing stellar core. For Y_e^f characteristic of unblocked and blocked collapse the hot inner-core masses are in the ratio $(Y_e^f(\text{UNBLOCKED})/Y_e^f(\text{BLOCKED}))^2$,

$$\begin{aligned} Y_e^f &= 0.27 \text{ (WITHOUT BLOCKING)} \Rightarrow M_{HC}^f \approx 0.5\ M_{\odot} \\ Y_e^f &= 0.34 \text{ (WITH BLOCKING)} \Rightarrow M_{HC}^f \approx 0.8\ M_{\odot} \ . \end{aligned} \tag{97}$$

Van Riper and Lattimer (1981) find a typical inner-core mass without blocking to be $M_{HC}^f \approx 0.49\ M_{\odot}$, while the blocked case gives $M_{HC}^f \approx 0.71\ M_{\odot}$. In other words there is a 50-60% increase in the neutronized inner-core mass due to neutron shell blocking of electron capture.

This increase in inner-core mass leads to a small yet significant increase in the post-bounce shock energy. As discussed in B^3 the infall kinetic energy, E_{kin}, is converted with a large efficiency factor into the shock energy, E_{shock}, at the bounce of the inner core. The infall kinetic energy is roughly the gravitational potential energy release, E_{grav}, times the pressure deficit, so that

$$E_{shock} \sim E_{kin} \sim E_{grav}\ (Y_e^i - Y_e^f) \ , \tag{98}$$

where

$$E_{grav} \sim G(M_{HC}^f)^2/R_{HC}^f \sim (M_{HC}^f)^{5/3} \ . \tag{99}$$

The dependence of E_{grav} on the final inner-core mass follows from the homology relation $R_{HC}^f \sim (M_{HC}^f)^{1/3}$. Clearly then since $M_{HC}^f \sim (Y_e^f)^2$

$$E_{shock} \sim (Y_e^f)^{10/3}\ (Y_e^i - Y_e^f) \tag{100}$$

which has a maximum value for $Y_e^f/Y_e^i = 10/13 \approx (0.33)/(0.43)$. For the blocked electron capture case in which $Y_e^f \approx 0.34$ the shock energy will be roughly 20% larger than in the completely unblocked case. Though this is a small increase in shock energy it must be kept in mind that the energy available for the ejection of the stellar mantle is the difference in two large, nearly equal quantities: the shock energy and the gravitational binding energy (B^3)

$$E_{ejection} = E_{shock} - E_{grav.\ binding} . \tag{101}$$

Therefore the extra shock energy due to blocking may be important.

The effect of the blocking-induced increase in the inner-core mass on convective overturn models of supernova explosions is not yet completely clear. There is a larger lepton-fraction in the neutronized core which aids the development of the inverted entropy gradient, but at the same time there is more mass to overturn. On balance, a larger core mass may narrowly go against overturn (Lattimer and Mazurek 1981; Bowers and Wilson 1980; Livio, Buchler, and Colgate 1979; Colgate 1981; Smarr et al. 1980).

It should be pointed out that there are other mechanisms which may increase the core mass and shock energy, notably rotation and mixing (Fowler 1981).

Finally, it can be inferred from the work of B^3 that some form of electron capture blocking, either the neutron shell blocking discussed here, or blocking of final neutrino phase space is important in getting a large shock energy. Both of these blocking mechanisms require a large mean nuclear mass to be effective. Further work on the nuclear equation of state for $10^9 \lesssim \rho$ (in g cm^{-3}) $\lesssim 10^{12}$ with a special effort made on the nuclear mass could be useful in determining the extend of blocking.

REFERENCES

Arnett, W. D. 1977, Ap. J., 218, 815.

_____. 1980, private communication.

Arnett, W. D., and Thielemann, F. K. 1981, in preparation.

Bertsch, G. F. 1980, Nucl. Phys., A354, 157c.

Bethe, H. A. et al. 1979, Nucl. Phys., A324, 487.

Baym, G., Bethe, H. A., and Brown, G. E. 1981, preprint.

Baym, G., Bethe, H. A., and Pethick, C. J. 1971, Nucl. Phys., A175, 225.

Bjorken, J. D., and Drell, S. D. 1964, Relativistic Quantum Mechanics (New York: McGraw-Hill).

Bloom, S. D., and Fuller, G. M. 1981, in preparation.

Bonche, P., and Vautherin, D. 1981, preprint.

Bowers, R., and Wilson, J. R. 1980, private communication.

_____. 1981, preprint.

Burbidge, E. M., Burbidge, G. R., Fowler, W. A., and Hoyle, F. 1957, Rev. Mod. Phys., 29, 547.

Cameron, A. G. W. 1959, Ap. J., 130, 453.

Colgate, S. A. 1981, private communication.

El Eid, M. F., and Hillebrandt, W. 1980, Astr. Ap. Suppl. Ser., 42, 215.

Epstein, R. I., and Pethick, C. J. 1980, to appear in Ap. J. .

Fowler, W. A. 1980, private communication.

_____. 1981, private communication.

Fowler, W. A., and Hoyle, F. 1964, Ap. J. Suppl., 9, 201.

Fuller, G. M., Fowler, W. A., and Newman, M. J. 1980, Ap. J. Suppl., 42, 447.

_____. 1981a, preprint.

_____. 1981b, preprint.

Hansen, C. J. 1966, Ph.D. thesis, Yale University.

Klapdor, H. V. 1976, Cern-Report 76-13, Proc. 3rd Int. Conf. Nuclei Far From Stability.

Lamb, D. Q., Lattimer, J. M., Pethick, C. J., and Ravenhall, D. G. 1978, Phys. Rev. Lett., 41, 1623.

Lattimer, J. M. 1980, private communication.

Lattimer, J. M., and Mazurek, T. J. 1981, preprint, to appear in Proceedings of Dumond – 1981.

Lederer, D. M. et al. 1978, Table of Isotopes, eds. Lederer, C. M and Shirley, V. S. (New York: Wiley & Sons).

Livio, M., Buchler, J.-R., and Colgate, S. A. 1979, Los Alamos preprint.

Mazurek, T. J., Truran, J. M., and Cameron, A. G. W. 1974, Ap. Space Sci., 27, 261.

Nilsson, S. G. 1955, Kgl. Danske Videnskab. Selskab, Mat.-Fys. Med, 29, 16.

Seeger, P. A., and Howard, W. M. 1975, Nucl. Phys., A238, 491.

Seeger, P. A., and Perisho, R. 1967, Los Alamos Scientific Laboratory Report, LA-3751.

Smarr, L., Wilson, J. R., Barton, R., and Bowers, R. 1980, preprint.

Tsuruta, S. and Cameron, A. G. W. 1965, Can. J. Phys., 43, 2056.

Tubbs, D. L., and Koonin, S. E. 1979, Ap. J. (Letters), 232, L59.

Van Riper, K. A., and Lattimer, J. M. 1981, preprint.

Wapstra, A. H., and Bos, K. 1977, Atomic Data and Nuclear Data Tables, 20, 1.

Weaver, T. A., and Woosley, S. E. 1980, private communication.

_____. 1981, in preparation.

Weaver, T. A., Zimmerman, G. B., and Woosley, S. E. 1978, Ap. J., 225, 1021.

Woosley, S. E., Fowler, W. A., Holmes, J. A., and Zimmerman, B. A. 1978, Atomic Data and Nuclear Data Tables, 23, 371.

Zyryonova, L. N. 1963, Once-Forbidden Beta-Transitions, (New York: Macmillan).

TABLE 1

ONE-ZONE COLLAPSE CALCULATION WITH ELECTRON CAPTURE ON FREE PROTONS AND HEAVY NUCLEI ($|M_{GT}|^2 \approx 2.5$, log ft ≈ 3.2). THE MEAN NUCLEUS HAS MASS NUMBER A, CHARGE $Z \approx Y_e A/(1 - X_n)$. THE OTHER QUANTITIES ARE DISCUSSED IN THE TEXT.

ρ_{10}	Y_e	kT (MeV)	X_n	S/k (per nucleon)	$\hat{\mu}$ (MeV)	μ_n (MeV)	A
0.3700	0.4200	0.6596	0.002418	0.905	4.208	-7.100	67.50
0.4987	0.4200	0.7001	0.003473	0.905	4.143	-7.136	67.66
0.6722	0.4200	0.7408	0.004657	0.905	4.071	-7.176	67.84
0.9060	0.4200	0.7822	0.005929	0.905	3.995	-7.218	68.05
1.2211	0.4200	0.8246	0.007260	0.905	3.919	-7.262	68.29
1.6458	0.4197	0.8682	0.008729	0.906	3.875	-7.293	68.61
2.2183	0.4186	0.9125	0.010736	0.910	3.959	-7.272	69.14
2.9899	0.4157	0.9558	0.013980	0.921	4.294	-7.146	70.03
4.0299	0.4105	0.9954	0.019108	0.941	4.933	-6.895	71.37
5.4317	0.4031	1.0290	0.026449	0.969	5.838	-6.537	73.13
7.3210	0.3940	1.0559	0.036130	1.004	6.941	-6.104	75.25
9.8675	0.3833	1.0763	0.048330	1.044	8.194	-5.619	77.68
13.2998	0.3711	1.0911	0.063426	1.090	9.565	-5.096	80.41
17.9259	0.3575	1.1014	0.082059	1.142	11.033	-4.547	83.43
24.1612	0.3421	1.1087	0.105198	1.201	12.575	-3.982	86.76
32.5653	0.3249	1.1160	0.134214	1.268	14.160	-3.414	90.39
43.8927	0.3054	1.1284	0.170923	1.345	15.744	-2.861	94.32
59.1601	0.2832	1.1540	0.217395	1.433	17.271	-2.343	98.52
79.7381	0.2580	1.2041	0.275227	1.532	18.687	-1.878	102.99
107.4739	0.2302	1.2919	0.344132	1.639	19.956	-1.477	107.75
144.8571	0.2009	1.4287	0.420715	1.746	21.086	-1.135	112.92

TABLE 2

ONE-ZONE COLLAPSE CALCULATION WITH ELECTRON CAPTURE ON FREE PROTONS BUT WITH CAPTURE ON HEAVY NUCLEI COMPLETELY BLOCKED ($|M_{GT}|^2 = 0$; log ft = ∞). NOTATION AS IN TABLE 1.

ρ_{10}	Y_e	kT (MeV)	X_n	S/k (per nucleon)	$\hat{\mu}$ (MeV)	μ_n (MeV)	A
0.3700	0.4200	0.6596	0.002417	0.905	4.208	-7.100	67.50
0.4987	0.4200	0.7001	0.003473	0.905	4.143	-7.136	67.66
0.6722	0.4200	0.7408	0.004657	0.905	4.071	-7.176	67.84
0.9060	0.4200	0.7822	0.005929	0.905	3.995	-7.218	68.05
1.2211	0.4200	0.8246	0.007258	0.905	3.919	-7.262	68.29
1.6458	0.4199	0.8683	0.008625	0.905	3.848	-7.304	68.58
2.2183	0.4199	0.9134	0.010029	0.905	3.792	-7.343	68.93
2.9899	0.4195	0.9599	0.011493	0.906	3.762	-7.371	69.36
4.0299	0.4190	1.0078	0.013083	0.907	3.780	-7.381	69.91
5.4317	0.4179	1.0567	0.014917	0.909	3.875	-7.360	70.62
7.3210	0.4162	1.1060	0.017168	0.913	4.081	-7.294	71.55
9.8675	0.4135	1.1554	0.020027	0.920	4.426	-7.172	72.75
13.2998	0.4098	1.2047	0.023649	0.929	4.913	-6.993	74.26
17.9259	0.4052	1.2542	0.028122	0.941	5.530	-6.765	76.07
24.1612	0.3999	1.3048	0.033486	0.957	6.250	-6.498	78.18
32.5653	0.3938	1.3578	0.039786	0.975	7.052	-6.204	80.59
43.8927	0.3871	1.4145	0.047120	0.996	7.923	-5.888	83.34
59.1601	0.3798	1.4763	0.055668	1.021	8.861	-5.554	86.47
79.7381	0.3717	1.5450	0.065732	1.050	9.869	-5.199	90.05
107.4739	0.3627	1.6226	0.077780	1.083	10.959	-4.823	94.18
144.857	0.3524	1.7122	0.092536	1.123	12.149	-4.418	99.01

TABLE 3

ONE-ZONE COLLAPSE CALCULATION WITH ELECTRON CAPTURE ON FREE PROTONS AND WITH CAPTURE ON HEAVY NUCLEI BUT WITH A MATRIX ELEMENT ($|M_{GT}|^2 \approx 0.1$, log ft = 4.6) CHARACTERISTIC OF CONFIGURATION MIXING, THERMAL, AND FORBIDDEN ELECTRON CAPTURE UNBLOCKING OF AN OTHERWISE BLOCKED MEAN NUCLEUS.

ρ_{10}	Y_e	kT (MeV)	X_n	S/k (per nucleon)	$\hat{\mu}$ (MeV)	μ_n (MeV)	A
0.3700	0.4200	0.6596	0.002417	0.905	4.208	-7.100	67.50
0.4987	0.4200	0.7001	0.003473	0.905	4.143	-7.136	67.66
0.6722	0.4200	0.7408	0.004657	0.905	4.071	-7.176	67.84
0.9060	0.4200	0.7822	0.005929	0.905	3.995	-7.218	68.05
1.2211	0.4200	0.8246	0.007258	0.905	3.919	-7.262	68.29
1.6458	0.4199	0.8683	0.008630	0.905	3.850	-7.304	68.58
2.2183	0.4197	0.9133	0.010068	0.906	3.801	-7.339	68.94
2.9899	0.4193	0.9597	0.011649	0.907	3.797	-7.356	69.40
4.0299	0.4183	1.0072	0.013537	0.910	3.873	-7.341	70.02
5.4317	0.4164	1.0552	0.015985	0.916	4.077	-7.274	70.88
7.3210	0.4134	1.1029	0.019321	0.925	4.449	-7.139	72.03
9.8675	0.4089	1.1497	0.023889	0.940	5.012	-6.926	73.52
13.2998	0.4029	1.1951	0.030013	0.962	5.762	-6.639	75.38
17.9259	0.3955	1.2393	0.038022	0.989	6.680	-6.289	77.61
24.1612	0.3865	1.2825	0.048333	1.024	7.749	-5.884	80.21
32.5653	0.3759	1.3257	0.061529	1.066	8.957	-5.432	83.22
43.8927	0.3636	1.3701	0.078423	1.116	10.291	-4.940	86.67
59.1601	0.3492	1.4180	0.100067	1.176	11.738	-4.417	90.60
79.7381	0.3327	1.4736	0.127721	1.246	13.266	-3.876	95.04
107.4739	0.3137	1.5441	0.162698	1.326	14.835	-3.335	100.03
144.8571	0.2924	1.6395	0.206072	1.416	16.398	-2.811	105.63

Figure 1

The zero-order shell model diagram of ^{74}Ge, a typical blocked nucleus at the blocking point. The approximate scales for single particle energies, temperature, and electron Fermi energy are shown. Blocked and forbidden transitions are as indicated. The blocked $1f_{5/2} \rightarrow 1f_{7/2}$ back-spinτflip electron capture is not shown.

SHELL BLOCKING OF ELECTRON CAPTURE DURING NEUTRONIZATION IN SUPERNOVA CORE COLLAPSE

(G.M. FULLER, 1980)

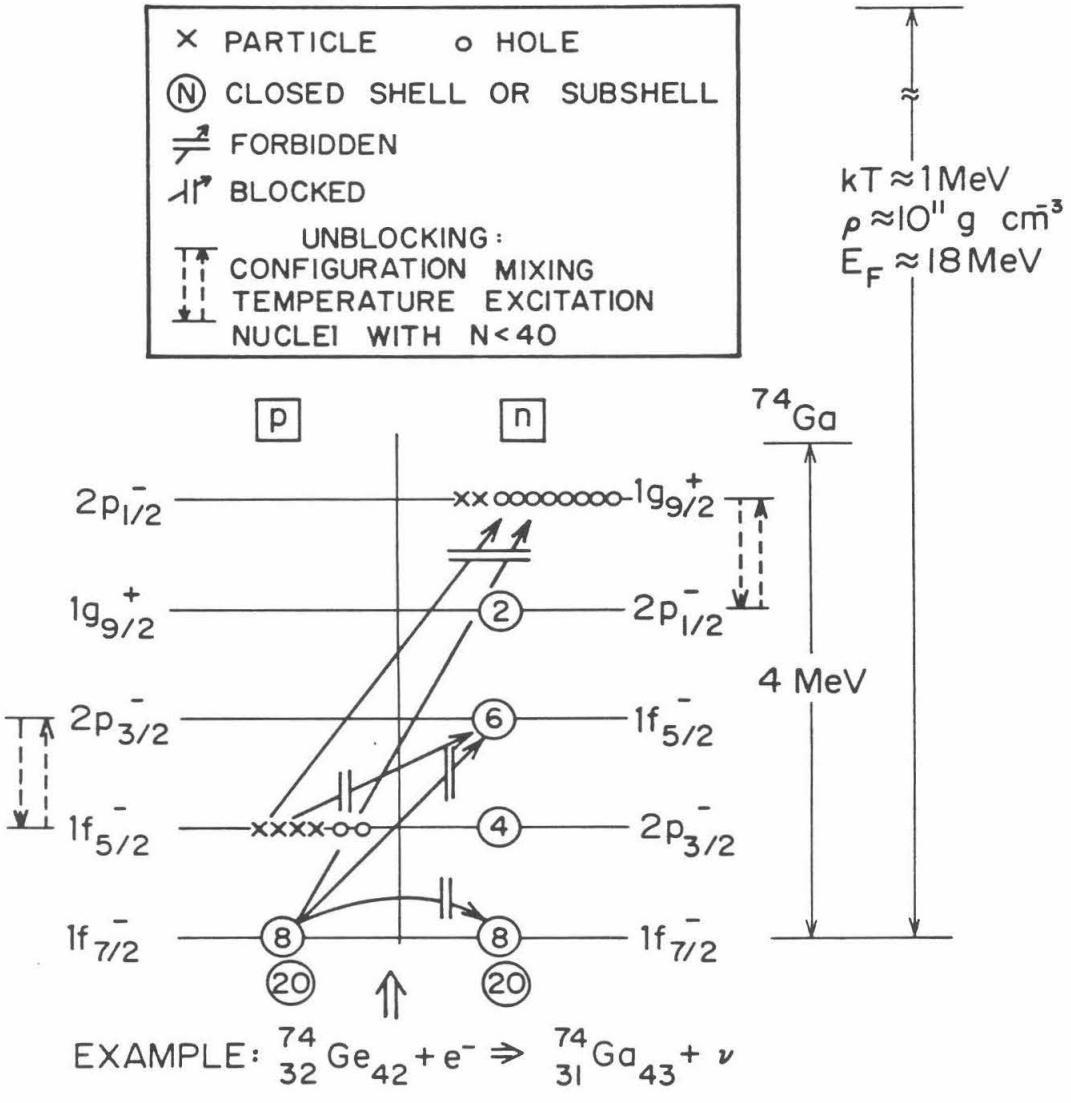

SHELL ENERGIES

SEEGER & PERISHO LA-3751 (1967)

SEEGER & HOWARD NUCL. PHYS. A238,491 (1975)

Fig. 1

APPENDIX

SHELL MODEL CALCULATIONS OF GAMOW-TELLER STRENGTH FUNCTIONS

The discussion in chapter III (F^2N II) refers to large scale moment-method calculations of Gamow-Teller strength functions for ^{56}Fe(ground state) → ^{56}Mn, ^{56}Fe(1^{st}-excited state) → ^{56}Mn, ^{60}Fe(ground state) → ^{60}Mn, ^{60}Fe(1^{st}-excited state) → ^{60}Mn, ^{64}Fe(ground state) → ^{64}Mn, and ^{64}Fe(1^{st}-excited state) → ^{64}Mn. This is the work of Bloom and Fuller (1981) and is in preparation. This appendix gives a very cursory description of these calculations and a presentation of some preliminary results.

The calculations of the Gamow-Teller strength functions for the above weak transitions were performed with the Cornelius vector shell model code at the Lawrence Livermore National Laboratory (Hausman 1976; Bloom and Hausman 1979; Bloom, Grimes, and Hausman 1980). The Cornelius program allows the treatment of many-Fermion systems of very large dimensionality through the representation of Slater determinants as binary vectors in the computer. One and two body operators are similarly represented as sums of binary masks with appropriate coefficients.

The two-body Hamiltonian used in these calculations is based on an analysis of and fit to many experimental and theoretical values for two-body matrix elements (Schiffer and True 1976; Scott and Moszkowski 1962; Bloom, Hausman, and Larsen 1980) and has been adjusted to fit, as closely as possible, both the M1-excitation and analog-antianalog separation energies in selected intermediate mass nuclei.

The procedure followed in these calculations is to generate wave functions for the ground and first excited states for each of ^{56}Fe, ^{60}Fe,

and ^{64}Fe via diagonalization of the two-body Hamiltonian described above in a large basis of appropriate fp-shell Slater determinants. A standard one-body Gamow-Teller operator is then used to generate a collective Gamow-Teller state ψ_{CGT},

$$|\psi_{CGT}\rangle = \sum_{ij} \langle i|\vec{\sigma}\tau_-|j\rangle \; a_i^{\dagger} a_j |\psi\rangle \tag{A1}$$

where $|\psi\rangle$ is the appropriate vector-representation wave function for either the ground or first excited state. As described in chapter II the Gamow-Teller collective state $|\psi_{CGT}\rangle$ is not generally an eigenstate of the daughter nucleus, and as a result $|\psi_{CGT}\rangle$ must be diagonalized with the two-body Hamiltonian in the daughter nucleus.

The Cornelius vector shell model code uses the Lanczos technique (see e.g., Whitehead et al. 1977) to diagonalize the Hamiltonian with $|\psi_{CGT}\rangle$. If we let $|\varphi_1\rangle = |\psi_{CGT}\rangle$ then for a Hermitian Hamiltonian H

$$\begin{aligned}
H|\varphi_1\rangle &= \alpha_1|\varphi_1\rangle + \beta_1|\varphi_2\rangle \\
H|\varphi_2\rangle &= \beta_1|\varphi_1\rangle + \alpha_2|\varphi_2\rangle + \beta_2|\varphi_3\rangle \\
H|\varphi_3\rangle &= \beta_2|\varphi_2\rangle + \alpha_3|\varphi_3\rangle + \beta_3|\varphi_4\rangle \\
&\vdots \qquad\qquad \vdots
\end{aligned} \tag{A2}$$

where the orthogonal $|\varphi_1\rangle$, $|\varphi_2\rangle$, ..., are referred to as the Lanczos vectors. The above process ceases when the Lanczos vectors span the dimensionality N of the basis of Slater determinants in $|\psi_{CGT}\rangle$ and, clearly, the Lanczos vectors form an orthonormal basis of dimension N which is an alternative to the shell model Slater determinant basis we started with. In this Lanczos vector basis, the Hamiltonian takes on a

tri-diagonal form,

$$\hat{H} = \begin{pmatrix} \alpha_1 & \beta_1 & & & \\ \beta_1 & \alpha_2 & \beta_2 & & \\ & \beta_2 & \alpha_3 & . & \\ & & . & . & . \\ & & & . & . \end{pmatrix} . \qquad \text{(A3)}$$

The eigenstates of this matrix are easily solved for due to the tri-diagonal nature of $\hat{H}$. If these eigenstates are denoted $\{|y\rangle\}$ then the eigenstates of the original Hamiltonian matrix $\{|x\rangle\}$, are given by

$$|x\rangle = \begin{pmatrix} . & . & & . \\ . & . & & . \\ . & . & & . \\ . & . & & . \\ \varphi_1 & \varphi_2 & \cdots & \varphi_N \\ . & . & & . \\ . & . & & . \\ . & . & & . \\ . & . & & . \end{pmatrix} |y\rangle \qquad \text{(A4)}$$

where the columns of the transformation matrix are the coefficients of the Slater determinants in φ_1, φ_2, etc.

Depending on the limitations of computer memory and time available the initial Lanczos vector $|\psi_{CGT}\rangle$ can be operated on with the Hamiltonian H a large number of times. The resulting Gamow-Teller strength-carrying states $|x\rangle$ are eigenstates of H. The total Gamow-Teller strength in $|\psi_{CGT}\rangle$ is given by

$$\langle\psi_{CGT}|\psi_{CGT}\rangle = \sum_x \langle\psi_{CGT}|x\rangle\langle x|\psi_{CGT}\rangle = \sum_x |\langle x|\psi_{CGT}\rangle|^2 . \qquad \text{(A5)}$$

Diagonalization after n iterations of the equation (A2) Lanczos process yields n daughter nucleus eigenstates $|x\rangle$ with Gamow-Teller strength $|\langle x|\psi_{CGT}\rangle|^2$ and excitation energy E_x. Diagonalization of H after N iterations yields the complete spectrum of Gamow-Teller strength-carrying states (strength and excitation energies), but this is usually a prohibitively expensive calculation.

Typical of the calculations performed here is the 15-iteration strength function calculation for the ground state of ^{56}Fe. The ground state wave function for ^{56}Fe ($J^\pi = 0^+$) contains 1184 orthonormal Slater determinants built from a model in which two proton holes are allowed to roam over the $1f_{7/2}$ proton orbit, while two neutron particles are allowed to roam over the $1f_{5/2}$ - $2p_{1/2}$ - $2p_{3/2}$ space of orbits and where the $1f_{7/2}$ neutron orbit is taken as closed. The $|\psi_{CGT}\rangle$ corresponding to this state (eq. [A1]) must have $J^\pi = 1^+$ by the Gamow-Teller operator selection rules, and is found to contain 646 Slater determinants (now 3p - 3h) from which 90 $J^\pi = 1^+$ ^{56}Mn eigenstates could be found from 90 iterations of the Lanczos process followed by diagonalization in energy E_x, spin J = 1, and isospin T = 3. This would be too expensive, however, and a smaller number of iterations is found to approximate the strength spectrum quite well (Whitehead 1980).

The results for 15 iteration strength function calculations for the collective Gamow-Teller state made from the ground state and first excited state of ^{56}Fe (E_x = 0.847 MeV, $J^\pi = 2^+$) are given in Tables 1 and 2 respectively. The first column in these tables gives the excitation energy (in MeV) E_x discussed above, while the second column gives the fraction of strength contained in the energy feature $|x\rangle$,

$$\frac{|M_{GT}|^2 \text{ (of } |x\rangle)}{\int |M_{GT}|^2 \, dE} = \frac{|\langle x|\psi_{CGT}\rangle|^2}{\langle \psi_{CGT}|\psi_{CGT}\rangle} \quad . \tag{A6}$$

The column labeled "width" gives the range of uncertainty (in MeV) of the excitation energy of feature $|x\rangle$. Only 13 of the 15 $|x\rangle$ states are listed in these tables since the remaining states at higher excitation energy carry negligible strength. Figures 1 and 2 plot the fraction of strength per MeV in each energy feature as a function of ^{56}Mn excitation energy, for the Gamow-Teller collective states corresponding to the ground and first excited state, respectively, of ^{56}Fe (both 15 and 21 interation calculations are shown). Figure 3 shows the <u>envelope</u> of these strength functions.

The total strength of the Gamow-Teller collective states corresponding to the ^{56}Fe ground state is $\langle \psi_{CGT}|\psi_{CGT}\rangle \approx 9.125$ (log ft ≈ 2.64), while that for the first excited state is $\langle \psi_{CGT}|\psi_{CGT}\rangle \approx 9.656$ (log ft = 2.61). The collective state corresponding to the ^{56}Fe first excited state can be diagonalized in spin J to give three component collective states: $J^\pi = 1^+$ ($|M_{GT}|^2 \approx 3.567$; log ft ≈ 3.04), $J^\pi = 2^+$ ($|M_{GT}|^2 \approx 1.311$; log ft ≈ 3.48), $J^\pi = 3^+$ ($|M_{GT}|^2 \approx 4.778$; log ft ≈ 2.92).

Similar calculations have been performed for the ground state ($J^\pi = 0^+$) and first excited state ($E_x \approx 0.84$, $J^\pi = 2^+$ in this calculation) of ^{60}Fe. The model of ^{60}Fe used here allows 2 proton holes to roam over the $1f_{7/2}$ proton orbit, while the $1f_{7/2}$ and $2p_{3/2}$ neutron orbits are taken as closed, and 2 neutron particles are allowed to roam over the $2p_{1/2} - 1f_{5/2}$ neutron orbit space. The collective states generated from these ^{60}Fe states then correspond to 3p - 3h wave functions. The 15 iteration diagonalization for the ^{60}Fe-ground-state collective wave functions is given in

Table 3. This collective state has total Gamow-Teller strength $\langle \psi_{CGT} | \psi_{CGT} \rangle \approx 7.326$ (log ft = 2.73). The 15 iteration diagonalization for the ^{60}Fe-first-excited-state collective wave function is given in Table 4. This collective state has total Gamow-Teller strength $\langle \psi_{CGT} | \psi_{CGT} \rangle \approx 7.036$ (log ft = 2.75)

The Gamow-Teller strength function for ^{64}Fe is especially interesting, since in the zero-order shell model discussed in chapter III this is a blocked nucleus. The model used for the calculation of the ^{64}Fe ground state and first excited state wave functions allows 2 proton holes to roam over the $1f_{7/2}$ proton orbit, while again taking the $1f_{7/2} - 2p_{3/2}$ neutron orbit space as closed, and now allowing 2 neutron holes to roam over the $2p_{1/2} - 1f_{5/2}$ neutron orbit space. Were the $2p_{1/2}$ neutron orbit to lie above the $1f_{5/2}$ neutron orbit the $1f_{5/2}$ orbit would be completely filled and, according to the chapter III sum rule, $|M_{GT}|^2 = 0$. Were the order of these orbits reversed the $1f_{5/2}$ orbit would have 2 neutron holes implying $|M_{GT}|^2 = 6 \cdot 2/6 \cdot 12/7 \approx 3.429$ (log ft = 3.06). The 15 interation diagonalizations of the Gamow-Teller collective wave functions for the ^{64}Fe ground state and first excited state are presented in Tables 5 and 6 respectively.

The strengths calculated in these collective states indicate a situation intermediate to the completely blocked and unblocked situations discussed above. The total Gamow-Teller strength in the collective wave functions corresponding to the ^{64}Fe ground state is $\langle \psi_{CGT} | \psi_{CGT} \rangle \approx 1.061$ (log ft $\approx$ 3.57); that in the collective wave function corresponding to the ^{64}Fe first excited state is $\langle \psi_{CGT} | \psi_{CGT} \rangle \approx 1.052$ (log ft $\approx$ 3.57). Note that the ^{64}Fe first excited state does not show any unblocking relative to the ^{64}Fe ground state.

REFERENCES

Bloom, S. D., and Fuller, G. M. 1981, in preparation.

Bloom, S. D., Grimes, S. M., and Hausman, R. F. 1980, preprint, UCRL-83803.

Bloom, S. D., and Hausman, R. F. 1976, preprint, UCRL-83368.

Bloom, S. D., Hausman, R. F., and Larsen, J. 1980, The (p,n) Reaction and the Nucleon-Nucleon Force (New York: Plenum Press).

Hausman, R. F. 1976, Ph.D. thesis, UCRL-52178.

Schiffer, J. P., and True, W. W. 1976, Rev. Mod. Phys., 48, 191.

Scott, B. L., and Moszkowski, S. A. 1962, Nucl. Phys., 29, 665.

Whitehead, R. R. 1980, preprint, University of Glasgow.

Whitehead, R. R., Watt, A., Cole, B. J., and Morrison, I. 1977, "Computational Methods for Shell Model Calculations," in Advances in Nuclear Physics, 9, 123.

TABLE 1

COLLECTIVE GAMOW-TELLER STATE ($J^{\pi} = 1^{+}$) DIAGONALIZATION IN ^{56}Mn CORRESPONDING TO ^{56}Fe GROUND STATE ($J^{\pi} = 0^{+}$)

(15 ITERATIONS)

ENERGY FEATURES — EXCITATION ENERGY (MeV) IN ^{56}Mn	$\frac{\lvert M_{GT}\rvert^2}{\int \lvert M_{GT}\rvert^2 \, dE}$	WIDTH (MeV)
0.2403	0.02590	0.0218
1.0584	0.00751	1.7138
1.3379	0.27320	0.6228
1.9326	0.17674	0.9659
2.6711	0.12725	1.2721
3.5858	0.14256	1.2202
4.5729	0.16727	1.1534
5.3929	0.06539	1.3156
6.6316	0.00989	1.5062
7.7594	0.00374	1.1639
9.1837	3.36×10^{-4}	1.5973
10.2276	1.65×10^{-4}	1.1640
11.1590	3.41×10^{-5}	0.8212

TABLE 2

COLLECTIVE GAMOW-TELLER STATE DIAGONALIZATION ($J^{\pi} = 1^{+}, 2^{+}, 3^{+}$) IN ^{56}Mn CORRESPONDING TO ^{56}Fe FIRST EXCITED STATE ($J^{\pi} = 1^{+}$)

(15 ITERATIONS)

ENERGY FEATURES — EXCITATION ENERGY (MeV) IN ^{56}Mn	$\frac{\lvert M_{GT}\rvert^2}{\int \lvert M_{GT}\rvert^2 \, dE}$	WIDTH (MeV)
0.0034	0.00348	0.1666
0.3492	0.00440	0.4335
1.2053	0.02175	0.7171
1.9045	0.11171	0.7569
2.7906	0.21023	1.0145
3.6169	0.18140	1.4016
4.6553	0.28376	1.1800
5.5082	0.14687	1.2553
6.7438	0.02943	1.3735
7.8883	0.00538	1.6026
9.1950	0.00144	1.1946
10.4249	1.42×10^{-4}	1.4164
11.6018	2.88×10^{-5}	1.010

TABLE 3

COLLECTIVE GAMOW-TELLER STATE DIAGONALIZATION IN ^{60}Mn CORRESPONDING TO ^{60}Fe GROUND STATE ($J^{\pi} = 0^{+}$)

(15 ITERATIONS)

ENERGY FEATURES — EXCITATION ENERGY (MeV) IN ^{60}Mn	$\frac{\lvert M_{GT}\rvert^2}{\int \lvert M_{GT}\rvert^2 \, dE}$	WIDTH (MeV)
0.4812	0.35754	0.0371
1.0663	0.06715	0.7680
1.5473	0.10816	1.4392
2.2428	0.17339	1.5169
3.1822	0.14494	1.9015
4.0733	0.11728	1.8117
5.1670	0.02660	1.8800
6.9233	0.00380	1.9256
8.5059	9.17×10^{-4}	2.0462
10.2376	1.48×10^{-4}	2.010
12.4310	2.66×10^{-5}	1.8586

TABLE 4

COLLECTIVE GAMOW-TELLER STATE DIAGONALIZATION IN ^{60}Mn CORRESPONDING TO ^{60}Fe FIRST EXCITED STATE ($J^{\pi} = 1^{+}, 2^{+}, 3^{+}$)

(15 ITERATIONS)

ENERGY FEATURES – EXCITATION ENERGY (MeV) IN ^{60}Mn	$\frac{\lvert M_{GT}\rvert^2}{\int \lvert M_{GT}\rvert^2 \, dE}$	WIDTH (MeV)
0.1410	0.00271	0.6941
0.4681	0.05540	0.4508
1.1955	0.12029	0.6413
2.0729	0.13106	1.1583
3.0659	0.28596	1.2533
3.9505	0.29493	1.2085
5.2626	0.08278	1.5356
6.4754	0.02328	1.7232
8.1336	0.00293	1.9765
9.8308	5.61×10^{-4}	1.9738
11.4984	8.33×10^{-5}	1.9631

TABLE 5

COLLECTIVE GAMOW-TELLER STATE DIAGONALIZATION IN ^{64}Mn CORRESPONDING TO ^{64}Fe GROUND STATE ($J^{\pi} = 0^{+}$)

(15 ITERATIONS)

ENERGY FEATURES – EXCITATION ENERGY (MeV) IN ^{64}Mn	$\frac{\lvert M_{GT}\rvert^2}{\int \lvert M_{GT}\rvert^2 \, dE}$	WIDTH (MeV)
0.0002	0.92953	4×10^{-5}
0.1464	1.03×10^{-6}	0.1232
0.3092	6.65×10^{-6}	0.0430
1.4885	7.41×10^{-7}	0.5151
1.9261	7.56×10^{-6}	0.6377
2.2786	0.06444	0.0094
2.8551	3.16×10^{-6}	1.0305
3.6195	0.00369	0.0302
4.2046	2.63×10^{-4}	0.1136
5.1170	7.80×10^{-4}	0.8745
5.1483	4.54×10^{-4}	1.1369
5.9131	8.22×10^{-4}	0.0386

TABLE 6

COLLECTIVE GAMOW-TELLER STATE DIAGONALIZATION IN ^{64}Mn CORRESPONDING TO ^{64}Fe FIRST EXCITED STATE

(15 ITERATIONS)

ENERGY FEATURES – EXCITATION ENERGY (MeV) IN ^{64}Mn	$\frac{\lvert M_{GT}\rvert^2}{\int \lvert M_{GT}\rvert^2}$	WIDTH (MeV)
0.0015	3.27×10^{-8}	0.0503
0.3075	9.86×10^{-5}	0.0055
0.6315	6.70×10^{-9}	1.3041
1.4034	0.02992	0.0022
1.8913	0.01028	0.0091
2.4121	0.00443	0.0171
3.4201	0.01314	0.0294
3.9716	0.05297	0.1088
4.0689	0.07448	0.0877
4.8664	0.01076	0.0268
5.5490	0.12833	0.0056
6.2392	4.48×10^{-4}	0.5716
6.3103	0.00120	0.3815
6.5675	0.67392	0.0035
6.7053	1.98×10^{-5}	0.1779

Figure 1

The fraction of the total Gamow-Teller strength contained in each energy feature is plotted against ^{56}Mn excitation energy for the collective state corresponding to the ^{56}Fe ground state. The vertical axis is in ($|M_{GT}|^2/\langle\Psi_{CGT}|\Psi_{CGT}\rangle$) PER MeV, so that the fraction of the total Gamow-Teller strength contained in an energy feature is given by the height of the bar times its width in MeV. Both 15 (light) and 21 (heavy) iteration calculations are shown.

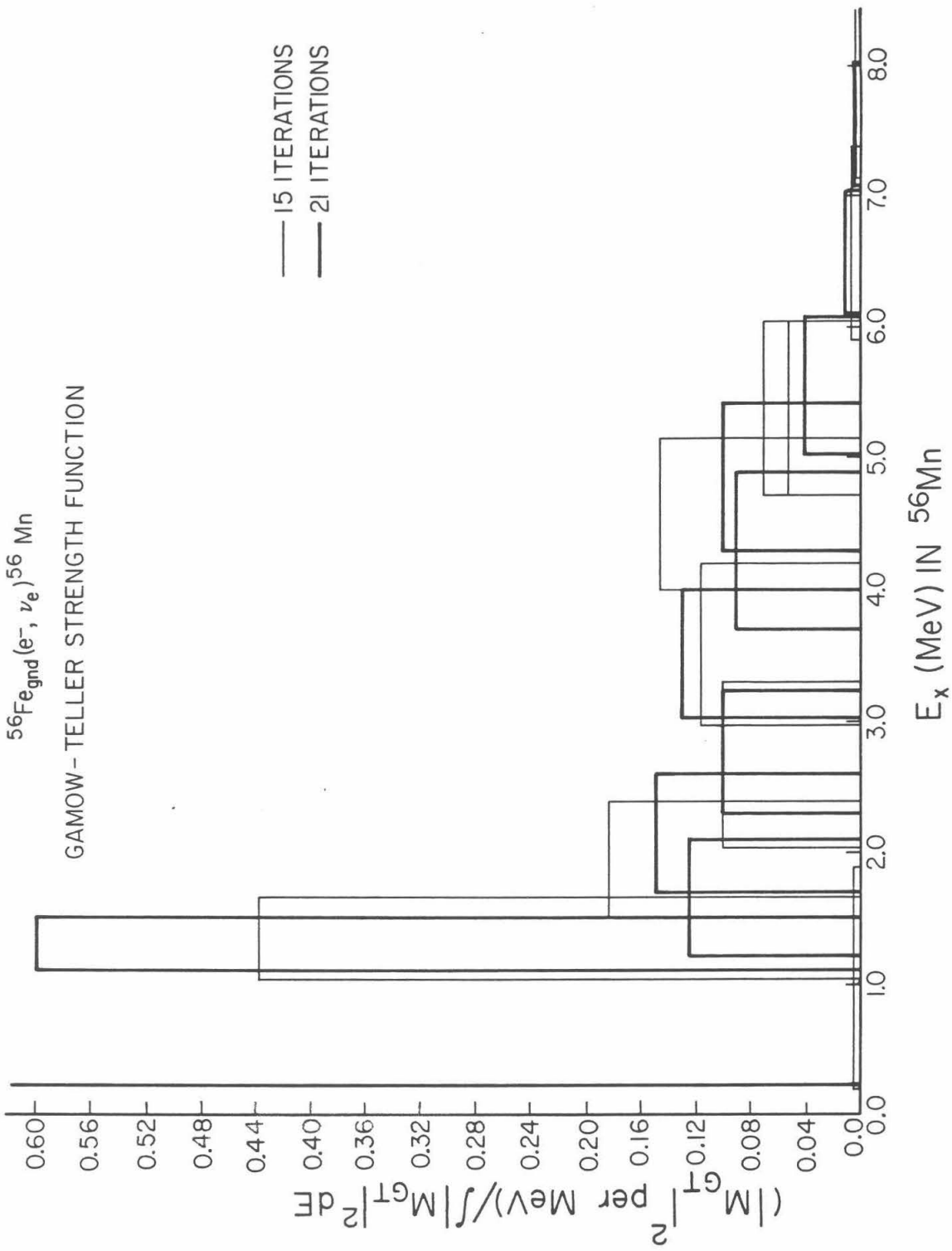
$^{56}Fe_{gnd}(e^-, \nu_e)^{56}$ Mn
GAMOW-TELLER STRENGTH FUNCTION
15 ITERATIONS
21 ITERATIONS
$(|M_{GT}|^2$ per MeV$)/\int|M_{GT}|^2 dE$
E_x (MeV) IN ^{56}Mn
0.0
0.04
0.08
0.12
0.16
0.20
0.24
0.28
0.32
0.36
0.40
0.44
0.48
0.52
0.56
0.60
1.0
2.0
3.0
4.0
5.0
6.0
7.0
8.0

Fig. 1

Figure 2

The fraction of the total Gamow-Teller strength contained in each energy feature is plotted against ^{56}Mn excitation energy for the collective state corresponding to the ^{56}Fe first excited state. The vertical axis is in $(|M_{GT}|^2/\langle\Psi_{CGT}|\Psi_{CGT}\rangle)$ PER MeV, so that the fraction of the total Gamow-Teller strength contained in an energy feature is given by the height of the bar times its width in MeV. Both 15 (light) and 21 (heavy) iteration calculations are shown.

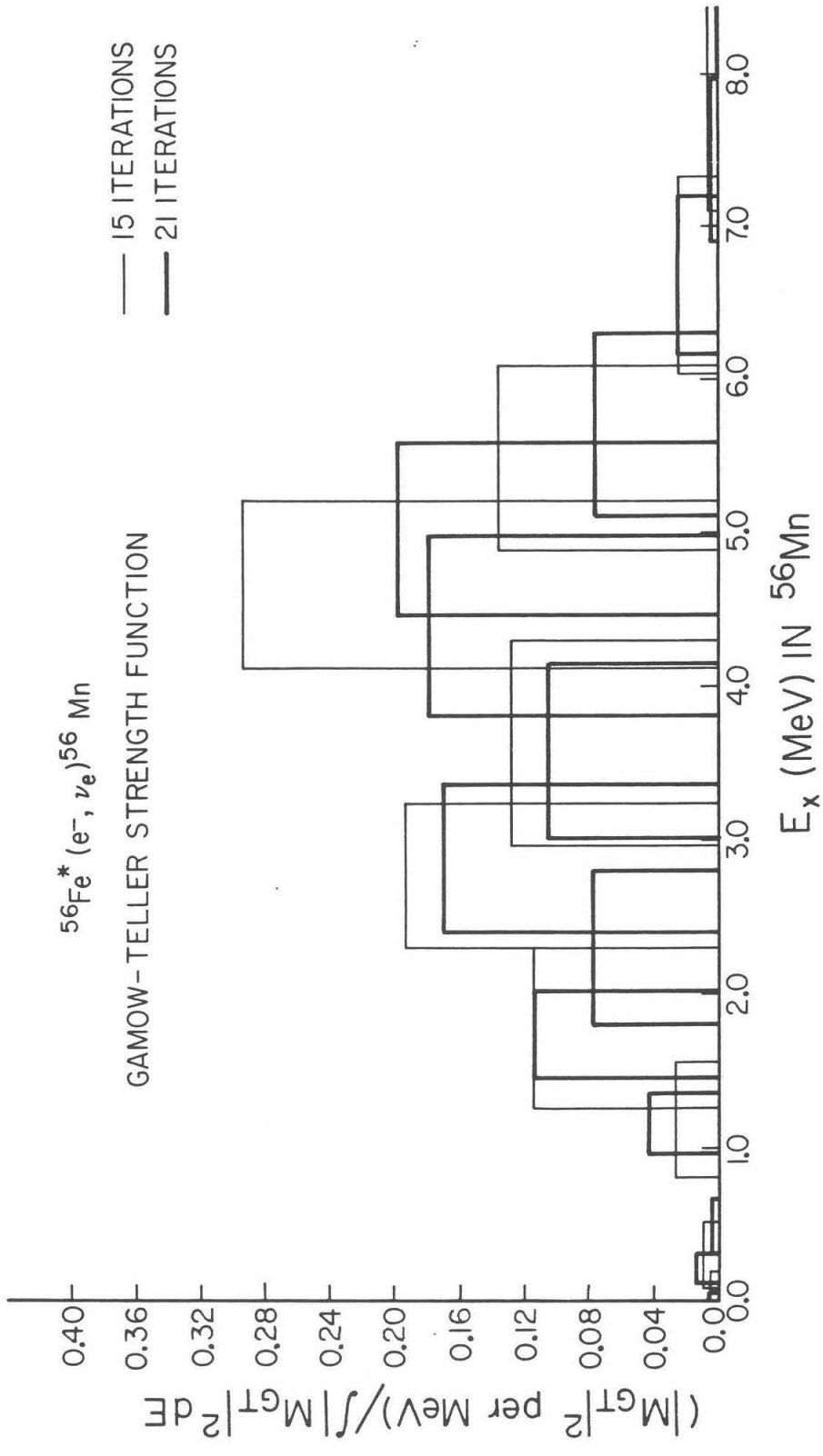
15 ITERATIONS
21 ITERATIONS
$^{56}Fe^{*}(e^{-}, \nu_e)^{56}Mn$
GAMOW-TELLER STRENGTH FUNCTION
E_x (MeV) IN ^{56}Mn
$(|M_{GT}|^2$ per MeV$)/\int |M_{GT}|^2 dE$
0.0
0.04
0.08
0.12
0.16
0.20
0.24
0.28
0.32
0.36
0.40
1.0
2.0
3.0
4.0
5.0
6.0
7.0
8.0

Fig. 2

Figure 3

The envelopes of the 15-iteration calculations of the ^{56}Fe ground and first excited state Gamow-Teller strength functions are shown. The heavy line corresponds to the ^{56}Fe ground state ($J^{\pi} = 0^{+}$), while the light line corresponds to the first excited state ($J^{\pi} = 2^{+}$). The arrows are drawn from the parent states to the approximate centroids of the appropriate Gamow-Teller strength distributions. These arrows denote electron capture transitions possible in a stellar interior. The ground state-to-ground state electron capture Q-value is given as $Q_{\beta} = -Q_{n} = 3.6954$ MeV.

$^{56}Fe\ (e^-, \nu_e)^{56}Mn$

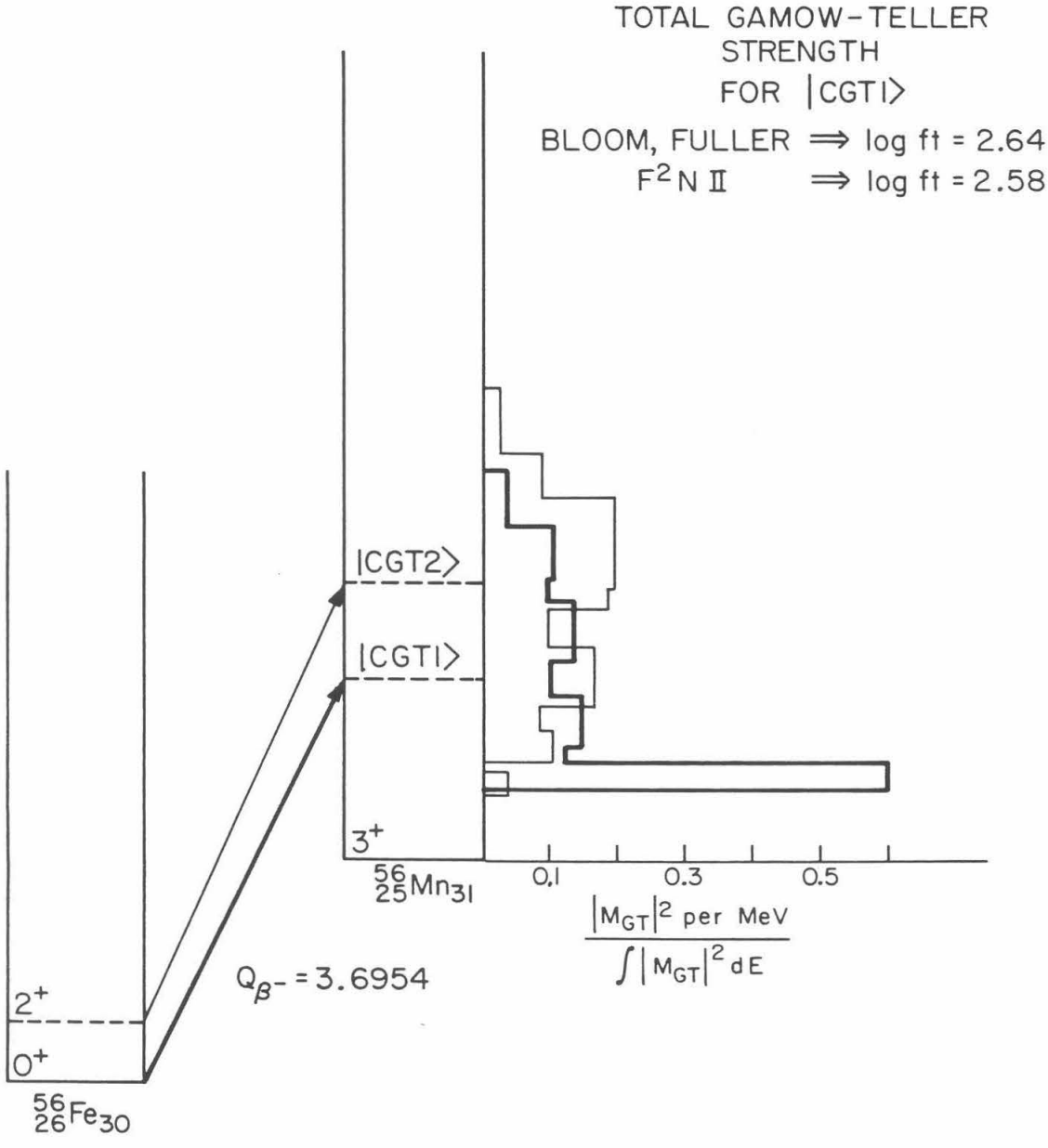

Fig. 3